

Reset Control and Control Allocation for High-precision Motion Systems



Ruud Beerens

Reset Control and Control Allocation for High-precision Motion Systems

Ruud Beerens

disc

The author has successfully completed the educational program of the Graduate School of the Dutch Institute of Systems and Control (DISC).

TU/e

**EINDHOVEN
UNIVERSITY OF
TECHNOLOGY**



The work described in this thesis was carried out at the Eindhoven University of Technology and is part of the research programme “CHAMeleon” with project number 13896, which is (partly) financed by the Netherlands Organisation for Scientific Research (NWO).

A catalogue record is available from the Eindhoven University of Technology Library.
ISBN: 978-90-386-4979-5

Reproduction: Ipskamp Printing, Enschede, the Netherlands



© 2020 by R. Beerens. All rights reserved.

Reset Control and Control Allocation for High-precision Motion Systems

PROEFSCHRIFT

ter verkrijging van de graad van doctor aan de
Technische Universiteit Eindhoven, op gezag van de
rector magnificus prof.dr.ir. F.P.T. Baaijens, voor een
commissie aangewezen door het College voor
Promoties, in het openbaar te verdedigen
op maandag 2 maart 2020 om 16:00 uur

door

Ruud Beerens

geboren te Oosterhout

Dit proefschrift is goedgekeurd door de promotoren en de samenstelling van de promotiecommissie is als volgt:

voorzitter: prof.dr. L.P.H. de Goey
1^e promotor: prof.dr.ir. N. van de Wouw
2^e promotor: prof.dr. H. Nijmeijer
copromotor: prof.dr.ir. W.P.M.H. Heemels
leden: prof.dr.ir. B. Jayawardhana (Rijksuniversiteit Groningen)
prof.dr.ir.habil. R.I. Leine (University of Stuttgart)
dr.ir. R. Tóth
prof.dr. L. Zaccarian (LAAS-CNRS and University of Trento)

Het onderzoek dat in dit proefschrift wordt beschreven is uitgevoerd in overeenstemming met de TU/e Gedragscode Wetenschapsbeoefening.

Summary

Reset Control and Control Allocation for High-precision Motion Systems

Motion control is a key enabling technology in a broad range of high-tech applications ranging from electron microscopes, pick-and-place machines, and copiers to wafer scanners, thereby representing an enormous value for the Dutch economy. The corresponding high-tech industries are currently facing numerous challenges in order to maintain their competitive position in the market. Namely, there is an ever increasing performance demand on speed and accuracy of motion systems, and essential system-level tradeoffs between cost and performance need to be made. In order to cope with these challenges, this thesis considers the development of novel motion control techniques for high-tech motion systems. In particular, two industrially relevant topics are addressed. Novel control architectures are developed for 1) motion systems with friction, and for 2) industrial over-actuated systems, where we aim to overcome the performance limitations inherent to classical control solutions for such systems.

For high-tech industrial motion platforms, current mechatronic design specifications often lead to the usage of high-cost equipment such as actuators, bearings, and sensors. When moving away from these stringent design requirements by using cheaper hardware components, the resulting system may suffer from nonlinearities induced by low-cost mechatronic system components. Specifically, the use of low-cost actuators and bearings can induce friction in the motion platform. It is well-known that friction is a performance-limiting factor in terms of speed and accuracy when state-of-practice, linear control techniques are employed. First, a classical PID controller (often embraced by industry for frictional systems) applied to a motion system with Coulomb friction results in long settling times, adversely affecting the machine throughput. Second, when a classical PID controller is applied to motion systems suffering from friction including the velocity-weakening Stribeck effect, stability of the setpoint (and thereby positioning accuracy) is compromised. The first part of this thesis involves the

design of two novel hybrid control architectures, and a learning controller, addressing the above-mentioned limitations for frictional motion systems. First, we propose a hybrid controller that significantly improves transient performance (in terms of settling time) of motion systems with unknown Coulomb friction. In particular, a reset integrator is applied to circumvent the depletion and refilling process of a linear integrator when the system overshoots the setpoint, thereby significantly reducing settling time. Stability properties of the closed-loop system are analyzed using a discontinuous Lyapunov-like function. Moreover, the effectiveness of the reset control strategy is experimentally demonstrated on a high-precision motion stage of an electron microscope. Second, we present a hybrid controller that achieves stability of the setpoint for systems with unknown Coulomb and Stribeck friction. The proposed reset integrator hence results in improved positioning accuracy. The closed-loop system dynamics are formulated in a hybrid systems framework, using a novel hybrid description of the Coulomb friction element, and stability of the setpoint is proven accordingly. The working principle of the controller is demonstrated experimentally on a motion stage of an electron microscope, showing superior performance over standard PID control. Both reset control strategies can be considered as hybrid extensions of the classical PID controller. By building upon a well-known control strategy embraced by industry, we reduce the threshold for control engineers to use the proposed performance-improving nonlinear controllers in industry. The third contribution is the design of a PID-based learning controller for systems with Coulomb and Stribeck friction, which perform a repetitive motion profile. In particular, we propose a time-varying integral controller gain. The integral gain is iteratively designed using measured performance data, by employing a sampled-data extremum-seeking approach. The proposed technique resembles iterative learning control, but does not require any model information, which is beneficial given the fact that friction is often uncertain or unknown.

The second part of the thesis is devoted to the modeling of and control design for two industrial over-actuated motion systems. By employing intelligent control solutions, the over-actuated topology of the considered systems can be exploited to improve performance, compared to classical, linear control solutions currently applied in industry. First, we design a control allocation framework for an industrial high-precision transportation and positioning system. The considered system consists of multiple carriers that move on horizontal tracks, actuated by inverted three-phase motors (i.e., coils in the tracks and permanent magnets on the carriers, so that the carriers do not have any electronics or cables attached to them). Compared to the state-of-practice (linear) controller, the developed allocation control architecture results in improved accuracy, increased freedom in motion profile design, and relaxed hardware design specifications (the latter allows for a more cost-effective system design). The benefits are experimentally demonstrated on an industrial platform. The second contribution is the development of a dynamical model and accompanying controller design for an industrial

sheetfed printer paper path. Sheets of paper are transported alternately by one or two pinches throughout the paper path, which gives rise to a hybrid system dynamics. In particular, the developed model is formulated in a hybrid systems framework, which facilitates the design of hybrid controller concepts (taking into account the hybrid nature of the system) for the considered application. As a stepping stone towards this goal, we propose a controller that regulates both the motion of the transported sheets and traction forces in the sheets, when transported by two pinches (exploiting the over-actuated topology). The effectiveness of the controller is illustrated by means of a simulation example, and demonstrated on an experimental paper path setup.

The control architectures presented in this thesis yield an improved performance of industrial motion systems, compared to state-of-practice linear controllers, and may allow for a cost-effective mechatronic system design. The proposed controllers can be designed and tuned using well-known loop-shaping techniques, enabling industrial acceptance of the proposed control architectures.

Societal summary

Motion control is a key enabling technology in a broad range of high-tech applications ranging from electron microscopes, pick-and-place machines, and copiers to wafer scanners, thereby representing an enormous value for the Dutch economy. The corresponding high-tech industries are currently facing numerous challenges, namely, there is an ever increasing performance demand on speed and accuracy of motion systems, and essential system-level tradeoffs between cost and performance need to be made. In order to cope with these challenges, this thesis considers the development of novel motion control techniques for high-tech motion systems. In particular, two industrially relevant topics are addressed. Novel control architectures are developed for 1) motion systems with friction, and for 2) industrial over-actuated systems, where we aim to overcome the performance limitations inherent to classical control solutions for such systems.

Current mechatronic design specifications often lead to the usage of high-cost equipment such as actuators, bearings, and sensors. When moving away from these stringent design requirements by using cheaper hardware components, the resulting system may suffer from undesired effects caused by friction, induced by low-cost mechatronic system components. Friction is a performance-limiting factor, that can typically not be overcome by classical control solutions. The first part of this thesis therefore involves the design of novel control architectures, addressing the limitations for frictional motion systems.

Another challenge currently faced by industry is the ever increasing demand on speed and accuracy of motion systems. The second part of this thesis is devoted to controller design of a specific class of industrial systems (i.e., over-actuated motion systems), that outperform the state-of-practice control solutions currently applied in industry.

The control architectures presented in this thesis yield an improved performance of industrial motion systems, compared to state-of-practice linear controllers, and may allow for a cost-effective mechatronic system design. The proposed controllers can be designed and tuned using conventional techniques already used in practice, enabling industrial acceptance of the proposed control architectures.

Contents

Summary	i
Societal summary	v
1 Introduction	1
1.1 Motion control for industrial high-precision systems	2
1.2 Objectives and contributions	7
1.3 Outline of this thesis	11
1.4 Embedding of the thesis in the NWO project	12
I Control of Motion Systems with Friction	15
2 Reset integral control for improved settling of motion systems with friction	17
2.1 Introduction	17
2.2 Reset integral control design	20
2.3 Hybrid system formulation	26
2.4 Stability analysis	29
2.5 Experimental case study on a high-accuracy positioning machine	32
2.6 Conclusions	40
2.A Proofs	41
3 Reset control for setpoint stability of motion systems with Stribeck friction	47
3.1 Introduction	47
3.2 System description and controller design	50
3.3 Hybrid system formulation of the closed loop	57
3.4 Stability analysis	60

3.5	Experimental case study	64
3.6	Conclusions	69
3.7	Final remarks	69
3.8	In retrospect: experimental case study on a Clegg reset controller	69
3.A	Proofs	74
4	PID-based learning control for repetitive positioning of frictional motion systems	103
4.1	Introduction	103
4.2	Control problem formulation	106
4.3	Time-varying PID controller	109
4.4	Sampled-data extremum-seeking for iterative controller tuning	113
4.5	Experimental case study	117
4.6	Conclusions	121
4.A	Proof of Proposition 4.7	123
II	Control of Over-actuated Motion Systems	127
5	Control allocation for a high-precision transportation and positioning system	129
5.1	Introduction	129
5.2	System description	131
5.3	Control architecture	135
5.4	Case study	141
5.5	Conclusions	152
6	Modeling and control of a sheetfed printer paper path	157
6.1	Introduction	157
6.2	Paper path modeling	160
6.3	Controller design	171
6.4	Experimental case study	180
6.5	Conclusions	185
6.A	Controllers	188
7	Conclusions and recommendations	191
7.1	Conclusions	191
7.2	Recommendations	194
A	Hybrid Dynamical Systems	199
	Bibliography	203
	List of Publications	213

About the author

215

Dankwoord

217

Chapter 1

Introduction

Motion control is a key enabling technology in a broad range of high-tech applications ranging from electron microscopes, pick-and-place machines, and high-precision transportation systems, to industrial printers and wafer scanners, thereby representing an enormous value for the Dutch economy. The corresponding high-tech industries are currently facing numerous challenges in order to maintain their competitive position in the market. Namely, there is an ever-increasing performance demand on speed and accuracy of motion systems, and essential system-level tradeoffs between cost and performance need to be made. In order to cope with these challenges, this thesis considers the development of novel motion control techniques for high-tech motion systems. In particular, two industrially relevant topics are addressed. Novel control architectures are developed for 1) motion systems with friction, and for 2) industrial over-actuated motion systems, where we aim to overcome the performance limitations inherent to classical control solutions for such systems.

This chapter provides a high-level introduction to the thesis, in order to highlight the main research goals and contributions. More detailed literature reviews on the different topics discussed in this thesis are given in the individual chapters. In Section 1.1, (recently developed) motion control techniques for industrial systems are briefly reviewed. In Section 1.1.1 and Section 1.1.2, control strategies for motion systems with friction, and for over-actuated motion systems are discussed, respectively, related to the two main topics addressed in this thesis. The objectives and contributions of this thesis are presented in Section 1.2, and the outline of this thesis is given in Section 1.3. Finally, the embedding of this thesis into the research programme *CHAMeleon*, of which this research was part, is presented in Section 1.4.

1.1 Motion control for industrial high-precision systems

Industrial high-precision motion systems are generally well-designed, such that the dynamics of these systems can be represented by linear system models (and are therefore referred to as “linear systems”). This allows for the use of linear feedback control techniques, which are applied in the vast majority of industrial motion systems. In particular, the classical, linear, proportional-derivative-integral (PID) type controller, see, e.g., [9, 125], is commonly employed due to its effectiveness in practical control problems. Control practitioners are often well-trained in linear controller design, and the existence of intuitive (graphical) design and tuning tools for linear controllers (e.g., loop-shaping [57, 138] or H_∞ controller synthesis techniques [154, Ch. 16-18]) makes linear control popular in practice.

Besides the requirement that the to-be-controlled mechatronic system must be linear in order to reliably employ linear control techniques, PID-type feedback controllers suffer from distinct performance limitations. Well-known examples of these limitations are the so-called “waterbed-effect” (i.e., increasing the bandwidth of a linear control system improves low-frequency disturbance rejection properties, but increases sensitivity to high-frequency disturbances), and the trade-off between low-frequency disturbance rejection and increasing overshoot when using integral action, see [134]. In order to (partly) overcome some of the performance limitations associated with linear control, *hybrid* or *reset* control strategies for linear systems have been developed in the past decades.

Whereas linear controllers only generate a *continuous* control signal, such hybrid control strategies are able to generate a mixed continuous/*discontinuous* control signal, thereby offering more freedom for controlling the system. The discrete part of the control signal is commonly the result of resetting (some of) the controller state(s) to a specified value, when certain conditions on the system and controller states are satisfied. A well-known early example of such a reset control strategy is the Clegg integrator [46], which resets the integrator state to zero upon a zero-crossing of the input, thereby reducing the amount of overshoot, compared to its linear counterpart. Subsequently, the more general First Order Reset Element and corresponding analysis procedures have been presented in [24, 42, 76, 107, 151]. A generalization of the Clegg integrator is presented in [96], which allows for the use of a stability analysis based on frequency response data, essentially realizing the use of reset elements in loop-shaped controller designs. Further developments led to the Split-path Nonlinear Integrator [97, 98] (which flips the sign of the output of the integral control action upon a zero-crossing of the position error to reduce overshoot), and the hybrid integrator-gain system [52, 136], which offers similar benefits to a Clegg reset integrator, but avoids a discontinuous control signal.

Despite the ongoing development of novel (hybrid) control techniques that balance certain performance tradeoffs for linear systems in a more desirable manner, the high-tech industry is still facing numerous challenges. In this thesis, two industrially relevant topics are addressed in order to cope with these challenges. First, there exist essential system-level tradeoffs between hardware cost and system performance. In particular, for high-tech industrial motion platforms, current mechatronic design specifications often lead to the usage of high-cost equipment such as actuators, bearings, and sensors, in order to realize a system that can be represented by a linear system model, and, hence, controlled by well-understood linear controllers. When moving away from these stringent design requirements by using cheaper hardware components, the resulting system may suffer from nonlinearities induced by low-cost mechatronic system components, such as nonlinear effects due to friction, backlash, or actuator nonlinearities. Such motion systems can then no longer be represented as a linear system, and, consequently, linear control techniques (and even the aforementioned hybrid controllers) may no longer be sufficient to realize the desired performance. In the first part of this thesis, we specifically address the performance limitations induced by friction, as a result of using cheaper hardware components such as bearings and actuators, while still guaranteeing high-end performance and ease of implementation and tuning.

The second challenge currently faced by industry is the ever-increasing demand on speed and accuracy of motion systems, preferably without having to invest in high-cost hardware. Although the hybrid control concepts discussed in this section provide already suitable tools to do so for (commonly) single-input linear motion systems, we address the performance improvement of *over-actuated motion systems* (i.e., motion systems with more actuators than rigid-body degrees of freedom) in the second part of the thesis. In particular, by employing intelligent control allocation-based solutions, the over-actuated topology of the considered systems can be exploited to improve performance, compared to classical, linear control solutions currently applied in industry.

1.1.1 Control of motion systems with friction

The study of friction dates back as far as the fifteenth and sixteenth century, where Leonardo Da Vinci reported his findings on sliding and rolling friction in his famous codices and manuscripts. Da Vinci's findings and experiments, recently summarized and revisited in [78] and [119], marked the start of the development of physical understanding of friction. Roughly one and a half century after Da Vinci wrote down his discoveries, Guillaume Amontons, and later Charles-Augustin de Coulomb, developed the first static friction models (see [6]) that are still widely recognized today. These models provide a static mapping between the velocity of the sliding body and the friction force, where the friction force is proportional to normal load, but independent of the contact surface

area (known as Amonton’s paradox). Morin [105] showed that, at zero velocity, the friction force balances with the external forces applied to the body, where static friction may be larger than Coulomb friction (which has eventually led to the mathematical *set-valued* description of static friction, see, e.g., [93]). In 1902, Stribeck showed a continuous, velocity-dependent decrease from static to Coulomb friction levels [139], commonly present in lubricated contacts and widely known as the *Stribeck effect*.

With static friction models, we can distinguish the logical states “stick” (i.e., zero velocity while the external forces do not exceed the static friction level) and “slip” (nonzero velocity), see, e.g., [20, Sec. 2]. However, static friction models do not capture well the physics in the “stick” regime. Indeed, there exists a small regime in which friction force is shown to be dominantly a (hysteresis) function of displacement rather than velocity [12, 53], which gives rise to an effect known as *presliding*. Such an effect can only be captured by more advanced *dynamic* friction models, proposed by, e.g., Dahl [51], who proposed a single-state dynamic model that is generalized to include the Stribeck effect in [39], leading to the well-known LuGre model. The latter enjoys suitable passivity properties in line with the dissipative nature of friction, see [13]. An extension of the LuGre model is proposed in [140], and other enhanced friction models are presented in, e.g., [4, 90, 124]. In this thesis, however, a static description of friction is adopted that, on one hand, captures the dominant frictional effects, and, on the other hand, is suitable for controller design and closed-loop analysis without introducing the complexity associated with the more enhanced (dynamic) friction models.

Friction is generally a performance-limiting factor in industrial high-precision motion systems, in the sense of achievable positioning accuracy and settling times. Many different control strategies for frictional motion systems have been developed in the past decades. Some of them use friction models for online compensation, see, e.g., [11, 12, 58, 91, 100, 101, 112, 140]. Such model-based friction compensation techniques, however, have a common disadvantage. Namely, model mismatch typically arises due to uncertainties in the friction characteristic or unreliable friction measurements, possibly resulting in over- or undercompensation of friction, which compromises positioning accuracy. Non-model-based control techniques do not aim at friction compensation using a friction model, but change the response by applying specific control signals, thereby obtaining the desired performance despite the apparent friction. Examples of such techniques are impulsive control, see, e.g., [115, 148], and dithering-based techniques, see, e.g., [79, 116]. Impulsive control applies a carefully determined impulsive control signal so that the system escapes stick phases with non-zero position errors. Dithering-based techniques apply a persistent high-frequency control signal to smooth the discontinuity induced by Coulomb friction. In general, these non-model-based control techniques are not straightforward to implement and to tune, and rely on the persistent injection of high-frequency control signals, which may be undesirable in industrial systems.

Despite the existence of the above control techniques, linear controllers are still applied in the vast majority of industrial motion systems with friction due to the existence of intuitive design and tuning tools. In particular, the classical PID controller is most commonly used for frictional systems, since the integrator action results in compensation of unknown static friction by integrating the position error.

However, PID control is prone to performance limitations as well. First, employing the classical PID controller on a motion system with Coulomb and viscous friction results in long settling times, see, e.g., [29, Remark 3]. Integrator action is frequently used in frictional systems to escape a stick phase by building up the control force to overcome the (commonly unknown) static friction. However, if the system overshoots the setpoint, the control signal must be pointed in the reverse direction to overcome the static friction again. To this end, the integrator buffer needs to deplete and refill, which takes increasingly more time with a decreasing position error. This results in long settling times, adversely affecting the machine throughput, see (—) in Figure 1.1. Second, the use of a linear PID controller on a motion system with friction including the velocity-weakening (i.e., Stribeck) effect may induce limit cycling (*hunting*, see, e.g., [74]). Whereas integrator action compensates for the static part of the friction, overcompensation of friction occurs as velocity increases, due to the velocity-weakening effect. Consequently, (asymptotic) stability of the setpoint is lost, so that the achievable positioning accuracy is limited, as illustrated by (—) in Figure 1.1.

In this thesis, we aim to overcome the aforementioned limitations of PID control for frictional motion systems in two particular ways. First, since hybrid or reset controllers have shown to be successful in overshoot reduction and transient performance improvement of *linear* systems (as highlighted in the brief literature overview in the previous section), it seems promising to develop such controllers for *nonlinear* (frictional) motion systems. Since integral action plays an impor-

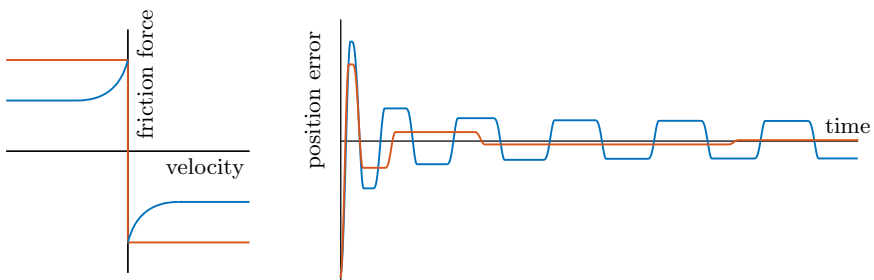


Figure 1.1. Friction characteristics and corresponding typical PID-controlled responses of a motion system with static friction (—), and with static and Stribeck friction (—).

tant role in (static) friction compensation, we embrace the reset control paradigm to modify the integral part of loop-shaped PID controllers, to overcome the limitations of PID control for motion systems with friction. The second strategy (tailored to motion systems performing a repetitive motion profile) is to employ a *time-varying* integrator gain, to counteract the velocity-weakening effect, and iteratively learn its characteristic. Such learning mechanism has resemblance with iterative feedback tuning (see, e.g., [73, 94]) and iterative learning control (see, e.g., [36, 146]). Since these methods have proven merit in a *linear* motion control setting, it motivates to apply a learning strategy to a *nonlinear* motion system with friction. More specifically, the optimal tuning of the time-varying integrator gain may be obtained by means of a sampled-data extremum-seeking control (ESC) framework (see, e.g., [85, 89]), since ESC is able to deal with unknown, uncertain, and time-varying nonlinear systems. By building upon the widely embraced PID control strategy, such reset and learning controllers can be designed and tuned using well-known loop-shaping techniques, enabling industrial acceptance of the proposed control architectures.

1.1.2 Control of over-actuated motion systems

Many control systems, reaching far beyond the field of high-tech motion systems, have more actuators than rigid-body degrees of freedom. Such an over-actuated system topology requires specific control solutions to distribute the control task over the available actuators. Numerous control strategies that deal with actuator redundancy have been presented. A well-known approach is optimal control, see, e.g., [68, 154], which, especially for linear systems, has received much attention in the literature. For instance, linear quadratic control [154, Ch. 15],[8], H_∞ -control [154, Ch. 16-18], and Model Predictive Control (MPC) [59, 103] are able to deal with actuator redundancy. Whereas such optimal control strategies commonly decide the control input and distribution directly, *control allocation*, see, e.g., [81, 118], separates the regulation task from the distribution task. This thesis takes the viewpoint that such a separated approach favors acceptance by industry, since the underlying motion controller can then be designed using well-known (e.g., loop-shaping) design techniques. Once the control signal is determined by the loop-shaped motion controller, an allocator then distributes the control force over the available actuators in a specific manner. The latter is often performed statically by solving an optimization problem online, respecting certain performance criteria on, e.g., position errors and power consumption. Actuator limitations can readily be taken into account as constraints to the optimization problem. Dynamic allocators exist as well, see, e.g., [80, 150], that deal with actuator limitations in a different manner. In the literature, control allocation has been applied on a broad range of applications. Examples are control allocation for flight control [113], and for marine vehicles [56]. For mechanical (motion) systems, control allocation is employed, e.g., on a dual-

stage actuator for harddisk drives [102], and robotic systems [95].

In this thesis, we address two industrial over-actuated systems. First, we design a control allocation framework for an industrial high-precision transport system, where multiple carriers move independently over horizontal tracks. The carriers are driven by several inverted three-phase actuators, which are located on the tracks and may influence multiple carriers at the same time. This gives rise to conflicting control objectives, hardware restrictions, and limited freedom in motion profile design when using the state-of-practice (linear) control solution currently applied by the manufacturer. We aim to tackle these restrictions by employing a static control allocation technique. Second, we develop a control allocation framework that improves the performance of an industrial sheetfed printer. The state-of-practice control solution results in unacceptable position tracking errors of the transported paper sheets, and undesired large traction forces in the sheets. Exploiting the over-actuated topology of the system, a manual control allocation scheme is designed, based on engineering insight, that addresses these control problems.

1.2 Objectives and contributions

The concise literature overview in Section 1.1 suggests that hybrid control strategies may improve the system's performance, compared to classical, linear control techniques. However, such control strategies are mostly employed to improve performance of *linear* systems. For the performance improvement of *nonlinear* motion systems with friction, hybrid controllers are generally lacking. Second, we embrace the philosophy of substituting the integrator in a classical PID controller with a time-varying integrator (and learn its characteristic), to counteract the velocity-weakening effect, for motion systems performing a repetitive motion profile. The first objective of the thesis is hence formalized as follows:

Objective 1. Develop (hybrid and learning) control techniques for motion systems with friction, that improve stability and performance properties compared to classical linear control solutions, and are applicable to industrial high-tech systems.

Objective 1 explicitly takes into account the practical implementability of the to-be-designed controllers on industrial systems. Since control practitioners are often well-trained in linear controller design, the application of a nonlinear or hybrid control strategy may impose a gap between state-of-practice linear controllers and novel controllers developed in academia. One way of bridging the gap between academia and industry is to build the design of hybrid and learning control elements upon the widely embraced PID-type controller, that can be designed and tuned using well-understood tools from linear control design methodologies.

Addressing the industrially relevant problem of improving performance of over-actuated motion systems, control allocation represents a promising approach to do so. Since the controller design phase is strictly separated from the distribution of the resulting control effort, control practitioners can still design the controller using well-known (loop-shaping) design techniques. The second objective of this thesis is therefore formalized as follows:

Objective 2. Develop control allocation techniques tailored to specific industrial over-actuated systems, that outperform the state-of-practice (linear) control solutions.

In order to bridge the gap between academia and industry, the developed control techniques should be verified and tested on industrial benchmark systems, which provides the third objective of this thesis:

Objective 3. Experimental validation of the proposed controllers on industrial benchmark systems.

The main contributions of this thesis are outlined in Section 1.2.1, and the specific contributions of each chapter are presented in Section 1.2.2.

1.2.1 Contributions of the thesis

The main contributions of this thesis can be summarized in terms of contributions on 1) novel controller designs that allow for cost-aware mechatronic system designs, 2) novel controller designs for frictional systems, 3) development of tailored control allocation techniques for industrial over-actuated systems, and 4) validation on industrial benchmark systems:

1. *Novel controller designs that allow for cost-aware mechatronic system designs:* all controller designs proposed in this thesis address cost-awareness in one way or another. Specifically, the first part of this thesis (Chapters 2-4) presents three controller designs for motion systems with friction. Friction in mechanical motion systems can be caused by the use of cheaper hardware components such as bearings or actuators. The proposed control techniques are designed such that high performance in the sense of speed and accuracy is obtained, despite the system being nonlinear due to the presence of friction. The second part of this thesis presents control allocation techniques for industrial over-actuated systems. Chapter 5 presents a control allocation framework for a high-precision transport and positioning system. The allocation framework not only achieves superior position tracking performance, compared to the state-of-practice linear control solution, but also minimizes power consumption to reduce operational costs. Moreover, the control allocation framework allows for relaxed hardware design specifications, allowing for a more cost-effective system

- design. Chapter 6 presents a dynamic model and a manual control allocation architecture for a next-generation industrial sheetfed printer. Whereas the current generation printers are driven by DC motors, the manufacturer opts for the use of stepper motors in future sheetfed printers, due to the lower hardware costs. We design a control framework that explicitly handles stepper motor control in an over-actuated context.
2. *Novel (hybrid and learning) controller designs for systems with friction, applicable to industrial applications:* considering the inherent performance limitations of PID control for frictional systems as discussed in Section 1.1.1, Chapters 2 and 3 present novel reset controllers to overcome these limitations. In particular, a reset controller that improves the transient performance of systems with Coulomb and viscous friction is proposed in Chapter 2, in the sense of significantly reducing settling times. A reset controller that achieves stability of the setpoint for systems with Stribeck friction is proposed in Chapter 3, thereby significantly improving positioning accuracy. In Chapter 4, a time-varying PID-based learning controller for systems with Stribeck friction performing a repetitive motion profile is proposed. High setpoint accuracy is obtained by iterative tuning of the controller parameters. All three control strategies are enhancements of the classical PID controller, which favors industrial acceptance.
 3. *Performance-enhancing control allocation techniques tailored for over-actuated industrial applications:* allocation-based controller designs for two industrial over-actuated systems are presented in this thesis. In Chapter 5, a control allocation framework for a high-precision transport and positioning system is presented, that outperforms the state-of-practice control solution in terms of accuracy. In Chapter 6, a dynamic model and a control architecture for an over-actuated stepper motor-driven sheetfed printer is presented. The control architecture exploits the over-actuated system topology and achieves improved tracking accuracy of the paper sheets throughout the paper path, compared to the state-of-practice control solution, and, at the same time, regulates traction forces in the sheets.
 4. *Validation on industrial benchmark systems:* all controllers proposed in this thesis are experimentally validated on industrial benchmark systems. The effectiveness of the (hybrid and learning) control strategies proposed in Chapters 2-4 are verified on a high-precision motion stage of an electron microscope. The control allocation architecture of Chapter 5 is experimentally validated on an industrial high-precision transport and positioning system. Finally, the working principle and the effectiveness of the control architecture for sheetfed printers in Chapter 6 are experimentally demonstrated on a prototype sheetfed printer paper path setup.

1.2.2 Contributions of the individual chapters

Chapter 2 presents a novel reset controller that significantly improves transient performance (in terms of settling time) of motion systems with unknown Coulomb and viscous friction. As discussed in Section 1.1.1, the classical PID controller is often employed in industry for frictional systems, since integrator action is instrumental in escaping a stick phase by building up the control force to overcome the (unknown) static friction. However, if the system overshoots the setpoint, the control signal must be pointed in the reverse direction to overcome the static friction again. To this end, the integrator buffer needs to deplete and refill. Despite achieving stability of the setpoint, this process takes increasingly more time with a decreasing position error. This results in long settling times, adversely affecting the machine throughput (cf. Figure 1.1). We therefore propose a reset integrator to circumvent the depletion and refilling process of a linear integrator when the system overshoots the setpoint, thereby significantly reducing settling time. Stability properties of the hybrid closed-loop system are analyzed using a discontinuous Lyapunov-like function and a meagre-limsup invariance argument. Moreover, the effectiveness of the reset control strategy is experimentally demonstrated on a high-precision motion stage of an electron microscope.

Chapter 3 presents a novel reset integral controller that achieves asymptotic stability of the setpoint for motion systems with unknown Coulomb and velocity-dependent friction, including the velocity-weakening Stribeck effect. For the classical (linear) PID controller and such a friction characteristic, asymptotic stability of the setpoint is typically not achieved and limit cycling occurs, as discussed in Section 1.1.1 and shown in Figure 1.1. The proposed reset integrator hence results in improved positioning accuracy, compared to the classical PID controller. The closed-loop system dynamics are formulated in a hybrid systems framework, using a novel hybrid description of the Coulomb friction element. Using this model, stability of the setpoint is proven. The working principle and effectiveness of the controller is demonstrated experimentally on a motion stage of an electron microscope, showing superior performance over standard PID control.

Chapter 4 presents a time-varying PID-based learning controller for systems with Coulomb and Stribeck friction, that perform a repetitive motion profile. In particular, we propose a time-varying integral controller gain, parametrized by a set of suitable basis functions. Due to the unknown nature of the friction characteristic, the optimal tuning of the time-varying integrator gain is iteratively obtained using measured performance data, by employing a sampled-data extremum-seeking control approach, see, e.g., [85, 89]. The proposed technique resembles iterative learning control and iterative feedback tuning, but does not require any model information. The working principle and effectiveness of the control architecture is experimentally validated on a high-precision motion stage of an electron microscope.

The developments presented in Chapter 4 are the result of a collaboration with Leroy Hazeleger. The author contributed to the controller design and underlying theoretical analysis, and assisted with the experimental validation of the proposed controller.

Chapter 5 presents the design of a control allocation framework for an industrial high-precision transportation and positioning system. The considered system consists of multiple carriers that move on horizontal tracks, actuated by inverted three-phase motors. The control allocation is performed in the $\alpha - \beta$ current frame (see, e.g., [144, Ch. 10]) to ensure a minimal set of decision variables. Exploiting the over-actuated topology of the system, the control effort is distributed in such a way that power consumption is minimized, thereby reducing operational costs. Moreover, a decentralized allocation algorithm is presented that enhances computational efficiency, such that the proposed control allocation technique can be implemented online at high sampling rates, and facilitates the scalability to larger system configurations. Compared to the state-of-practice (linear) control solution currently applied by the manufacturer, the developed allocation control architecture results in improved positioning and tracking accuracy, increased freedom in motion profile design, and relaxed hardware design specifications (the latter allows for a more cost-effective system design). The benefits are experimentally demonstrated on an industrial platform.

Chapter 6 presents the development of a dynamical model and a control framework for an industrial sheetfed printer paper path. In such a system, sheets of paper are transported by pinches, consisting of two sets of rollers between which the paper is clamped and transported accordingly. Sheets are transported alternately by one or two pinches throughout the paper path, which gives rise to a hybrid system dynamics, where the double-pinch transport phase is over-actuated. The developed dynamical model is formulated in a hybrid systems framework, which facilitates the design of hybrid controller concepts (taking into account the hybrid nature of the system) for the considered application. We propose a controller that regulates both the motion of the transported sheets and traction forces in the sheets, when transported by two pinches (exploiting the over-actuated topology). The effectiveness of the controller is illustrated by means of a simulation study, and demonstrated on an experimental paper path setup.

1.3 Outline of this thesis

This thesis consists of two parts. Part I consists of Chapters 2-4, which presents novel (hybrid and learning) controller designs for motion systems with friction. Part II consists of Chapters 5 and 6, which presents control allocation techniques for over-actuated industrial motion systems. Chapters 2-5 are based on research papers and are self-contained. Also Chapter 6 contains sufficient background

information to be self-contained, so that all chapters can be read independently. Conclusions and recommendations for future work are presented in Chapter 7.

1.4 Embedding of the thesis in the NWO project

The research presented in this thesis is part of the research programme *CHAMeleon: hybrid solutions for cost-aware high-performance motion control* with project number 13896, which is (partly) financed by the Netherlands Organisation for Scientific Research (NWO).

The objective of this programme is to design novel control techniques that cope with the tradeoffs between cost and performance and between performance and system adaptability to changing operating conditions. The research programme consists of two main topics. Topic I can be subdivided into two objectives: *i)* to develop control strategies that deal with nonlinearities in the motion system, as a result of the use of cheaper hardware components, and *ii)* to develop controllers that venture beyond the state-of-practice, linear controllers, overcoming fundamental limitations inherent to linear control solutions. Topic II involves the design of performance optimization techniques to ensure optimal performance in diverse, uncertain, and changing conditions of machine usage. The research reported in this thesis has been mainly devoted to Topic I. Novel hybrid controller designs for nonlinear motion systems with friction, and control allocation techniques that outperform linear controllers are presented in this thesis, in line with objective *i)* and *ii)*, respectively. Additionally, the control architecture in Chapter 4 employs a performance optimization technique for optimal tuning of the controller, which contributes to Topic II.

Part I

**Control of Motion Systems
with Friction**

Reset integral control for improved settling of motion systems with friction

Abstract – In this chapter, we present a reset control approach to improve the transient performance of a PID-controlled motion system subject to Coulomb and viscous friction. A reset integrator is applied to circumvent the depletion and refilling process of a linear integrator when the solution overshoots the setpoint, thereby significantly reducing the settling time. Robustness for unknown static friction levels is obtained. The closed-loop system is formulated through a hybrid systems framework, within which stability is proven using a discontinuous Lyapunov-like function and a meagre-limsup invariance argument. The working principle of the proposed reset controller is analyzed in an experimental benchmark study on a high-precision positioning stage of an electron microscope.

2.1 Introduction

In this chapter, we present a reset integral control approach to improve settling (transient) performance of a PID-controlled mechanical motion system subject to friction. Friction is a performance-limiting factor in many high-precision positioning systems, in the sense of, e.g., achievable setpoint accuracy and settling times. Control of motion systems with friction has been an active field of research in the past decades, and many different control solutions have been developed. Several control approaches rely on developing as-accurate-as-possible friction models in order to compensate for friction in the control loop, see, e.g., [11, 12,

This chapter is based on [19] and [20].

58, 91, 100, 101, 140] and the references therein, or for controller synthesis, see, e.g., [3, 127]. However, model-based friction compensation techniques may suffer from over- and undercompensation of friction due to unreliable friction measurements, uncertainties in the friction characteristic, and model mismatches. Consequently, the system may exhibit limit cycles or nonzero steady-state errors (thereby losing stability of the setpoint), as thoroughly analyzed in [121]. Adaptive control methods, see, e.g., [7, 43, 106], have inherently some robustness to a changing friction characteristic by adapting friction model parameters online, but model mismatches (and the associated performance limitations) still remain. Non-model-based control techniques do not aim at friction compensation using a friction model, but change the response by applying specific control signals, thereby obtaining the desired performance despite the apparent friction. Impulsive control (see, e.g., [115, 148, 149]) applies a carefully determined impulsive control signal to a mass with friction to escape the stick phases with a non-zero position error. In [148], finite-time stability of the setpoint is achieved, which is a strong result in terms of settling time, but exact knowledge of the mass, and knowledge of a lower and upper uncertainty bound on the friction characteristic are required, which may hinder practical implementation. Dithering-based techniques (see, e.g., [79, 116, 143]) apply a persistent high-frequency control signal to smooth the discontinuity induced by Coulomb friction. Asymptotic stability of the setpoint is, however, not achieved due to the persistent injection of an oscillatory signal. Sliding mode control (see, e.g., [145]) has inherently some robustness to frictional disturbances, but first-order sliding mode control induces chattering. Second-order sliding mode control has been applied to setpoint control of frictional systems in, e.g., [14, 15]. Once the sliding surface is reached, the setpoint is approached from one side (i.e., the velocity does not change sign), rendering the Coulomb friction a constant disturbance. Although an exponential convergence result is obtained, the resulting control force is discontinuous with high-frequency content. A switched controller in [114] achieves stability of the setpoint by applying a constant control force, whose sign depends on the sign of the position error. By design of the controller, chattering occurs when the system is close to the setpoint. In general, these non-model-based control techniques have a common disadvantage. Namely, the persistent injection of high-frequency control signals may excite unmodeled high-frequency system dynamics, which is highly undesirable in motion systems, and, therefore, these techniques are not appealing for being used in industrial applications.

Despite the existence of the above control techniques, linear controllers are still applied in the vast majority of industrial motion systems. Control practitioners are often well-trained in linear control design (loop-shaping), and the existence of intuitive tuning tools for linear controllers makes them undiminished popular in industry. In particular, the classical proportional-integral-derivative (PID) controller [9, 125] is most commonly used for frictional systems, since the integrator action results in compensation of unknown static friction by integrat-

ing the position error. However, PID control is prone to performance limitations as well. Firstly, the integrator action in the presence of the velocity-weakening (i.e., Stribeck) effect may induce limit cycling (*hunting*), thereby losing asymptotic stability of the setpoint [12, 74, 101]. A second limitation is the slow convergence (and resulting long settling times) in the presence of static friction, see, e.g., [29, Remark 3]. Integrator action is required to escape a stick phase by building up the control force to overcome the (possibly unknown) static friction. However, if the solution overshoots the setpoint, the control signal must be pointed in the reverse direction to overcome the static friction again. To this end, the integrator buffer needs to deplete and refill. Despite achieving stability of the setpoint, this process takes increasingly more time with a decreasing position error. This results in long settling times, adversely affecting the machine throughput.

In this chapter, we address the second limitation in the context of PID control. In particular, we propose a reset integral control scheme that significantly improves transient performance in terms of settling time, and is applicable as an add-on to loop-shaped PID controllers, as designed for industrial motion applications. By building upon a well-known control strategy embraced by the industry, we aim at reducing the threshold for control engineers to use a nonlinear control technique in an industrial environment. Inspired by the Clegg integrator [46] and the First Order Reset Element [76], reset controllers (see, e.g., [1, 107] and [40, 96, 108] for corresponding analysis tools) have been used to increase tracking performance in motion control applications. The hybrid integrator-gain system in [52] offers similar benefits to the First Order Reset Element, but it induces less high-frequency excitations. The Split-path Nonlinear Integrator, see [97], flips the sign of the integral control action upon a zero-crossing, to reduce overshoot in linear motion systems. Overshoot reduction using reset control is also addressed in [25, 120, 152], and in [77] by a variable gain integral controller. Improved disturbance attenuation using reset control is presented in [153]. To the best of the author's knowledge, reset integrators have indeed been used to enhance performance of *linear* motion systems as in the works above, but have not yet been applied to improve settling performance of (nonlinear) systems with friction.

The main contributions of this chapter can be summarized as follows. The first one is a novel reset control design for systems with friction that both improves transient performance with respect to a classical PID controller, and achieves robust stability with respect to uncertainties in the static friction. The reset mechanism is robust to velocity measurement noise, and can be readily made robust for asymmetric static friction, if needed. Moreover, the proposed controller minimizes the risk of exciting unmodeled high-frequency dynamics, despite the presence of a discontinuous control signal, thereby addressing a major concern of control engineers in industry. The second contribution is the stability analysis of the resulting *hybrid* closed-loop system, which exploits a

meagre-limsup invariance argument [63, Sec. 8.4]. The third contribution is a demonstration of the transient performance improvements using the proposed reset control architecture by means of a case study on an industrial high-precision positioning application (a manipulation stage of an electron microscope).

The chapter is organized as follows. In Section 2.2, a model of the considered motion system with a classical PID controller is presented together with the reset integrator control law. A numerical example showing the achievable transient performance benefits is then briefly discussed. The closed-loop dynamics are written in a hybrid systems formalism in Section 2.3 and a stability analysis is given in Section 2.4. In Section 2.5, a case study on a high-precision positioning application is discussed, and conclusions are presented in Section 2.6.

Notation: $\text{sign}(\cdot)$ (with a lower-case s) denotes the classical sign function, i.e., $\text{sign}(y) := y/|y|$ for $y \neq 0$ and $\text{sign}(0) := 0$. $\text{Sign}(\cdot)$ (with an upper-case S) denotes the *set-valued* sign function, i.e., $\text{Sign}(y) := \{\text{sign}(y)\}$ for $y \neq 0$, and $\text{Sign}(y) := [-1, 1]$ for $y = 0$. For $c > 0$, the deadzone function is defined as: $\text{dz}_c(x) := 0$ if $|x| \leq c$, $\text{dz}_c(x) := x - c$ if $x > c$, $\text{dz}_c(x) := x + c$ if $x < -c$. A function $f: D \rightarrow \mathbb{R}$ is lower semicontinuous if $\liminf_{x \rightarrow x_0} f(x) \geq f(x_0)$ for each point x_0 in its domain D . The lower right Dini derivative D_+h of a function h is defined as $D_+h(t) := \liminf_{\epsilon \rightarrow 0^+} \frac{h(t+\epsilon) - h(t)}{\epsilon}$. The logical OR and AND are denoted by \vee and \wedge , respectively. The hybrid systems modeling framework and corresponding solution concept of [63], used in this chapter, is introduced in Appendix A.

2.2 Reset integral control design

In this section, we describe the considered motion system with friction and its friction characteristics, and discuss the design of the reset control law in Section 2.2.1. We then show a simulation example in Section 2.2.2 to illustrate the achievable transient performance improvements.

2.2.1 System modelling and reset control design

Consider a single-degree-of-freedom mass m sliding on a horizontal plane with position z_1 and velocity z_2 . The mass is subject to a control input \bar{u} and a friction force belonging to a friction set $\Psi(z_2)$ for a velocity z_2 , where $z_2 \mapsto \Psi(z_2)$ is a set-valued mapping. The system dynamics are then given by the differential inclusion

$$\dot{z}_1 = z_2, \quad \dot{z}_2 \in \frac{1}{m} (\Psi(z_2) + \bar{u}). \quad (2.1)$$

The set-valued friction characteristic Ψ consists of Coulomb friction with *unknown* static friction $\bar{F}_s > 0$, and a viscous contribution γz_2 , where $\gamma \geq 0$ is the

viscous friction coefficient:

$$\Psi(z_2) := -\bar{F}_s \text{Sign}(z_2) - \gamma z_2. \quad (2.2)$$

Existence of solutions² to (2.1)-(2.2) follows from [55, Sec. 7, Thm. 1] because the set-valued mapping in (2.1) is outer semicontinuous and locally bounded with nonempty compact convex values.

Since this chapter is primarily focused on robust compensation of unknown Coulomb friction and on transient performance improvement, we have assumed that a velocity-weakening (Stribeck) effect is absent in the friction characteristic Ψ (in the presence of such an effect, a velocity-dependent compensation control term may be employed as in [21]). The goal is to control the mass to the constant setpoint $(z_1, z_2) = (r, 0)$.

Let us formulate the control problem addressed in this chapter.

Problem 2.1. *Design a reset PID controller for input \bar{u} in (2.1)-(2.2) that 1) globally asymptotically stabilizes the setpoint $(z_1, z_2) = (r, 0)$ robustly w.r.t. any unknown static friction \bar{F}_s , for any constant r , and 2) improves the settling time (transient performance), compared to a classical PID controller with the same controller gains.*

The presence of an integrator action in \bar{u} is motivated by the fact that it is able to compensate for an *unknown* static friction \bar{F}_s , which is typically the case in motion applications, so that the controller can robustly deal with the Coulomb friction effect. Before presenting our proposed *reset* PID controller, we first introduce the *classical* PID controller generating \bar{u} as

$$\begin{aligned} \bar{u} &= -\bar{k}_p(z_1 - r) - \bar{k}_d z_2 - \bar{k}_i z_3, \\ \dot{z}_3 &= z_1 - r, \end{aligned} \quad (2.3)$$

where $\bar{k}_p, \bar{k}_d, \bar{k}_i > 0$ represent the proportional, derivative and integral gains, respectively. We apply then the following definitions to obtain mass-normalized system dynamics that favor clarity in the analysis of the upcoming sections:

$$k_p := \frac{\bar{k}_p}{m}, \quad k_d := \frac{\bar{k}_d + \gamma}{m}, \quad k_i := \frac{\bar{k}_i}{m}, \quad F_s := \frac{\bar{F}_s}{m}. \quad (2.4)$$

By using (2.4), the resulting mass-normalized, closed-loop dynamics given by (2.1)-(2.3) satisfy

$$\begin{aligned} \dot{z}_1 &= z_2, \\ \dot{z}_2 &\in -F_s \text{Sign}(z_2) - k_p(z_1 - r) - k_d z_2 - k_i z_3, \\ \dot{z}_3 &= z_1 - r, \end{aligned} \quad (2.5)$$

with the state vector $z = (z_1, z_2, z_3) \in \mathbb{R}^3$. We select the (normalized) controller gains such that the next assumption is satisfied.

²A solution is any locally absolutely continuous function z that satisfies (2.1) for almost all t .

Assumption 2.2. *The control parameters k_p , k_d , k_i satisfy $k_i > 0$, $k_p > 0$, $k_p k_d > k_i$.*

When $F_s = 0$ (a special, *linear* case of our setting), this assumption is equivalent, by the Routh-Hurwitz stability criterion, to ensuring global exponential stability of the equilibrium $z_1 = r$, $z_2 = z_3 = 0$ through a stabilizing PID controller. Assumption 2.2 is hence not restrictive.

In [29], it is proven that the set of equilibria

$$\mathcal{A} := \{z = (r, 0, z_3) \mid |z_3| \leq F_s/k_i\} \quad (2.6)$$

of (2.5) is globally asymptotically stable under Assumption 2.2. However, the PID-controlled system (2.5) typically results in long settling times due to the depletion and refilling of the integral buffer that is required to overcome the static friction F_s upon overshoot, resulting in a change of sign of the integrator state of the PID (as illustrated in [19, Sec. V and Fig. 3]). This process is generally slow and takes increasingly more time with a decreasing position error, resulting in long periods of stick and thus a poor transient performance in the sense of settling times. Note that the system is said to be in a *stick* or *slip* phase when the state belongs respectively to the sets

$$\mathcal{E}_{\text{stick}} := \{z \in \mathbb{R}^3 \mid z_2 = 0, |k_i z_3 + k_p(z_1 - r)| \leq F_s\} \quad (2.7a)$$

$$\mathcal{E}_{\text{slip}} := \mathbb{R}^3 \setminus \mathcal{E}_{\text{stick}}. \quad (2.7b)$$

In this chapter, we propose a novel *reset* PID control scheme to solve Problem 2.1. In particular, the objective of the proposed reset integral controller is to obtain a significantly faster settling time (i.e., the time for the position error to reach and remain in a specified accuracy band) compared to the *classical* PID design in (2.3), resulting in (2.5). To this end, we replace the integrator in the PID controller (2.3) with a reset integrator. The key mechanism behind the reset integrator is that a large part of the time-consuming depletion and refilling process of the integrator buffer (needed to overcome the static friction) is circumvented, whenever the system overshoots the setpoint. The reset in (2.8c) below ensures that the control force after a reset points in the direction of the setpoint, as close as possible to the (unknown) static friction value. This results in the following reset PID controller:

$$\bar{u} = -\bar{k}_p(z_1 - r) - \bar{k}_d z_2 - \bar{k}_i z_3, \quad (2.8a)$$

$$\dot{z}_3 = z_1 - r, \quad (2.8b)$$

$$z_3^+ = -\alpha z_3 - (1 + \alpha) \frac{k_p}{k_i} (z_1 - r), \quad (2.8c)$$

where z_3^+ denotes the updated value of z_3 upon a reset, occurring only when the conditions (2.8e) below are satisfied. The design parameter $\alpha \in [0, 1]$ enables

the reset to be scaled, and its role is elaborated further in Section 2.5. Position z_1 and velocity z_2 do not change at a reset:

$$z_1^+ = z_1, \quad z_2^+ = z_2. \quad (2.8d)$$

The integrator should be reset (as in (2.8e) below) whenever i) the system overshoots the setpoint, and ii) it enters a stick phase. Resetting the integrator when the system is in stick minimizes the risk of exciting high-frequency system dynamics because the discontinuity associated with the controller reset is compensated by the set-valued friction. We will elaborate further on this in Section 2.2.2 below. Intuitively speaking, condition i) is met when the position error and the proportional-integral (PI) component of the controller have opposite sign. The satisfaction of condition ii) requires the detection of zero velocity, which may be hard in practice due to measurement noise. Although robust zero-velocity detection mechanisms exist, we choose to evaluate the product of the PI control force and the velocity signal in order to robustly detect hitting zero velocity (see also Remark 2.3 below). Finally, we introduce a design parameter $\varepsilon > 0$ whose purpose is to avoid Zeno behavior [63, pp. 28–29]. This discussion motivates the controller reset conditions:

$$\begin{aligned} & k_i(z_1 - r)(k_p(z_1 - r) + k_i z_3) \leq 0, \\ \wedge & -z_2(k_p(z_1 - r) + k_i z_3) \leq 0, \\ \wedge & |k_p k_i(z_1 - r)^2 + k_i^2(z_1 - r)z_3| \geq \varepsilon. \end{aligned} \quad (2.8e)$$

In Section 2.3, we further elaborate on the reset map in (2.8c), the reset conditions in (2.8e), and the role of ε by showing that the reset conditions correspond indeed to (robust) detection of overshoot and stick (see (2.7a)). Moreover, we show in Section 2.4 that the reset map in (2.8c) preserves global asymptotic stability of the set of equilibria (2.6) for $\alpha \in [0, 1]$ and $\varepsilon > 0$. Summarizing, the resulting closed-loop system with the proposed reset PID controller is given by (2.5), (2.8c)-(2.8e).

2.2.2 Illustrative example

To illustrate the achievable transient performance benefits of the proposed reset controller, we perform a simulation study using a numerical time-stepping scheme [2, Ch. 10] that is able to correctly deal with the set-valued friction characteristic Ψ .

Let $r = 0$ be the constant position setpoint. First, consider system (2.5), where only the *classical* PID controller (2.3) is employed. The mass m is unitary and the friction parameters are $\bar{F}_s = 0.981$ N, and $\gamma = 0.5$. We take $\bar{k}_p = 18$ N/m, $\bar{k}_d = 2.5$ Ns/m, and $\bar{k}_i = 40$ N/(ms), satisfying Assumption 2.2, and initial conditions $z_1(0) = -0.05$ m, $z_2(0) = 0$ m/s, and $z_3(0) = 0$ ms. The position response is visualized in Figure 2.1a and 2.1b (---), where the long periods of

stick (see (2.7a)) and the resulting long settling times are evident. The control force \bar{u} in (2.3) is presented in Figure 2.1c, where the depletion and refilling process of the integrator buffer, causing long periods of stick, is clearly visible. This process takes increasingly more time with a decreasing position error, which results in increasingly longer periods of stick when the position error decreases.

Now consider the closed-loop system (2.5), (2.8c)-(2.8e), where the proposed reset controller is employed. We take $\alpha = 1$ and $\varepsilon = 10^{-8}$. The position response is given in Figure 2.1a and 2.1b (—), where the circles indicate the instants of controller resets. As it can be observed in the control force \bar{u} in Figure 2.1c, the reset mechanism circumvents a large part of the depletion and refilling process of the integrator, resulting in a significant decrease of the settling time. Note that the overshoot behavior is not influenced by the controller, as resets take place only as soon as a stick condition is reached.

The discontinuity in the control force (see Figure 2.1c) caused by the proposed reset mechanism does not increase the risk of exciting high-frequency system dynamics, compared to the application of the classical PID controller, by design of the reset conditions in (2.8e). This is an important feature of the proposed reset controller in view of practical applications, as in Section 2.5. The essential insight is that, for both the linear and the proposed reset integrator, discontinuities in the *net force* acting on the mass (see Figure 2.1e) are similar and primarily induced by friction. Consider Figure 2.1d. Discontinuities are indeed experienced *only* when the system enters the stick phase, even for the case without resets, and are thus inherent to the frictional nature of the system. The proposed controller is designed in such a way that resets occur when the system enters a stick phase (as we will elaborate further in Section 2.3). From (2.7a) and (2.8c), it is evident that stick is preserved after the reset, so that the discontinuity in the control force is fully compensated by the resulting friction due to its set-valued nature. As a result, although the discontinuity in the friction force (compensating for the controller reset) is larger (see Figure 2.1d), the discontinuity in the *net force* acting on the mass is *not* larger (see Figure 2.1e), as we will now elaborate.

Due to the fact that solutions to (2.11) are absolutely continuous *during flow* by definition and that each solution x cannot exhibit more than one consecutive jump (due to the definition of g and \mathcal{D} in (2.11)), solutions from \mathcal{C} always enter \mathcal{D} at a point at which $v = 0$ (see also the right plot in Figure 2.3 below). As a result, jumps only occur at zero velocity (except for the first jump if the initial conditions are chosen in the interior of \mathcal{D}). Given a state x , the net force $F_{net}(x)$ acting on the mass takes a value in the set $m\phi - \bar{F}_s \text{Sign}(v) - \bar{k}_d v$. Consider the case of *no* controller reset and, correspondingly, a solution x^* to only (2.11a) (with $\mathcal{C} = \mathbb{R}^3$) which experiences a slip-to-stick transition at time t^* . Also consider times t_-^* and t_+^* arbitrarily close to the left and right of t^* , respectively. At $t = t_-^*$, we have that $F_{net}(x^*(t_-^*)) = m\phi^*(t_-^*) - \bar{F}_s \text{sign}(v^*(t_-^*)) - \bar{k}_d v^*(t_-^*) \neq 0$, which is associated to a nonzero deceleration. At $t = t_+^*$, we

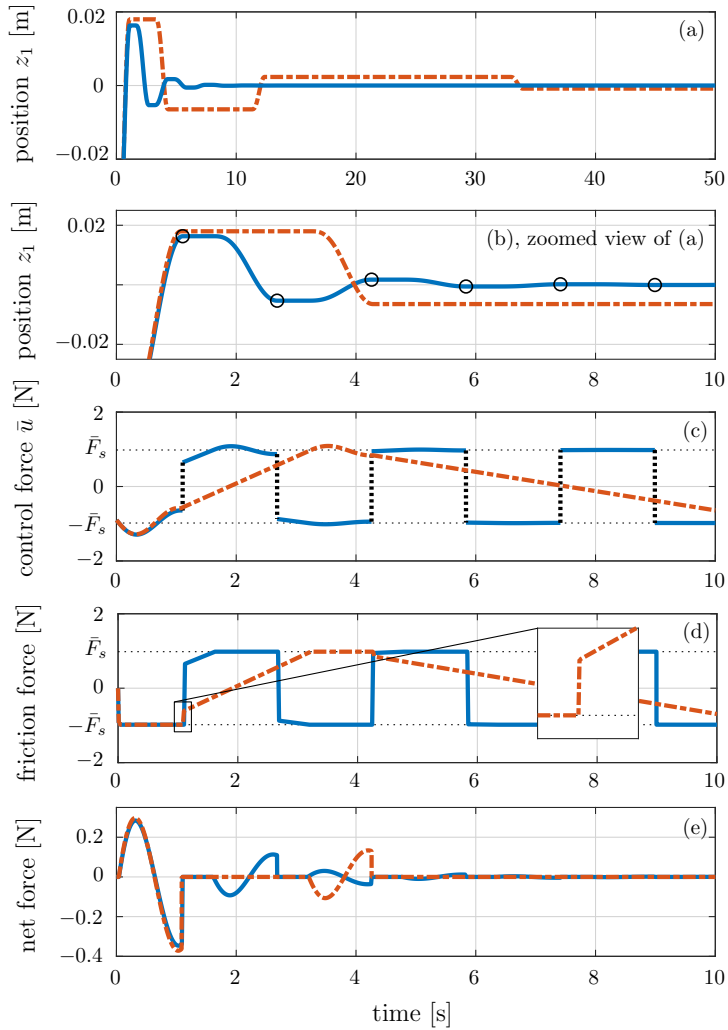


Figure 2.1. Simulated position response with Coulomb and viscous friction (a), zoomed view (b), control force (c), friction force (d), and net force acting on the system (e), for the classical PID controller (---), and the proposed reset controller (—) with the same controller gains. The circles indicate the instants of a controller reset.

have $F_{net}(x^*(t_+^*)) \in m\phi(t_+^*) - \bar{F}_s \text{Sign}(0)$. We have $v^*(t_+^*) = 0$ and $|\phi^*(t_+^*)| \leq F_s$ since $x^*(t_+^*) \in \mathcal{E}_{stick}$, and thus $m|\phi^*(t_+^*)| \leq \bar{F}_s$. It then follows from the combination of the system dynamics and the set-valued friction force law that the actual friction force (taken from the set $\bar{F}_s \text{Sign}(0)$) equals $-m\phi^*(t_+^*)$ and thus $F_{net}(x^*(t_+^*)) = 0$. Note that this result is independent of the sign of ϕ^* due to the set-valued friction force law, as shown in Figure 2.1.

Therefore, the proposed hybrid PID controller achieves a significant transient performance improvement w.r.t. a classical PID controller, while not increasing the risk of exciting high-frequency system dynamics.

2.3 Hybrid system formulation

In this section, we rewrite the closed-loop reset control system (2.5), (2.8c)-(2.8e) in the hybrid systems formalism of [63] to elaborate on the design of the proposed reset law. Furthermore, the derived hybrid system is used later for the stability analysis of Section 2.4.

Let us start with a useful state transformation, which allows for a simpler description of the system, transforms any constant setpoint r to the setpoint 0, and which facilitates the construction of a Lyapunov-like function for the stability analysis in Section 2.4. Following [29], this state transformation is

$$x := \begin{bmatrix} \sigma \\ \phi \\ v \end{bmatrix} := \begin{bmatrix} -k_i(z_1 - r) \\ -k_p(z_1 - r) - k_i z_3 \\ z_2 \end{bmatrix}, \quad (2.9)$$

where σ is a generalized position error, ϕ is the controller state encompassing the proportional and integral control actions, and v is the velocity of the mass. The state transformation in (2.9) rewrites the stick set in (2.7a) as

$$\mathcal{E}_{stick} = \{x \in \mathbb{R}^3 \mid v = 0, |\phi| \leq F_s\}. \quad (2.10)$$

The generalized controller state ϕ represents all the nonzero components of the control action at zero velocity (that is, the proportional and integral terms), and the difference between ϕ and the static friction F_s at $v = 0$ determines then whether the system resides in a stick phase or not, see (2.10).

With the state transformation (2.9), we rewrite the closed-loop dynamics (2.5) with the reset law (2.8c)-(2.8d) in the hybrid formalism of [63] as in (2.11) below. Note that the reset law (2.8c)-(2.8d) expressed in the state x yields a scaled sign change of ϕ when the reset criteria are met.

$$\dot{x} \in F(x) := \begin{bmatrix} -k_i v \\ \sigma - k_p v \\ \phi - k_d v - F_s \text{Sign}(v) \end{bmatrix}, \quad x \in \mathcal{C}, \quad (2.11a)$$

$$x^+ = g(x) := \begin{bmatrix} \sigma \\ -\alpha\phi \\ v \end{bmatrix}, \quad x \in \mathcal{D}, \quad (2.11b)$$

where F and g are the flow and jump map, respectively. Using (2.9), the reset conditions in (2.8e) transform into

$$\mathcal{D} := \{x \in \mathbb{R}^3 \mid \phi\sigma \leq 0, \phi v \leq 0, |\phi\sigma| \geq \varepsilon\}. \quad (2.11c)$$

Finally, the flow set is given by

$$\mathcal{C} := \overline{\mathbb{R}^3 \setminus \mathcal{D}}. \quad (2.11d)$$

Let us elaborate on the rationale behind the design of the jump set \mathcal{D} using Figures 2.2 and 2.3, which show the response of the example in Section 2.2.2 in the coordinates x . Recall that we want the integrator to be reset (i.e., a jump is desired in the hybrid formulation in (2.11)) when the system satisfies the following two conditions at the same time: 1) it enters a stick phase, and 2) the position overshoots the setpoint. Namely, a reset in such conditions greatly reduces the time needed for the depletion and refilling of the integrator buffer, and consequently the stick duration. This is the key mechanism for improving the transient performance in terms of settling using reset control and contributes to solving item 2) of Problem 2.1. Let us now discuss Figures 2.2 and 2.3:

- 1) Suppose the solution has initial condition $\sigma > 0$, $\phi > 0$, and $v = 0$, and starts in a stick phase (time interval 1 in Figure 2.2). Due to the dynamics of the integrator, $\phi > F_s$ will eventually be reached, which results in a slip phase (intervals 2 and 3 in Figure 2.2). The solution enters a stick phase again (interval 4 in Figure 2.2) when $v = 0$ is reached and the controller state ϕ satisfies $0 < \phi < F_s$, see the phase portraits in Figure 2.3. At this point, the condition $\phi v \leq 0$ is satisfied.

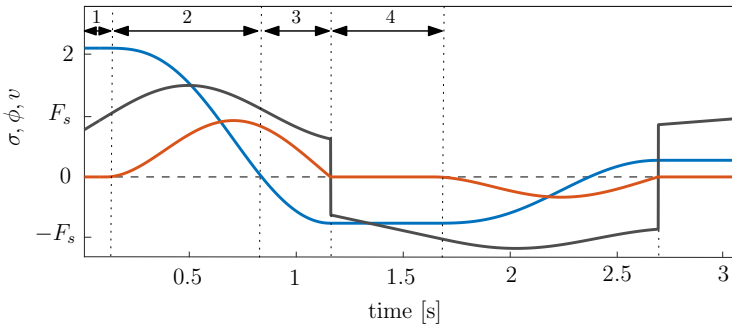


Figure 2.2. Evolution of the states σ (—), ϕ (—), and v (—) with the proposed controller, see the example in Section 2.2.2. The integrator resets through a sign change of ϕ are clearly visible by the discontinuities in its evolution.

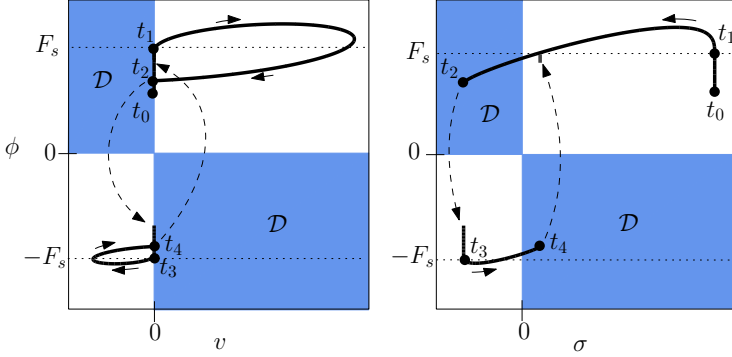


Figure 2.3. Phase portraits corresponding to the response in Figure 2.2. The jump criteria $\phi v \leq 0$ (left) and $\phi \sigma \leq 0$ (right) are indicated by the blue areas. The discrete jumps, initiated at the black dots, are indicated by dashed arrows. For the sake of clarity, the condition $|\phi \sigma| \geq \varepsilon$ is not taken into account in the figure.

A reset should not take place if the solution enters a stick phase *without* the occurrence of an overshoot, due to, e.g., different initial conditions, tuning, or friction characteristics. In such situations the solution still enters a stick phase and item 1) is satisfied. For this reason, we require the additional condition $\phi \sigma \leq 0$ in the jump set \mathcal{D} in (2.11c):

- 2) Before an overshoot of the setpoint (interval 2 in Figure 2.2), we have positive σ and ϕ , and thus $\phi \sigma > 0$. After an overshoot (interval 3 in Figure 2.2), σ changes sign so that $\phi \sigma \leq 0$. Along with item 1), we conclude that the requirement $\phi \sigma \leq 0$ in \mathcal{D} indeed enforces that a reset only takes place when the solution enters a stick phase *after* an overshoot.

Finally, the condition $|\phi \sigma| \geq \varepsilon$ in (2.11c), for some design parameter $\varepsilon > 0$, prevents a jump when σ or ϕ are zero, so that Zeno behavior is avoided. We will transform this criterion into a more intuitive one in Section 2.5 (while leaving intact the stability results presented in the next section), where we provide tuning guidelines for ε as well.

Remark 2.3. *To detect the stick phase, the criterion $\phi v \leq 0$ is chosen in the jump set \mathcal{D} in (2.11c) rather than just $v = 0$, since the latter is hard to check in practice due to velocity measurement noise. Although measurement noise around zero velocity may also render the product ϕv sign indefinite due to chattering in the sign of v , the additional condition $\phi \sigma \leq 0$ in \mathcal{D} prevents the system from experiencing undesired multiple jumps. Indeed, after the first reset, the jump map (2.11b) ensures that $\phi \sigma > 0$, thus $x^+ \notin \mathcal{D}$. In this way the design of the reset condition warrants robustness against measurement noise in v . \lrcorner*

Remark 2.4. The jump set \mathcal{D} is expressed in (2.11c) in terms of the new states x . The states ϕ and σ are not measurable in the case of an unknown mass m , as one can see from (2.9) and (2.4). The same observation clearly holds for the condition in (2.8e). However, even for an unknown mass m , we can define from (2.9) and (2.4) the measurable states

$$\varsigma := m\sigma = -\bar{k}_i(z_1 - r), \quad (2.12a)$$

$$\varphi := m\phi = -\bar{k}_p(z_1 - r) - \bar{k}_i z_3. \quad (2.12b)$$

This leads to jump conditions that can be checked based on the measurable states ς and φ , in which m does not appear. Note that for some $\epsilon > 0$, $|\varphi\varsigma| \geq \epsilon$ can replace $|\phi\sigma| \geq \epsilon$ since ϵ is a design parameter. \lrcorner

2.4 Stability analysis

In this section, we show that (2.13) is globally asymptotically stable for (2.11), solving item 1) of Problem 1. To this end, the set of equilibria (2.6) is rewritten by the state transformation in (2.9) as

$$\mathcal{A} = \{x \in \mathbb{R}^3 \mid \sigma = v = 0, |\phi| \leq F_s\}. \quad (2.13)$$

Let us now formalize the intended stability result by the next theorem.

Theorem 2.5. Under Assumption 2.2, for each $\alpha \in [0, 1]$ and $\epsilon > 0$, \mathcal{A} in (2.13) is globally asymptotically stable for the hybrid dynamics (2.11).

The remainder of this section is devoted to the proof of Theorem 2.5. In particular, we establish in Lemma 2.9 that \mathcal{A} is globally attractive, and in Lemma 2.11 that \mathcal{A} is Lyapunov stable for (2.11). The proof builds upon the results in [29], but is significantly challenged by the addition of the reset controller that gives rise to a *hybrid* (and no longer purely continuous-time) closed-loop system.

Consider the discontinuous Lyapunov-like function $V : \mathbb{R}^3 \rightarrow \mathbb{R}$ proposed in [29] and defined as

$$V(x) := \begin{bmatrix} \sigma \\ v \end{bmatrix}^\top \begin{bmatrix} \frac{k_d}{k_i} & -1 \\ -1 & k_p \end{bmatrix} \begin{bmatrix} \sigma \\ v \end{bmatrix} + \min_{F \in F_s, \text{Sign}(v)} (\phi - F)^2. \quad (2.14)$$

We start by providing some properties of solutions while flowing, as in Lemma 2.6 below. To this end, we note that (2.11a) (and function (2.14)) suggests that during flow there are three relevant affine subsystems corresponding to the system being in slip with nonnegative or nonpositive velocity, and being in stick (cf. (2.7b) and (2.10)). With the definitions

$$A := \begin{bmatrix} 0 & 0 & -k_i \\ 1 & 0 & -k_p \\ 0 & 1 & -k_d \end{bmatrix}, \quad b := \begin{bmatrix} 0 \\ 0 \\ F_s \end{bmatrix}, \quad P := \begin{bmatrix} \frac{k_d}{k_i} & 0 & -1 \\ 0 & 1 & 0 \\ -1 & 0 & k_p \end{bmatrix}, \quad (2.15)$$

these three subsystems are defined as

$$\dot{\xi} = f_1(\xi) := A\xi - b, \quad \xi(t_0) = \xi_1, \quad (2.16a)$$

$$\dot{\xi} = f_0(\xi) := \begin{bmatrix} 0 & 0 & 0 \\ 1 & 0 & 0 \\ 0 & 0 & 0 \end{bmatrix} \xi, \quad \xi(t_0) = \xi_0, \quad (2.16b)$$

$$\dot{\xi} = f_{-1}(\xi) := A\xi + b, \quad \xi(t_0) = \xi_{-1}. \quad (2.16c)$$

For $\xi = (\xi_\sigma, \xi_\phi, \xi_v) \in \mathbb{R}^3$ and $|\xi|_P^2 := \xi^T P \xi$, define also

$$V_1(\xi) := \left\| \begin{bmatrix} \xi_\sigma \\ \xi_\phi - F_s \\ \xi_v \end{bmatrix} \right\|_P^2, V_0(\xi) := \left\| \begin{bmatrix} \xi_\sigma \\ 0 \\ 0 \end{bmatrix} \right\|_P^2, V_{-1}(\xi) := \left\| \begin{bmatrix} \xi_\sigma \\ \xi_\phi + F_s \\ \xi_v \end{bmatrix} \right\|_P^2. \quad (2.16d)$$

With these definitions in place, we can state Lemma 2.6 below. Item (i) asserts that flowing solutions to (2.11) are unique (in spite of the differential inclusion in (2.11a)), whereas item (ii) relates such a (unique) flowing solution with the solution of one of the subsystems (2.16a)-(2.16c). The solution x to a hybrid dynamical system and its hybrid time domain $\text{dom } x$ are defined respectively in [63, Def. 2.6] and [63, Def. 2.3].

Lemma 2.6. *For each solution x to (2.11), each interval $I^j := \{t: (t, j) \in \text{dom } x\} =: [t_j, t_{j+1}]$ with nonempty interior, and for all $t \in (t_j, t_{j+1})$,*

(i) *if $\hat{x} = (\hat{\sigma}, \hat{\phi}, \hat{v})$ is a solution to (2.11) on $[t, t'] \times \{j\}$ with $t < t' \leq t_{j+1}$ and $\hat{x}(t, j) = x(t, j)$, then \hat{x} coincides with x on $[t, t'] \times \{j\}$;*

(ii) *one can select $k \in \{-1, 0, 1\}$ and $T > 0$ such that the unique solution $\xi = (\xi_\sigma, \xi_\phi, \xi_v)$ to (2.16) with initial condition $\xi_k = x(t, j)$ and $t_0 = t$, coincides on $[t, t+T]$ with $x(\cdot, j)$ and, additionally, V in (2.14) and V_k in (2.16d) evaluated along ξ satisfy for all $\tau \in [t, t+T]$:*

$$V(\xi(\tau)) = V_k(\xi(\tau)) \text{ and} \quad (2.17a)$$

$$\frac{d}{d\tau} V_k(\xi(\tau)) \leq -c|\xi_v(\tau)|^2, \quad (2.17b)$$

with

$$c := 2(k_p k_d - k_i) > 0. \quad (2.18)$$

Proof. See Appendix 2.A.1 □

Exploiting Lemma 2.6, we are ready to present the properties of V in (2.14) in Lemma 2.7 below. We will use fact that the distance of a point $x \in \mathbb{R}^3$ to the attractor \mathcal{A} in (2.13) is obtained from the definition as

$$|x|_{\mathcal{A}}^2 := \left(\inf_{y \in \mathcal{A}} |x - y| \right)^2 = \sigma^2 + v^2 + \text{d}_{z_{F_s}}(\phi)^2, \quad (2.19)$$

by separating the cases $\phi < -F_s$, $|\phi| \leq F_s$, $\phi > F_s$.

Lemma 2.7. V in (2.14) is lower semicontinuous (lsc) and enjoys the following properties:

1. $V(x) = 0$ for all $x \in \mathcal{A}$ and there exists $c_1 > 0$ such that $c_1|x|_{\mathcal{A}}^2 \leq V(x)$ for all $x \in \mathbb{R}^3$.
2. Given c in (2.18), each solution x satisfies

$$V(x(t_2, j)) - V(x(t_1, j)) \leq -c \int_{t_1}^{t_2} v(t, j)^2 dt \quad (2.20)$$

for all t_1, t_2 in each (flow) interval $I^j := \{t: (t, j) \in \text{dom } x\}$ with nonempty interior, and $t_1 \leq t_2$.

3. For all $x \in \mathcal{D}$ in (2.11c) it holds that

$$V(g(x)) - V(x) \leq 0. \quad (2.21)$$

Proof. See Appendix 2.A.2. □

The properties of V in Lemma 2.7 imply that maximal solutions are complete [63, Sec. 2.3], as per the next lemma.

Lemma 2.8. For each initial condition $\bar{x} \in \mathbb{R}^3$, each maximal solution x to (2.11) with $x(0, 0) = \bar{x}$ is complete.

Proof. See Appendix 2.A.3. □

We can now prove global attractivity of \mathcal{A} in (2.13) through a meagre-limsup invariance principle [63, Thm. 8.11] in the next lemma.

Lemma 2.9. The set of equilibria \mathcal{A} in (2.13) is globally attractive for hybrid dynamics (2.11).

Proof. See Appendix 2.A.4. □

Finally, we now turn to proving stability of \mathcal{A} in (2.13). As in [29], we need the auxiliary function

$$\hat{V}(x) := \frac{1}{2}k_1\sigma^2 + \frac{1}{2}k_2(\text{dz}_{F_s}(\phi))^2 + k_3|\sigma||v| + \frac{1}{2}k_4v^2, \quad (2.22)$$

in order to prove stability through bound (2.24) below, in spite of the discontinuity of V in (2.14). Indeed, because of such discontinuity at points in the attractor \mathcal{A} , an upper bound of the type $c_2|x|_{\mathcal{A}}^2$ (for some $c_2 > 0$) for $V(x)$ does not hold in \mathbb{R}^3 , unlike the lower bound in Lemma 2.7 (item 1), and stability of \mathcal{A} cannot be concluded directly from V . However, such lower and upper bounds, together with suitable growth bounds along solutions, can be established for V and \hat{V} , respectively, in the following partition of the state space, i.e., $R := \{x \mid v(\phi - \text{sign}(v)F_s) \geq 0\}$ and $\hat{R} := \mathbb{R}^3 \setminus R$, as characterized in the next lemma.

Lemma 2.10. *For suitable positive scalars k_1, k_2, k_3, k_4 in (2.22), there exist positive scalars $c_1, c_2, \hat{c}_1, \hat{c}_2$ such that*

$$c_1|x|_{\mathcal{A}}^2 \leq V(x) \leq c_2|x|_{\mathcal{A}}^2, \quad \forall x \in R, \quad (2.23a)$$

$$\hat{c}_1|x|_{\mathcal{A}}^2 \leq \hat{V}(x) \leq \hat{c}_2|x|_{\mathcal{A}}^2, \quad \forall x \in \mathbb{R}^3, \quad (2.23b)$$

$$\hat{V}^\circ(x) := \max_{\mathbf{v} \in \partial \hat{V}(x), \mathbf{f} \in F(x)} \langle \mathbf{v}, \mathbf{f} \rangle \leq 0, \quad \forall x \in \hat{R}, \quad (2.23c)$$

$$\hat{V}(g(x)) - \hat{V}(x) \leq 0 \quad \forall x \in \hat{R}, \quad (2.23d)$$

where $\partial \hat{V}(x)$ denotes the generalized gradient of \hat{V} at x as in [45, §1.2], F is as in (2.11a), and g is as in (2.11b).

Proof. Equations (2.23a)-(2.23b) are proved analogously to [29, (19a)-(19b)]. This is also true for (2.23c), since the flow map F is the same as well. Finally, (2.23d) holds since $(dz_{F_s}(-\alpha\phi))^2 \leq (dz_{F_s}(\phi))^2$ for $\alpha \in [0, 1]$. \square

By composing the relations of Lemma 2.10 and Lemma 2.7 for V and \hat{V} , the bound (2.24) of the next lemma can be obtained, which establishes (uniform global) stability (see [63, Def. 3.6]) of \mathcal{A} in (2.13).

Lemma 2.11. *Given the scalars $c_1, c_2, \hat{c}_1, \hat{c}_2$ in (2.23), each solution x to (2.11) satisfies*

$$|x(t, j)|_{\mathcal{A}} \leq \sqrt{\frac{c_2 \hat{c}_2}{c_1 \hat{c}_1}} |x(0, 0)|_{\mathcal{A}} \quad \forall (t, j) \in \text{dom } x. \quad (2.24)$$

Proof. See Appendix 2.A.5. \square

Remark 2.12. *Since \mathcal{A} is compact, and the hybrid system (2.11) satisfies the hybrid basic conditions [63, Assumption 6.5], the stability and global attractivity results proven above imply uniform global asymptotic stability for (2.11) in terms of a class- \mathcal{KL} estimate. They also imply global robust \mathcal{KL} asymptotic stability of \mathcal{A} for (2.11) [63, Thm. 7.21] and semiglobal practical robust asymptotic stability of \mathcal{A} [63, Thm. 7.12 and Lemma 7.20]. The last result is useful when the friction characteristic also contains the velocity-weakening (Stribeck) effect, which may be considered as a perturbation of Ψ in (2.2). We can then use the practical stability result to show that \mathcal{A} is globally input-to-state stable w.r.t. the perturbation size in the same way as in [29, Prop. 2]. \lrcorner*

2.5 Experimental case study on a high-accuracy positioning machine

In this section, we demonstrate the working principle and the effectiveness of the proposed reset controller on an industrial high-precision positioning stage.

The considered stage represents a sample manipulation stage of an electron microscope [142]. In particular, we show 1) the robust stability properties of the controller in the presence of unknown static friction and measurement noise, 2) that the transient performance is indeed improved w.r.t. the classical PID controller, as in item 2 of Problem 1, and 3) how the tuning of the reset controller affects performance.

2.5.1 Experimental setup

The experimental setup is presented in Figure 2.4. The setup consists of a Maxon RE25 DC servo motor ① connected to a spindle ② via a coupling ③ that is stiff in the rotational direction while being flexible in the translational direction. The spindle drives a nut ④, transforming the rotary motion of the spindle to a translational motion of the attached carriage ⑤, with a ratio of $7.96 \cdot 10^{-5}$ m/rad. The position of the carriage is measured by a linear Renishaw encoder ⑥ with a resolution of 1 nm (and peak noise level of 4 nm). A coiled spring ⑦ connects the carriage to the fixed world frame to eliminate any backlash between the spindle and the nut. The desired position accuracy to be achieved is 10 nm, as specified by the manufacturer.

For frequencies up to 200 Hz, the system dynamics can be well described by (2.1) for which Theorem 2.5 applies when interconnected with the reset PID

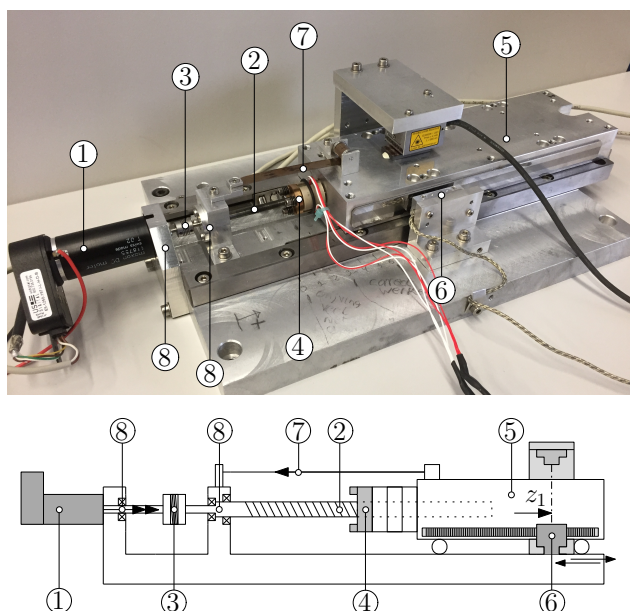


Figure 2.4. Experimental setup of a nano-positioning motion stage.

controller. In this case, z_1 represents the position of the carriage. The mass $m = 172.6$ kg consists of the transformed inertia of the motor and the spindle (with an *equivalent* mass of 171 kg), and of the mass of the carriage (1.6 kg). For frequencies higher than 200 Hz, the motor-spindle and carriage decouple dynamically due to the finite rotational stiffness of the coupling between the motor ① and the spindle ③.

The friction force for Ψ in (2.1) is mainly induced by the bearings supporting the motor axis and the spindle (see ⑧ in Figure 2.4), and by the contact between the spindle and the nut. Since the system is rigid and behaves as a single mass for frequencies up to 200 Hz, these friction forces can be summed up to provide a single net friction characteristic Ψ in (2.1). For illustrative purposes, the net friction characteristic is identified by performing experiments for the static and velocity-dependent parts separately. The static friction values are determined by gradually increasing the actuator force from zero until breakaway of the carriage is measured. At this stick-to-slip transition, the input force is equal to the static friction force. The experiment is repeated for different positions, and for both directions of motion. On average, the static friction values are 32.7 N and 33.1 N for positive and negative motions, respectively, indicating a small level of asymmetry in the friction characteristic. The velocity-dependent part of the friction characteristic is obtained by performing closed-loop experiments, where the carriage tracks a constant *velocity setpoint*. The force applied by the actuator is then equal to the velocity-dependent friction force at one particular (constant) velocity. These experiments are repeated for multiple velocities and initial positions of the carriage.

The resulting overall friction characteristic is visualized in Figure 2.5, where it can be observed that the experimental setup shows dominantly static Coulomb friction. On the other hand, it also shows a small Stribeck effect. The Stribeck effect, however, is insignificant as compared to the static friction, and does not require an additional compensation term in \bar{u} . As we will show below, the closed-loop with a (reset) PID controller results in asymptotic stability of the position setpoint, instead of hunting limit cycling (which may occur in the presence of a more pronounced Stribeck effect). This indicates that the considered system controlled by either the classical PID controller or the proposed reset controller has some robustness to small Stribeck effects. Finally, we emphasize that we *do not* use any information about the friction characteristic in the controller, but we provide the measured friction for illustrative purposes only. Namely, the proposed controller is robust for unknown static friction due to the presence of integral action.

2.5.2 Reset controller tuning

The purpose of the experimental case study is to demonstrate the transient performance benefits that can be obtained with the proposed reset controller, in

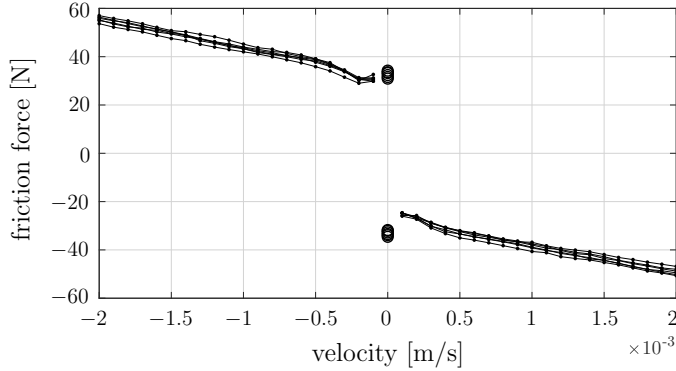


Figure 2.5. Measured friction characteristic. The circles are static friction values obtained from breakaway experiments, and the solid lines connect velocity-dependent friction values for different initial positions.

terms of settling time, relative to the classical PID controller. The PID controller gains $\bar{k}_p = 10^7$ N/m, $\bar{k}_d = 2 \cdot 10^3$ Ns/m, and $\bar{k}_i = 10^8$ N/(ms) are obtained by well-known linear loop-shaping techniques often applied in industry [57], and result in a bandwidth of 36 Hz and sufficient robustness margins. The proposed reset integrator does not require additional tuning constraints other than the “linear” stability conditions in Assumption 2.2 (indeed necessary for the special case $\bar{F}_s = 0$) that are equivalent to

$$\bar{k}_i > 0, \quad \bar{k}_p > 0, \quad \frac{\bar{k}_p(\bar{k}_d + \gamma)}{m} > \bar{k}_i.$$

The last one holds since $\gamma > 0$ and the PID controller gains above satisfy $\frac{\bar{k}_p \bar{k}_d}{m} > \bar{k}_i$.

Secondly, we discuss the role of the tuning parameter α . Most importantly, $\alpha \in [0, 1]$ directly affects the transient performance (a larger α leads to a faster convergence). Additionally, α accommodates the developments in Sections 2.2-2.4 for symmetric friction to possible asymmetries in the experimental friction characteristics. On the one hand, α closer to one yields a larger reset and a correspondingly shorter stick duration. Choosing α as large as possible is thus favorable for the transient performance improvement, and we will show the implications of the value for α on the transient performance in the next subsection. On the other hand, a smaller α results in a relaxed reset, hence a longer stick duration, which enhances robustness for frictional asymmetry as explained in detail in Remark 2.13 below.

Remark 2.13. *A smaller α yields robustness to an asymmetric friction characteristic. If the static friction value in the positive direction of motion is significantly larger than the static friction value in the negative direction of motion, the*

integrator has to build up a larger control force in the positive direction. It may then happen that after the reset ensuing the beginning of a stick phase, the value for the proportional and integral action exceeds the static friction value, resulting in an immediate escape from the stick phase and possibly unstable behavior. In other words, a controller reset (with α large) combined with asymmetric friction may lead to overcompensation, compromising the stability of the setpoint as analyzed in [121]. Hence, in the presence of frictional asymmetry, a smaller α is beneficial for robustness. Note that robustness for the worst-case asymmetry in the friction characteristic (i.e., zero friction in one direction of the velocity, and nonzero friction in the other) is ensured by $\alpha = 0$. However, the friction in the application considered here has only mild asymmetry (see Figure 2.5). \lrcorner

The last tuning parameter ϵ comes from the criterion $|\varphi\varsigma| \geq \epsilon$ which replaces $|\phi\sigma| \geq \epsilon$ in \mathcal{D} , as noted in Remark 2.4. The purpose of $|\varphi\varsigma| \geq \epsilon$ is to prevent a discrete jump when the measurable states ς or φ in (2.12) are zero, so that Zeno behavior is avoided. For practical implementation, we redefine this criterion to the more intuitive criteria $|\varsigma| \geq \eta_1$, $|\varphi| \geq \eta_2$, with $\eta_1, \eta_2 > 0$. We choose $\eta_1 = \bar{k}_i \cdot 10^{-8} = 1$ N/s, so that resets are inhibited when the carriage is within the desired position error accuracy band of 10^{-8} m (10 nm). Also, $\eta_2 = 1$ N·m·s is chosen so that resets are inhibited when φ is small, in order to avoid Zeno behavior. Note that this is achieved for any $\eta_2 > 0$. Using as in Remark 2.4 the measurable states ς and φ in (2.12), and the above alternative criteria, the jump set used for the experiments is then given by

$$\mathcal{D}^* := \{(\varsigma, \varphi, v) \in \mathbb{R}^3 \mid \varphi\varsigma \leq 0, \varphi v \leq 0, |\varsigma| \geq \eta_1, |\varphi| \geq \eta_2\}. \quad (2.25)$$

Note that ς is obtained from the position error measurement $z_1 - r$, and φ is obtained from both the position error measurement, and a recording of the integrator state z_3 . We emphasize also that our main result in Theorem 2.5 and its proof hold unchanged if \mathcal{D}^* replaces \mathcal{D} in (2.11c).

Remark 2.14. *We emphasize that the tuning of the controller gains \bar{k}_p , \bar{k}_d , and \bar{k}_i is not necessarily optimal in the sense of minimizing settling times. The gains are chosen such that standard linear stability and robustness margins are satisfied. Optimal tuning for settling may further improve the transient performance.* \lrcorner

2.5.3 Transient performance comparison

We now demonstrate the transient performance benefits of the proposed reset controller. According to standard operation of the nano-positioning stage in an electron microscope, a fourth-order reference trajectory is applied to the stage so that it moves by one millimeter in one second. After the trajectory has ended, the stage has a nonzero positioning error due to the presence of friction. This is the starting point of our window of interest during the experiments, and from

this point on, the goal is to control the system towards a specified position error accuracy of 10 nm using the proposed reset controller. In particular, we will show the *relative* improvement in terms of settling time (i.e., the required time for the position error to reach and remain in the error band of 10 nm), as compared to the underlying classical PID controller without resets.

The responses for the position error $z_1 - r$ and the corresponding scaled control force $\bar{u}/(4\bar{k}_i)$ are presented in Figure 2.6 for the classical PID and the reset PID (with different values of α). All experiments are performed with the same initial conditions. Variations in the position errors and time instants of the initial stick phases between the presented responses are due to the fact that the friction characteristic is slightly different for each experiment, due to, e.g., small temperature changes as a result of continued system operation. Since the setup operates on a very small position error regime, even minor changes in the friction may have a significant impact on the response. It can be observed in Figure 2.6 that the application of the reset controller (see the three bottom plots for different values for α) results in shorter stick periods and hence decreased settling times, as compared to the classical PID controller (see the top plot). In particular, in the presented responses, the desired accuracy is achieved at respectively, 56.7, 25.3 and 8.4 seconds corresponding to values for α of 0.3, 0.8 and 1. In contrast to the reset controller, the classical PID controller (with the same controller gains), did not reach the desired accuracy within the maximal measurement window of 120 seconds.

To further illustrate the results, we present in Figure 2.7 the cumulative position error (CPE) of the carriage. Due to sampling of the position error in the experiments, the discrete-time CPE is determined as $\text{CPE}(t^{(k)}) := \sum_{l=1}^k |z_1(t^{(l)}) - r|$, $k \in \{1, \dots, N\}$, where $k = 1$ corresponds to the beginning of the first stick phase for the considered experiment, and $k = N$ to the end of the experiment. The CPE values at the end of the experiment at $k = N$, i.e., $\text{CPE}(t^{(N)})$, are $3.2 \cdot 10^{-3}$ m, $2.1 \cdot 10^{-3}$ m, $9.8 \cdot 10^{-4}$ m, and $7.9 \cdot 10^{-4}$ m for the cases of no reset, $\alpha = 0.3$, $\alpha = 0.8$, and $\alpha = 1$, respectively, from which the performance improvement in terms of position accuracy is evident.

Finally, we emphasize that false resets are not triggered due to the robust design of the jump set \mathcal{D} (and its implementable version \mathcal{D}^* in (2.25)) with respect to velocity measurement noise, as pointed out in Remark 2.3. The inset in the second subplot in Figure 2.6 shows that indeed a reset is triggered as soon as the velocity hits zero (characterizing the start of a stick phase, as in (2.7a)). After the reset has occurred, the velocity signal keeps crossing zero during the stick phase, due to noise, but undesired multiple resets are prevented by the robust design of the reset conditions, in accordance with Remark 2.4.

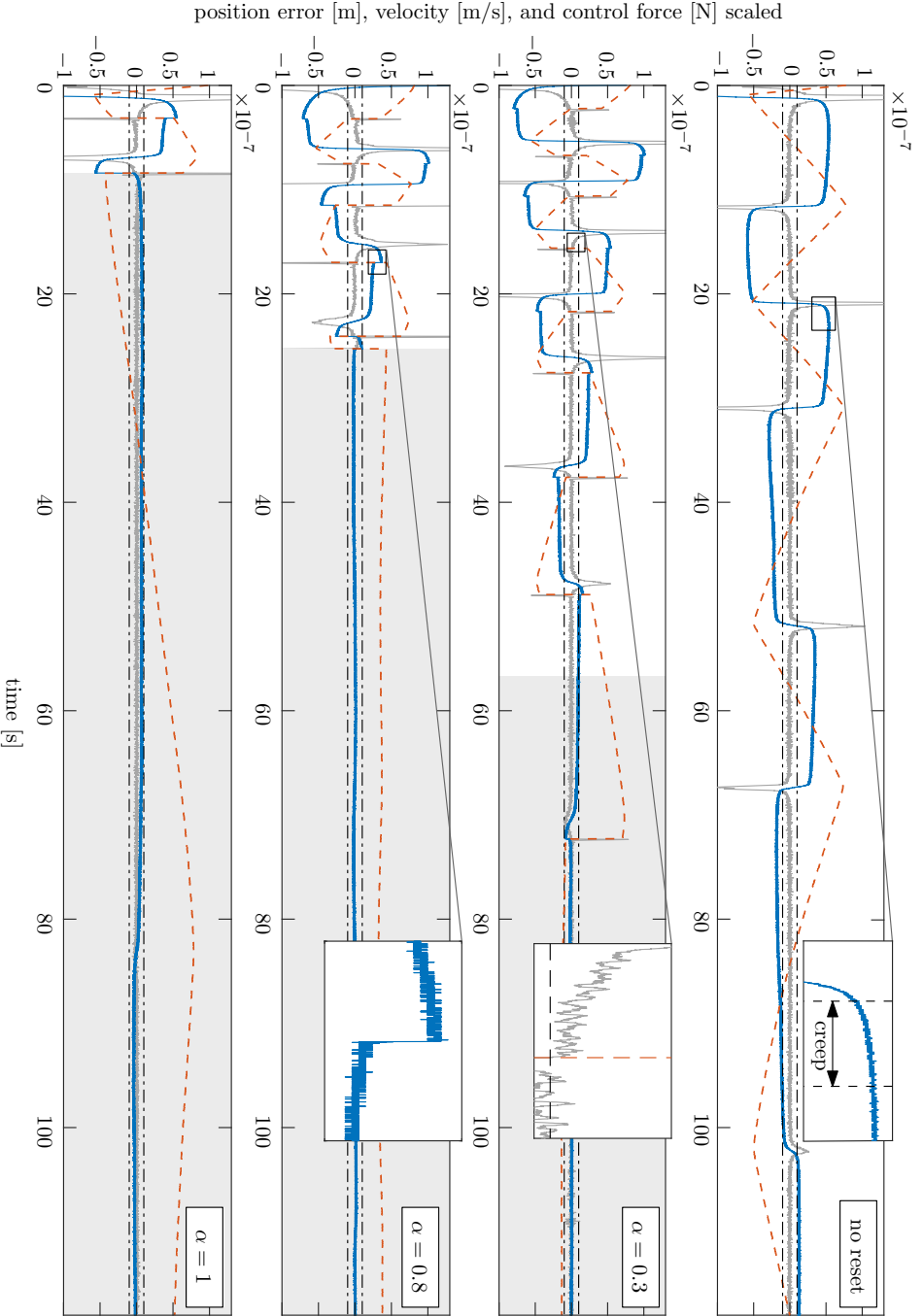


Figure 2.6. Experimental results for various values of α . Position error $z_1 - r$ (—); velocity (—); total control force scaled by $4k_i$ (---). The accuracy band of 10 nm is indicated by the black, dashed-dotted lines. The response resides within the desired accuracy from 56.7, 25.8, and 8.4 seconds onwards corresponding to values for α of 0.3, 0.8, and 1, respectively, as indicated by the gray patches.

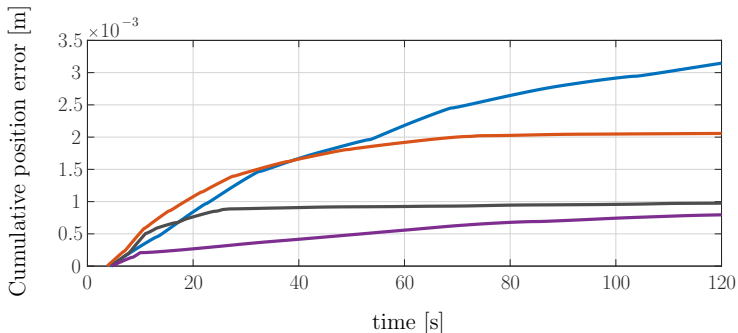


Figure 2.7. Cumulative position error for the cases without reset (—), $\alpha = 0.3$ (—), $\alpha = 0.8$ (—), and $\alpha = 1$ (—).

2.5.4 Unmodeled frictional effects

We now discuss the impact of frictional effects on the response shown in Figure 2.6, that are not contained in the static set-valued friction model of (2.2). Due to the low position error levels in the operating conditions of the setup, microscopic frictional effects that are present in the friction characteristic are significant compared to the static friction effect in this particular application. The experimental results above show that the proposed control strategy also exhibits some robustness against these effects, although not formally taken into account in the stability analysis of Section 2.4.

Frictional creep

As compared to the response in the example of Section 2.2.2, a controller reset occurs some time after the beginning of a macroscopic stick phase. This effect is caused by frictional creep³ (see, e.g., [11, Ch. 2]) at the start of (and during) a macroscopic stick phase (see the inset in the first subplot of Figure 2.6). Such an effect hinders a discrete jump at the end of a macroscopic slip phase because of the nonzero velocity. Hitting $v = 0$ (so that $\varphi v \leq 0$ in \mathcal{D}^* is satisfied) can be detected only when creep stops. This is illustrated by the inset in the second subplot of Figure 2.6, where we highlight the velocity signal during such a period of creep. A nonzero velocity is indeed observed during creep, and the controller is reset only as soon as the velocity signal hits zero (indicated by the black dashed horizontal line). The reset delay associated to creep allows then the integrator buffer to deplete, which, in turn, causes a milder reset. This milder reset further motivates to choose $\alpha = 1$ despite the (minor) asymmetry in the friction characteristics (see Figure 2.5).

³or microslip in the so-called presliding regime (see, e.g., [5], [131]), which can be captured by more enhanced (dynamic) frictional models, as illustrated in Section 1.1.1.1.

Frictional stiffness effects

A second phenomenon caused by unmodeled frictional effects are the small stick-to-stick jumps in the position error response upon resets, see the inset in the third subplot of Figure 2.6. This phenomenon can be explained by the presence of stiffness-like characteristics in the friction, see e.g., [12, Sec. 2.1]. The associated effects are significant due to the fact that the setup operates in regimes with nano-scale position errors. To illustrate this, note that the magnitude of these stiffness-like effects can be estimated by dividing the difference in the control force associated with a controller reset, by the resulting change in position. This results in values between $8 \cdot 10^8$ and $7 \cdot 10^9$ N/m. Although these estimated stiffness coefficients are very large, the associated effect is significant due to the small position errors in the operating conditions. Note that the system still resides in the stick phase in macroscopic sense after the controller reset. In this case, these effects are not unfavourable, as they force the system towards the setpoint. On the other hand, the position error after such a jump is smaller, so that it takes more time for the integrator to compensate for the static friction.

2.6 Conclusions

We proposed a novel reset integrator control strategy for motion systems with friction that achieves, firstly, robust global asymptotic stability of the setpoint for unknown static friction and, secondly, improves transient performance by reducing the settling time. The reset conditions are designed so that a controller reset is correctly triggered despite measurement noise, and does not increase the risk of exciting high-frequency system dynamics. Global asymptotic stability of the setpoint is proven based on a generalized invariance principle for hybrid dynamical systems. An experimental case study on a high-precision positioning application shows the improved settling time when using the proposed reset controller, as compared to its classical PID counterpart.

2.A Proofs

2.A.1 Proof of Lemma 2.6

The proof of Lemma 2.6 is based on the proofs of [29, Lemma 1 and Claim 1]. Note that $c > 0$ in (2.18) by Assumption 2.2.

Item (i). Define $\delta = (\delta_\sigma, \delta_\phi, \delta_v) := x - \hat{x}$ on $[t, t'] \times \{j\}$ so that $\delta(t, j) = 0$. Since both x and \hat{x} flow on $[t, t'] \times \{j\}$, we have that almost everywhere in $[t, t']$:

$$\dot{\delta} \in A\delta + \begin{bmatrix} 0 \\ 0 \\ F_s(-\text{Sign}(v) + \text{Sign}(v - \delta_v)) \end{bmatrix},$$

and

$$\overline{\left(\frac{\delta^\top \delta}{2}\right)} \in \delta^\top A\delta + \delta_v[-F_s \text{Sign}(v) + F_s \text{Sign}(v - \delta_v)].$$

With λ denoting the largest singular value of A , we have

$$\frac{d}{d\tau} \left(\frac{\delta(\tau, j)^\top \delta(\tau, j)}{2} \right) \leq \lambda |\delta(\tau, j)|^2 + M(\tau, j)$$

$$M(\tau, j) := \max_{\substack{f_2 \in F_s \text{Sign}(v(\tau, j) - \delta_v(\tau, j)) \\ f_1 \in F_s \text{Sign}(v(\tau, j))}} \delta_v(\tau, j)[f_2 - f_1].$$

Whether $v(\tau, j) - \delta_v(\tau, j)$ and $v(\tau, j)$ are positive, zero or negative, inspecting all cases reveals that $M(\tau, j) \leq 0$ for all $\tau \in [t, t']$. As a result, $\frac{d}{d\tau} \left(\frac{\delta(\tau, j)^\top \delta(\tau, j)}{2} \right) \leq \lambda |\delta(\tau, j)|^2$ for almost all $\tau \in [t, t']$, and standard comparison theorems (such as [83, Sec. 3.4]) imply from $\delta(t, j) = 0$ that $\delta = 0$ on $[t, t'] \times \{j\}$.

Item (ii). For each possible initial condition $(\bar{\sigma}, \bar{\phi}, \bar{v}) := x(t, j)$, k in item (ii) is selected based on Table 2.1. The proof is then carried out analogously to [29, Appendix A] by substituting into (2.11) the solution ξ to the k -th affine subsystem $\dot{\xi} = f_k(\xi)$ among (2.16a)-(2.16c) and verifying that (2.11) holds for ξ . Moreover, by evaluating V and V_k along the same ξ , and finally by differentiating $V_k(\xi(\cdot))$ w.r.t. time, we obtain (2.17). \square

Table 2.1. Selection of k in item (ii) of Lemma 2.6 for each possible initial condition.

Initial condition $(\bar{\sigma}, \bar{\phi}, \bar{v}) := x(t, j)$	k
$(\bar{v} > 0) \vee (\bar{v} = 0 \wedge \bar{\phi} > F_s) \vee (\bar{v} = 0 \wedge \bar{\phi} = F_s \wedge \bar{\sigma} > 0)$	1
$(\bar{v} = 0 \wedge \bar{\phi} = F_s \wedge \bar{\sigma} \leq 0)$ $\vee (\bar{v} = 0 \wedge \bar{\phi} < F_s) \vee (\bar{v} = 0 \wedge \bar{\phi} = -F_s \wedge \bar{\sigma} \geq 0)$	0
$(\bar{v} = 0 \wedge \bar{\phi} = -F_s \wedge \bar{\sigma} < 0) \vee (\bar{v} = 0 \wedge \bar{\phi} < -F_s) \vee (\bar{v} < 0)$	-1

2.A.2 Proof of Lemma 2.7

Based on Assumption 2.2, the proof of V being lsc and of item (1) is identical to [29, Proof of Lemma 2].

Item (2). To prove this item, we use [66, Thm. 9] with the variant in [66, Sec. 5 (point a.)], as in the following Fact 2.15. The statement is specialized for an integrable function l , so that the standard integral can replace the upper integral in [66, Thm. 9], as noted after [66, Def. 8].

Fact 2.15. [66] *Given $t_2 > t_1 \geq 0$, suppose that h is lower semicontinuous and that l is locally integrable in $[t_1, t_2]$. If $D_+h(\tau) \leq l(\tau)$ for all $\tau \in [t_1, t_2]$, then $h(t_2) - h(t_1) \leq \int_{t_1}^{t_2} l(\tau)d\tau$.*

By the preliminary Lemma 2.6, (2.20) in item (2) is a mere application of Fact 2.15 for $h(\cdot) = V(x(\cdot, j))$ and $l(\cdot) = -cv(\cdot, j)^2$ where $x = (\sigma, \phi, v)$ is a solution to (2.11). So, we need to check that the assumptions of Fact 2.15 are verified. We already established above that $V(\cdot)$ is lsc. Solutions x to (2.11) are such that for each $j \in \mathbb{Z}_{\geq 0}$, $t \mapsto x(t, j)$ is locally absolutely continuous by [63, Def. 2.4 and 2.6]. Then, because the composition of a lsc and a continuous function is lsc [128, Exercise 1.40], the Lyapunov-like function V in (2.14) evaluated along the flow portion of a solution to (2.11) is lsc in t . Because of the local absolute continuity of flowing portions of solutions, $-cv(\cdot, j)^2$ is locally integrable.

Finally, it was proven in item (ii) of Lemma 2.6 that on I^j , the solution x to (2.11) coincides with the solution ξ to one of the three affine systems in (2.16) (numbered k) on $[t, t + T]$. Moreover, that same item states that $V(\xi(\cdot))$ coincides in $[t, t + T]$ with the function $V_k(\xi(\cdot))$ in (2.17), which is differentiable, hence $V(x(\cdot, j))$ is at least differentiable from the right at t and the lower right Dini derivative coincides with the right derivative. In particular, we established in (2.17) that this right derivative is upper bounded by $-cv(\cdot, j)^2$.

Item (3). For all $x \in \mathcal{D}$ in (2.11c), $V(g(x)) - V(x) = \min_{F \in F_s \text{ Sign}(v)} (-\alpha\phi - F)^2 - \min_{F \in F_s \text{ Sign}(v)} (\phi - F)^2$ where for each v , the set $F_s \text{ Sign}(v)$ is compact. We obtain

$$V(g(x)) - V(x) = \begin{cases} (\alpha^2 - 1)\phi^2 + 2(\alpha + 1)\phi F_s \text{sign}(v), & \text{if } v \neq 0, \\ (\alpha dz_{\frac{F_s}{\alpha}}(\phi))^2 - (dz_{F_s}(\phi))^2, & \text{if } v = 0, \end{cases} \quad (2.26)$$

by evaluating the different cases for v and ϕ . The inequality in (2.21) follows from (2.26) since $0 \leq \alpha \leq 1$ and $\phi v \leq 0$ in the jump set \mathcal{D} . \square

2.A.3 Proof of Lemma 2.8

The proof is based on [63, Prop. 6.10], which can be applied since (2.11) satisfies the so-called hybrid basic conditions [63, As. 6.5]. Condition (VC) of [63,

Prop. 6.10] holds for every $\xi \in \mathcal{C} \setminus \mathcal{D}$, otherwise we would contradict completeness in [29, Lem. 1]. Therefore, each solution x satisfies exactly one of [63, Prop. 6.10, (a)-(c)]. Note that (2.20) and (2.21) imply together that

$$V(x(t, j)) \leq V(x(0, 0)) \quad (2.27)$$

for each $(t, j) \in \text{dom } x$. If [63, Prop. 6.10, (b)] is verified (that is, $\lim_{t \rightarrow \sup_t \text{dom } x} |x(t, \sup_j \text{dom } x)| = +\infty$), then also V grows unbounded because of the lower bound of V in Item 1 of Lemma 2.7. But this is a contradiction of (2.27), so we can exclude [63, Prop. 6.10, (b)] for each solution. Also [63, Prop. 6.10, (c)] can be excluded since $\mathcal{C} \cup \mathcal{D}$ is \mathbb{R}^3 in (2.11). Then only [63, Prop. 6.10, (a)] remains, i.e., each solution x is complete. \square

2.A.4 Proof of Lemma 2.9

[63, Thm. 8.11] is applicable because [63, As. 6.5] is satisfied by (2.11). Note that, since each maximal solution x to (2.11) is complete by Lemma 2.8, the conclusions of [63, Thm. 8.11] will hold for each maximal solution x once we verify that each such x satisfies the meagre-limsup conditions (a)-(b) below. More specifically, introduce the continuous functions $x \mapsto \ell_c(x) := v^2$ and $x \mapsto \ell_d(x) := 1$. Then, [63, Thm. 8.11] holds if:

- (a) if $\sup_t \text{dom } x = \infty$, then $t \mapsto \ell_c(x(t, j(t)))$ is weakly meagre (as defined on [63, p. 178]), where $j(t) := \min_{(t, j) \in \text{dom } x} j$;
- (b) for each maximal solution x^* to (2.11), if $(t, j-1), (t, j), (t, j+1) \in \text{dom } x^*$, then $\ell_d(x^*(t, j)) = 0$.

Let us check condition (a). Lemma 2.7 (items 2-3) implies, for each solution x and a generic $(t, j) \in \text{dom } x$, that $V(x(t, j)) - V(x(0, 0)) \leq -c \int_0^t v(\tau, j(\tau))^2 d\tau$, by splitting into flow intervals and jumps. We then have $\int_0^t \ell_c(x(\tau, j(\tau))) d\tau \leq \frac{V(x(0, 0)) - V(x(t, j))}{c} \leq \frac{V(x(0, 0))}{c}$ by Lemma 2.7 (item 1). By letting $t \rightarrow +\infty$, this means that $t \mapsto \ell_c(x(t, j(t)))$ is absolutely integrable on $\mathbb{R}_{\geq 0}$ and is hence weakly meagre (see [63, p. 178]).

Let us check condition (b). For all maximal solutions x^* to (2.11), there are no $(t, j-1), (t, j), (t, j+1) \in \text{dom } x^*$ since each x^* cannot exhibit two or more consecutive jumps (by the definitions of g and \mathcal{D} , if both $(t, j-1)$ and $(t, j) \in \text{dom } x^*$, then $x^*(t, j-1) \in \mathcal{D}$ and $x^*(t, j) \in \mathcal{C} \setminus \mathcal{D}$). So, condition (b) is (vacuously) satisfied.

Since (a) and (b) above hold, then [63, Thm. 8.11] concludes that for each solution x , $\Omega(x) \subset \{\chi \in \overline{\text{rg } x} : v = 0\}$, where $\Omega(x)$ is the ω -limit set of solution x [63, Def. 6.17] and $\overline{\text{rg } x}$ denotes the closure of the range of x . Due to the properties of $\Omega(x)$ in [63, Prop. 6.21], its weak invariance implies that for each complete solution x , $\Omega(x)$ does not contain points where $\sigma \neq 0$ or $|\phi| > F_s$,

because from these points all complete solutions eventually exhibit a nonzero velocity component. As a consequence, $\Omega(x) \subset \mathcal{A}$ for each complete solution x , which implies by [63, Prop. 6.21] that all complete solutions converge to \mathcal{A} , i.e., global attractivity of \mathcal{A} . \square

2.A.5 Proof of Lemma 2.11

Consider the two mutually exclusive cases:

Case (A): $x(t, j) \notin R$ for all $(t, j) \in \text{dom } x$. Since $R \cup \hat{R} = \mathbb{R}^3$, $x(t, j) \in \hat{R}$ for all $(t, j) \in \text{dom } x$. (2.23c) implies that \hat{V} does not increase while such a solution x flows. In other words: for any such x , for each $j \in \mathbb{Z}_{\geq 0}$ such that $I^j := \{t : (t, j) \in \text{dom } x\}$ has a nonempty interior, for each $t_1, t_2 \in I^j$ satisfying $t_1 \leq t_2$, we have that

$$\hat{V}(x(t_1, j)) \leq \hat{V}(x(t_2, j)) \quad (2.28)$$

because in (2.23c) $\hat{V}^\circ(x(t, j)) \leq 0$ for all $t \in [t_1, t_2]$. Moreover, (2.23d) implies that \hat{V} does not increase over jumps of x , that is,

$$\hat{V}(x(t, j)) \leq \hat{V}(x(t, j-1)) \quad (2.29)$$

for all $(t, j), (t, j-1) \in \text{dom } x$. By (2.23b), we have then

$$\hat{c}_1 |x(t, j)|_{\mathcal{A}}^2 \leq \hat{V}(x(t, j)) \leq \hat{V}(x(0, 0)) \leq \hat{c}_2 |x(0, 0)|_{\mathcal{A}}^2$$

for all $(t, j) \in \text{dom } x$. This implies (2.24) since $1 \leq \sqrt{\frac{c_2}{c_1}}$.

Case (B): there exists $(\bar{t}, \bar{j}) \in \text{dom } x$ such that $x(\bar{t}, \bar{j}) \in R$. Consider the $(\bar{t}, \bar{j}) \in \text{dom } x$ such that $\bar{t} + \bar{j}$ is smallest and $x(\bar{t}, \bar{j}) \in R$ (the existence of such a “smallest” time follows from R being closed). Then, following the analysis of Case (A) for hybrid times up to (\bar{t}, \bar{j}) (which can possibly be $(0, 0)$), we obtain

$$\hat{c}_1 |x(t, j)|_{\mathcal{A}}^2 \leq \hat{c}_2 |x(0, 0)|_{\mathcal{A}}^2 \quad (2.30)$$

for all $(t, j) \in \text{dom } x$ with $t + j \leq \bar{t} + \bar{j}$. Since $x(\bar{t}, \bar{j}) \in R$, we apply (2.23a) and (2.30) to obtain $V(x(\bar{t}, \bar{j})) \leq c_2 |x(\bar{t}, \bar{j})|_{\mathcal{A}}^2 \leq c_2 \frac{\hat{c}_2}{\hat{c}_1} |x(0, 0)|_{\mathcal{A}}^2$. Finally, by Lemma 2.7, items 1-3,

$$c_1 |x(t, j)|_{\mathcal{A}}^2 \leq V(x(t, j)) \leq V(x(\bar{t}, \bar{j})) \leq c_2 \frac{\hat{c}_2}{\hat{c}_1} |x(0, 0)|_{\mathcal{A}}^2 \quad (2.31)$$

for all $(t, j) \in \text{dom } x$ with $t + j \geq \bar{t} + \bar{j}$. Analogously as [29, Eqs. (21b)-(21c)], the combination of (2.30) and (2.31) proves (2.24). \square

Reset control for setpoint stability of motion systems with Stribeck friction

Abstract – In this chapter, we present a reset control approach to achieve stability of the setpoint of a PID-based motion system subject friction including a Coulomb part and a velocity-weakening (Stribeck) contribution. Whereas classical PID control results in limit cycling around the setpoint (hunting), the proposed reset mechanism realizes stability of the setpoint, and significant overshoot reduction. Moreover, robustness for unknown static friction levels, and an unknown Stribeck contribution, is obtained. The closed-loop system dynamics are formulated in a hybrid systems framework, using a novel hybrid description of the Coulomb friction element, and asymptotic stability of the setpoint is proven accordingly. The working principle of the controller is demonstrated experimentally on a motion stage of an electron microscope, showing superior performance over classical PID control.

3.1 Introduction

In this chapter, we present a reset integral control approach for setpoint stabilization of motion systems with unknown Coulomb and Stribeck friction. Friction is a performance-limiting factor in many high-precision motion systems, in the sense that it limits achievable positioning accuracy and settling times. Many different control techniques for frictional motion systems have been presented in the literature. Several control solutions rely on developing as-accurate-as-possible friction models, used for online compensation in a control loop, see, e.g., [11, 12,

This chapter is based on [18]. Related preliminary results are reported in [28].

58, 90, 100], or for controller synthesis, see, e.g., [3, 127]. Model-based friction compensation methods are typically prone to model mismatches due to, e.g., unreliable friction measurements, or a changing or uncertain friction characteristic. These techniques, therefore, may suffer from over- or undercompensation of friction, resulting in loss of stability of the setpoint [121], thereby limiting the achievable positioning accuracy. Adaptive control methods, see, e.g., [7, 43, 106], have some robustness to a changing friction characteristic, but model mismatches (and the associated performance limitations) still remain. Also non-model-based control techniques have been proposed, examples of which are impulsive control (see, e.g., [115, 148]), dithering-based techniques (see, e.g., [79, 116, 143]), sliding-mode control (see, e.g., [14, 15]), or switched control [114]. These non-model-based controllers, however, employ high-frequency control signals, risking excitation of high-frequency system dynamics. Moreover, tuning and implementation of such controllers is not straightforward.

Despite availability of a wide range of control techniques for frictional systems, linear controllers are still used in the vast majority of industrial motion systems due to the existence of intuitive design and tuning tools. In industry, the classical proportional-integral-derivative (PID) controller is most commonly used for motion systems with friction. Namely, integrator action is capable of compensating for unknown static friction, due to the build up of control force by integrating the position error. However, PID control suffers from two distinct performance limitations when applied to frictional motion systems. First, the use of a classical PID controller on motion systems with with static (Coulomb) friction results in long settling times, see Chapter 2, adversely affecting machine throughput. This limitation has been addressed in the previous chapter, where a reset integrator is proposed that significantly improves transient performance and decreases settling times. The second limitation of PID control for frictional motion systems is that, for friction characteristics including the velocity-weakening (i.e., Stribeck) effect, stability of the setpoint is not achieved, so that the achievable positioning accuracy is limited. Whereas integrator action compensates for the static part of the friction, overcompensation of the friction occurs as velocity increases, due to the velocity-weakening effect. As a result, the system overshoots the setpoint and ends up in a stick-slip limit cycle (i.e., *hunting*), see, e.g., [10, 74], compromising stability of the setpoint. In particular, the Stribeck effect can be viewed as a specific perturbation of the Coulomb friction model, where only input-to-state stability with respect to such perturbation is achieved, see [29, Prop. 2].

In this chapter, we address the setpoint stabilization problem of a PID-controlled motion system with Stribeck friction. In particular, we propose a reset integral controller (which design is essentially different compared to the one presented in the previous chapter) that achieves stability of the setpoint, despite the presence of *unknown* static friction, and an *unknown* velocity-weakening effect in the friction characteristic. We aim at lowering the threshold for control

practitioners to use a nonlinear control strategy in industry, by building upon the well-known PID controller. In particular, the proposed reset enhancements can be used in parallel to a classical, loop-shaped PID controller.

Reset and hybrid controllers have been an active field of research in the past decades. Developments started with the Clegg integrator [46] and the First Order Reset Element [76]. Since then, reset controllers have mainly been used to improve performance of *linear* motion systems, see, e.g., [1, 107]. Specific examples are the hybrid integrator-gain system [52], improving tracking performance while minimizing high-frequency content in the control signal. Overshoot reduction of linear systems using hybrid control is presented in, e.g., [25, 97]. Analysis and design tools for reset controllers are presented in [40, 96, 108]. In the context of frictional systems, reset control has been applied in Chapter 2 of this thesis, where transient performance of PID-based systems with Coulomb friction is improved. In general, reset controllers have been applied to improve *performance* of motion systems, but, to the best of the author's knowledge, not yet for *stabilization* of nonlinear, frictional motion systems, as we consider in this chapter.

The contributions of this chapter are as follows. The first one is the design of a novel reset controller for systems with Stribeck friction, aiming at achieving stability of a constant setpoint. The second contribution is the development of a hybrid model formulation of the closed-loop system, where the Coulomb friction element is modeled through a *hybrid* representation, instead of the commonly used set-valued force law (see, e.g., [2, Sec. 1.3]). The third contribution is a stability analysis of the hybrid closed-loop system, and the fourth contribution is an experimental demonstration of the effectiveness of the proposed controller on an industrial high-precision positioning system (a manipulation stage of an electron microscope).

The remainder of this chapter is organized as follows. In Section 3.2, a model of the considered motion system with a *classical* PID controller is presented, along with some useful properties of the closed-loop system that we use throughout the chapter. Subsequently, the reset integrator control law is presented, and a model-based example illustrates the working principles of the proposed reset controller. The closed-loop dynamics are written as a hybrid system in Section 3.3, and we present a comprehensive stability analysis in Section 3.4. In Section 3.5, the proposed reset controller is experimentally demonstrated in a case study on a high-accuracy positioning system, and conclusions are presented in Section 3.6. Finally, we present a brief discussion on employing the Clegg integrator for frictional systems in Section 3.8, which insight have been obtained in retrospect to the main developments in this chapter.

Notation: For a vector $x \in \mathbb{R}^n$, $|x|$ denotes its Euclidean norm. \mathbb{B} denotes the closed unit ball of appropriate dimensions, in the Euclidean norm. $\text{sign}(\cdot)$ (with a lower-case s) denotes the classical sign function, i.e., $\text{sign}(y) := y/|y|$ for $y \neq 0$ and $\text{sign}(0) := 0$. $\text{Sign}(\cdot)$ (with an upper-case S) denotes the *set-valued* sign

function, i.e., $\text{Sign}(y) := \{\text{sign}(y)\}$ for $y \neq 0$, and $\text{Sign}(y) := [-1, 1]$ for $y = 0$. For $c > 0$, the deadzone function $y \mapsto \text{dz}_c(y)$ is defined as: $\text{dz}_c(y) := 0$ if $|y| \leq c$, $\text{dz}_c(y) := y - c$ if $y > c$, $\text{dz}_c(y) := y + c$ if $y < -c$. $e_3 := (0, 0, 1)^\top$ is the third unit vector of \mathbb{R}^3 .

The hybrid systems modeling framework and corresponding solution concept of [63], used in this chapter, is introduced in Appendix A. In addition, the function $j(\cdot)$ is defined as $j(t) := \min_{(t,j) \in \text{dom } \psi} j$. For a hybrid system \mathcal{H} , $\psi \in \mathcal{S}_{\mathcal{H}}(x)$ (respectively, $\psi \in \mathcal{S}_{\mathcal{H}}(S)$) means that ψ is a maximal solution to \mathcal{H} with $\psi(0, 0) = x$ (respectively, $\psi(0, 0) \in S$), and $\text{rge } \psi$ denotes the range of ψ .

3.2 System description and controller design

In this section, we first describe the motion system with friction and formulate the control problem addressed in this chapter. We then discuss a *classical* PID controller, and provide some useful properties of the PID controlled system that we use throughout the chapter. Thereafter, we discuss the design of the reset control law and provide an illustrative example.

A single-degree-of-freedom mass m sliding on a horizontal plane with position z_1 and velocity z_2 is subject to a control input \bar{u} and a friction force belonging to a set $\Psi(z_2)$, governed by the dynamics

$$\begin{aligned} \dot{z}_1 &= z_2, \\ \dot{z}_2 &\in \frac{1}{m} (\Psi(z_2) + \bar{u}). \end{aligned} \tag{3.1}$$

The friction characteristic is modeled by the following set-valued mapping of the velocity:

$$z_2 \rightrightarrows \Psi(z_2) := -\bar{F}_s \text{Sign}(z_2) - \alpha z_2 + \bar{f}(z_2), \tag{3.2}$$

where \bar{F}_s is the static friction, αz_2 the viscous friction contribution (with $\alpha \geq 0$ the viscous friction coefficient), and \bar{f} a nonlinear velocity-dependent friction contribution, encompassing the Stribeck effect (for which some (mild) requirements are given in Assumption 3.2 below).

With the goal to control the mass to the constant setpoint $(z_1, z_2) = (r, 0)$, the control problem of this chapter is formulated as follows.

Problem 3.1. *Design a reset PID controller for input \bar{u} in (3.1)-(3.2), that globally asymptotically stabilizes the setpoint $(z_1, z_2) = (r, 0)$, in the presence of unknown static friction \bar{F}_s and an unknown velocity-dependent friction characteristic $\bar{f}(z_2)$.*

The presence of integrator action in the controller is motivated by the fact that it is able to compensate for an *unknown* static friction force \bar{F}_s , so that the controller can robustly overcome the Coulomb friction force. However, due to

the overcompensation of friction in the slip phase, limit cycling occurs so that stability of the setpoint is not possible with a *classical* PID controller. Enhancing the classical PID controller with resets instead results in stability of the setpoint, as we will show in this chapter.

3.2.1 Classical PID controller

Let us start with a *classical* PID controller for input \bar{u} in (3.1), i.e.,

$$\begin{aligned}\bar{u} &= -\bar{k}_p(z_1 - r) - \bar{k}_d z_2 - \bar{k}_i z_3, \\ \dot{z}_3 &= z_1 - r,\end{aligned}\tag{3.3}$$

where z_3 is the integral state of the PID controller, and \bar{k}_p , \bar{k}_d , \bar{k}_i represent the proportional, derivative and integral gains, respectively. We now present some properties of the resulting closed-loop system (3.1)-(3.3) that we use throughout this chapter. With state vector $z := (z_1, z_2, z_3)^\top$, we can formulate the closed-loop model as

$$\dot{z} = \begin{bmatrix} \dot{z}_1 \\ \dot{z}_2 \\ \dot{z}_3 \end{bmatrix} \in \begin{bmatrix} z_2 \\ \frac{1}{m} (\Psi(z_2) - \bar{k}_p(z_1 - r) - \bar{k}_d z_2 - \bar{k}_i z_3) \\ z_1 - r \end{bmatrix}.\tag{3.4}$$

As in Chapter 2, we introduce mass-normalized parameters that allow for a simpler description of the system, transform any constant setpoint r to the setpoint 0, and facilitate the construction of Lyapunov functions for the stability analysis in Section 3.4:

$$k_p := \frac{\bar{k}_p}{m}, \quad k_d := \frac{\bar{k}_d + \alpha}{m}, \quad k_i := \frac{\bar{k}_i}{m}, \quad F_s := \frac{\bar{F}_s}{m}, \quad f := \frac{\bar{f}}{m}.\tag{3.5}$$

Next, consider the following state transformation:

$$\hat{x} := \begin{bmatrix} \hat{\sigma} \\ \hat{\phi} \\ \hat{v} \end{bmatrix} = \begin{bmatrix} -k_i(z_1 - r) \\ -k_p(z_1 - r) - k_i z_3 \\ z_2 \end{bmatrix},\tag{3.6}$$

where $\hat{\sigma}$ represents the normalized position error, $\hat{\phi}$ is the controller state encompassing the proportional and integral control actions, and \hat{v} is the velocity of the mass. After the reparametrization in (3.5) and the change of coordinates in (3.6), the model (3.4) is equivalent to

$$\dot{\hat{x}} = \begin{bmatrix} \dot{\hat{\sigma}} \\ \dot{\hat{\phi}} \\ \dot{\hat{v}} \end{bmatrix} \in \begin{bmatrix} -k_i \hat{v} \\ \hat{\sigma} - k_p \hat{v} \\ \hat{\phi} - k_d \hat{v} - F_s \text{Sign}(\hat{v}) + f(\hat{v}) \end{bmatrix} =: \hat{\mathcal{F}}_x(\hat{x}).\tag{3.7}$$

With the model in the new coordinates in place, we formally define “stick” and “slip”. The system is said to be in a *stick* or *slip* phase when the state \hat{x} belongs respectively to the sets

$$\mathcal{E}_{\text{stick}} := \{\hat{x} \in \mathbb{R}^3 \mid v = 0, |\hat{\phi}| \leq F_s\}, \quad (3.8a)$$

$$\mathcal{E}_{\text{slip}} := \mathbb{R}^3 \setminus \mathcal{E}_{\text{stick}}. \quad (3.8b)$$

The controller state $\hat{\phi}$ represents all nonzero components of the control action at zero velocity (that is, the proportional and integral terms), and the difference between $\hat{\phi}$ and F_s at $\hat{v} = 0$ determines whether the system resides in a stick phase or not, see (3.8a).

Let us now adopt the following assumptions on the velocity-dependent friction characteristic f and the controller gains.

Assumption 3.2. *The function f is continuously differentiable and satisfies*

- (i) $|f(\hat{v})| \leq F_s$ for all \hat{v} ;
- (ii) $\hat{v}f(\hat{v}) \geq 0$ for all \hat{v} ;
- (iii) f is globally Lipschitz with Lipschitz constant $L > 0$;
- (iv) for some $\varepsilon_v > 0$ and $L_2 \in (k_d, L]$, $f(\hat{v}) = L_2\hat{v}$ for all $|\hat{v}| \leq \varepsilon_v$.

A possible f satisfying Assumption 3.2 is depicted in Figure 3.1. As for item (iv) of the assumption, we emphasize that ε_v can be selected arbitrarily small. As a result, this part of the assumption is hardly restrictive (note that items (i)-(iii) are not restrictive as well).

Assumption 3.3. *The control parameters k_p, k_d, k_i satisfy $k_p > 0, k_i > 0, k_p k_d > k_i$.*

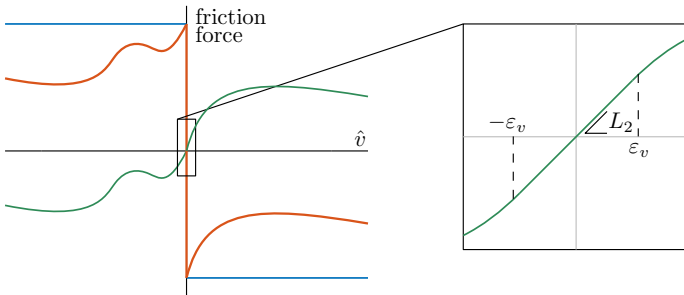


Figure 3.1. Example of a friction force satisfying Assumption 3.2. Total friction Ψ (—), static contribution \bar{F}_s (—), velocity-dependent contribution \bar{f} (—). For $|\hat{v}| \leq \varepsilon_v$, f satisfies $f(\hat{v}) = L_2\hat{v}$.

The selection of gains according to Assumption 3.3 is equivalent to the origin being globally asymptotically stable for (3.7) in the frictionless case (i.e., $F_s = 0$ and $f(\hat{v}) = 0$ for all \hat{v}) by the Routh-Hurwitz criterion, and is therefore not restrictive.

Before introducing the controller reset policy, we show some useful properties of the PID-controlled mass in (3.7). Consider the set-valued mapping

$$\begin{aligned} \hat{\mathcal{F}}_x(\hat{x}) &:= \begin{bmatrix} -k_i \hat{v} \\ \hat{\sigma} - k_p \hat{v} \\ \hat{\phi} - k_d \hat{v} - F_s \text{Sign}(\hat{v}) + f(\hat{v}) \end{bmatrix} \\ &= \begin{bmatrix} 0 & 0 & -k_i \\ 1 & 0 & -k_p \\ 0 & 1 & -k_d \end{bmatrix} \begin{bmatrix} \hat{\sigma} \\ \hat{\phi} \\ \hat{v} \end{bmatrix} - e_3(F_s \text{Sign}(\hat{v}) - f(\hat{v})) \\ &=: A\hat{x} - e_3(F_s \text{Sign}(\hat{v}) - f(\hat{v})). \end{aligned} \quad (3.9)$$

Given (3.9), we have the next claim that shows the decomposition of the differential inclusion model in (3.7) into three subsystems. As it will turn out, the claim will simplify the analysis of the differential inclusion (3.7) (and later in (3.21b)).

Claim 3.4. *Let Assumptions 3.2-3.3 hold and consider the differential inclusion*

$$\dot{\hat{x}} \in \hat{\mathcal{F}}_x(\hat{x}) \quad (3.10)$$

and the initial conditions in Table 3.1.

- (i) *For each initial condition $\hat{x}_0 \in \mathbb{R}^3$, there exists a complete solution² \hat{x} to (3.10) and the solution is unique.*

Table 3.1. Initial conditions considered in Claim 3.4.

$(\hat{v}_0 > 0) \vee (\hat{v}_0 = 0 \wedge \hat{\phi}_0 > F_s)$	(3.11)
$\vee (\hat{v}_0 = 0 \wedge \hat{\phi}_0 = F_s \wedge \hat{\sigma}_0 > 0)$	
$(\hat{v}_0 = 0 \wedge \hat{\sigma}_0 > 0 \wedge \hat{\phi}_0 \in [-F_s, F_s])$	
$\vee (\hat{v}_0 = 0 \wedge \hat{\sigma}_0 = 0 \wedge \hat{\phi}_0 \in [-F_s, F_s])$	(3.12)
$\vee (\hat{v}_0 = 0 \wedge \hat{\sigma}_0 < 0 \wedge \hat{\phi}_0 \in (-F_s, F_s])$	
$(\hat{v}_0 < 0) \vee (\hat{v}_0 = 0 \wedge \hat{\phi}_0 < -F_s)$	(3.13)
$\vee (\hat{v}_0 = 0 \wedge \hat{\phi}_0 = -F_s \wedge \hat{\sigma}_0 < 0).$	

²A solution is any locally absolutely continuous function \hat{x} that satisfies (3.9) for almost all t .

- (ii) For each initial condition $\hat{x}_0 = (\hat{\sigma}_0, \hat{\phi}_0, \hat{v}_0)$ in (3.11), there exists $T > 0$ such that the unique solution \hat{x} to (3.10) (with $\hat{x}(0) = \hat{x}_0$) coincides over $[0, T]$ with the unique solution \tilde{x} (with $\tilde{x}(0) = \hat{x}_0$) to

$$\dot{\hat{x}} = A\tilde{x} - e_3(F_s - f(\tilde{v})), \quad (3.14)$$

which satisfies $\tilde{v}(t) > 0$ for all $t \in (0, T]$.

- (iii) For each initial condition $\hat{x}_0 = (\hat{\sigma}_0, \hat{\phi}_0, \hat{v}_0)$ in (3.12), there exists $T > 0$ such that the unique solution \hat{x} to (3.10) (with $\hat{x}(0) = \hat{x}_0$) coincides over $[0, T]$ with the unique solution \tilde{x} (with $\tilde{x}(0) = \hat{x}_0$) to

$$\dot{\hat{x}} := \begin{bmatrix} \dot{\tilde{\sigma}} \\ \dot{\tilde{\phi}} \\ \dot{\tilde{v}} \end{bmatrix} = \begin{bmatrix} 0 \\ \tilde{\sigma} \\ 0 \end{bmatrix}, \quad (3.15)$$

which satisfies $\tilde{v}(t) = 0$ for all $t \in [0, T]$.

- (iv) For each initial condition $\hat{x}_0 = (\hat{\sigma}_0, \hat{\phi}_0, \hat{v}_0)$ in (3.13), there exists $T > 0$ such that the unique solution \hat{x} (with $\hat{x}(0) = \hat{x}_0$) to (3.10) coincides over $[0, T]$ with the unique solution \tilde{x} (with $\tilde{x}(0) = \hat{x}_0$) to

$$\dot{\hat{x}} = A\tilde{x} - e_3(-F_s - f(\tilde{v})), \quad (3.16)$$

which satisfies $\tilde{v}(t) < 0$ for all $t \in (0, T]$.

Proof. see Appendix 3.A.1. □

3.2.2 Reset controller design

In order to solve Problem 3.1, we replace the integrator in (3.4) and (3.7) with a *reset* integrator. The integrator performs two particular resets, which design is best explained in the *original* coordinates z . The key mechanism of these resets is to enforce that the integrator control force (given by $\bar{k}_i z_3$) *always points in the direction of the setpoint*, namely

$$(z_1 - r)z_3 \geq 0, \quad (3.17)$$

which is then satisfied along all hybrid solutions of the resulting closed loop³. Due to the phase lag associated with a *linear* integrator, this goal cannot be achieved with a classical PID controller, see, e.g., [134]. We will show in this chapter that the frictional system augmented with the reset controller indeed results in stability of the setpoint, solving Problem 3.1.

³Note that this controller design philosophy imposes an initialization constraint on the integrator state z_3 .

In order to end up with well-defined reset conditions satisfying (3.17), we introduce a boolean state $\hat{b} \in \{-1, 1\}$, to capture whether the mass moves *towards* the setpoint (i.e., $\hat{b} = 1$), or *away from* the setpoint (i.e., $\hat{b} = -1$). The latter occurs typically after an overshoot of the position error. More precisely, \hat{b} is suitably initialized and always satisfies

$$\hat{b}(z_1 - r)z_2 \leq 0, \quad (3.18)$$

along all hybrid solutions. To ensure (3.17) and (3.18), we employ the following resets. The first reset entails a sign change of the integrator state z_3 at a zero-crossing of the position error $z_1 - r$. We also toggle \hat{b} at this instant because a zero-crossing of the position marks the start of overshoot. The first reset law is then given by

$$z_3^+ = -z_3, \quad \hat{b}^+ = -\hat{b}, \quad (3.19a)$$

occurring when the following reset condition is satisfied:

$$z_1 - r = 0 \quad \wedge \quad \hat{b} = 1. \quad (3.19b)$$

The reset in (3.19a), (3.19b) has some resemblance with the one proposed in [97], designed for overshoot reduction of linear control systems without friction. However, in [97] a sign change of the *output* of the integral control force is employed, whereas in (3.19a) the sign of the integrator *state* is changed. Besides the fact that the reset in (3.19a) is required to obtain stability of the setpoint, it results in overshoot reduction as well, as we will illustrate in Section 3.2.3.

The second reset yields a reset of the integrator state z_3 to zero, when the velocity z_2 hits zero *after overshoot*, i.e.,

$$z_3^+ = 0, \quad \hat{b}^+ = -\hat{b}, \quad (3.19c)$$

occurring when the following reset condition is satisfied:

$$z_2 = 0 \quad \wedge \quad \hat{b} = -1. \quad (3.19d)$$

The reset in (3.19c)-(3.19d) is required to obtain asymptotic stability of the setpoint. Indeed, if it were absent, the reset in (3.19a) would not allow the integrator state z_3 to decrease in absolute sense. A sufficiently large initial condition for z_3 would then hinder asymptotic stability of the setpoint. Summarizing, the resulting closed-loop system with the proposed reset PID controller is given by (3.1)-(3.3), and (3.19).

3.2.3 Illustrative example

We will illustrate the working principle of the proposed reset controller by means of a simulation example, using a numerical time-stepping scheme [2, Ch. 10]

in order to correctly deal with the set-valued friction characteristic Ψ . First consider system (3.4), where only a *classical* PID controller (3.3) is employed. The mass m is unitary, the static friction is $\bar{F}_s = 0.981$ N, and the velocity-dependent friction contribution is given by

$$f(\hat{v}) = \begin{cases} L_2 \hat{v}, & |\hat{v}| \leq \varepsilon_v \\ (\bar{F}_s - \bar{F}_c) \kappa \hat{v} / (1 + \kappa |\hat{v}|)^{-1}, & |\hat{v}| > \varepsilon_v, \end{cases} \quad (3.20)$$

with $\bar{F}_c = \bar{F}_s/3$ the Coulomb friction, $\kappa = 20$ is the Stribeck shape parameter, $L_2 = 12.8$ Ns/m, and $\varepsilon_v = 10^{-3}$ m/s. We take $\bar{k}_p = 18$ N/m, $\bar{k}_d = 2$ Ns/m, and $\bar{k}_i = 30$ N/(ms), satisfying Assumption 3.3. The constant position setpoint is $r = 0$, and the initial conditions are $z_1(0) = -0.05$ m, $z_2(0) = 0$ m/s, and $z_3(0) = 0$ ms. The position response is presented in the top plot of Figure 3.2 (—), where limit cycling (hunting) is evident.

Now consider the closed-loop system (3.1)-(3.3), (3.19), where the PID controller with reset enhancements is employed (the same controller gains are used as in the classical PID case). The reset controller achieves, first, asymptotic stability of the setpoint $(z_1, z_2) = (0, 0)$ (as we will prove in the next sections), and, second, a significant overshoot reduction compared to the classical PID response, see the top plot in Figure 3.2 (—). Controller resets according to (3.19a)-(3.19b)

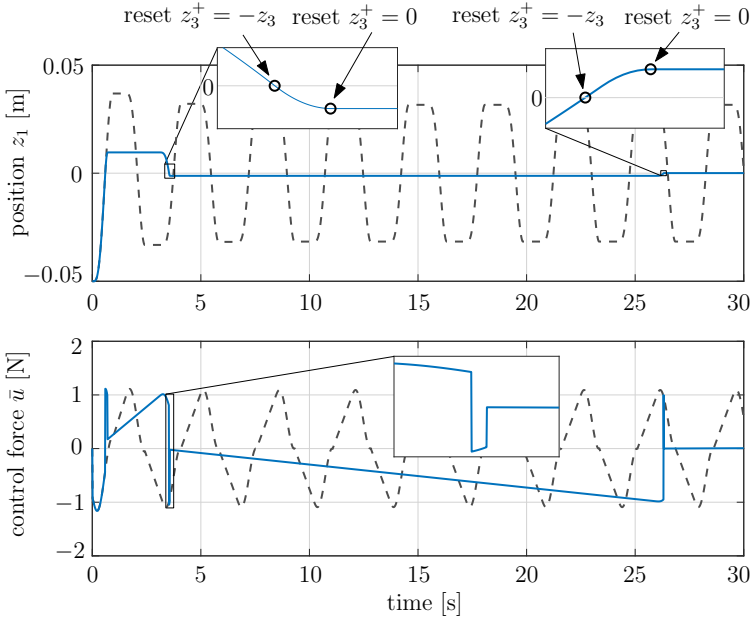


Figure 3.2. Simulated response of z_1 and control force \bar{u} for the classical (—) and reset (—) PID controller.

(i.e., at a zero-crossing of the position error) and according to (3.19c)-(3.19d) (i.e., when the velocity hits zero after the previous reset has occurred) are indicated in the insets. The arising (discontinuous) control force is presented in the bottom plot of Figure 3.2.

3.3 Hybrid system formulation of the closed loop

In this section, we rewrite the closed-loop reset control system (3.1)-(3.3), (3.19) in the hybrid formalism of [63] in Section 3.3.1. We provide an analysis of relevant properties of the resulting hybrid system in Section 3.3.2.

3.3.1 Hybrid system formulation

Using the state transformation in (3.6), and the mass normalization in (3.5), we reformulate the proposed closed-loop reset control system as a hybrid system, denoted by $\hat{\mathcal{H}}$. Consider hereto the augmented state vector ranging in a constrained set, comprising a correct initialization of \hat{b} and the controller state $\hat{\phi}$:

$$\begin{aligned} \hat{\xi} &:= (\hat{x}, \hat{b}) = (\hat{\sigma}, \hat{\phi}, \hat{v}, \hat{b}) \in \hat{\Xi}, \\ \hat{\Xi} &:= \{(\hat{x}, \hat{b}) \in \mathbb{R}^3 \times \{-1, 1\} : \hat{b}\hat{v}\hat{\sigma} \geq 0, \hat{\sigma}\hat{\phi} \geq \frac{k_p}{k_i}\hat{\sigma}^2, \hat{b}\hat{v}\hat{\phi} \geq 0\}. \end{aligned} \quad (3.21a)$$

The first two constraints in $\hat{\Xi}$ come from the reset mechanism in (3.19a)-(3.19d) and impose that $\hat{b}\hat{v}$ and $\hat{\sigma}$, and $\hat{\sigma}$ and $\hat{\phi}$ never have opposite signs. More specifically, we exclude $\hat{\sigma}\hat{\phi} < \frac{k_p}{k_i}\hat{\sigma}^2$ because of the design philosophy of the controller: the fact that z_3 should always point in the direction of the setpoint implies $(z_1 - r)z_3 \geq 0$, and thus, by (3.6), that $\hat{\sigma}\hat{\phi} \geq \frac{k_p}{k_i}\hat{\sigma}^2$. Finally, it should also be imposed that $\hat{b}\hat{v}$ and $\hat{\phi}$ never have opposite signs, as realized by the third constraint in $\hat{\Xi}$. We present the closed-loop model (3.7), augmented with the resets, as the following hybrid system $\hat{\mathcal{H}}$:

$$\hat{\mathcal{H}}: \begin{cases} \dot{\hat{\xi}} \in \hat{\mathcal{F}}(\hat{\xi}), & \hat{\xi} \in \hat{\mathcal{C}}, \\ \hat{\xi}^+ = \hat{g}_\sigma(\hat{\xi}), & \hat{\xi} \in \hat{\mathcal{D}}_\sigma, \\ \hat{\xi}^+ = \hat{g}_v(\hat{\xi}), & \hat{\xi} \in \hat{\mathcal{D}}_v \end{cases} \quad (3.21b)$$

$$\quad (3.21c)$$

Herein, the flow map is given by

$$\hat{\mathcal{F}}(\hat{\xi}) := \begin{bmatrix} -k_i\hat{v} \\ \hat{\sigma} - k_p\hat{v} \\ \hat{\phi} - k_d\hat{v} - F_s \text{Sign}(\hat{v}) + f(\hat{v}) \\ 0 \end{bmatrix} = \begin{bmatrix} \hat{\mathcal{F}}_x(\hat{x}) \\ 0 \end{bmatrix}, \quad (3.21d)$$

and the jump maps are given by

$$\hat{g}_\sigma(\hat{\xi}) := \begin{bmatrix} \hat{\sigma} \\ -\hat{\phi} \\ \hat{v} \\ -\hat{b} \end{bmatrix}, \quad \hat{g}_v(\hat{\xi}) := \begin{bmatrix} \hat{\sigma} \\ \frac{k_p}{k_i} \hat{\sigma} \\ \hat{v} \\ -\hat{b} \end{bmatrix}. \quad (3.21e)$$

The flow and jump sets are given by

$$\hat{C} := \hat{\Xi}, \quad (3.21f)$$

$$\hat{D}_\sigma := \{\hat{\xi} \in \hat{\Xi} : \hat{\sigma} = 0, \hat{b} = 1\}, \quad (3.21g)$$

$$\hat{D}_v := \{\hat{\xi} \in \hat{\Xi} : \hat{v} = 0, \hat{b} = -1\}, \quad (3.21h)$$

$$\hat{D} := \hat{D}_\sigma \cup \hat{D}_v. \quad (3.21i)$$

We emphasize that the sets \hat{D}_σ and \hat{D}_v are disjoint, because they correspond to two different values of \hat{b} .

3.3.2 Properties of $\hat{\mathcal{H}}$

We now present some useful properties of the hybrid closed-loop system $\hat{\mathcal{H}}$. An immediate consequence of Claim 3.4 is the uniqueness of flowing solutions to (3.21) as in the next lemma:

Lemma 3.5. *Let Assumptions 3.2-3.3 hold. For each solution $\hat{\xi}_1$ to (3.21), each interval $I^j := \{t: (t, j) \in \text{dom } \hat{\xi}_1\} =: [t_j, t_{j+1}]$ with nonempty interior, and for all $t \in (t_j, t_{j+1})$, if $\hat{\xi}_2$ is a solution to (3.21) on $[t, t'] \times \{j\}$ with $t < t' \leq t_{j+1}$ and $\hat{\xi}_2(t, j) = \hat{\xi}_1(t, j)$, then $\hat{\xi}_2(\tau, j) = \hat{\xi}_1(\tau, j)$ for all $\tau \in [t, t']$.*

Proof. The lemma follows immediately from Claim 3.4, item (i) since for each $\hat{\xi}$, $\hat{\mathcal{F}}(\hat{\xi}) = \left[\hat{\mathcal{F}}_x(\hat{x}) \right]$, and $\dot{\hat{b}} = 0$ in (3.21b). \square

Maximal solutions to $\hat{\mathcal{H}}$ are complete as per the next lemma.

Lemma 3.6. *Under Assumptions 3.2-3.3, all maximal solutions $\hat{\xi}$ to (3.21) with $\hat{\xi}(0, 0) = \hat{\xi}_0 \in \hat{C} \cup \hat{D}$, are complete.*

Proof. See Appendix 3.A.2. \square

Consider the set

$$\hat{\mathcal{A}} := \{\hat{\xi} \in \hat{\Xi} : \hat{\sigma} = 0, |\hat{\phi}| \leq F_s, \hat{v} = 0\}, \quad (3.22)$$

corresponding to the set of all possible equilibria for the flow map (3.21d) of $\hat{\mathcal{H}}$ for the state $\hat{\xi} \in \hat{\Xi}$. It is immediate to show the next result.

Lemma 3.7. *For each $\hat{\xi} \in \mathcal{S}_{\hat{\mathcal{H}}}(\hat{\mathcal{A}})$, $\text{rge } \hat{\xi} \subset \hat{\mathcal{A}}$, i.e., $\hat{\mathcal{A}}$ is strongly forward invariant [63, Def. 6.25].*

Proof. The claim follows by inspection of all possible solutions with initial condition in $\hat{\mathcal{A}}$, which may flow in $\hat{\mathcal{C}}$ or jump in $\hat{\mathcal{D}}_\sigma$ or $\hat{\mathcal{D}}_v$. Indeed, for flow in $\hat{\mathcal{C}} \cap \hat{\mathcal{A}}$, Claim 3.4(iii) guarantees that $\hat{\sigma}$, $\hat{\phi}$, and \hat{v} remain constant; $\hat{g}_\sigma(\hat{\mathcal{A}}) \subset \hat{\mathcal{A}}$; $\hat{g}_v(\hat{\mathcal{A}}) \subset \hat{\mathcal{A}}$. Then, $\hat{\mathcal{A}}$ is strongly forward invariant since solutions are complete by Lemma 3.6. \square

We formalize in the next lemma that solutions to the hybrid system (3.21) are bounded, which is an important stepping stone towards the stability analysis in Section 3.4 below.

Lemma 3.8. *Under Assumptions 3.2-3.3, for each compact set $\mathcal{K} \subset \hat{\mathcal{C}} \cup \hat{\mathcal{D}}$, there exists $M > 0$ such that each solution $\hat{\xi} \in \mathcal{S}_{\hat{\mathcal{H}}}(\mathcal{K})$ satisfies $\hat{\xi}(t, j) \in M\mathbb{B}$ for all $(t, j) \in \text{dom } \hat{\xi}$.*

Proof. See Appendix 3.A.3. \square

Next, we establish a useful property of $\hat{\mathcal{H}}$, namely that stick-to-slip transitions must occur at instants of time separated by a guaranteed “waiting” time (or dwell time). This dwell time is uniform in any compact set of initial conditions, therefore it is semiglobal. To formalize such dwell time result, define the sets

$$\begin{aligned} \hat{\mathcal{S}}_1 &:= \{\hat{\xi} \in \hat{\Xi} : \hat{\sigma} \geq 0, \hat{\phi} \geq F_s, \hat{v} = 0, \hat{b} = 1\}, \\ \hat{\mathcal{S}}_{-1} &:= \{\hat{\xi} \in \hat{\Xi} : \hat{\sigma} \leq 0, \hat{\phi} \leq -F_s, \hat{v} = 0, \hat{b} = 1\}, \end{aligned} \quad (3.23)$$

which are intuitively associated with stick-to-slip transitions, see also (3.8). We show in Lemma 3.9 that, when the velocity \hat{v} reaches one of these sets, there exists a uniform semiglobal dwell time before the velocity changes its sign, unless it reaches the set of equilibria $\hat{\mathcal{A}}$. This result plays an important role in the stability analysis of $\hat{\mathcal{H}}$, since it rules out undesired Zeno solutions in $\hat{\mathcal{H}}$ (and in the hybrid model we present later in Section 3.4.1, where we use a *hybrid* description for the Coulomb friction element).

Lemma 3.9. *Let Assumptions 3.2-3.3 hold. For each compact set $\mathcal{K} \subset \hat{\mathcal{C}} \cup \hat{\mathcal{D}}$, there exists $\delta(\mathcal{K}) > 0$ such that each solution $\hat{\xi} = (\hat{\sigma}, \hat{\phi}, \hat{v}, \hat{b}) \in \mathcal{S}_{\hat{\mathcal{H}}}(\mathcal{K})$ with $\hat{\xi}(t, j) \in \hat{\mathcal{S}}_1$ ($\hat{\xi}(t, j) \in \hat{\mathcal{S}}_{-1}$, respectively) for $(t, j) \in \text{dom } \hat{\xi}$ satisfies $\hat{v}(\tau, j(\tau)) \geq 0$ ($\hat{v}(\tau, j(\tau)) \leq 0$, respectively) for all $\tau \in [t, t + \delta(\mathcal{K})]$.*

Proof. See Appendix 3.A.5. \square

Intuitively speaking, Lemma 3.9 entails the existence of a uniform dwell time between two subsequent stick-to-slip transitions or velocity reversals. Finally, we show that solutions are complete also in the ordinary-time direction (i.e., t -completeness) as long as these evolve outside $\hat{\mathcal{A}}$ in (3.22).

Lemma 3.10. *Under Assumptions 3.2-3.3, all maximal solutions $\hat{\xi}$ to (3.21) with $\hat{\xi}(t, j) \notin \hat{A}$ for all $(t, j) \in \text{dom } \hat{\xi}$, satisfy $\sup_t \text{dom } \hat{\xi} = +\infty$.*

Proof. see Appendix 3.A.7. □

Note that solutions in the set of equilibria \hat{A} may evolve in different ways, i.e., different flow/jump combinations, including Zeno solutions. In any case, stability of the closed-loop system is preserved by Lemma 3.7.

3.4 Stability analysis

Using the properties of the closed-loop system $\hat{\mathcal{H}}$ as analyzed in the previous section, we prove in this section that the set of equilibria \hat{A} in (3.22) is globally asymptotically stable for closed-loop system $\hat{\mathcal{H}}$ in (3.21). In order to arrive at such a result, we take the following steps. First, we introduce a hybrid system \mathcal{H}_δ in Section 3.4.1, that is (semiglobally) equivalent to $\hat{\mathcal{H}}$ in (3.21). In particular, we exploit a hybrid description of the set-valued Coulomb friction element and show that solutions to $\hat{\mathcal{H}}$ are contained in the solution set of \mathcal{H}_δ . We then prove global asymptotic stability of a suitable attractor to the proposed hybrid model \mathcal{H}_δ in Section 3.4.2. Finally, we formalize global asymptotic stability of \hat{A} for dynamics $\hat{\mathcal{H}}$ in Theorem 3.14 below, and prove the theorem using the aforementioned ingredients in Section 3.4.3.

3.4.1 Hybrid model \mathcal{H}_δ

We now present a hybrid model \mathcal{H}_δ based on a hybrid description of the Coulomb friction element. The proposed model \mathcal{H}_δ captures the evolution between the logical states “stick” and “slip” (cf. (3.8)) via appropriate jump policies. To this end, we introduce the state $q \in \{-1, 0, 1\}$, which is used to distinguish whether the system is in stick ($q = 0$), slip with nonnegative velocity ($q = 1$), or slip with nonpositive velocity ($q = -1$). With the state q , it becomes possible to write the Coulomb friction element in $\hat{\mathcal{H}}$ as a *hybrid* system, instead of a differential inclusion. Moreover, we introduce a timer $\tau \in [0, 2\delta]$ that ensures the absence of Zeno solutions in \mathcal{H}_δ , related to the existence of a uniform $\delta > 0$ (in a semiglobal fashion) by Lemma 3.9.

Consider the hybrid system \mathcal{H}_δ in (3.24), parameterized by $\delta > 0$, with overall state

$$\begin{aligned} \xi &:= (\sigma, \phi, v, b, q, \tau) \in \Xi, \\ \Xi &:= \{\xi \in \mathbb{R}^3 \times \{-1, 1\} \times \{-1, 0, 1\} \times [0, 2\delta] : \\ &\quad qv \geq 0, bq\sigma \geq 0, \sigma\phi \geq \frac{k_p}{k_i}\sigma^2, bq\phi \geq 0\}. \end{aligned} \tag{3.24a}$$

For each $\delta > 0$, \mathcal{H}_δ is defined as

$$\mathcal{H}_\delta : \begin{cases} \dot{\xi} = \mathcal{F}(\xi), & \xi \in \mathcal{C}_{\text{slip}} \cup \mathcal{C}_{\text{stick}} \\ \xi^+ \in \bigcup_{\substack{p \in \{\sigma, v, 1, -1, 0\} \\ \xi \in \mathcal{D}_p}} \{g_p(\xi)\} =: \mathcal{G}(\xi), & \xi \in \bigcup_{p \in \{\sigma, v, 1, -1, 0\}} \mathcal{D}_p. \end{cases} \quad (3.24b)$$

The flow map is given by

$$\mathcal{F}(\xi) := \begin{bmatrix} -k_i v \\ \sigma - k_p v \\ -k_d v + |q|\phi - q(F_s - h(v)) \\ 0 \\ 0 \\ 1 - \text{dz}_1(\tau/\delta) \end{bmatrix}, \quad (3.24d)$$

with h defined from the velocity-dependent contribution of the friction f as

$$v \mapsto h(v) := |f(v)|. \quad (3.24e)$$

The jump maps are given by

$$\begin{aligned} g_\sigma(\xi) &:= [\sigma \quad -\phi \quad v \quad -b \quad q \quad \tau]^\top, \\ g_v(\xi) &:= \left[\sigma \quad \frac{k_p}{k_i} \sigma \quad v \quad -b \quad q \quad \tau \right]^\top, \\ g_1(\xi) &:= [\sigma \quad \phi \quad v \quad b \quad 1 \quad 0]^\top, \\ g_{-1}(\xi) &:= [\sigma \quad \phi \quad v \quad b \quad -1 \quad 0]^\top, \\ g_0(\xi) &:= [\sigma \quad \phi \quad v \quad b \quad 0 \quad \tau]^\top. \end{aligned} \quad (3.24f)$$

The flow and jump sets are defined as

$$\begin{aligned} \mathcal{C}_{\text{slip}} &:= \{\xi \in \Xi : |q| = 1\}, \\ \mathcal{C}_{\text{stick}} &:= \{\xi \in \Xi : q = 0, v = 0, |\phi| \leq F_s\}, \\ \mathcal{D}_\sigma &:= \{\xi \in \Xi : |q| = 1, \sigma = 0, b = 1\}, \\ \mathcal{D}_v &:= \{\xi \in \Xi : q = 0, v = 0, b = -1\}, \\ \mathcal{D}_1 &:= \{\xi \in \Xi : q = 0, v = 0, \phi \geq F_s, b = 1, \tau \in [\delta, 2\delta]\}, \\ \mathcal{D}_{-1} &:= \{\xi \in \Xi : q = 0, v = 0, \phi \leq -F_s, b = 1, \tau \in [\delta, 2\delta]\}, \\ \mathcal{D}_0 &:= \{\xi \in \Xi : |q| = 1, v = 0\}, \end{aligned} \quad (3.24g)$$

and are visualized in Figure 3.3. Based on (3.24g), we define

$$\begin{aligned} \mathcal{C} &:= \mathcal{C}_{\text{slip}} \cup \mathcal{C}_{\text{stick}}, \\ \mathcal{D} &:= \mathcal{D}_\sigma \cup \mathcal{D}_v \cup \mathcal{D}_1 \cup \mathcal{D}_{-1} \cup \mathcal{D}_0, \end{aligned} \quad (3.24h)$$

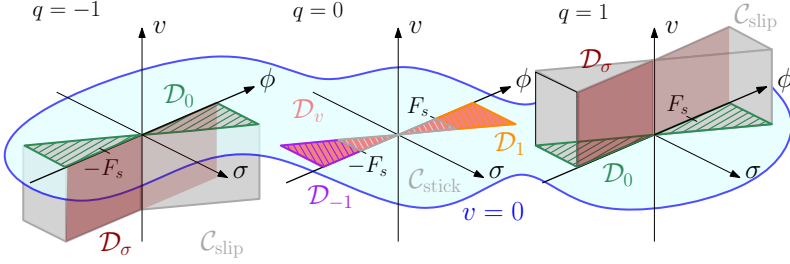


Figure 3.3. Projections to the (σ, ϕ, v) space of the flow and jump sets in (3.24g), indicating the sector condition $\sigma\phi \geq \frac{k_p}{k_t}\sigma^2$.

and note that $\mathcal{C} \cup \mathcal{D} \subset \Xi$. The hybrid automaton corresponding to \mathcal{H}_δ is depicted in Figure 3.4.

We will now show that the hybrid automaton model \mathcal{H}_δ in (3.24) captures all solutions to the original closed-loop model $\hat{\mathcal{H}}$ in (3.21) in a semiglobal fashion, which verifies the equivalence between the two models. For a hybrid solution ψ , we use the notation $j_\psi(t) := \min_{(t,j) \in \text{dom } \psi} j$ to emphasize that for the same $t \geq 0$, $j_\xi(t)$ may be different from $j_{\hat{\xi}}(t)$. We then have the next lemma.

Lemma 3.11. *Let Assumptions 3.2-3.3 hold. For each compact set $\mathcal{K} \subset \hat{\mathcal{C}} \cup \hat{\mathcal{D}}$, there exists $\delta(\mathcal{K}) > 0$ such that for each solution $\hat{\xi} = (\hat{\sigma}, \hat{\phi}, \hat{v}, \hat{b}) \in \mathcal{S}_{\hat{\mathcal{H}}}(\mathcal{K})$, there exists q_0, τ_0 such that, for some solution $\xi = (\sigma, \phi, v, b, q, \tau) \in \mathcal{S}_{\mathcal{H}_\delta(\mathcal{K})}((\hat{\xi}_0, q_0, \tau_0))$, it holds for all $t \geq 0$ such that $\hat{\xi}(t, j(t)) \notin \hat{\mathcal{A}}$ that*

$$\begin{aligned} \hat{\sigma}(t, j_{\hat{\xi}}(t)) &= \sigma(t, j_\xi(t)), \quad \hat{\phi}(t, j_{\hat{\xi}}(t)) = \phi(t, j_\xi(t)), \\ \hat{v}(t, j_{\hat{\xi}}(t)) &= v(t, j_\xi(t)), \quad \hat{b}(t, j_{\hat{\xi}}(t)) = b(t, j_\xi(t)). \end{aligned} \quad (3.25)$$

Proof. see Appendix 3.A.8. □

Note that the statement of Lemma 3.11 builds directly upon the t -completeness of maximal solutions $\hat{\xi}$ by Lemma 3.10.

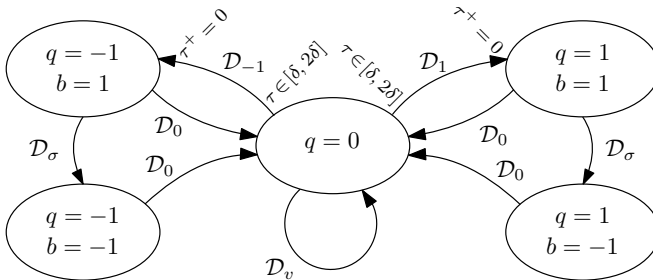


Figure 3.4. Hybrid-automaton illustration of (3.24).

3.4.2 Stability analysis of \mathcal{H}_δ

Define the set

$$\mathcal{A} := \{\xi \in \Xi : \sigma = v = 0, \phi \in F_s \text{ Sign}(bq)\}. \quad (3.26)$$

We prove global asymptotic stability of \mathcal{A} for (3.24). To this end, consider the Lyapunov function

$$\begin{aligned} V(\xi) = & \begin{bmatrix} \sigma \\ v \end{bmatrix}^\top \begin{bmatrix} \frac{k_d}{k_i} & -1 \\ -1 & k_p \end{bmatrix} \begin{bmatrix} \sigma \\ v \end{bmatrix} + |q|(\phi - bqF_s)^2 \\ & + (1 - |q|)dz_{F_s}^2(\phi) + 2\frac{k_p}{k_i}F_s(bq\sigma + (1 - |q|)|\sigma|), \end{aligned} \quad (3.27)$$

where the first three terms can be seen as a smooth version of the Lyapunov function employed in [29, Eq. (13)]. Consider the following definitions. For a jump map $g_p : \mathbb{R}^n \rightarrow \mathbb{R}^n$ indexed by p , and function $V : \mathbb{R}^n \rightarrow \mathbb{R}^n$, $\Delta V_p(\xi) := V(g_p(\xi)) - V(\xi)$. We denote $\partial V(y)$ as the Clarke generalized gradient of V at y (see [45, Ch. 2] for a formal definition). With these definitions in place, the next lemma asserts that V is nonincreasing along solutions to \mathcal{H}_δ .

Lemma 3.12. *Under Assumptions 3.2-3.3, the Lyapunov function V in (3.27) satisfies the next properties.*

1. For each $\xi \in \mathcal{C} \cup \mathcal{D}$, $V(\xi) \geq 0$ and $V(\xi) = 0$ if and only if $\xi \in \mathcal{A}$;
2. $V^\circ(\xi) := \max_{\nu \in \partial V(\xi)} \langle \nu, \mathcal{F}(\xi) \rangle \leq -2(k_p k_d - k_i)v^2 - 2|q||\sigma|h(v) - 2k_p qv(F_s - h(v)) \leq 0$ for all $\xi \in \mathcal{C}$;
3. $\Delta V_\sigma(\xi) = 0$ for all $\xi \in \mathcal{D}_\sigma$;
4. $\Delta V_v(\xi) \leq 0$ for all $\xi \in \mathcal{D}_v$;
5. $\Delta V_i(\xi) \leq 0$ for all $\xi \in \mathcal{D}_i$, $i \in \{1, -1\}$;
6. $\Delta V_0(\xi) \leq 0$ for all $\xi \in \mathcal{D}_0$.

Proof. See Appendix 3.A.9. □

We now turn to global asymptotic stability of the set \mathcal{A} for \mathcal{H}_δ . Its proof is based on a hybrid invariance principle presented in [135].

Proposition 3.13. *Under Assumptions 3.2-3.3 and $\delta > 0$, the set \mathcal{A} in (3.26) is globally asymptotically stable for \mathcal{H}_δ in (3.24).*

Proof. See Appendix 3.A.10. □

3.4.3 Global asymptotic stability of $\hat{\mathcal{A}}$ for $\hat{\mathcal{H}}$

We now exploit the fact that solutions to $\hat{\mathcal{H}}$ are contained in \mathcal{H}_δ (by Lemma 3.11), and the fact that \mathcal{A} is globally asymptotically stable for \mathcal{H}_δ (by Proposition 3.13) to prove global asymptotic stability of $\hat{\mathcal{A}}$ for $\hat{\mathcal{H}}$. Consider hereto the following theorem.

Theorem 3.14. *Under Assumptions 3.2-3.3, $\hat{\mathcal{A}}$ in (3.22) is globally asymptotically stable for $\hat{\mathcal{H}}$ in (3.21).*

Proof. see Appendix 3.A.11. □

3.5 Experimental case study

In this section, we demonstrate the working principle and the effectiveness of the proposed reset controller on the sample manipulation stage of an electron microscope, discussed in Section 2.5.1. First, we show that employing a *classical* (linear) PID controller indeed leads to limit cycling (hunting), as pointed out in Section 3.1. Second, we discuss particular conditions for the *robust* detection of a zero crossing of the position error, and for the detection of zero velocity, facilitating the application of our proposed reset controller. Then, we show 1) the stability properties of the reset controller in the presence of friction with unknown static and velocity-dependent contributions (including the Stribeck effect), and 2) that overshoot is reduced with respect to the classical PID controller.

For frequencies up to 200 Hz, the system dynamics can be well described by (3.1) for which Theorem 3.14 applies when interconnected with the proposed reset PID controller. In this case, z_1 represents the position of the carriage. The mass $m = 172.6$ kg consists of the transformed inertia of the motor and the spindle (with an *equivalent* mass of 171 kg), and of the mass of the carriage (1.6 kg). The friction force is mainly induced by the bearings supporting the motor axis and the spindle (see ⑧ in Figure 2.4), by the contact between the spindle and the nut, and, to a lesser extent, by the contact between the carriage and the guidance. The contact between the spindle and the nut is lubricated, which induces the Stribeck effect. Since the system is rigid and behaves as a single mass for frequencies up to 200 Hz, these friction forces can be summed up to provide a single net friction characteristic Ψ in (3.1). The desired position accuracy to be achieved is 10 nm, as specified by the manufacturer.

Remark 3.15. *The experimental setup is also used in the case study of Chapter 2, where dominantly Coulomb and viscous friction was present. For the experiments in this chapter, however, a different carriage position and spindle orientation, and different lubrication conditions are used, that result in a significant Stribeck effect instead, as illustrated in the next section.* ┘

3.5.1 Classical PID control

Experiments with a classical PID controller have been performed with controller gains $\bar{k}_p = 10^7$ N/m, $\bar{k}_d = 2 \cdot 10^3$ Ns/m, and $\bar{k}_i = 10^8$ N/(ms) satisfying Assumption 3.3. Indeed, the conditions in Assumption 3.3 are equivalent to $\bar{k}_p > 0$, $\bar{k}_i > 0$, and $\frac{\bar{k}_p(\bar{k}_d + \alpha)}{m} > \bar{k}_i$. The latter holds since $\alpha > 0$ and the PID controller gains above satisfy $\frac{\bar{k}_p \bar{k}_d}{m} > \bar{k}_i$. The position response and corresponding control force are visualized in Figure 3.5 for three different experiments. Limit cycling, and thus the lack of asymptotic stability of the setpoint, is clearly visible, and confirms the presence of a significant Stribeck effect.

3.5.2 Reset PID control

We now employ the proposed reset controller, with the same controller gains as for the classical PID case. Note first that the jump sets and maps of the reset controller (3.3), (3.19) are given by

$$\hat{\mathcal{D}}_\sigma := \{(z, \hat{b}) : (z_1 - r) = 0, \hat{b} = 1\}, \quad (3.28a)$$

$$\hat{\mathcal{D}}_v := \{(z, \hat{b}) : z_2 = 0, (z_1 - r)z_3 \geq 0, \hat{b} = -1\}, \quad (3.28b)$$

$$\hat{g}_\sigma = (z_1, z_2, -z_3, -\hat{b}), \quad (3.28c)$$

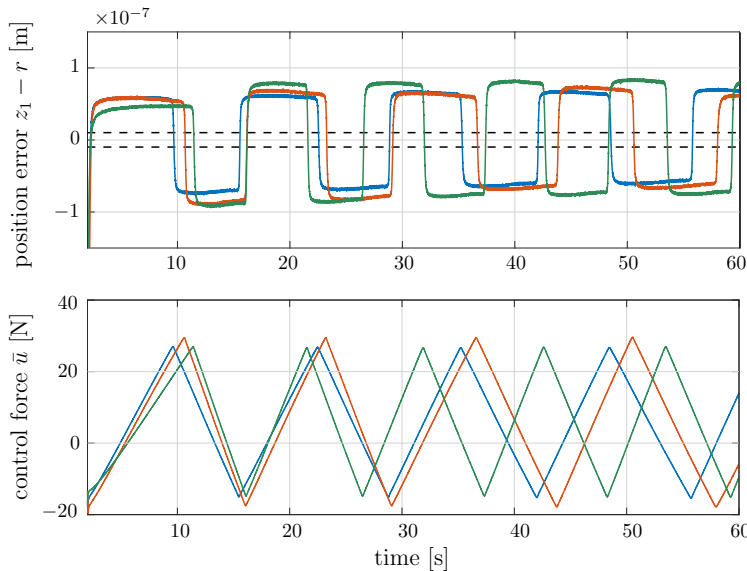


Figure 3.5. Position response and control force for three experiments with a classical PID controller. The desired accuracy band (see $--$) in the top plot) is clearly not achieved with the classical PID controller

$$\hat{g}_v = (z_1, z_2, 0, -\hat{b}). \quad (3.28d)$$

The controller reset conditions in (3.28) are not robust to measurement noise, in the sense that detecting $(z_1 - r) = 0$ and in particular $z_2 = 0$ in the presence of noise is challenging. We therefore need to apply robust detection laws for a zero-crossing of z_1 , and for z_2 hitting zero. Moreover, a suitable stopping criterion is employed such that resets are disabled as soon as the position error is within the desired accuracy band of 10 nm, specified by the manufacturer. Such a stopping criterion prevents the system from experiencing multiple (undesired) consecutive controller resets, that are (possibly) triggered by measurement noise, when the system is sufficiently close to the setpoint. Although other robust detection mechanisms exist, we choose here to apply the following conditions. Overshoot (i.e., a zero-crossing of $(z_1 - r)$) is detected in the same way as in (2.8e), by evaluating the product of the PI control force and the position error. Hitting zero velocity is detected in the same way as in (2.8e) as well, by evaluating the product between the PI control force and the velocity. The robust reset conditions are then given by the following jump sets:

$$\bar{\mathcal{D}}_\sigma := \{(z, \hat{b}): \bar{k}_i(z_1 - r)(\bar{k}_p(z_1 - r) + \bar{k}_i z_3) \leq 0, \hat{b} = 1\}, \quad (3.29a)$$

$$\bar{\mathcal{D}}_v := \{(z, \hat{b}): -z_2(\bar{k}_p(z_1 - r) + \bar{k}_i z_3) \geq 0, (z_1 - r)z_3 \geq 0, \hat{b} = -1\}. \quad (3.29b)$$

Controller resets are disabled whenever $|z_1 - r| \leq 10$ nm, *after a reset in $\bar{\mathcal{D}}_v$* to avoid chattering due to resets triggered by measurement noise. Note that $\bar{k}_i(z_1 - r)(\bar{k}_p(z_1 - r) + \bar{k}_i z_3) \leq 0$ in (3.29a) is satisfied as soon as $(z_1 - r)$ hits zero (see also Sections 2.2 and 2.3), corresponding to a zero-crossing of the position error. Moreover, $-z_2(\bar{k}_p(z_1 - r) + \bar{k}_i z_3) \geq 0$ in (3.29b) is satisfied (after a zero-crossing of the error) as soon as the velocity z_2 hits zero (as desired), similar to the zero velocity detection mechanism in Sections 2.2 and 2.3.

Consider Figure 3.6, where the position error and control force for three experiments with the proposed reset controller are presented. The controller resets are enabled as soon as the PI control force and the position error have the same sign after the first zero crossing of the error, indicated by the vertical dashed lines. First and foremost, we observe that, using the reset enhancements, the system settles within the desired accuracy band of 10 nm after a single reset in $\bar{\mathcal{D}}_\sigma$ and $\bar{\mathcal{D}}_v$, see the top subplot (in contrast to the classical PID controller, which does not result in the desired positioning accuracy, cf. Figure 3.5). Secondly, the controller reset in $\bar{\mathcal{D}}_\sigma$ suppresses overshoot, compared to the classical PID controller with the same gains. Third, the reset conditions in the jump sets $\bar{\mathcal{D}}_\sigma$ and $\bar{\mathcal{D}}_v$ indeed cause the controller to reset at the correct instances, despite the presence of measurement noise. The corresponding control force, displayed in the lower subplot, is discontinuous due to the controller resets, as highlighted in the inset.

Let us now analyze the response at the nanometer scale in more detail. Consider hereto the position error response as a result of the controller resets in

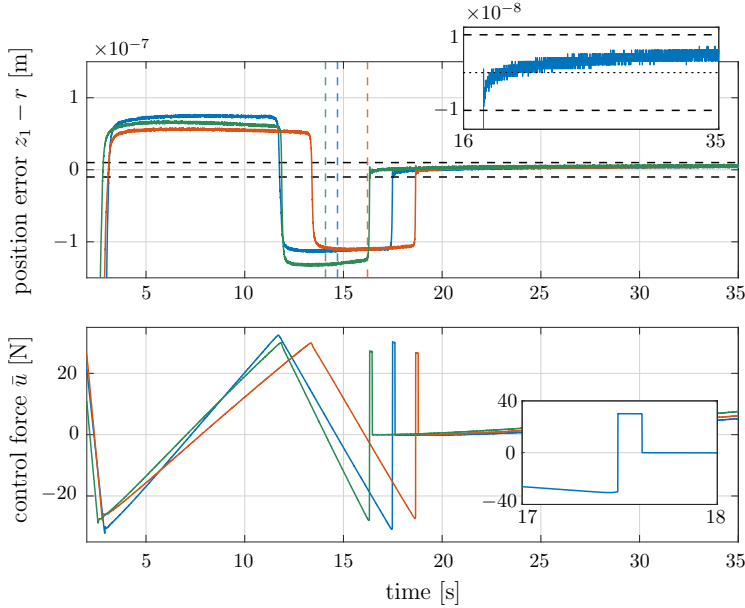


Figure 3.6. Position response and control force for three experiments with the *reset* PID controller.

more detail, using Figure 3.7. In this figure, a time interval where $\hat{b} = -1$ is indicated in gray; its boundaries then indicate a reset instant. Similarly, the white areas correspond to an interval where $\hat{b} = 1$. First, consider the upper left subplot, which shows a zoomed view of the position error of the blue response of Figure 3.6. As soon as the error crosses zero, a controller reset is triggered that toggles the sign of z_3 , according to (3.28c). As a result of stiffness-like effects in the friction characteristic of the system (see Section 2.5.4, [12, Sec. 2.1]) combined with the sudden (large) change in system, a “jump” in the position error is observed, which prevents the system from actual overshooting the setpoint. Thereafter, the reset according to (3.28d) occurs which resets z_3 zero. Similarly, due to the stiffness effects, a jump in the position error occurs again (but lower in magnitude due to the smaller discontinuity in the control force, compared to a reset in \bar{D}_σ). We then observe that the position error crosses zero slowly as a result of frictional creep effects (see Sections 1.1.1 and 2.5.4, and [131]), see the inset in the top subplot of Figure 3.6, but the position error remains well within the desired accuracy band of 10 nm, so further resets are disabled according to our stopping criterion.

Remark 3.16. *The stopping criterion, i.e., $|z_1 - r| \leq 10$ nm, is evaluated only after each reset in (3.28d), because having zero integral action in combination*

with the presence of static friction yields robustness to other force disturbances. \lrcorner

Next, we analyze the reset conditions in (3.29a) and (3.29b). Consider hereto the upper right and lower subplot in Figure 3.7, which show the reset conditions as a function of time for the blue response in Figure 3.6. From the upper left and right subplots, it is evident that indeed a reset according to (3.28c) occurs whenever $\dot{b} = 1$ and $\bar{k}_i(z_1 - r)(\bar{k}_p(z_1 - r) + \bar{k}_i z_3) \leq 0$, which is satisfied as soon as the position error crosses zero (see also Figure 3.6). Because overshoot is prevented due to the frictional stiffness effects, the reset condition $\bar{k}_i(z_1 - r)(\bar{k}_p(z_1 - r) + \bar{k}_i z_3) \leq 0$ remains true after the reset. However, $\dot{b} = -1$ prevents further resets in \mathcal{D}_σ , which shows that the proposed reset controller exhibits further robustness characteristics with respect to such small-scale frictional effects as well.

Now consider the lower left subplot, and recall that a reset according to (3.28d) should occur whenever $\dot{b} = -1$ (satisfied because of the occurrence of the previous reset according (3.28c)), and when the velocity hits zero. Detecting the latter is successfully done by evaluating the inequality $-z_2(\bar{k}_p(z_1 - r) + \bar{k}_i z_3) \geq 0$, cf. (3.29b), even though the velocity signal experiences lag due to online lowpass filtering to reduce noise. Since the error

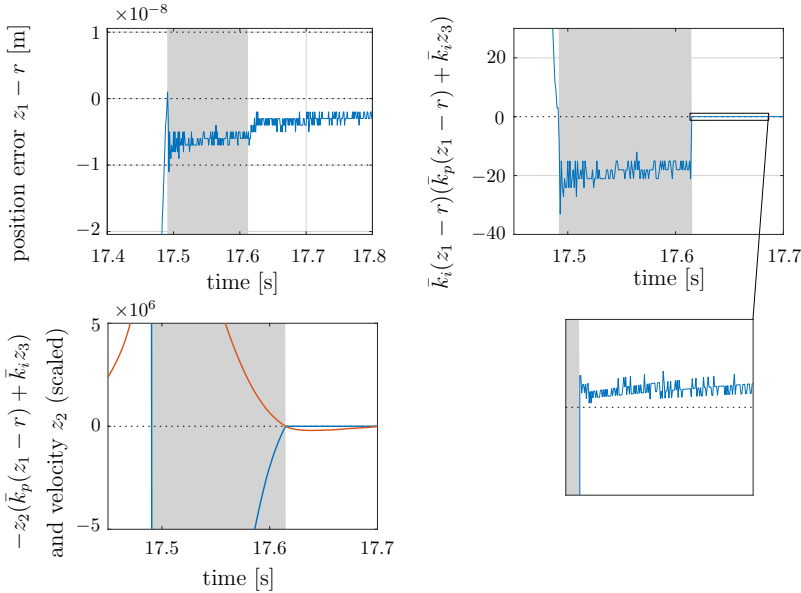


Figure 3.7. Zoomed view of a position response (top left), and controller reset conditions (top right and lower left, (—)). The lower left subplot also depicts the velocity signal (—).

$z_1 - r$ is now within the desired accuracy band, the stopping criterion prevents further resets.

Summarizing, the use of the proposed reset control strategy results in a high setpoint-accuracy, in contrast to the use of a classical PID controller, which results in limit cycling. Moreover, overshoot is suppressed, and the controller reset conditions rely only on measurable signals, causing the controller to reset at the correct instances, despite the presence of inevitable measurement noise.

3.6 Conclusions

We proposed a novel reset integrator control strategy for motion systems with Coulomb and velocity-dependent friction (including the Stribeck effect) that achieves 1) global asymptotic stability of the setpoint for unknown static and unknown velocity-dependent friction, and, 2) reduces overshoot with respect to the classical PID controller with the same controller gains. The closed-loop system dynamics is formulated as a hybrid system, using a novel hybrid description of the Coulomb friction element, and global asymptotic stability of the setpoint is proven. The working principle and effectiveness of the controller are experimentally demonstrated in a case study on a high-precision positioning application, using reset conditions that are designed such that controller resets are correctly triggered despite the presence of measurement noise.

3.7 Final remarks

The developments in this chapter focussed primarily on stabilization of the setpoint, whereas transient performance in terms of settling time has not been addressed explicitly. Stability of the setpoint is indeed achieved with the proposed reset controller, but the intervals of stick in the resulting position error response increase with a decreasing position error, clearly illustrated in Figure 3.2. As discussed in Chapter 2, such a response leads to large settling times. The reset controller proposed in Chapter 2 addresses transient performance instead (although not taking into account the Stribeck effect), which design philosophy may be applied to the reset controller proposed in this chapter, so that settling times may be reduced in this case as well.

3.8 In retrospect: experimental case study on a Clegg reset controller

So far, we have proposed and analyzed a reset control strategy for setpoint stabilization of motion systems with Stribeck friction. The controller contains two resets in order to guarantee setpoint stability, as proven in Section 3.4 and

validated experimentally in Section 3.5. In this section, we show experimentally that the application of a Clegg reset integrator, see [46], also removes the hunting limit cycle (present when a classical PID controller is employed), and results in a high positioning accuracy as well. Although setpoint stability is not proven formally here for such Clegg integrator applied to a frictional motion control problem, the Clegg reset integrator is easier to implement. In particular, there is no need for velocity measurements to detect the reset conditions, as opposed to the controller in the main result of this chapter.

In hindsight of the developments presented so far in this chapter, the key mechanism of breaching persistent friction-induced limit cycling is to prevent overcompensation of friction in the slip phase (subsequent to a stick phase). In other words, the control force acting on the system should decrease more than the decrease in friction force associated with the velocity-weakening effect. Due to the unknown nature of the friction characteristic, we will show experimentally that a sufficient decrease in control force can be realized by employing a Clegg reset integrator as well.

Let us first analyze the friction-induced limit cycles in more detail. To this end, consider the PID controlled inertia subject to Stribeck friction as in (3.1)-(3.3) (where we assume that $r = 0$ and $m = 1$, without loss of generality). The mechanical energy of the system given by

$$E = \frac{1}{2}z_2^2 + \frac{1}{2}k_p z_1^2. \quad (3.30)$$

Consider Figure 3.8, which depicts a simulation result of closed-loop system (3.1)-(3.3) with a friction characteristic and controller parameters as in Section 3.2.3, and initial conditions $z_1(0) = -0.3$ m, $z_2(0) = 0$ m/s, and $z_3(0) = 0$ ms. After the transient, hunting is indeed observed in the top subplot. The middle subplot denotes the control force, where it can be seen that the integrator builds up control force during a stick phase, eventually compensating for the static friction. As soon as the mass starts to slip, the friction force decreases due to the velocity-weakening effect, but the integral buffer has not yet been depleted such that the control force overcompensates the friction force. This repeating process results in a stick-slip limit cycle around the setpoint. The energy E in (3.30) as a function of time is presented in the lower left subplot, where the energy during a single interval of slip $[t_a, t_b]$ is highlighted in gray. Observe that $E(t_a) = E(t_b)$ since $z_2(t_a) = z_2(t_b) = 0$, and $z_1(t_a) = z_1(t_b)$. The rate of change in mechanical energy is nonzero only in the slip phases, and is for the PID-controlled system (3.1)-(3.3) given by

$$\begin{aligned} \dot{E} &= -z_2 \bar{F}_s \operatorname{sign}(z_2) + z_2 \bar{f}(z_2) - \bar{k}_d z_2^2 - \bar{k}_i z_2 z_3 \\ &\leq -\bar{k}_d z_2^2 - \bar{k}_i z_2 z_3, \quad \forall z_2 \neq 0, \end{aligned} \quad (3.31)$$

because $z_2 \bar{F}_s \operatorname{sign}(z_2) > z_2 \bar{f}(z_2)$ by Assumption 3.2. As a result, only the sign-indefinite term $-\bar{k}_i z_2 z_3$ contributes to an increase in E so that $E(t_b) = E(t_a)$ is

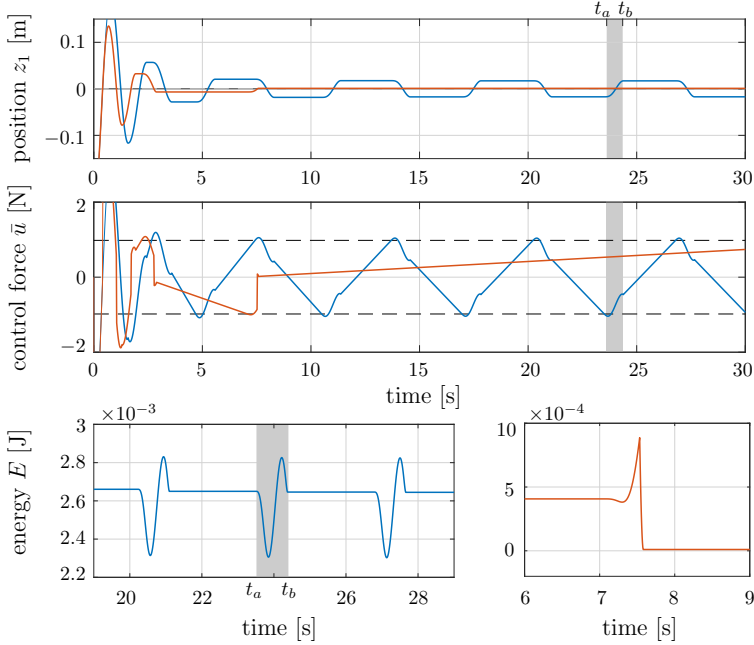


Figure 3.8. Position response, control force, and energy (as in (3.30)) for a PID controller with linear integrator (—) and Clegg reset integrator (—).

indeed obtained. By manipulating the integrator state z_3 on the interval $[t_a, t_b]$, we may achieve a net energy dissipation in the slip phase such that a limit cycle is prevented.

Consider the following PID-based controller, where the linear integrator action as in (3.3) is now replaced by a Clegg integrator (see [46]) augmented with a temporal regularization, see [151, Eq. (8)-(10)], i.e.,

$$\begin{bmatrix} \dot{z}_3 \\ \dot{\tau} \end{bmatrix} = \begin{bmatrix} z_1 \\ 1 \end{bmatrix} \quad \text{when } z_1 z_3 \geq 0 \text{ or } \tau \leq \rho \quad (3.32a)$$

$$\begin{bmatrix} z_3^+ \\ \tau^+ \end{bmatrix} = \begin{bmatrix} 0 \\ 0 \end{bmatrix} \quad \text{when } z_1 z_3 \leq 0 \text{ and } \tau \geq \rho \quad (3.32b)$$

$$\bar{u} = -\bar{k}_p z_1 - \bar{k}_d z_2 - \bar{k}_i z_3, \quad (3.32c)$$

with $\tau \geq 0$ a timer variable. The integrator in (3.32) acts like a linear integrator whenever its input (i.e., the position error z_1) and state (i.e., z_3) have the same sign, and resets its state z_3 to zero otherwise. A controller reset hence occurs at a zero-crossing of z_1 . Furthermore, we employ the temporal regularization to eliminate Zeno behavior (see [63, Def. 2.5] and Appendix A). In practice, the

temporal regularization avoids chattering of the control signal by imposing that after any controller reset, at least a time interval of length $\rho > 0$ has to expire before a subsequent reset is allowed.

Consider again the rate of change in the energy in (3.31). For the reset controller (3.32), it holds that the term $-\bar{k}_i z_2 z_3$ is positive before overshoot (i.e., a zero-crossing of z_1), similar to the classical PID controller. After overshoot, however, z_1 changes sign such that a reset according to (3.32b) is triggered, rendering the term $-\bar{k}_i z_2 z_3$ strictly negative (because z_2 is nonzero during slip). Hence, by employing the controller reset, we *enforce* a strict decrease in energy in the slip phase *after overshoot*, which is not obtained by the classical PID controller. As a result of this dissipation, it is expected that a limit cycling can not be maintained. Consider the simulation results in Figure 3.8, where, with the Clegg integrator applied, indeed a net decrease in energy is obtained during each slip interval, as depicted in the lower right subplot. The top subplot shows a decreasing error response, *indicating* stability of the setpoint.

We now demonstrate the working principle of the Clegg reset controller (3.32) on the experimental setup discussed in Section 2.5.1. Note that the application of a *classical* PID controller results in limit cycles, as already demonstrated in Figure 3.5. Several experiments with the Clegg integral controller (3.32) have been performed. Three responses are visualized in Figure 3.9, where we enable resets after 10 s (i.e., on the interval $[0, 10]$ a classical integrator is active). Using the Clegg reset controller, the system consistently achieves a setpoint accuracy close to the noise level of the position measurements, and well within the specified accuracy band of 10 nm, after two resets. The lower subplot in Figure 3.9 shows the control force. The effect of resetting the integrator to zero upon a zero-crossing of z_1 is evident. Moreover, the dwell-time parameter τ in (3.32) avoids persistent controller resets when the setpoint has been reached within the measurement accuracy, thereby avoiding a chattering control signal (see the insets in Figure 3.9). Moreover, the reset mechanism avoids that the integrator state grows when the system is close to the setpoint, so that the control force is significantly lower than the static friction value, providing robustness to other force disturbances.

As the experimental results indicate, employing the Clegg integrator on a system with Stribeck friction may result in a high setpoint accuracy, in contrast to the classical PID controller. The essential insight is that a Clegg integrator realizes a sufficient reduction of the control force that counteracts the decrease in friction force as a result of the Stribeck effect. Overcompensation of friction is thereby avoided (a formal proof of stability has not been given, which is an interesting challenge for future research). We care to emphasize that such insight played a key role in the design of the reset controller in the main result of this chapter as well.

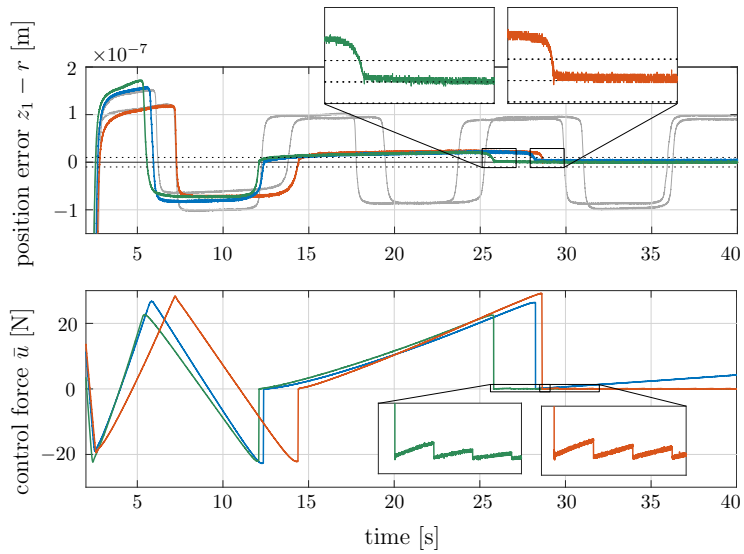


Figure 3.9. Position response for two experiments with the classical PID controller (—), and position response and control force for three experiments with the Clegg reset controller (3.32) (—, —, —).

3.A Proofs

3.A.1 Proof of Claim 3.4

We prove each item separately.

Item (i). As for completeness of solutions from each $\hat{x}_0 \in \mathbb{R}^3$, note first that the set-valued mapping $\hat{\mathcal{F}}_x$ is outer semicontinuous, locally bounded, and such that, for each $\hat{x} \in \mathbb{R}^3$, $\hat{\mathcal{F}}(\hat{x})$ is nonempty and convex. Then, results such as [63, Prop. 6.10] guarantee completeness of maximal solutions because no finite escape times can occur for (3.10).

We prove then uniqueness of complete solutions from \hat{x}_0 . With L in Assumption 3.2(iii), define

$$f_L(\hat{v}) := L\hat{v} - f(\hat{v}), \quad (3.33)$$

and note that f_L is nondecreasing. Indeed, for $\hat{v}_1 < \hat{v}_2$, $-L(\hat{v}_2 - \hat{v}_1) \leq f(\hat{v}_2) - f(\hat{v}_1) \leq L(\hat{v}_2 - \hat{v}_1)$ from Assumption 3.2(iii), hence $L\hat{v}_1 - f(\hat{v}_1) \leq L\hat{v}_2 - f(\hat{v}_2)$, so that $\hat{v}_1 < \hat{v}_2$ implies

$$f_L(\hat{v}_1) := L\hat{v}_1 - f(\hat{v}_1) \leq L\hat{v}_2 - f(\hat{v}_2) =: f_L(\hat{v}_2).$$

By defining

$$\Psi_L(\hat{v}) := F_s \text{Sign}(\hat{v}) + f_L(\hat{v}), \quad (3.34)$$

(3.10) is equivalently rewritten as

$$\begin{aligned} \dot{\hat{x}} &\in \begin{bmatrix} 0 & 0 & -k_i \\ 1 & 0 & -k_p \\ 0 & 1 & L - k_d \end{bmatrix} \hat{x} - \begin{bmatrix} 0 \\ 0 \\ 1 \end{bmatrix} \Psi_L(\hat{v}) \\ &=: A_L \hat{x} - e_3 \Psi_L(\hat{v}). \end{aligned} \quad (3.35)$$

Consider two complete solutions $\hat{x}_a = (\hat{\sigma}_a, \hat{\phi}_a, \hat{v}_a)$ and $\hat{x}_b = (\hat{\sigma}_b, \hat{\phi}_b, \hat{v}_b)$ with the same initial condition \hat{x}_0 , i.e., $\hat{x}_a(0) = \hat{x}_b(0) = \hat{x}_0$, and we show now that $\hat{x}_a(t) = \hat{x}_b(t)$ for all $t \geq 0$. Define $\eta = (\eta_1, \eta_2, \eta_3) := \hat{x}_a - \hat{x}_b$, so that $\eta(0) = 0$. The solutions \hat{x}_a and \hat{x}_b are complete, so we have by (3.35) that for almost all $t \geq 0$

$$\dot{\eta}(t) \in A_L \eta(t) - e_3 (\Psi_L(\hat{v}_a(t)) - \Psi_L(\hat{v}_b(t))).$$

With λ denoting the maximum singular value of A_L , we have for almost all $t \geq 0$

$$\begin{aligned} \frac{d}{dt} \frac{|\eta(t)|^2}{2} &\in \eta(t)^\top A_L \eta(t) + \eta_3(t) (\Psi_L(\hat{v}_b(t)) - \Psi_L(\hat{v}_a(t))) \\ \implies \frac{d}{dt} \frac{|\eta(t)|^2}{2} &\leq \lambda |\eta(t)|^2 + N(t), \end{aligned} \quad (3.36)$$

where

$$N(t) := \max_{\substack{f_b \in \Psi_L(\hat{v}_b(t) - \eta_3(t)) \\ f_a \in \Psi_L(\hat{v}_a(t))}} \eta_3(t) (f_b - f_a). \quad (3.37)$$

Note that $N(t)$ in (3.37) can be rewritten equivalently by (3.34) as

$$N(t) = \max_{\substack{f'_b \in F_s \text{ Sign}(\hat{v}_a(t) - \eta_3(t)) \\ f'_a \in F_s \text{ Sign}(\hat{v}_a(t))}} \eta_3(t) \left(f'_b - f'_a + f_L(\hat{v}_a(t) - \eta_3(t)) - f_L(\hat{v}_a(t)) \right).$$

Whether $\hat{v}_a(t)$ and $\hat{v}_a(t) - \eta_3(t)$ are positive, zero, or negative, inspection of all cases reveals that $N(t) \leq 0$ for all $t \geq 0$ because we established above that f_L is nondecreasing. As a result, (3.36) satisfies

$$\frac{d}{dt} \frac{|\eta(t)|^2}{2} \leq \lambda |\eta(t)|^2, \quad (3.38)$$

for almost all $t \geq 0$. Then, $\eta(0) = 0$ implies $\eta(t) = 0$ for all $t \geq 0$ by standard comparison theorems (e.g., [83, Lem. 3.4]).

Item (ii). The proof of this item and the following ones is based on the proof of [29, Claim 1]. We only consider $\hat{v}_0 = 0$, $\hat{\phi}_0 > F_s$ because the other cases are handled similarly. From (3.14) we have $\dot{\tilde{v}} = \tilde{\phi} - k_d \tilde{v} - F_s + f(\tilde{v})$ with $\tilde{v}_0 = 0$, $\tilde{\phi}_0 > F_s$ so that $\dot{\tilde{v}}(0) > 0$. Hence, there exists $T > 0$ such that for all $t \in (0, T]$, $\tilde{v}(t) > 0$ and $F_s \text{ Sign}(\tilde{v}(t)) = \{F_s\}$. Therefore, this unique solution \tilde{x} to (3.14) substituted in (3.10) satisfies indeed $\dot{\tilde{x}}(t) \in \hat{\mathcal{F}}_x(\tilde{x}(t))$ for almost all $t \in [0, T]$.

Item (iii). We only consider $\hat{v}_0 = 0$, $\hat{\sigma}_0 > 0$, $\hat{\phi}_0 \in [-F_s, F_s)$ because the other cases are handled similarly. The explicit solution to (3.15) is then $\tilde{\sigma}(t) = \hat{\sigma}_0 > 0$, $\tilde{\phi}(t) = \hat{\phi}_0 + \hat{\sigma}_0 t$, $\tilde{v}(t) = 0$ on the interval $[0, T] := [0, \frac{F_s - \hat{\phi}_0}{\hat{\sigma}_0}]$. This unique solution \tilde{x} to (3.15) substituted in (3.10) satisfies indeed $\dot{\tilde{x}}(t) \in \hat{\mathcal{F}}_x(\tilde{x}(t))$ for almost all $t \in [0, T]$ because for all $t \in [0, T]$ a value of $\text{Sign}(0)$ can be selected such that $0 \in \hat{\phi}_0 + \hat{\sigma}_0 t - F_s \text{ Sign}(0)$.

Item (iv). This item is proven as item (ii).

3.A.2 Proof of Lemma 3.6

First, we show that for each $\hat{\xi}_0 = (\hat{\sigma}_0, \hat{\phi}_0, \hat{v}_0, \hat{b}_0) \in \hat{\mathcal{C}} \cup \hat{\mathcal{D}}$ there exists a nontrivial solution $\hat{\xi}$ to $\hat{\mathcal{H}}$ starting from $\hat{\xi}_0$ (i.e., $\text{dom } \hat{\xi}$ contains at least one point different from $(0, 0)$). For convenience, we rephrase the conditions in $\hat{\mathcal{C}} = \hat{\Xi}$ as:

$$h_1(\hat{\xi}) := \hat{b}\hat{\sigma}\hat{v} \geq 0, \quad h_2(\hat{\xi}) := \hat{\sigma}\hat{\phi} - \frac{k_p}{k_i}\hat{\sigma}^2 \geq 0, \quad h_3(\hat{\xi}) := \hat{b}\hat{v}\hat{\phi} \geq 0. \quad (3.39)$$

We divide into the cases $\hat{b}_0 = 1$ and $\hat{b}_0 = -1$.

For $\hat{b}_0 = 1$, a nontrivial solution exists for $\hat{\xi}_0 \in \hat{\mathcal{D}}_\sigma$, where $\hat{\sigma}_0 = 0$. We then need to show that for each $\hat{\xi}_0 \in \hat{\mathcal{C}} \setminus \hat{\mathcal{D}}_\sigma$, there exists a nontrivial flowing solution (i.e., an absolutely continuous function $\hat{\xi}: [0, T] \rightarrow \mathbb{R}^4$ with $T > 0$ satisfying $\dot{\hat{\xi}}(t) \in \hat{\mathcal{F}}(\hat{\xi}(t))$ for almost all $t \in [0, T]$, such that $\hat{\xi}(0) = \hat{\xi}_0$ and $\hat{\xi}(t) \in \hat{\mathcal{C}}$ for all $t \in (0, T]$). We then list all possible cases for $\hat{\xi}_0 \in \hat{\mathcal{C}} \setminus \hat{\mathcal{D}}_\sigma$, and show that there exists a nontrivial flowing solution starting from each of these cases.

1. $\hat{\sigma}_0 > 0$, $\hat{v}_0 > 0$, $\hat{\phi}_0 > \frac{k_p}{k_i} \hat{\sigma}_0$ or $\hat{\sigma}_0 < 0$, $\hat{v}_0 < 0$, $\hat{\phi}_0 < \frac{k_p}{k_i} \hat{\sigma}_0$: a nontrivial flowing solution defined as above exists because these points belong to the interior of $\hat{\mathcal{C}}$.

2. $\hat{\sigma}_0 > 0$, $\hat{v}_0 > 0$, $\hat{\phi}_0 = \frac{k_p}{k_i} \hat{\sigma}_0$ or $\hat{\sigma}_0 < 0$, $\hat{v}_0 < 0$, $\hat{\phi}_0 = \frac{k_p}{k_i} \hat{\sigma}_0$: in the former case, we need to verify that the corresponding flowing solution belongs to $\hat{\mathcal{C}}$ in (3.21f). Since $\hat{\sigma}_0$, \hat{v}_0 , and $\hat{\phi}$ are strictly positive, it holds $h_1(\hat{\xi}(t)) > 0$ and $h_3(\hat{\xi}(t)) > 0$ for $t \in [0, T]$ with $T > 0$. Since $\hat{\phi}_0 = \frac{k_p}{k_i} \hat{\sigma}_0$, it holds that $h_2(\hat{\xi}(0)) = 0$. It is sufficient to verify that $\dot{h}_2(\hat{\xi}(0)) > 0$ to conclude the existence of a nontrivial flowing solution. Indeed, $\dot{h}_2(\hat{\xi}(0)) = -k_i \hat{v}_0 \hat{\phi}_0 + \hat{\sigma}_0(\hat{\sigma}_0 - k_p \hat{v}_0) - 2 \frac{k_p}{k_i} \hat{\sigma}_0 (-k_i \hat{v}_0) = \hat{\sigma}_0^2 > 0$. The latter case follows analogously.

3. $\hat{\sigma}_0 > 0$, $\hat{v}_0 = 0$, $\hat{\phi}_0 > \frac{k_p}{k_i} \hat{\sigma}_0$ or $\hat{\sigma}_0 < 0$, $\hat{v}_0 = 0$, $\hat{\phi}_0 < \frac{k_p}{k_i} \hat{\sigma}_0$: in the former case, $\hat{\sigma}_0 > 0$, $\hat{v}_0 = 0$, $\hat{\phi}_0 > \frac{k_p}{k_i} \hat{\sigma}_0 > 0$ can only correspond to an initial condition in (3.11) or (3.12) in Claim 3.4, which both give rise to $\hat{v}(t) \geq 0$ for all $t \in [0, T]$ by Claim 3.4, items (ii) and (iii). Then, it holds $h_1(\hat{\xi}(t)) \geq 0$ and $h_3(\hat{\xi}(t)) \geq 0$ for $t \in [0, T]$ with $T > 0$ (by shrinking $T > 0$ if needed). Moreover, $\dot{h}_2(\hat{\xi}(0)) = -k_i \hat{v}_0 \hat{\phi}_0 + \hat{\sigma}_0(\hat{\sigma}_0 - k_p \hat{v}_0) - 2 \frac{k_p}{k_i} \hat{\sigma}_0 (-k_i \hat{v}_0) = \hat{\sigma}_0^2 > 0$, so it also holds that $h_2(\hat{\xi}(t)) \geq 0$ for $t \in [0, T]$ with $T > 0$ and a nontrivial flowing solution exists. The latter case follows analogously.

4. $\hat{\sigma}_0 > 0$, $\hat{v}_0 = 0$, $\hat{\phi}_0 = \frac{k_p}{k_i} \hat{\sigma}_0$ or $\hat{\sigma}_0 < 0$, $\hat{v}_0 = 0$, $\hat{\phi}_0 = \frac{k_p}{k_i} \hat{\sigma}_0$: analogous to item 3) above.

For $\hat{b}_0 = -1$, a nontrivial solution exists for $\hat{\xi}_0 \in \hat{\mathcal{D}}_v$, where $\hat{v}_0 = 0$. We then need to show that for each $\hat{\xi}_0 \in \hat{\mathcal{C}} \setminus \hat{\mathcal{D}}_v$, there exists a nontrivial flowing solution. We then list all possible cases for $\hat{\xi}_0 \in \hat{\mathcal{C}} \setminus \hat{\mathcal{D}}_v$, and show that there exists a nontrivial flowing solution starting from each of these cases.

1' $\hat{v}_0 > 0$, $\hat{\sigma}_0 < 0$, $\hat{\phi}_0 < \frac{k_p}{k_i} \hat{\sigma}_0$ or $\hat{v}_0 < 0$, $\hat{\sigma}_0 > 0$, $\hat{\phi}_0 > \frac{k_p}{k_i} \hat{\sigma}_0$: a nontrivial flowing solution defined as above exists because these points belong to the interior of $\hat{\mathcal{C}}$.

2' $\hat{v}_0 > 0$, $\hat{\sigma}_0 < 0$, $\hat{\phi}_0 = \frac{k_p}{k_i} \hat{\sigma}_0$ or $\hat{v}_0 < 0$, $\hat{\sigma}_0 > 0$, $\hat{\phi}_0 = \frac{k_p}{k_i} \hat{\sigma}_0$: in the former case, the conditions for h_1 and h_3 hold trivially. The condition for h_2 holds because $\dot{h}_2(\hat{\xi}(0)) = \hat{\sigma}_0^2 > 0$. The latter case follows analogously.

3' $\hat{v}_0 > 0$, $\hat{\sigma}_0 = 0$, $\hat{\phi}_0 < \frac{k_p}{k_i} \hat{\sigma}_0$ or $\hat{v}_0 < 0$, $\hat{\sigma}_0 = 0$, $\hat{\phi}_0 > \frac{k_p}{k_i} \hat{\sigma}_0$: in the former case, the condition for h_3 holds trivially, the condition for h_1 holds because $\dot{\sigma}(0) = -k_i \hat{v}(0) < 0$, and the condition for h_2 holds because $\dot{h}_2(\hat{\xi}(0)) = -k_i \hat{v}_0 \hat{\phi}_0 > 0$. The latter case follows analogously.

4' $\hat{v}_0 > 0$, $\hat{\sigma}_0 = 0$, $\hat{\phi}_0 = \frac{k_p}{k_i} \hat{\sigma}_0$ or $\hat{v}_0 < 0$, $\hat{\sigma}_0 = 0$, $\hat{\phi}_0 = \frac{k_p}{k_i} \hat{\sigma}_0$: in the former case, the condition for h_1 holds because $\dot{\sigma}(0) = -k_i \hat{v}(0) < 0$, the condition for

\hat{h}_2 holds because $\dot{\hat{h}}_2(\hat{\xi}(0)) = 0$ and, after some computations, $\ddot{\hat{h}}_2(\hat{\xi}(0)) = 0$ and $\ddot{\hat{h}}_2(\hat{\xi}(0)) = 3k_i^2\hat{v}_0^2 > 0$. Finally, the condition for h_3 holds because $\dot{h}_3(\hat{\xi}(0)) > 0$. The latter case follows analogously.

Second, we show that solutions are complete through [62, Thm. S3], which is applicable because the hybrid system $\hat{\mathcal{H}}$ satisfies the Basic Assumptions of [62, p. 43]. Then, only one of the cases (a)-(c) of the theorem holds. First, [62, Thm. S3, case (b)] cannot occur because the flow map is a linear system with bounded input. Second, [62, Thm. S3, case (c)] cannot occur because $\hat{g}_\sigma(\hat{\mathcal{D}}_\sigma) \cup \hat{g}_v(\hat{\mathcal{D}}_v) \subset \hat{\mathcal{C}} \cup \hat{\mathcal{D}}$ (as it can be verified through (3.21e), (3.21g), (3.21h)). Then only [62, Thm. S3, case (a)] remains, i.e., each solution $\hat{\xi}$ is complete.

3.A.3 Proof of Lemma 3.8

Consider dynamics (3.21) and notice that the state \hat{b} is bounded because it evolves in a bounded set. Focusing the attention on the remaining states $\hat{x} = (\hat{\sigma}, \hat{\phi}, \hat{v})$, their flow obeys the dynamics in (3.9) where A is Hurwitz due to Assumption 3.3, and the term multiplying e_3 is bounded by F_s , due to Assumption 3.2. In particular, from standard BIBO results for linear systems, there exist scalars $k_A \geq 1$ and $h_A > 0$ such that any solution $\hat{\xi} = (\hat{x}, \hat{b})$ satisfies ⁴

$$|\hat{x}(t, j)|^2 \leq k_A |\hat{x}(t_j, j)|^2 + h_A, \quad \forall t \in [t_j, t_{j+1}], \quad (3.40)$$

where $t_j, j \geq 1$, denotes a jump time, $t_0 = 0$ and possibly $t_{j+1} = +\infty$ with the last flowing interval being open and unbounded. Consider now a solution to (3.21) which may: a) flow forever (i.e., experiences no jumps), in which case bound (3.40) with $j = 0$ provides the desired global bound; b) exhibit one jump only, in which case a global bound is obtained by concatenating twice bound (3.40); c) flow and/or jump multiple times, in which case, due the peculiar toggling nature of \hat{b} , the solution alternately jumps from $\hat{\mathcal{D}}_\sigma$ and $\hat{\mathcal{D}}_v$. Hence, the solution jumps from $\hat{\mathcal{D}}_v$ at either t_1 or (at most) at t_2 . Consider the scenario of a first jump happening from $\hat{\mathcal{D}}_\sigma$ at time $(t_1, 0)$, which leads to $|\hat{\xi}(t_1, 1)|^2 = |\hat{\xi}(t_1, 0)|^2$ due to the design of \hat{g}_σ in (3.21e), and then a second jump from $\hat{\mathcal{D}}_v$ at time $(t_2, 1)$, which leads to $|\hat{\xi}(t_2, 2)|^2 \leq |\hat{\xi}(t_2, 1)|^2$ due to the design of \hat{g}_v in (3.21e) and of $\hat{\mathcal{D}}_v$ in (3.21h) (in particular the condition $\hat{\sigma}\hat{\phi} \geq \frac{k_p}{k_i}\hat{\sigma}^2$). For this described scenario, concatenating bounds yields

$$\max_{\substack{(t,j) \in \text{dom } \hat{\xi} \\ t+j \leq t_2+2}} |\hat{x}(t, j)|^2 \leq \bar{k}_A |\hat{x}(0, 0)|^2 + \bar{h}_A, \quad (3.41)$$

where we used $\bar{k}_A := k_A^2 \geq k_A \geq 1$, $\bar{h}_A := h_A(1 + k_A) > h_A$. This described scenario can be viewed as the worst-case-scenario, because bound (3.41) also applies

⁴Note that classical BIBO bounds involve the norm not squared, but those easily extend to (3.40) by using $(k|x_0| + h)^2 \leq (k^2 + 2kh)|x_0|^2 + (h^2 + 2kh)$.

to the other scenario where the jump from $\hat{\mathcal{D}}_\sigma$ does not occur and the jump from $\hat{\mathcal{D}}_v$ occurs at t_1 , because $\bar{k}_A \geq k_A$ and $\bar{h}_A \geq h_A$. Then, we can consider only this described worst-case-scenario without loss of generality. Inequality (3.41) hence establishes a uniform bound for all solutions, until a first jump from $\hat{\mathcal{D}}_v$.

To complete the proof we must establish a (uniform) bound on solutions performing a jump from $\hat{\xi}(t_2, 1) \in \hat{\mathcal{D}}_v$. To this end, consider the following Lyapunov-like function, inspired by [29, Eq. (14)]:

$$W(\hat{\xi}) = \begin{bmatrix} \hat{\sigma} \\ \hat{v} \end{bmatrix}^\top \begin{bmatrix} \frac{k_d}{k_i} & -1 \\ -1 & k_p \end{bmatrix} \begin{bmatrix} \hat{\sigma} \\ \hat{v} \end{bmatrix} + \min_{F \in F_s \text{ Sign}(\hat{v})} (\hat{b}\hat{\phi} - F)^2. \quad (3.42)$$

For W in (3.42) it holds that the matrix $\begin{bmatrix} \frac{k_d}{k_i} & -1 \\ -1 & k_p \end{bmatrix}$ is positive definite (by Assumption 3.3), and it holds that $\frac{\hat{\phi}^2}{2} - F_s^2 \leq (\hat{b}\hat{\phi} - F)^2 \leq 2\hat{\phi}^2 + 2F_s^2$ (since $F \in [-F_s, F_s]$). Using these properties, we construct the following bounds:

$$W(\hat{\xi}) \leq \bar{c}_W |\hat{x}|^2 + 2F_s^2, \quad |\hat{x}|^2 \leq \underline{c}_W W(\hat{\xi}) + \underline{c}_W F_s^2, \quad (3.43)$$

for some scalars $\bar{c}_W \geq 1$, $\underline{c}_W \geq 1$. Bounds (3.43) show that boundedness of $W(\hat{x})$ is equivalent to boundedness of $|\hat{x}|$. Given

$$c_3 := 2(k_p k_d - k_i) > 0 \quad (3.44)$$

by Assumption 3.3, W enjoys the following useful properties in the next claim.

Claim 3.17. *Function W in (3.42) with c_3 in (3.44) enjoys the following properties along dynamics (3.21):*

1. For all $i \in \{\sigma, v\}$, for all $\hat{\xi} \in \mathcal{D}_i$,

$$W(g_i(\hat{\xi})) - W(\hat{\xi}) \leq 0. \quad (3.45)$$

2. For any $\hat{\xi} = (\hat{\sigma}, \hat{\phi}, \hat{v}, \hat{b}) \in \mathcal{S}_{\hat{\pi}}$ and each flowing interval $I^j := \{t: (t, j) \in \text{dom } \hat{\xi}\}$ with $\hat{b}(t_j, j) = -1$,

$$W(\hat{\xi}(t_2, j)) - W(\hat{\xi}(t_1, j)) \leq \int_{t_1}^{t_2} -c_3 \hat{v}(t, j)^2 dt, \quad (3.46)$$

for all $t_1, t_2 \in I^j$ with $t_1 \leq t_2$.

3. There exists a scalar $\bar{W} > 0$ such that any solution $\hat{\xi} = (\hat{\sigma}, \hat{\phi}, \hat{v}, \hat{b}) \in \mathcal{S}_{\hat{\pi}}$ satisfying $\hat{\xi}(t_j, j-1) \in \hat{\mathcal{D}}_v$, jumping to $\hat{\xi}(t_j, j) = \hat{g}_v(\hat{\xi}(t_j, j-1))$ and then flowing up to $\hat{\xi}(t_{j+1}, j) \in \hat{\mathcal{D}}_\sigma$ satisfies:

$$W(\hat{\xi}(t_j, j)) \geq \bar{W} \implies W(\hat{\xi}(t_{j+1}, j)) \leq W(\hat{\xi}(t_j, j)). \quad (3.47)$$

Proof. see Appendix 3.A.4. □

For function W we use bounds (3.43) with (3.40) to arrive at

$$W(\hat{\xi}(t, j)) \leq k_W W(\hat{\xi}(t_j, j)) + h_W, \quad \forall t \in [t_j, t_{j+1}], \quad (3.48)$$

along any flowing solution, where $k_W := \bar{c}_W c_W k_A \geq 1$ (since $\bar{c}_W \geq 1$, $c_W \geq 1$, and $k_A \geq 1$) and $h_W := \bar{c}_W (k_A c_W F_s^2 + h_A) + 2F_s^2 > 0$.

We are now ready to complete bound (3.41) beyond hybrid time $(t_2, 2)$. To simplify the notation, we focus on solutions exhibiting infinitely many jumps, by noting that the analysis also applies to solutions that eventually stop jumping, because the last bound established below will hold on the last (unbounded) flowing interval. Given any such solution $\hat{\xi}$ that keeps exhibiting jumps, denote

$$W_0 := W(\hat{\xi}(t_2, 2)) \leq \bar{c}_W (\bar{k}_A |\hat{x}(0, 0)|^2 + \bar{h}_A) + 2F_s^2, \quad (3.49)$$

where we combined (3.41) and (3.43). Due to the peculiar toggling nature of \hat{b} in dynamics (3.21), jumps must occur alternatively from $\hat{\mathcal{D}}_v$ at times $(t_2, 1)$, $(t_4, 3)$ and so on (at jump times with even indices), and from $\hat{\mathcal{D}}_\sigma$ at jump times with odd indices. We proceed by induction. Assume that at time $(t_{2i}, 2i)$ (after a jump from $\hat{\mathcal{D}}_v$) we have

$$W(\hat{\xi}(t_{2i}, 2i)) \leq \max\{k_W \bar{W} + h_W, W_0\}, \quad (3.50)$$

which is clearly true for $i = 1$ (the base case of induction), because of (3.49). As for the induction step, (3.48) yields

$$W(\hat{\xi}(t, 2i)) \leq k_W W(\hat{\xi}(t_{2i}, 2i)) + h_W, \quad \forall t \in [t_{2i}, t_{2i+1}]. \quad (3.51)$$

We obtain that $W(\hat{\xi}(t_{2i+1}, 2i)) \leq \max\{k_W \bar{W} + h_W, W(\hat{\xi}(t_{2i}, 2i))\}$ because for $W(\hat{\xi}(t_{2i}, 2i)) \geq \bar{W}$, it holds that $W(\hat{\xi}(t_{2i+1}, 2i)) \leq W(\hat{\xi}(t_{2i}, 2i))$ (by (3.47) in Claim 3.17), and for $W(\hat{\xi}(t_{2i}, 2i)) < \bar{W}$, it holds that $W(\hat{\xi}(t_{2i+1}, 2i)) \leq k_W \bar{W} + h_W$ (by (3.50)). Then, $W(\hat{\xi}(t_{2i+1}, 2i)) \leq \max\{k_W \bar{W} + h_W, W(\hat{\xi}(t_{2i}, 2i))\}$ can be propagated to the subsequent time interval using the nonincreasing properties of W established in (3.45) and (3.46) of Claim 3.17, as follows:

$$W(\hat{\xi}(t, 2i+1)) \leq \max\{k_W \bar{W} + h_W, W(\hat{\xi}(t_{2i}, 2i))\}, \quad \forall t \in [t_{2i+1}, t_{2(i+1)}]. \quad (3.52)$$

Finally, using again the nonincrease in (3.45) and bound (3.50), we obtain

$$\begin{aligned} W(\hat{\xi}(t_{2(i+1)}, 2(i+1))) &\leq \max\{k_W \bar{W} + h_W, W(\hat{\xi}(t_{2i}, 2i))\} \\ &\leq \max\{k_W \bar{W} + h_W, W_0\}, \end{aligned}$$

which corresponds to (3.50), completes the induction proof, and establishes then that (3.50) holds for all $i \geq 1$.

Summarizing, we combine bounds (3.51) and (3.52) (together with (3.49) and $k_W \geq 1$ and $h_W > 0$) to obtain, for all $(t, j) \in \text{dom } \hat{\xi}$ such that $t + j \geq t_2 + 2$,

$$W(\hat{\xi}(t, j)) \leq \max\{k_W^2 \bar{W} + k_W h_W + h_W, \\ k_W \bar{c}_W \bar{k}_A |\hat{x}(0, 0)|^2 + k_W (\bar{c}_W \bar{h}_A + 2F_s^2) + h_W\}.$$

That is, W remains bounded which, combined with (3.43), implies boundedness of \hat{x} , and the fact that \hat{b} evolves in a bounded set completes the proof of uniform boundedness of solutions to $\hat{\mathcal{H}}$.

3.A.4 Proof of Claim 3.17

We prove the claim item by item.

Proof of item 1. For all $\hat{\xi} \in \hat{\mathcal{D}}_\sigma$, we have

$$W(g_\sigma(\hat{\xi})) - W(\hat{\xi}) = \min_{F \in F_s \text{ Sign}(\hat{v})} ((\hat{b}\hat{\phi})^+ - F)^2 - \min_{F \in F_s \text{ Sign}(\hat{v})} (\hat{b}\hat{\phi} - F)^2 = 0,$$

because $(\hat{b}\hat{\phi})^+ = (\hat{b}\hat{\phi})$. For all $\hat{\xi} \in \hat{\mathcal{D}}_v$, we have

$$\begin{aligned} W(g_v(\hat{\xi})) - W(\hat{\xi}) &= \min_{F \in F_s \text{ Sign}(0)} ((\hat{b}\hat{\phi})^+ - F)^2 - \min_{F \in F_s \text{ Sign}(0)} (\hat{b}\hat{\phi} - F)^2 \\ &= \min_{F \in [-F_s, F_s]} \left(\frac{k_p}{k_i} \hat{\sigma} - F\right)^2 - \min_{F \in [-F_s, F_s]} (-\hat{\phi} - F)^2 \\ &= \min_{F \in [-F_s, F_s]} \left(\frac{k_p}{k_i} \hat{\sigma} - F\right)^2 - \min_{F \in [-F_s, F_s]} (\hat{\phi} - F)^2 \\ &= dz_{F_s}^2 \left(\frac{k_p}{k_i} \hat{\sigma}\right) - dz_{F_s}^2 (\hat{\phi}) \leq 0, \end{aligned}$$

because $|\hat{\phi}| \geq \frac{k_p}{k_i} |\hat{\sigma}|$ due to the fact that $\hat{\sigma} \hat{\phi} \geq \frac{k_p}{k_i} \hat{\sigma}^2$ in $\hat{\mathcal{D}}_v$.

Proof of item 2. By Claim 3.4, for each initial condition, the component \hat{x} of the (unique) flowing solution $\hat{\xi}$ coincides with the unique solution \tilde{x} to one of (3.14)-(3.16) on a finite time interval with length T . Because such unique solution to (3.14), (3.15), (3.16) has respectively \tilde{v} positive, zero, negative over such interval with length T by Claim 3.4, it can be shown respectively that for all t in such interval

$$W\left(\begin{bmatrix} \tilde{x}(t) \\ -1 \end{bmatrix}\right) = W_1(\tilde{x}(t)), \quad W\left(\begin{bmatrix} \tilde{x}(t) \\ -1 \end{bmatrix}\right) = W_0(\tilde{x}(t)), \quad W\left(\begin{bmatrix} \tilde{x}(t) \\ -1 \end{bmatrix}\right) = W_{-1}(\tilde{x}(t)),$$

with

$$W_1(\tilde{x}) := \begin{bmatrix} \tilde{\sigma} \\ \tilde{v} \end{bmatrix}^\top \begin{bmatrix} \frac{k_d}{k_i} & -1 \\ -1 & k_p \end{bmatrix} \begin{bmatrix} \tilde{\sigma} \\ \tilde{v} \end{bmatrix} + (-\tilde{\phi} - F_s)^2 \quad (3.53)$$

$$W_0(\tilde{x}) := \frac{k_d}{k_i} \tilde{\sigma}^2 \quad (3.54)$$

$$W_{-1}(\tilde{x}) := \begin{bmatrix} \tilde{\sigma} \\ \tilde{v} \end{bmatrix}^\top \begin{bmatrix} \frac{k_d}{k_i} & -1 \\ -1 & k_p \end{bmatrix} \begin{bmatrix} \tilde{\sigma} \\ \tilde{v} \end{bmatrix} + (-\tilde{\phi} + F_s)^2, \quad (3.55)$$

in the same way as [29, Claim 1, item 2)].

In the rest of the proof we consider W_1 (or W_0 or W_{-1} , respectively) instead of W during the flow of $\hat{\xi}$ only when the component \hat{x} of the solution $\hat{\xi}$ coincides with the solution \tilde{x} to (3.14) (or (3.15) or (3.16), respectively). So, we can exploit the conditions satisfied by $\hat{\xi}$ while flowing in the flow set (3.21f), in particular $\hat{b}\hat{\sigma}\hat{v} \geq 0$. For $\hat{b} = -1$ we have then $\tilde{\sigma}(t)\tilde{v}(t) \leq 0$. When considering the solution \tilde{x} to (3.14) (resp. (3.16)), $\tilde{v}(t) > 0$ (resp. $\tilde{v}(t) < 0$), so $\hat{\sigma}(t)\hat{v}(t) \leq 0$ implies $\tilde{\sigma}(t) \leq 0$ (resp. $\tilde{\sigma}(t) \geq 0$). We use these conditions for the bounds in the following (3.56). Some computations yield the derivative of W_1 along solutions to (3.14), of W_0 along solutions to (3.15), and of W_{-1} along solutions to (3.16), respectively, as

$$\begin{aligned} \frac{d}{d\tau} W_1(\tilde{x}(t)) &= -c_3\tilde{v}(t)^2 + 2\tilde{\sigma}(t)(F_s - f(\tilde{v}(t))) \\ &\quad - 2k_p\tilde{v}(t)(F_s - f(\tilde{v}(t))) + 2F_s\tilde{\sigma}(t) - 2F_s k_p\tilde{v}(t) \\ &\leq -c_3\tilde{v}(t)^2 \\ \frac{d}{d\tau} W_0(\tilde{x}(t)) &= 0 \leq -c_3\tilde{v}(t)^2 \\ \frac{d}{d\tau} W_{-1}(\tilde{x}(t)) &= -c_3\tilde{v}(t)^2 - 2\tilde{\sigma}(t)(F_s + f(\tilde{v}(t))) \\ &\quad + 2k_p\tilde{v}(t)(F_s + f(\tilde{v}(t))) - 2F_s\tilde{\sigma}(t) + 2F_s k_p\tilde{v}(t) \\ &\leq -c_3\tilde{v}(t)^2, \end{aligned} \quad (3.56)$$

where the bounds were justified before and, as for W_0 , \hat{v} is identically zero. We now use (3.56) together with the reasoning in [29, Sec. V.A] as follows: $\hat{\xi} \mapsto W(\hat{\xi})$ and $t \mapsto W(\hat{\xi}(t))$ are lower semicontinuous by the same argument as in [29, Sec. V.A]. Moreover, $W_1(\tilde{x}(\cdot))$, $W_0(\tilde{x}(\cdot))$, and $W_{-1}(\tilde{x}(\cdot))$ are differentiable, thus $W\left(\begin{bmatrix} \hat{x}(\cdot) \\ -1 \end{bmatrix}\right)$ is at least differentiable from the right. The lower right Dini derivative coincides with the right derivative, and the right derivative is upper bounded on each interval with length T by $-c_3\hat{v}(t, j)^2$ from (3.56). This allows to invoke [66, Thm. 9] same as in [29, Fact 1], which leads to (3.46).

Proof of item 3. Consider any solution $\hat{\xi} = (\hat{\sigma}, \hat{\phi}, \hat{v}, \hat{b}) = (\hat{x}, \hat{b}) \in \mathcal{S}_{\mathcal{H}}$ to (3.21) satisfying $\hat{\xi}(t_j, j-1) \in \hat{\mathcal{D}}_v$ in (3.21h), jumping to $\hat{\xi}(t_j, j) = \hat{g}_v(\hat{\xi}(t_j, j-1))$ in (3.21e) and then necessarily flowing up to $\hat{\xi}(t_{j+1}, j) \in \hat{\mathcal{D}}_\sigma$, because we consider $W(\hat{\xi}(t_j, j)) > \bar{W}$, and this implies $|\hat{\sigma}(t_j, j)|$ sufficiently large, as argued below. Moreover, \hat{b} is constant and equal to 1 along this interval of flow. Using the expression of $\hat{\mathcal{F}}_x(\hat{x})$ in (3.9), and the fact that matrix A therein is Hurwitz by Assumption 3.3, by linearity we may split the arising response in a homogeneous (or free, or zero-input) response \hat{x}_h from $\hat{x}_0 = \hat{x}(t_j, j) = \hat{\sigma}(t_j, j) \begin{bmatrix} 1 \\ \frac{k_p}{k_i} \\ 0 \end{bmatrix}$ (by (3.21e)

and (3.21h)), and a forced response \hat{x}_f from a zero initial condition caused by the bounded input $|e_3(F_s \text{Sign}(\hat{v}) - f(\hat{v}))| \leq F_s$ (where the bound comes from Assumption 3.2). Let us drop the dependence on “ j ” to simplify the following derivations.

Inspired by (3.42), define

$$\hat{V}(\hat{x}) := \hat{x}^T \hat{P} \hat{x} := \hat{x}^T \begin{bmatrix} \frac{k_d}{k_i} & 0 & -1 \\ 0 & 1 & 0 \\ -1 & 0 & k_p \end{bmatrix} \hat{x},$$

with $\hat{P} > 0$ (by Assumption 3.3), and satisfying

$$A^T \hat{P} + \hat{P} A = - \begin{bmatrix} 0 & 0 & 0 \\ 0 & 0 & 0 \\ 0 & 0 & c_3 \end{bmatrix},$$

with $c_3 > 0$ in (3.44), which provides a weak Lyapunov function for $\dot{\hat{x}} = A\hat{x}$, due to observability of the pair $([0 \ 0 \ c_3], A)$. Recall that the solution $\hat{\xi}$ necessarily flows at (t_j, j) , because we consider $W(\hat{\xi}(t_j, j)) \geq \bar{W}$, which implies $|\hat{\sigma}(t_j, j)|$ sufficiently large (as argued below in the proof). Then, the interval $[t_j, t_{j+1}]$ is nonempty by [63, Def. 2.6], so $t_{j+1} > t_j$. Then, \hat{V} being a weak Lyapunov function for $\dot{\hat{x}} = A\hat{x}$, and the observability of $([0 \ 0 \ c_3], A)$ imply that there exists a positive $\eta < 1$ such that

$$\hat{V}(\hat{x}_h(t_{j+1})) = \eta^2 \hat{V}(\hat{x}_0) = \eta^2 \hat{\sigma}(t_j, j)^2 \hat{V} \left(\begin{bmatrix} 1 \\ \frac{k_p}{k_i} \\ 0 \end{bmatrix} \right), \quad (3.57)$$

because $V(\hat{x}_h(\cdot))$ would remain constant on $[t_j, t_{j+1}]$ only for \hat{x} identically zero, which is excluded by the fact that we consider $|\hat{\sigma}(t_j, j)|$ sufficiently large. On the other hand, from BIBO stability of dynamics (3.7), we have that

$$|\hat{x}(t_{j+1}) - \hat{x}_h(t_{j+1})| = |\hat{x}_f(t_{j+1})| \leq \hat{h}_A, \quad (3.58)$$

for some $\hat{h}_A > 0$ (cf. (3.40)). Consider now the homogeneous of degree 1 function $\hat{U}(\hat{x}) := \sqrt{\hat{V}(\hat{x})}$, which is globally Lipschitz (namely, $|U(\hat{x}) - U(\hat{x}_h)| \leq L_U |\hat{x} - \hat{x}_h|$ for all $\hat{x}, \hat{x}_h \in \mathbb{R}^3$ and some Lipschitz constant $L_U > 0$) because its gradient is constant along rays starting at the origin. Using (3.57) and (3.58), we have

$$\begin{aligned} \hat{U}(\hat{x}(t_{j+1})) &\leq \hat{U}(\hat{x}_h(t_{j+1})) + L_U |\hat{x}(t_{j+1}) - \hat{x}_h(t_{j+1})| \\ &\leq \eta |\hat{\sigma}(t_j, j)| U_0 + L_U \hat{h}_A, \end{aligned}$$

where $U_0 := \hat{U} \left(\begin{bmatrix} 1 \\ \frac{k_p}{k_i} \\ 0 \end{bmatrix} \right)$ is a positive constant. As a consequence we have

$$\begin{aligned} \hat{V}(\hat{x}(t_{j+1})) &\leq \left(\eta |\hat{\sigma}(t_j, j)| U_0 + L_U \hat{h}_A \right)^2 \\ &= \hat{V}(\hat{x}_0) \left(\eta + \frac{L_U \hat{h}_A}{|\hat{\sigma}(t_j, j)| U_0} \right)^2. \end{aligned} \quad (3.59)$$

For $\eta \in (0, 1)$ it is possible to select $\tilde{\eta}_V \in (\eta, 1)$ and $\sigma_{M1} > 0$ sufficiently large such that

$$\eta + \frac{LU\hat{h}_A}{\sigma_{M1}U_0} = \tilde{\eta}_V. \quad (3.60)$$

With this equation, we obtain for $\tilde{\eta}_V \in (\eta, 1)$

$$|\hat{\sigma}(t_j, j)| \geq \sigma_{M1} \implies \hat{V}(\hat{x}(t_{j+1})) \leq \tilde{\eta}_V^2 \hat{V}(\hat{x}_0). \quad (3.61)$$

Consider now function W defined in (3.42) and relate it to \hat{V} through

$$\hat{V}(\hat{x}_0) = \hat{\sigma}(t_j, j)^2 \begin{bmatrix} \frac{1}{k_p} \\ \frac{k_p}{k_i} \end{bmatrix}^\top \begin{bmatrix} \frac{k_d}{k_i} & 0 \\ 0 & 1 \end{bmatrix} \begin{bmatrix} \frac{1}{k_p} \\ \frac{k_p}{k_i} \end{bmatrix} = \left(\frac{k_d}{k_i} + \frac{k_p^2}{k_i^2} \right) \hat{\sigma}(t_j, j)^2. \quad (3.62)$$

Introduce $\sigma_{M2} := \frac{k_i}{k_p} F_s \max\{1, \frac{1}{1-\sqrt{\tilde{\eta}_V}}\}$ (recall $\tilde{\eta}_V < 1$). For $|\hat{\sigma}(t_j, j)| \geq \sigma_{M2}$, we have

$$\begin{aligned} W(\hat{\xi}(t_j, j)) &= \hat{\sigma}(t_j, j)^2 \frac{k_d}{k_i} + \left(\frac{k_p}{k_i} |\hat{\sigma}(t_j, j)| - F_s \right)^2 \\ &\geq \frac{k_d}{k_i} \left(|\hat{\sigma}(t_j, j)| - \frac{k_i}{k_p} F_s \right)^2 + \frac{k_p^2}{k_i^2} \left(|\hat{\sigma}(t_j, j)| - \frac{k_i}{k_p} F_s \right)^2 \\ &= \left(\frac{k_d}{k_i} + \frac{k_p^2}{k_i^2} \right) \hat{\sigma}(t_j, j)^2 \left(1 - \frac{k_i F_s}{k_p |\hat{\sigma}(t_j, j)|} \right)^2 \\ &\geq \hat{V}(\hat{x}_0) \tilde{\eta}_V, \end{aligned}$$

where, in the given order, the first equality follows from $\hat{x}(t_j, j) = \hat{\sigma}(t_j, j) \begin{bmatrix} 1 \\ \frac{k_p}{k_i} \\ 0 \end{bmatrix}$ (cf. (3.21e)) and $\min_{F \in [-F_s, F_s]} (\hat{\phi}(t_j, j) - F)^2 = (|\hat{\phi}(t_j, j)| - F_s)^2$ for $|\hat{\sigma}(t_j, j)| \geq \frac{k_i}{k_p} F_s$, the first inequality follows from $|\hat{\sigma}(t_j, j)| \geq \frac{k_i}{k_p} F_s$, the second inequality follows from the expression of $\hat{V}(\hat{x}_0)$ in (3.62), and $|\hat{\sigma}(t_j, j)| \geq \sigma_{M2} \geq \frac{k_i}{k_p} F_s \frac{1}{1-\sqrt{\tilde{\eta}_V}}$. Then,

$$|\hat{\sigma}(t_j, j)| \geq \sigma_{M2} \implies W(\hat{\xi}(t_j, j)) \geq \tilde{\eta}_V \hat{V}(\hat{x}_0). \quad (3.63)$$

Finally, during flow with $\hat{b} = 1$, we have $\hat{b}\hat{v}\hat{\sigma} \geq 0$ and $\hat{\sigma}\hat{\phi} \geq \frac{k_p}{k_i}\hat{\sigma}^2$ (cf. (3.21f)). So, if $\hat{\sigma}(t_j, j) > 0$, we have from $\hat{b}\hat{v}\hat{\sigma} \geq 0$ that $\hat{v} \geq 0$, and from $\hat{\sigma}\hat{\phi} \geq \frac{k_p}{k_i}\hat{\sigma}^2$ that $\hat{\phi} \geq 0$ on $[t_j, t_{j+1}]$. Similarly, for $\hat{\sigma}(t_j, j) < 0$ we have $\hat{v} \leq 0$ and $\hat{\phi} \leq 0$. In both cases $\hat{v}(t_{j+1}, j) \geq 0$, $\hat{\phi}(t_{j+1}, j) \geq 0$ and $\hat{v}(t_{j+1}, j) \leq 0$, $\hat{\phi}(t_{j+1}, j) \leq 0$, we have $W(\hat{\xi}(t_{j+1}, j)) \leq \hat{V}(\hat{x}(t_{j+1})) + F_s^2$, which may be combined with (3.61) and (3.63) to obtain

$$\begin{aligned} W(\hat{\xi}(t_{j+1}, j)) &\leq \hat{V}(\hat{x}(t_{j+1})) + F_s^2 \leq \tilde{\eta}_V^2 \hat{V}(\hat{x}_0) + F_s^2 \\ &\leq \tilde{\eta}_V W(\hat{\xi}(t_j, j)) + F_s^2 \leq W(\hat{\xi}(t_j, j)), \end{aligned} \quad (3.64)$$

by taking $W(\hat{\xi}(t_j, j)) \geq \bar{W} := \max\{2F_s^2 + \sigma_M^2 \left(\frac{k_d}{k_i} + 2\frac{k_p^2}{k_i^2}\right), \frac{F_s^2}{1-\eta_V}\}$ for $\sigma_M := \max\{\sigma_{M1}, \sigma_{M2}\}$, where $W(\hat{\xi}(t_j, j)) \geq \frac{F_s^2}{1-\eta_V}$ guarantees the last inequality in (3.64) and $W(\hat{\xi}(t_j, j)) \geq 2F_s^2 + \sigma_M^2 \left(\frac{k_d}{k_i} + 2\frac{k_p^2}{k_i^2}\right)$ guarantees that $|\hat{\sigma}(t_j, j)| \geq \sigma_M$ holds (which was used in (3.64)) because from (3.42) we have from $\hat{x}(t_j, j) = \hat{\sigma}(t_j, j) \begin{bmatrix} 1 \\ \frac{k_p}{k_i} \\ 0 \end{bmatrix}$ and $\min_{F \in [-F_s, F_s]} (\hat{\phi} - F)^2 = dz_{F_s}^2(\hat{\phi}) \leq (|\hat{\phi}| + F_s)^2$:

$$\begin{aligned} W(\hat{\xi}(t_j, j)) &\leq \frac{k_d}{k_i} \hat{\sigma}(t_j, j)^2 + \left(\frac{k_p}{k_i} |\hat{\sigma}(t_j, j)| + F_s\right)^2 \\ &\leq \left(\frac{k_d}{k_i} + 2\frac{k_p^2}{k_i^2}\right) \hat{\sigma}(t_j, j)^2 + 2F_s^2. \end{aligned} \quad (3.65)$$

3.A.5 Proof of Lemma 3.9

We start with the next auxiliary claim, where L_2 is defined in Assumption 3.2(iv).

Claim 3.18. *Let Assumptions 3.2-3.3 hold.*

- (i) *For each $M > 0$, there exists $\delta_0(M) > 0$ such that for each initial condition $\tilde{x}_0 = (\tilde{\sigma}_0, \check{\phi}_0, 0) \in M\mathbb{B}$, the unique solution \tilde{x} (with $\tilde{x}(0) = \tilde{x}_0$) to (3.14) coincides over $[0, \delta_0(M)]$ with the unique solution \check{x} (with $\check{x}(0) = \tilde{x}_0$) to*

$$\dot{\check{x}} = A\check{x} - e_3(F_s - L_2\check{v}). \quad (3.66)$$

- (ii) *There exists $\delta_1 > 0$ such that for each initial condition $\check{x}_0 = (\check{\sigma}_0, \check{\phi}_0, 0)$ with*

$$\check{\sigma}_0 \geq 0, \check{\phi}_0 \geq F_s, \begin{bmatrix} \check{\sigma}_0 \\ \check{\phi}_0 \end{bmatrix} \neq \begin{bmatrix} 0 \\ F_s \end{bmatrix} \quad (3.67)$$

- ($\check{\sigma}_0 \leq 0, \check{\phi}_0 \leq -F_s, \begin{bmatrix} \check{\sigma}_0 \\ \check{\phi}_0 \end{bmatrix} \neq \begin{bmatrix} 0 \\ -F_s \end{bmatrix}$, respectively), the unique solution \check{x} (with $\check{x}(0) = \check{x}_0$) to (3.66) satisfies for all $t \in (0, \delta_1]$, $\check{v}(t) > 0$ and $\check{\phi}(t) > F_s$ ($\check{v}(t) < 0$ and $\check{\phi}(t) < -F_s$, respectively).*

Proof. see Appendix 3.A.6. □

We now turn to proving Lemma 3.9. We only consider the case $\hat{\xi}(t, j) \in \hat{\mathcal{S}}_1$, because the case $\hat{\xi}(t, j) \in \hat{\mathcal{S}}_{-1}$ relies on parallel arguments. Within the proof, we also exploit that maximal solutions are complete by Lemma 3.6, e.g., when we conclude that a maximal solution must flow if it cannot jump.

Evolution 3.9.1 (equilibrium)

Consider first $\hat{\xi}(t, j) = (0, F_s, 0, 1) \in \hat{\mathcal{S}}_1$. Since $(0, F_s, 0, 1) \in \hat{\mathcal{A}}$, we conclude by Lemma 3.7 that $\hat{v}(\tau, j(\tau)) = 0$ for all $\tau \geq t$.

We can then assume without loss of generality that $\hat{\xi}(t, j) \neq (0, F_s, 0, 1)$ in the rest of the proof. To prove the statement, we show that \hat{v} is nonnegative for all possible evolutions of $\hat{\xi}$ from $\hat{\xi}(t, j)$.

By Lemma 3.8, we know that for each compact set \mathcal{K} , there exists $M > 0$ such that for all $(t, j) \in \text{dom } \hat{\xi}$, when $\hat{\xi}(t, j) \in \hat{\mathcal{S}}_1$, it holds that $\hat{\xi}(t, j) \in \hat{\mathcal{S}}_1 \cap M\mathbb{B}$. Define

$$\delta'(\mathcal{K}) = \min\{\delta_0(M), \delta_1\} > 0$$

with $\delta_0(M)$ and δ_1 as in Claim 3.18 and consider the time interval $[t, t + \delta'(\mathcal{K})]$.

Evolution 3.9.2 (flow only).

Suppose $\hat{\xi} = (\hat{x}, \hat{b})$ with $\hat{\xi}(t, j) \in \hat{\mathcal{S}}_1 \setminus \{(0, F_s, 0, 1)\} \cap M\mathbb{B}$ flows on $[t, t + \delta'(\mathcal{K})]$. Note that this flowing solution from $\hat{\xi}(t, j)$ is unique by Lemma 3.5.

Since $\hat{\xi}(t, j) \in \hat{\mathcal{S}}_1 \setminus \{(0, F_s, 0, 1)\} \cap M\mathbb{B}$ by Lemma 3.8, it holds that $\hat{x}(t, j) = (\hat{\sigma}(t, j), \hat{\phi}(t, j), 0) \in M\mathbb{B}$. Then, Claim 3.18(i) ensures that the unique solution \tilde{x} to (3.14) with $\tilde{x}(t) = \hat{x}(t, j)$ coincides over the interval $[t, t + \delta'(\mathcal{K})]$ with the unique solution \check{x} to (3.66) with $\check{x}(t) = \hat{x}(t, j)$, which is such that $\check{v}(\tau) > 0$ and $\check{\phi}(\tau) > F_s$ for all $\tau \in (t, t + \delta'(\mathcal{K})]$ by Claim 3.18(ii) because $\check{x}(t) = \hat{x}(t, j) \in \hat{\mathcal{S}}_1 \setminus \{(0, F_s, 0, 1)\}$ and satisfies (3.67).

This solution \tilde{x} , in turn, coincides on the interval $[t, t + \delta'(\mathcal{K})]$ with the component \hat{x} of $\hat{\xi}$ by Claim 3.4(ii), since $\hat{\xi}(t, j) \in \hat{\mathcal{S}}_1 \setminus \{(0, F_s, 0, 1)\}$ and $\check{v}(\tau) > 0$ for all $\tau \in (t, t + \delta'(\mathcal{K})]$. Then, $\hat{v}(\tau, j(\tau)) \geq 0$ and $\hat{\phi}(\tau, j(\tau)) \geq F_s$ for all $\tau \in [t, t + \delta'(\mathcal{K})]$.

Evolution 3.9.3 (flow and jumps).

The only other possible evolution of $\hat{\xi}$ entails a jump in $\hat{\mathcal{D}}_\sigma$ for some $\tau_1 \in [t, t + \delta'(\mathcal{K})]$ such that $\hat{\sigma}(\tau_1, j) = 0$ (the solution $\hat{\xi}$ cannot jump in $\hat{\mathcal{D}}_v$ due to $\hat{b}(t, j) = 1$ and $\hat{b} = 0$ in (3.21d)). Since $[t, \tau_1] \subset [t, t + \delta'(\mathcal{K})]$, we know from Evolution 3.9.2 that $\hat{v}(\tau_1, j) \geq 0$ and $\hat{\phi}(\tau_1, j) \geq F_s$ if $\hat{\xi}$ flows in $\hat{\mathcal{C}}$ before jumping in $\hat{\mathcal{D}}_\sigma$. Then, by \hat{g}_σ in (3.21e), $\hat{\sigma}(\tau_1, j + 1) = \hat{\sigma}(\tau_1, j) = 0$, $\hat{\phi}(\tau_1, j + 1) = -\hat{\phi}(\tau_1, j) \leq -F_s$, $\hat{v}(\tau_1, j + 1) = \hat{v}(\tau_1, j) \geq 0$, $\hat{b}(\tau_1, j + 1) = -\hat{b}(\tau_1, j) = -1$. Define τ_2 as the time $\tau_2 \geq \tau_1$ such that

$$\hat{v}(\tau, j + 1) > 0 \text{ for all } \tau \in (\tau_1, \tau_2), \text{ and } \hat{v}(\tau_2, j + 1) = 0. \quad (3.68)$$

Note that $\tau_2 = \tau_1$ is not excluded, and indeed the solution $\hat{\xi}$ can only flow over (τ_1, τ_2) until the velocity becomes zero since, with $\hat{b}(\tau_1, j + 1) = -1$, jumps can only occur in $\hat{\mathcal{D}}_v$, where \hat{v} has to be 0.

Note also that from (3.68) that for all $\tau \in [\tau_1, \tau_2]$

$$\begin{aligned}\hat{\sigma}(\tau, j+1) &= \hat{\sigma}(\tau_1, j+1) + \int_{\tau_1}^{\tau} -k_i \hat{v}(\tilde{\tau}, j+1) d\tilde{\tau} \leq 0 \\ \hat{\phi}(\tau, j+1) &= \hat{\phi}(\tau_1, j+1) + \int_{\tau_1}^{\tau} (\hat{\sigma}(\tilde{\tau}, j+1) - k_p \hat{v}(\tilde{\tau}, j+1)) d\tilde{\tau} \\ &\leq \hat{\phi}(\tau_1, j+1) \leq -F_s,\end{aligned}$$

hence

$$\begin{aligned}\hat{v}(\tau_2, j+1) &= 0, \quad \hat{\sigma}(\tau_2, j+1) \leq 0, \\ \hat{\phi}(\tau_2, j+1) &\leq -F_s, \quad \begin{bmatrix} \hat{\sigma}(\tau_2, j+1) \\ \hat{\phi}(\tau_2, j+1) \end{bmatrix} \neq \begin{bmatrix} 0 \\ F_s \end{bmatrix}\end{aligned}\tag{3.69}$$

where $\begin{bmatrix} 0 \\ -F_s \end{bmatrix}$ does not need to be considered, similar to the reasoning as in Evolution 3.9.1.

We rule out the possibility that $\hat{\xi}$ flows from (3.69) at $(\tau_2, j+1)$. Indeed, if $\hat{\xi}$ would flow, Claim 3.4(iv) would imply that there exists some $T > 0$ such that the solution component \hat{x} coincides over $[\tau_2, \tau_2 + T]$ with the unique solution \tilde{x} to (3.16) with $\tilde{x}(\tau_2) = \hat{x}(\tau_2, j+1)$, which satisfies $\tilde{v}(\tau) < 0$ for all $\tau \in (\tau_2, \tau_2 + T]$. Such a flowing evolution, however, is not possible because the condition $\hat{b}\hat{v}\hat{\phi} \geq 0$ would be violated on $(\tau_2, \tau_2 + T]$ by shrinking T if needed. Then, the only possible evolution from (3.69) at $(\tau_2, j+1)$ is a jump in \hat{D}_v .

Now consider two cases for $\hat{\sigma}(\tau_2, j+1)$ in (3.69) by defining

$$\hat{\sigma}_{\text{th}} := \frac{F_s}{2} \frac{k_i}{k_p} > 0 \text{ and } \delta'' := \frac{F_s}{2\hat{\sigma}_{\text{th}}} = \frac{k_p}{k_i} > 0,\tag{3.70}$$

by Assumption 3.3.

Evolution 3.9.3.1 (two possible solutions)

First, consider $\hat{\sigma}(\tau_2, j+1) \in [-\hat{\sigma}_{\text{th}}, 0]$. By \hat{g}_v in (3.21e), $\hat{\sigma}(\tau_2, j+2) = \hat{\sigma}(\tau_2, j+1) \in [-\hat{\sigma}_{\text{th}}, 0]$, $\hat{\phi}(\tau_2, j+2) = \frac{k_p}{k_i} \hat{\sigma}(\tau_2, j+1) \in [-\frac{F_s}{2}, 0]$ and $\hat{b}(\tau_2, j+2) = 1$. If $\hat{\sigma}(\tau_2, j+2) = 0$, then the lemma is proven. Otherwise, no jump can occur over $[\tau_2, \tau_2 + \delta'']$ with δ'' in (3.70), and $\hat{v}(\tau, j+2) = 0$ for all $\tau \in [\tau_2, \tau_2 + \delta'']$. Then, $\hat{v}(\tau, j(\tau)) \geq 0$ for all $\tau \in [t, t + \delta'']$ (with $\tau_2 \geq t$ from before).

Evolution 3.9.3.2 (one possible solution)

Second, consider $\hat{\sigma}(\tau_2, j+1) \in (-\infty, -\hat{\sigma}_{\text{th}})$. Recall that $\hat{\sigma}(\tau_1, j+1) = 0$ and note that for all $\tau \in [\tau_1, \tau_2]$,

$$|\dot{\hat{\sigma}}(\tau, j+1)| \leq |\dot{\hat{x}}(\tau, j+1)| \leq |A|M + 2F_s,$$

from (3.21d) and by Lemma 3.8. Hence, from $\hat{\sigma}(\tau_2, j+1) = \hat{\sigma}(\tau_1, j+1) + \int_{\tau_1}^{\tau_2} \dot{\hat{\sigma}}(\tau, j+1) d\tau = \int_{\tau_1}^{\tau_2} \dot{\hat{\sigma}}(\tau, j+1) d\tau$, we have

$$|\hat{\sigma}(\tau_2, j+1)| \leq (|A|M + 2F_s)(\tau_2 - \tau_1).\tag{3.71}$$

Since $|\hat{\sigma}(\tau_2, j+1)| \geq \hat{\sigma}_{\text{th}}$ for $\hat{\sigma}(\tau_2, j+1) \in (-\infty, -\hat{\sigma}_{\text{th}})$, (3.71) implies

$$\begin{aligned} (|A|M + 2F_s)(\tau_2 - \tau_1) &\geq \hat{\sigma}_{\text{th}} \\ \iff \tau_2 - \tau_1 &> \frac{\hat{\sigma}_{\text{th}}}{|A|M + 2F_s} =: \delta'''(\mathcal{K}) > 0. \end{aligned}$$

Then, $\hat{v}(\tau, j(\tau)) \geq 0$ for all $\tau \in [t, \tau_1 + \delta'''(\mathcal{K})]$ (with $\tau_1 \geq t$ from before).

The proof is completed by selecting $\delta(\mathcal{K}) := \min\{\delta'(\mathcal{K}), \delta'', \delta'''(\mathcal{K})\}$.

3.A.6 Proof of Claim 3.18

We prove each item separately.

Item (i). (3.14) can be written as

$$\dot{\tilde{x}} = A\tilde{x} - e_3\mathbf{u}, \text{ with } |\mathbf{u}| \leq 2F_s, \quad (3.72)$$

where A is Hurwitz by Assumption 3.3 and bounded-input-bounded-output stability holds for (3.72). Then, for each $M > 0$ and $\tilde{x}_0 \in M\mathbb{B}$, there exist $\mathcal{M}(M)$ such that $|\tilde{x}(t)| \leq \mathcal{M}(M)$ for all $t \geq 0$. Define

$$\delta_0(M) := \frac{\varepsilon_v}{|A|\mathcal{M}(M) + 2F_s} > 0, \quad (3.73)$$

which is indeed uniform over the initial condition \hat{x}_0 . Then, (3.72) yields for $t \geq 0$

$$\begin{aligned} |\dot{\tilde{v}}(t)| &\leq |\dot{\tilde{x}}(t)| \leq |A||\tilde{x}(t)| + 2F_s \\ &\leq |A|\mathcal{M}(M) + 2F_s \leq \frac{\varepsilon_v}{\delta_0(M)}. \end{aligned} \quad (3.74)$$

So, (3.74) and $\tilde{v}(0) = 0$ imply that as long as $t \in [0, \delta_0(M)]$, it holds that $|\tilde{v}(t)| \leq \varepsilon_v$. By Assumption 3.2(iv), (3.14) boils down to the differential equation in (3.66) and solutions with the same initial condition coincide over $[0, \delta_0(M)]$.

Item (ii). Define $\check{\varphi} := \check{\phi} - F_s$ and rewrite (3.66) as

$$\begin{aligned} \begin{bmatrix} \dot{\check{\sigma}} \\ \dot{\check{\phi}} \\ \dot{\check{v}} \end{bmatrix} &= \begin{bmatrix} 0 & 0 & -k_i \\ 1 & 0 & -k_p \\ 0 & 1 & -k_d + L_2 \end{bmatrix} \begin{bmatrix} \check{\sigma} \\ \check{\phi} \\ \check{v} \end{bmatrix} \\ &=: A_{L_2}\check{x}. \end{aligned} \quad (3.75)$$

Expand the matrix exponential governing the solution to (3.75) from $\check{x}(0) = (\check{\sigma}_0, \check{\phi}_0, 0)$:

$$\check{\sigma}(t) = \check{\sigma}_0(1 + \mathcal{O}(t^3)) + \check{\varphi}_0(-\frac{k_i t^2}{2} + \mathcal{O}(t^3)), \quad (3.76a)$$

$$\check{\varphi}(t) = \check{\sigma}_0(t + \mathcal{O}(t^3)) + \check{\varphi}_0(1 - \frac{k_p t^2}{2} + \mathcal{O}(t^3)), \quad (3.76b)$$

$$\check{v}(t) = \check{\sigma}_0 \left(\frac{t^2}{2} + \mathcal{O}(t^3) \right) + \check{\varphi}_0 \left(t - \frac{(k_a - L_2)t^2}{2} + \mathcal{O}(t^3) \right), \quad (3.76c)$$

where $\mathcal{O}(t^3)$ denotes the terms of order t^3 or higher in the Taylor expansion, and $\check{\varphi}_0 \geq 0$ since $\check{\phi}_0 \geq F_s$ by (3.67). Based on (3.76b)-(3.76c), note that

$$\begin{aligned} \exists \delta_a > 0: \forall t \in (0, \delta_a] \quad t + \mathcal{O}(t^3) &> 0 \\ \exists \delta_b > 0: \forall t \in (0, \delta_b] \quad 1 - \frac{k_p t^2}{2} + \mathcal{O}(t^3) &> 0 \\ \exists \delta_c > 0: \forall t \in (0, \delta_c] \quad \frac{t^2}{2} + \mathcal{O}(t^3) &> 0 \\ \exists \delta_d > 0: \forall t \in (0, \delta_d] \quad t - \frac{(k_a - L_2)t^2}{2} + \mathcal{O}(t^3) &> 0, \end{aligned}$$

where $\delta_a, \dots, \delta_d$ do *not* depend on the initial condition $\check{\sigma}_0, \check{\varphi}_0$. Take $\delta_1 := \min\{\delta_a, \delta_b, \delta_c, \delta_d\} > 0$. Then, for $t \in (0, \delta_1]$, $\check{v}(t) > 0$ and $\check{\varphi}(t) > 0$ (since in (3.76) at least one among $\check{\sigma}_0$ and $\check{\varphi}_0$ is strictly positive and both are nonnegative by (3.67)), i.e., $\check{v}(t) > 0$ and $\check{\phi}(t) > F_s$.

3.A.7 Proof of Lemma 3.10

Suppose by contradiction that there exists a maximal solution $\hat{\xi}$ such that $\hat{\xi}(t', j') \notin \hat{\mathcal{A}}$ for all $(t', j') \in \text{dom } \hat{\xi}$, and $\sup_t \text{dom } \hat{\xi} = \bar{T} < +\infty$. Then, since solutions are complete by Lemma 3.6, $\sup_j \text{dom } \hat{\xi} = +\infty$. Because of the alternating sign of \hat{b} in the jump maps and jump sets in (3.21), we note that jumps in $\hat{\mathcal{D}}_\sigma$ and $\hat{\mathcal{D}}_v$ occur alternately. An infinite amount of jumps in $\hat{\mathcal{D}}$ yields then an infinite amount of jumps in $\hat{\mathcal{D}}_v$. Moreover, $\hat{\xi}$ is bounded by Lemma 3.8, so $\text{rge } \hat{\xi} \subset \mathcal{K}$ for some compact set \mathcal{K} , and for this compact set \mathcal{K} , Lemma 3.9 guarantees the existence of $\delta(\mathcal{K})$ and a certain dwell-time for $\hat{\xi}$. Because there are infinitely many jumps in $\hat{\mathcal{D}}_v$, there exists $(\tau, j-1) \in \text{dom } \hat{\xi}$ with $\tau \in [\bar{T} - \frac{\delta(\mathcal{K})}{2}, \bar{T}]$ such that $\hat{\xi}(\tau, j-1) \in \hat{\mathcal{D}}_v$. For the case $\hat{\xi}(\tau, j-1) \in \hat{\mathcal{D}}_v$ and $\hat{\sigma}(\tau, j-1) \geq 0$, we show now that $\hat{\xi}(t, j) \in \hat{\mathcal{S}}_1$ for some $t \geq \tau$. The case $\hat{\xi}(\tau, j-1) \in \hat{\mathcal{D}}_v$ and $\hat{\sigma}(\tau, j-1) \leq 0$ follows from parallel arguments. Indeed, $\hat{\xi}(\tau, j) = \hat{g}_v(\hat{\xi}(\tau, j-1))$ satisfies $\hat{\sigma}(\tau, j) \geq 0$, $\hat{v}(\tau, j) = 0$, $\hat{b}(\tau, j) = 1$ and $\hat{\phi}(\tau, j) = \frac{k_p}{k_i} \hat{\sigma}(\tau, j) \geq 0$. If $\hat{\phi}(\tau, j) \geq F_s$, then $\hat{\xi}(\tau, j) \in \hat{\mathcal{S}}_1$. If $\hat{\phi}(\tau, j) \in [0, F_s)$ and $\hat{\sigma}(\tau, j) > 0$, we have by Claim 3.4, item (iii) that $\hat{\phi}(\tau', j) = \sigma(\tau, j) > 0$ for all $\tau' \in [\tau, t] := [\tau, \tau + \frac{F_s - \hat{\phi}(\tau, j)}{\hat{\sigma}(\tau, j)}]$ so that $\hat{\phi}(t, j) = F_s$ and $\hat{\xi}(t, j) \in \hat{\mathcal{S}}_1$. Finally, $\hat{\phi}(\tau, j) \in [0, F_s)$, $\hat{\sigma}(\tau, j) = 0$ is not considered since $\hat{\xi}(t', j') \notin \hat{\mathcal{A}}$ for all $(t', j') \in \text{dom } \hat{\xi}$. We have then shown that $\hat{\xi}(t, j) \in \hat{\mathcal{S}}_1$ for some $t \geq \tau$, so the conclusions of Lemma 3.9 apply for $\hat{\xi}(t, j)$, and we show next that this leads to a contradiction of the fact that $\sup_t \text{dom } \hat{\xi} = \bar{T} < +\infty$. Evolution 3.9.1 given in the proof of Lemma 3.9 does not apply since $\hat{\xi}(t', j') \notin \hat{\mathcal{A}}$ for all $(t', j') \in \text{dom } \hat{\xi}$ by assumption. Evolution 3.9.2 given in the proof of Lemma 3.9 implies that $\hat{\xi}$ flows over $[t, t + \delta(\mathcal{K})] \times \{j\}$ and since $t + \delta(\mathcal{K}) \geq \tau + \delta(\mathcal{K}) \geq \bar{T} + \frac{\delta(\mathcal{K})}{2}$, we have a

contradiction. Evolution 3.9.3.1 given in the proof of Lemma 3.9 implies for the only relevant solution (with $\hat{\xi}(t', j') \notin \hat{\mathcal{A}}$ for all $(t', j') \in \text{dom } \hat{\xi}$) that $\hat{\xi}$ flows over $[\tau_2, \tau_2 + \delta(\mathcal{K})] \times \{j + 2\}$ with $\tau_2 \geq t$ and, by the same argument as above, we have a contradiction. Evolution 3.9.3.2 given in the proof of Lemma 3.9 implies that $\hat{\xi}$ flows over $[\tau_1, \tau_1 + \delta(\mathcal{K})] \times \{j + 1\}$ with $\tau_1 \geq t$ and, by the same argument as above, we have a contradiction. Hence, the solution $\hat{\xi}$ exhibits an infinite amount of flow and satisfies $\sup_t \text{dom } \hat{\xi} = +\infty$.

3.A.8 Proof of Lemma 3.11

The proof of this lemma is structured in two parts. Part A shows that (3.25) holds when the timer τ is discarded (as well as its corresponding flow/jump equations and conditions in flow/jump maps). Part A entails defining an auxiliary hybrid system *without the timer* as in (3.78) below, and then proving Claim 3.19. Part B shows that (3.25) still holds when the timer τ is considered, due to the intrinsic dwell time of each solution $\hat{\xi}$ proven in Lemma 3.9. Part B proves then the statement of this lemma. Note also that in both the lemma and the auxiliary Claim 3.19, the statements need to be proven only for all $t \geq 0$ such that $\hat{\xi}$ does *not* belong to $\hat{\mathcal{A}}$, since the set $\hat{\mathcal{A}}$ is strongly forward invariant as per Lemma 3.7.

Part A: the timer τ is discarded

Consider the following auxiliary hybrid system \mathcal{H} that corresponds simply to discarding in \mathcal{H}_δ the timer τ , its corresponding flow/jump equations and conditions in flow/jump maps. The overall state vector of \mathcal{H} is

$$\begin{aligned} \zeta &:= (\sigma, \phi, v, b, q) \in Z, \\ Z &:= \{\mathbb{R}^3 \times \{-1, 1\} \times \{-1, 0, 1\} : \\ &\quad qv \geq 0, bq\sigma \geq 0, \sigma\phi \geq \frac{k_p}{k_i}\sigma^2, bq\phi \geq 0\}. \end{aligned} \quad (3.78a)$$

\mathcal{H} is defined as

$$\mathcal{H}: \begin{cases} \dot{\zeta} = F(\zeta), & \zeta \in C_{\text{slip}} \cup C_{\text{stick}}, \\ \zeta^+ \in \bigcup_{p \in \{\sigma, v, 1, -1, 0\} : \zeta \in D_p} \{\gamma_p(\zeta)\}, & \zeta \in \bigcup_{p \in \{\sigma, v, 1, -1, 0\}} D_p. \end{cases} \quad (3.78b)$$

$$(3.78c)$$

The flow map of \mathcal{H} is given by

$$F(\zeta) := \begin{bmatrix} -k_i v \\ \sigma - k_p v \\ -k_d v + |q|\phi - q(F_s - h(v)) \\ 0 \\ 0 \end{bmatrix}. \quad (3.78d)$$

The jump maps are given by

$$\begin{aligned}
\gamma_\sigma(\zeta) &:= [\sigma \quad -\phi \quad v \quad -b \quad q]^\top, \\
\gamma_v(\zeta) &:= \left[\sigma \quad \frac{k_p}{k_i} \sigma \quad v \quad -b \quad q \right]^\top, \\
\gamma_1(\zeta) &:= [\sigma \quad \phi \quad v \quad b \quad 1]^\top, \\
\gamma_{-1}(\zeta) &:= [\sigma \quad \phi \quad v \quad b \quad -1]^\top, \\
\gamma_0(\zeta) &:= [\sigma \quad \phi \quad v \quad b \quad 0]^\top.
\end{aligned} \tag{3.78e}$$

The flow and jump sets are defined as

$$\begin{aligned}
C_{\text{slip}} &:= \{\zeta \in Z : |q| = 1\} \\
C_{\text{stick}} &:= \{\zeta \in Z : q = 0, v = 0, |\phi| \leq F_s\} \\
D_\sigma &:= \{\zeta \in Z : |q| = 1, \sigma = 0, b = 1\}, \\
D_v &:= \{\zeta \in Z : q = 0, v = 0, b = -1\}, \\
D_1 &:= \{\zeta \in Z : q = 0, v = 0, \phi \geq F_s, b = 1\}, \\
D_{-1} &:= \{\zeta \in Z : q = 0, v = 0, \phi \leq -F_s, b = 1\}, \\
D_0 &:= \{\zeta \in Z : |q| = 1, v = 0\},
\end{aligned} \tag{3.78f}$$

and, finally,

$$\begin{aligned}
C &:= C_{\text{slip}} \cup C_{\text{stick}}, \\
D &:= D_\sigma \cup D_v \cup D_1 \cup D_{-1} \cup D_0.
\end{aligned} \tag{3.78g}$$

Based on the auxiliary hybrid system in (3.78), consider the next intermediate claim.

Claim 3.19. *For each solution $\hat{\xi} = (\hat{\sigma}, \hat{\phi}, \hat{v}, \hat{b}) \in \mathcal{S}_{\hat{\mathcal{H}}}$ with $\hat{\xi}(0, 0) = \hat{\xi}_0 \in \hat{\mathcal{C}} \cup \hat{\mathcal{D}}$, there exists q_0 such that, for some solution $\zeta = (\sigma, \phi, v, b, q) \in \mathcal{S}_{\mathcal{H}}((\hat{\xi}_0, q_0))$, for all $t \geq 0$ such that $\hat{\xi}(t, j(t)) \notin \hat{\mathcal{A}}$, (3.25) holds.*

Proof. For each solution $\hat{\xi}$ to (3.21), we are going to construct a suitable hybrid signal q such that $(\hat{\xi}, q)$ is a solution ζ to \mathcal{H} in (3.78) (as in [63, Def. 2.6 and p. 124]) for all $t \geq 0$ such that $\hat{\xi}(t, j(t)) \notin \hat{\mathcal{A}}$ and modulo a reparametrization of the jump counter of $\hat{\xi}$ (yielding possibly different $j_\xi(t)$ and $j_{\hat{\xi}}(t)$ for the same $t \geq 0$). Then, (3.25) holds by construction.

Each solution $\hat{\xi}$ to (3.21) can only flow in $\hat{\mathcal{C}}$, jump in $\hat{\mathcal{D}}_\sigma$ or jump in $\hat{\mathcal{D}}_v$, and in each of these three cases the definition of solution in [63, Def. 2.6 and p. 124] implies the following. If $\hat{\xi}$ flows in $\hat{\mathcal{C}}$, for each $j \in \mathbb{Z}_{\geq 0}$ such that $I^j := \{t :$

$(t, j) \in \text{dom } \hat{\xi}\}$ has nonempty interior,

$$\left. \begin{aligned} \hat{b}(t, j)\hat{v}(t, j)\hat{\sigma}(t, j) &\geq 0 \\ \hat{\sigma}(t, j)\hat{\phi}(t, j) &\geq \frac{k_p}{k_i}\hat{\sigma}(t, j)^2 \\ \hat{b}(t, j)\hat{v}(t, j)\hat{\phi}(t, j) &\geq 0 \end{aligned} \right\} \text{ for all } t \in I^j; \quad (3.79a)$$

$$\hat{\xi}(t, j) \in \hat{\mathcal{F}}(\hat{\xi}(t, j)) \text{ for almost all } t \in I^j. \quad (3.79b)$$

If $\hat{\xi}$ jumps in $\hat{\mathcal{D}}_\sigma$, for each $(t, j) \in \text{dom } \hat{\xi}$ such that $(t, j+1) \in \text{dom } \hat{\xi}$,

$$\hat{\sigma}(t, j) = 0, \quad \hat{b}(t, j) = 1, \quad \hat{v}(t, j)\hat{\phi}(t, j) \geq 0; \quad (3.80a)$$

$$\hat{\sigma}(t, j+1) = \hat{\sigma}(t, j), \quad \hat{\phi}(t, j+1) = -\hat{\phi}(t, j), \quad (3.80b)$$

$$\hat{v}(t, j+1) = \hat{v}(t, j), \quad \hat{b}(t, j+1) = -\hat{b}(t, j).$$

If $\hat{\xi}$ jumps in $\hat{\mathcal{D}}_v$, for each $(t, j) \in \text{dom } \hat{\xi}$ such that $(t, j+1) \in \text{dom } \hat{\xi}$,

$$\hat{v}(t, j) = 0, \quad \hat{\sigma}(t, j)\hat{\phi}(t, j) \geq \frac{k_p}{k_i}\hat{\sigma}(t, j)^2, \quad \hat{b}(t, j) = -1; \quad (3.81a)$$

$$\hat{\sigma}(t, j+1) = \hat{\sigma}(t, j), \quad \hat{\phi}(t, j+1) = \frac{k_p}{k_i}\hat{\sigma}(t, j), \quad (3.81b)$$

$$\hat{v}(t, j+1) = \hat{v}(t, j), \quad \hat{b}(t, j+1) = -\hat{b}(t, j).$$

Let us then consider the construction of the suitable hybrid signal q starting from time $(0, 0)$ and separately in these three cases (3.79), (3.80), (3.81).

Suppose $\hat{\xi}$ flows in $\hat{\mathcal{C}}$ on the interval $I^0 =: [t_0, t_1] = [0, t_1]$ with $t_1 > 0$. Note that for each $\hat{\xi} \in \hat{\Xi}$, $\hat{\mathcal{F}}(\hat{\xi}) = \left[\hat{\mathcal{F}}_x(\hat{x}) \right]$, and the evolution according to $\hat{\mathcal{F}}_x$ is determined in Claim 3.4(ii)-(iv). For convenience, we report the cases (3.11)-(3.13) here as

$$\begin{aligned} S_1 := \{ \hat{x} \in \mathbb{R}^3 : (\hat{v} > 0) \vee (\hat{v} = 0 \wedge \hat{\phi} > F_s) \\ \vee (\hat{v} = 0 \wedge \hat{\phi} = F_s \wedge \hat{\sigma} > 0) \}, \end{aligned} \quad (3.82)$$

$$\begin{aligned} S_0 := \{ \hat{x} \in \mathbb{R}^3 : (\hat{v} = 0 \wedge \hat{\sigma} > 0 \wedge \hat{\phi} \in [-F_s, F_s]) \}, \\ \vee (\hat{v} = 0 \wedge \hat{\sigma} = 0 \wedge \hat{\phi} \in [-F_s, F_s]) \\ \vee (\hat{v} = 0 \wedge \hat{\sigma} < 0 \wedge \hat{\phi} \in (-F_s, F_s]) \} \end{aligned} \quad (3.83)$$

$$\begin{aligned} S_{-1} := \{ \hat{x} \in \mathbb{R}^3 : (\hat{v} < 0) \vee (\hat{v} = 0 \wedge \hat{\phi} < -F_s) \\ \vee (\hat{v} = 0 \wedge \hat{\phi} = -F_s \wedge \hat{\sigma} < 0) \}. \end{aligned} \quad (3.84)$$

Note that S_1, S_0, S_{-1} form a partition of \mathbb{R}^3 (i.e., $\cup_{i \in \{1, 0, -1\}} S_i = \mathbb{R}^3$ and $S_i \cap S_k = \emptyset$ for each $i, k \in \{1, 0, -1\}$ with $i \neq k$). For $\hat{\xi}(0, 0) = (\hat{x}(0, 0), \hat{b}(0, 0))$,

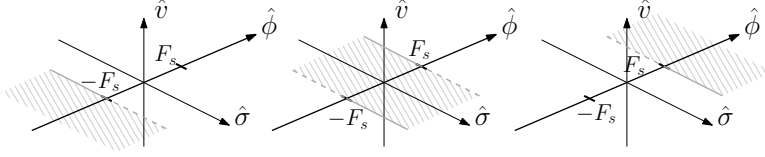


Figure 3.10. Intersections of the sets S_{-1} , S_0 , S_1 with $\{\hat{x} \in \mathbb{R}^3: \hat{v} = 0\}$. Solid and dashed lines at the boundary of each set mean respectively that those points belong and do not belong to that set.

assign $q(0,0)$ as 1, 0, -1 if $\hat{x}(0,0)$ belongs respectively to S_1 , S_0 , S_{-1} . Consider t_1^* as the smallest time in $(0, t_1]$ ($t_1^* > 0$ by Claim 3.4) such that

$$t_1^* = t_1, \quad \hat{x}(t,0) \in S_{q(0,0)} \forall t \in [0, t_1^*], \quad \text{or} \quad (3.85a)$$

$$t_1^* < t_1, \quad \hat{x}(t,0) \in S_{q(0,0)} \forall t \in [0, t_1^*), \hat{x}(t_1^*,0) \notin S_{q(0,0)}. \quad (3.85b)$$

Note that no other cases than (3.85a)-(3.85b) need considering since solutions are locally absolutely continuous during flow by [63, Def. 2.4]. Hence, the solutions need to hit the set $\{\hat{x} \in \mathbb{R}^3: \hat{v} = 0\}$ to traverse from S_i to S_k (with $i, k \in \{1, 0, -1\}$ and $i \neq k$). The intersections of the sets S_{-1} , S_0 , S_1 with $\{\hat{x} \in \mathbb{R}^3: \hat{v} = 0\}$ are visualized in Figure 3.10.

Define $q(t,0) = q(0,0)$ for all $t \in [0, t_1^*]$. We show now that, under (3.79),

$$(\hat{\xi}(t,0), q(t,0)) \in C_{\text{slip}} \cup C_{\text{stick}} \quad \text{for all } t \in [0, t_1^*] \quad (3.86a)$$

$$\begin{bmatrix} \dot{\hat{\xi}}(t,0) \\ \dot{q}(t,0) \end{bmatrix} = F \left(\begin{bmatrix} \hat{\xi}(t,0) \\ q(t,0) \end{bmatrix} \right) \quad \text{for almost all } t \in [0, t_1^*]. \quad (3.86b)$$

Indeed, consider separately the cases $q(0,0)$ equal to 1, 0, -1 and note that by the definition of t_1^* in (3.85), they imply respectively that $v(t,0)$ is nonnegative, zero, nonpositive for all $t \in [0, t_1^*]$. As for $q(0,0) = 1$, we have that for all $t \in [0, t_1^*]$, $q(t,0) = 1$ by our construction, $\hat{v}(t,0) \geq 0$ by the definition of t_1^* in (3.85), $\hat{b}(t,0)q(t,0)\hat{\sigma}(t,0) \geq 0$, $\hat{\sigma}(t,0)\hat{\phi}(t,0) \geq \frac{k_p}{k_i}\hat{\sigma}(t,0)^2$, and $\hat{b}(t,0)q(t,0)\hat{\phi}(t,0) \geq 0$ by (3.79a) and the first two relationships. Then, for all $t \in [0, t_1^*]$, $(\hat{\xi}(t,0), q(t,0)) \in C_{\text{slip}}$ in (3.78f), so (3.86a) holds true. Moreover, (3.79b) and Claim 3.4(ii) yield that for almost all $t \in [0, t_1^*]$

$$\begin{aligned} \dot{\hat{x}}(t,0) &= A\hat{x}(t,0) - e_3(F_s - f(\hat{v}(t,0))) \\ \dot{\hat{b}}(t,0) &= 0, \end{aligned}$$

so that for almost all $t \in [0, t_1^*]$

$$\begin{bmatrix} \dot{\hat{\xi}}(t,0) \\ \dot{q}(t,0) \end{bmatrix} = \begin{bmatrix} -k_i\hat{v}(t,0) \\ \hat{\sigma}(t,0) - k_p\hat{v}(t,0) \\ -k_d\hat{v}(t,0) + \hat{\phi}(t,0) - (F_s - f(\hat{v}(t,0))) \\ 0 \end{bmatrix} = F \left(\begin{bmatrix} \hat{\xi}(t,0) \\ q(t,0) \end{bmatrix} \right)$$

and (3.86b) holds true as well. As for $q(0, 0) = 0$, we have that for all $t \in [0, t_1^*]$, $q(t, 0) = 0$ by our construction, $\hat{v}(t, 0) = 0$ and $|\hat{\phi}(t, 0)| \leq F_s$ by the definition of t_1^* in (3.85), $\hat{\sigma}(t, 0)\hat{\phi}(t, 0) \geq \frac{k_p}{k_i}\hat{\sigma}(t, 0)^2$ by (3.79a). Then, for all $t \in [0, t_1^*]$, $(\hat{\xi}(t, 0), q(t, 0)) \in C_{\text{stick}}$ in (3.78f), so (3.86a) holds true. Moreover, (3.79b) and Claim 3.4(iii) yield that for almost all $t \in [0, t_1^*]$, $\hat{x}(t, 0) = \begin{bmatrix} \hat{\sigma}(t, 0) \\ 0 \end{bmatrix}$ and $\hat{b}(t, 0) = 0$, so that for almost all $t \in [0, t_1^*]$, $\begin{bmatrix} \hat{\xi}(t, 0) \\ q(t, 0) \end{bmatrix} = F \left(\begin{bmatrix} \hat{\xi}(t, 0) \\ q(t, 0) \end{bmatrix} \right)$, and (3.86b) holds true as well. As for $q(0, 0) = -1$, we follow similar steps to $q(0, 0) = 1$.

We now show that given $q(t_1^*, 0)$ and $\hat{x}(t_1^*, 0)$ and if $t_1^* < t_1$ as in (3.85b) (this analysis is indeed not needed if (3.85a) holds), we can select q so that $(\hat{\xi}, q)$ jumps in D_1 , D_0 or D_{-1} . Consider all the following possible cases, whereby we note that, e.g., $q(t_1^*, 0) = 1$ and $\hat{x}(t_1^*, 0) \in S_1$ is not a case to consider by the definition of t_1^* in (3.85b).

As for $q(t_1^*, 0) = 1$ and $\hat{x}(t_1^*, 0) \in S_0$, $\begin{bmatrix} \hat{\xi}(t_1^*, 0) \\ q(t_1^*, 0) \end{bmatrix} \in D_0$ since for all $t \in [0, t_1^*]$, $\hat{x}(t, 0) \in S_1$, hence we can deduce $\hat{b}(t, 0)\hat{\sigma}(t, 0) \geq 0$, $\hat{\sigma}(t, 0)\hat{\phi}(t, 0) \geq \frac{k_p}{k_i}\hat{\sigma}(t, 0)^2$, and $\hat{b}(t, 0)\hat{\phi}(t, 0) \geq 0$ from (3.79a). Moreover, $\begin{bmatrix} \xi(t_1^*, 1) \\ q(t_1^*, 1) \end{bmatrix} = \gamma_0 \left(\begin{bmatrix} \hat{\xi}(t_1^*, 0) \\ q(t_1^*, 0) \end{bmatrix} \right) = \begin{bmatrix} \hat{\xi}(t_1^*, 0) \\ 0 \end{bmatrix}$, where we note that both $(t_1^*, 0)$ and $(t_1^*, 1)$ belong to $\text{dom } \xi = \text{dom } q$ whereas $(t_1^*, 1)$ does *not* belong to $\text{dom } \hat{\xi}$, and this corresponds to the necessary reparameterization of the jump counter of $\hat{\xi}$ mentioned at the beginning of the proof of the claim. Parallel arguments hold in the case $q(t_1^*, 0) = -1$ and $\hat{x}(t_1^*, 0) \in S_0$.

As for $q(t_1^*, 0) = 0$ and $\hat{x}(t_1^*, 0) \in S_1$, the definition of t_1^* in (3.85b), $\hat{x}(t_1^*, 0) \in S_1$ and $q(t_1^*, 0) = 0$, and the local absolute continuity of solutions [63, Def. 2.4] imply that $\hat{v}(t_1^*, 0) = 0$ and $\hat{\phi}(t_1^*, 0) = F_s$. The latter implies $\hat{\sigma}(t_1^*, 0) \geq 0$ from $\hat{\sigma}(t_1^*, 0)\hat{\phi}(t_1^*, 0) \geq \frac{k_p}{k_i}\hat{\sigma}(t_1^*, 0)^2 \geq 0$ in (3.79a). Moreover, $\hat{x}(t_1^*, 0) \in S_1$ implies $\hat{b}(t_1^*, 0) = 1$ from the fact that $\hat{\xi}$ flows on $[0, t_1]$ with $t_1 > t_1^*$, and the condition $\hat{b}\hat{v}\hat{\phi} \geq 0$ in (3.79a) (since $\hat{\phi}(t_1^*, 0) = F_s$ and $\hat{v}(t, 0) > 0$ for all $t \in (t_1^*, t_1^* + T']$ for some $T' > 0$ by Claim 3.4(ii), the condition $\hat{b}\hat{v}\hat{\phi} \geq 0$ gives $\hat{b} = 1$). We have then $\begin{bmatrix} \hat{\xi}(t_1^*, 0) \\ q(t_1^*, 0) \end{bmatrix} \in D_1$ since $q(t_1^*, 0) = 0$ in this case, $\hat{v}(t_1^*, 0) = 0$ and $\hat{\phi}(t_1^*, 0) = F_s$ (as motivated above), $\hat{\sigma}(t_1^*, 0)\hat{\phi}(t_1^*, 0) \geq \frac{k_p}{k_i}\hat{\sigma}(t_1^*, 0)^2$ (by (3.79a)) and $\hat{b}(t_1^*, 0) = 1$ (as just motivated). Moreover, $\begin{bmatrix} \xi(t_1^*, 1) \\ q(t_1^*, 1) \end{bmatrix} = \gamma_1 \left(\begin{bmatrix} \hat{\xi}(t_1^*, 0) \\ q(t_1^*, 0) \end{bmatrix} \right) = \begin{bmatrix} \hat{\xi}(t_1^*, 0) \\ 1 \end{bmatrix}$. Parallel arguments hold in the case $q(t_1^*, 0) = 0$ and $\hat{x}(t_1^*, 0) \in S_{-1}$.

As for $q(t_1^*, 0) = -1$ and $\hat{x}(t_1^*, 0) \in S_1$, $\begin{bmatrix} \hat{\xi}(t_1^*, 0) \\ q(t_1^*, 0) \end{bmatrix} \in D_0$ since for all $t \in [0, t_1^*]$, $\hat{x}(t, 0) \in S_{-1}$, hence we can deduce $\hat{b}(t, 0)\hat{\sigma}(t, 0) \leq 0$, $\hat{\sigma}(t, 0)\hat{\phi}(t, 0) \geq \frac{k_p}{k_i}\hat{\sigma}(t, 0)^2$, and $\hat{b}(t, 0)\hat{\phi}(t, 0) \leq 0$ from (3.79a). It also holds $\begin{bmatrix} \xi(t_1^*, 1) \\ q(t_1^*, 1) \end{bmatrix} = \gamma_0 \left(\begin{bmatrix} \hat{\xi}(t_1^*, 0) \\ q(t_1^*, 0) \end{bmatrix} \right) = \begin{bmatrix} \hat{\xi}(t_1^*, 0) \\ 0 \end{bmatrix}$. Similarly to the previous case $q(t_1^*, 0) = 0$ and $\hat{x}(t_1^*, 0) \in S_1$, we have

$\hat{v}(t_1^*, 0) = 0$ and $\hat{\phi}(t_1^*, 0) \geq F_s$. $\hat{x}(t_1^*, 0) \in S_1$ and $\hat{\phi}(t_1^*, 0) > F_s$ imply again $\hat{b}(t_1^*, 0) = 1$ from the fact that $\hat{\xi}$ flows on $[0, t_1^*]$ with $t_1 > t_1^*$, and the condition $\hat{b}\hat{v}\hat{\phi} \geq 0$ in (3.79a). Hence, $\left[\begin{smallmatrix} \hat{\xi}(t_1^*, 1) \\ q(t_1^*, 1) \end{smallmatrix} \right] \in D_1$ and $\left[\begin{smallmatrix} \hat{\xi}(t_1^*, 2) \\ q(t_1^*, 2) \end{smallmatrix} \right] = \gamma_1\left(\left[\begin{smallmatrix} \hat{\xi}(t_1^*, 1) \\ q(t_1^*, 1) \end{smallmatrix} \right]\right) = \left[\begin{smallmatrix} \hat{\xi}(t_1^*, 0) \\ 1 \end{smallmatrix} \right]$. Parallel arguments hold in the case $q(t_1^*, 0) = 1$ and $\hat{x}(t_1^*, 0) \in S_{-1}$. This concludes the examination of all possible cases. It is then sufficient to repeat the reasoning presented for a flow on $[0, t_1^*]$ and the reasoning presented for jumps in D_1, D_0, D_{-1} to cover the whole interval I^0 by identifying possibly t_2^*, t_3^* , etc.

Suppose $\hat{\xi}$ jumps in \hat{D}_σ at $(0, 0)$. We make the following observation. If $\hat{\xi}$ jumps in \hat{D}_σ , $\hat{b}(0, 1) = -1$ so it cannot jump in \hat{D}_σ at $(0, 1)$. If $\hat{\xi}$ jumps in \hat{D}_v at $(0, 1)$, then $\hat{v}(0, 2) = \hat{v}(0, 1) = 0$ (otherwise a jump in \hat{D}_v cannot occur), $\hat{\sigma}(0, 2) = \hat{\sigma}(0, 1) = \hat{\sigma}(0, 0) = 0$ (otherwise a jump in \hat{D}_σ could not have occurred) and $\hat{\phi}(0, 2) = \frac{k_p}{k_i}\hat{\sigma}(0, 1) = 0$ due to \hat{g}_v in (3.21e). Then, two consecutive jumps in \hat{D}_σ and \hat{D}_v are such that $\hat{\xi}(0, 2) \in \hat{A}$ and we do not need to prove anything in this case due to Lemma 3.7.

Based on this observation, the only case to consider is when $\hat{\xi}$ (which is complete by Lemma 3.6) flows in \hat{C} after the jump in \hat{D}_σ . If $\hat{x}(0, 1) \in S_1$, $\hat{v}(0, 1) = \hat{v}(0, 0) \geq 0$ and we need $q(0, 1)$ to be 1. This is achieved by selecting $q(0, 0) = 1$. Since $|q(0, 0)| = 1$, $q(0, 0)\hat{v}(0, 0) \geq 0$, $\hat{\sigma}(0, 0) = 0$ and $\hat{b}(0, 0) = 1$ (the last two by (3.80a)), $\left[\begin{smallmatrix} \hat{\xi}(0, 0) \\ q(0, 0) \end{smallmatrix} \right] \in D_\sigma$ and $\left[\begin{smallmatrix} \hat{\xi}(0, 1) \\ q(0, 1) \end{smallmatrix} \right] = \gamma_\sigma\left(\left[\begin{smallmatrix} \hat{\xi}(0, 0) \\ q(0, 0) \end{smallmatrix} \right]\right)$ because the first four components of γ_σ in (3.78e) coincide with \hat{g}_σ in (3.21e), and $q(0, 1) = q(0, 0) = 1$ as needed. If $\hat{x}(0, 1) \in S_{-1}$, parallel arguments yield the same conclusion by selecting $q(0, 0) = -1$. If $\hat{x}(0, 1) \in S_0$, $\hat{v}(0, 1) = \hat{v}(0, 0) = 0$ and $|\hat{\phi}(0, 1)| \leq F_s$. Since $\hat{\sigma}(0, 1) = 0$, $\hat{\xi}(0, 1) \in \hat{A}$ and we do not need to prove anything in this case.

Suppose $\hat{\xi}$ jumps in \hat{D}_v at $(0, 0)$. As noted for the case of $\hat{\xi}$ jumping in \hat{D}_σ , $\hat{\xi}(0, 1)$ cannot jump in \hat{D}_v again and if it jumps in \hat{D}_σ , $\hat{\xi}(0, 2) \in \hat{A}$. Then, the only case to consider is when $\hat{\xi}$, which is complete by Lemma 3.6, flows in \hat{C} after the jump in \hat{D}_v . Then, $\hat{\xi}$ flows in either S_0, S_1 , or S_{-1} , depending on $\hat{\sigma}(0, 1)$, and in all cases we select $q(0, 0) = 0$ in order jump in the corresponding D_v in (3.78f). If $\hat{x}(0, 1) \in S_0$, we need $q(0, 1)$ to be 0. Since $q(0, 0) = 0$, $\hat{v}(0, 0) = 0$, $\hat{\sigma}(0, 0)\hat{\phi}(0, 0) \geq \frac{k_p}{k_i}\hat{\sigma}(0, 0)^2$, $\hat{b}(0, 0) = -1$ (the last three by (3.81a)), $\left[\begin{smallmatrix} \hat{\xi}(0, 0) \\ q(0, 0) \end{smallmatrix} \right] \in D_v$ and $\left[\begin{smallmatrix} \hat{\xi}(0, 1) \\ q(0, 1) \end{smallmatrix} \right] = \gamma_v\left(\left[\begin{smallmatrix} \hat{\xi}(0, 0) \\ q(0, 0) \end{smallmatrix} \right]\right)$ because the first four components of γ_v coincide with \hat{g}_v in (3.21e) and $q(0, 1) = q(0, 0) = 0$ as needed. If $\hat{x}(0, 1) \in S_1$, we need $q(0, 2)$ to be 1, which is achieved by jumping additionally in D_1 . Indeed, we have $q(0, 1) = 0$, $\hat{v}(0, 1) = 0$, $\hat{\sigma}(0, 1)\hat{\phi}(0, 1) = \frac{k_p}{k_i}\hat{\sigma}(0, 1)^2$ (because $\hat{\phi}(0, 1) = \frac{k_p}{k_i}\hat{\sigma}(0, 0)$ and $\hat{\sigma}(0, 1) = \hat{\sigma}(0, 0)$), $\hat{\phi}(0, 1) \geq F_s$ (because $\hat{x}(0, 1) \in \hat{S}_1$), and $\hat{b}(0, 1) = -\hat{b}(0, 0) = 1$ so that $\left[\begin{smallmatrix} \hat{\xi}(0, 1) \\ q(0, 1) \end{smallmatrix} \right] \in D_1$ and $\left[\begin{smallmatrix} \hat{\xi}(0, 2) \\ q(0, 2) \end{smallmatrix} \right] = \gamma_1\left(\left[\begin{smallmatrix} \hat{\xi}(0, 1) \\ q(0, 1) \end{smallmatrix} \right]\right) =$

$\left[\hat{\xi}_1^{(0,1)} \right]$ with $q(0, 2) = 1$ as needed. The case $\hat{x}(0, 1) \in S_{-1}$ follows from parallel arguments.

Up to now, we have shown that if $\hat{\xi}$ flows in $\hat{\mathcal{C}}$, jumps in $\hat{\mathcal{D}}_\sigma$ or jumps in $\hat{\mathcal{D}}_v$ at $(0, 0)$, then the hybrid signal q can be selected suitably. Based on the same observation at the beginning of the cases of a jump in $\hat{\mathcal{D}}_\sigma$ or $\hat{\mathcal{D}}_v$ at $(0, 0)$, we can discard in the proof without loss of generality the cases of two consecutive jumps in $\hat{\mathcal{D}}_\sigma$ and $\hat{\mathcal{D}}_v$, or in $\hat{\mathcal{D}}_v$ and $\hat{\mathcal{D}}_\sigma$, since after these two jumps, $\hat{\xi}$ would belong to $\hat{\mathcal{A}}$. For the proof, this implies that each jump in $\hat{\mathcal{D}}_\sigma$ or in $\hat{\mathcal{D}}_v$ is preceded (except at $(0, 0)$, which we have already addressed) and followed by a flow in $\hat{\mathcal{C}}$. In the latter case, we have already shown how to select q so that the appropriate flow for $(\hat{\xi}, q)$ occurs in \mathcal{H} . So, if we show that, regardless of the selection of q dictated by the preceding flow (the former case), a jump in D_σ or in D_v for $(\hat{\xi}, q)$ can be achieved, then the procedure outlined for $\hat{\xi}$ flowing in $\hat{\mathcal{C}}$, jumping in $\hat{\mathcal{D}}_\sigma$ or in $\hat{\mathcal{D}}_v$ at $(0, 0)$, can be easily extended for all $t \geq 0$ such that $\hat{\xi}(t, j(t)) \notin \hat{\mathcal{A}}$ and the proof of the claim is complete. So, we show this last point, i.e., that regardless of the selection of q dictated by the preceding flow, a jump in D_σ or in D_v for $(\hat{\xi}, q)$ can be achieved.

Suppose $\hat{\xi}$ jumps in $\hat{\mathcal{D}}_\sigma$ at (t, j) after a flow in $\hat{\mathcal{C}}$. Note that because of the extra jumps in D_1, D_0, D_{-1} that have appeared so far, we may need to reparametrize the jump counter as follows. For each $(t, j) \in \text{dom } \hat{\xi}$, there exist $j^* \geq 0$ such that $(t, j + j^*) \in \text{dom } q$. If $|q(t, j + j^*)| = 1$ from the preceding flow, a jump in D_σ is achieved since $|q(t, j + j^*)| = 1, \hat{\sigma}(t, j) = 0$, and $\hat{b}(t, j) = 1$ (both by (3.80a)), $q(t, j + j^*)\hat{v}(t, j) \geq 0$ and $q(t, j + j^*)\hat{\phi}(t, j) \geq 0$ (both since $(\hat{\xi}, q)$ flowed in C_{slip}). If $q(t, j + j^*) = 0$ from the preceding flow, $(\hat{\xi}, q)$ flowed in C_{stick} so $\hat{v}(t, j) = 0$ and $|\hat{\phi}(t, j)| \leq F_s$. These two conditions together with $\hat{\sigma}(t, j) = 0$ (by (3.80a)), imply that $\hat{\xi}(t, j) \in \hat{\mathcal{A}}$ so there is nothing to check.

Suppose $\hat{\xi}$ jumps in $\hat{\mathcal{D}}_v$ at (t, j) after a flow in $\hat{\mathcal{C}}$. Adopt the same jump reparametrization through j^* described for a jump in $\hat{\mathcal{D}}_\sigma$. If $q(t, j + j^*) = 0$ from the preceding flow, a jump in D_v is achieved thanks to (3.81a). If $|q(t, j + j^*)| = 1$ from the preceding flow, $(\hat{\xi}, q)$ flowed in C_{slip} so that

$$\begin{aligned} \hat{b}(t, j)q(t, j + j^*)\hat{\sigma}(t, j) &\geq 0, \\ \hat{\sigma}(t, j)\hat{\phi}(t, j) &\geq \frac{k_p}{k_i}\hat{\sigma}(t, j)^2, \\ \hat{b}(t, j)q(t, j + j^*)\hat{\phi}(t, j) &\geq 0. \end{aligned} \tag{3.87}$$

Then, a jump in D_0 is possible since $|q(t, j + j^*)| = 1, \hat{v}(t, j) = 0$ (by (3.81a)) and (3.87) holds since $(\hat{\xi}, q)$ flowed in C_{slip} . By jumping in D_0 , $\hat{\xi}$ does not change and $q(t, j + j^* + 1) = 0$ so that we fall back to the case $q(t, j + j^*) = 0$ just analyzed. \square

Part B: the timer τ is considered

\mathcal{H} has been written so that the only difference with \mathcal{H}_δ (for any $\delta > 0$) is the presence of the timer τ that must satisfy the condition $\tau \in [\delta, 2\delta]$ for jumps to occur in \mathcal{D}_1 and \mathcal{D}_{-1} , whereas the timer τ and this condition are absent in \mathcal{H} . Note that if $\tau(0, 0) = \tau_0 \in [0, 2\delta]$, then $\tau(t, j) \leq 2\delta$ for all $(t, j) \in \text{dom } \tau$ because of the flow and jump maps for τ in (3.24d) and (3.24f). Then, the lemma is proven if we show that for each compact set \mathcal{K} , there exists $\delta(\mathcal{K}) > 0$ such that for each solution $\hat{\xi} \in \mathcal{S}_{\mathcal{H}}(\mathcal{K})$, the solution ζ corresponding to $\hat{\xi}$ and constructed as in Claim 3.19, is by itself such that if it jumps in D_1 or D_{-1} in (3.78f) at (t, j) , it can evolve without jumping in $D_1 \cup D_{-1}$ for any $(t', j') \in \text{dom } \zeta$ with $t' \in (t, t + \delta(\mathcal{K}))$ and $j' \geq j$. Let us take $(t, j) = (0, 0)$ without loss of generality. We only show that if the solution ζ corresponding to $\hat{\xi}$ jumps in D_1 , then it can evolve without jumping in $D_1 \cup D_{-1}$, since parallel arguments hold for when such ζ jumps in D_{-1} .

If $\hat{\xi}$ is such that ζ jumps in D_1 , Claim 3.19 guarantees by the construction of ζ in its proof that also $\hat{v}(0, 0) = 0$, $\hat{\phi}(0, 0) \geq F_s$, $\hat{\sigma}(0, 0)\hat{\phi}(0, 0) \geq \frac{k_p}{k_i}\hat{\sigma}(0, 0)^2$ (hence $\hat{\sigma}(0, 0) \geq 0$), $\hat{b}(0, 0) = 1$. Then, $\hat{\xi}(0, 0) \in \hat{\mathcal{S}}_1$ in (3.23), so the conclusions of Lemma 3.9 hold for $\hat{\xi}$, and consequently for the corresponding ζ by Claim 3.19. We prove this lemma by using for each compact set \mathcal{K} the same $\delta(\mathcal{K}) > 0$ as in Lemma 3.9, which can be found due to boundedness of solutions in Lemma 3.8. Evolution 3.9.1 given in the proof of Lemma 3.9 is not relevant here since $\hat{\xi}(0, 0) \in \hat{\mathcal{A}}$ in that case, so we only need to show that in both Evolutions 3.9.2 and 3.9.3 given in the proof of Lemma: 3.9, $\hat{\xi}$ is such that ζ can evolve without jumping in D_1 or D_{-1} .

Consider Evolution 3.9.2 for $\hat{\xi}$ given in the proof of Lemma 3.9, namely $\hat{\xi} = (\hat{x}, \hat{b})$ flowing in $\hat{\mathcal{C}}$ on $[0, \delta(\mathcal{K})] \times \{0\}$. Since \hat{x} flows with $\hat{v}(t, 0) > 0$ for all $t \in (0, \delta(\mathcal{K}))$ as proven in Lemma 3.9, we can select $q(t, 0) = 1$ for all $t \in [0, \delta(\mathcal{K})]$ as we did in the proof of Claim 3.19. With this q , ζ can flow in C_{slip} on $[0, \delta(\mathcal{K})] \times \{0\}$ since $q(t, 0) = 1$, $q(t, 0)\hat{v}(t, 0) \geq 0$ (by the selection of q and Lemma 3.9), $\hat{b}(t, 0)q(t, 0)\hat{\sigma}(t, 0) \geq 0$, $\hat{\sigma}(t, 0)\hat{\phi}(t, 0) \geq \frac{k_p}{k_i}\hat{\sigma}(t, 0)^2$, and $\hat{b}(t, 0)q(t, 0)\hat{\phi}(t, 0) \geq 0$ (the last three since $\hat{\xi}$ flows in $\hat{\mathcal{C}}$). Since ζ evolves indeed without jumping in D_1 or D_{-1} , the statement of this lemma is proven for Evolution 3.9.2.

Consider Evolution 3.9.3 for $\hat{\xi}$ given in the proof of Lemma 3.9, namely $\hat{\xi}$ possibly flowing in $\hat{\mathcal{C}}$ on $[0, t_1] \times \{0\}$ for some $t_1 \geq 0$, jumping in $\hat{\mathcal{D}}_\sigma$ at $(t_1, 0)$, possibly flowing in $\hat{\mathcal{C}}$ on $[t_1, t_2] \times \{1\}$ for some $t_2 \geq t_1$, jumping in $\hat{\mathcal{D}}_v$ at $(t_2, 1)$ and possibly flowing in $\hat{\mathcal{C}}$ on $[t_2, t_3] \times \{2\}$ for some $t_3 \geq t_2$. If $t_1 > 0$, flow in $\hat{\mathcal{C}}$ occurs as in Evolution 3.9.2, we select $q(t, 0) = 1$ for all $t \in [0, t_1]$ and ζ flows in C_{slip} on $[0, t_1] \times \{0\}$. Since $q(t_1, 0) = 1$, ζ can jump in D_σ as shown in the proof of Claim 3.19, and $q(t_1, 1) = 1$. If $t_1 < t_2$, flow in $\hat{\mathcal{C}}$ occurs, $\hat{v}(t, 1) > 0$ for all $t \in (t_1, t_2)$ as proven in Lemma 3.9 (see (3.68)), we select $q(t, 1) = 1$ for all $t \in [t_1, t_2]$, and ζ flows in C_{slip} . With $q(t_2, 1) = 1$ and since $\hat{\xi}$ jumps in $\hat{\mathcal{D}}_v$

at $(t_2, 1)$, the construction in the proof of Claim 3.19 shows that a jump of ζ in D_0 is possible (so, $q(t_2, 2) = 0$), followed by a jump of ζ in D_v (so, $q(t_2, 3) = 0$). We now distinguish the cases in Evolutions 3.9.3.1 and 3.9.3.2 given in the proof of Lemma 3.9. If $\hat{\sigma}(t_2, 1) \in [-\hat{\sigma}_{\text{th}}, 0]$ as in Evolution 3.9.3.1, we have in the nontrivial case $\hat{\sigma}(t_2, 1) \neq 0$ (if $\hat{\sigma}(t_2, 1) = 0$, then $\hat{\xi}(t_2, 2) \in \hat{\mathcal{A}}$) that $\hat{\xi}$ flows with $\hat{v}(t, 2) = 0$ for all $t \in [t_2, t_2 + \delta(\mathcal{K})]$, so ζ can flow in $\mathcal{C}_{\text{stick}}$ on at least $[t_2, t_2 + \delta(\mathcal{K})]$. If $\hat{\sigma}(t_2, 1) \in (-\infty, -\hat{\sigma}_{\text{th}})$ as in Evolution 3.9.3.2, $\hat{\xi}$ flows in $\hat{\mathcal{C}}$ on $[t_1, t_2] \times \{1\}$ with $t_2 - t_1 > \delta(\mathcal{K})$, whereby ζ flows in $\mathcal{C}_{\text{slip}}$. These possible evolutions indeed evolve without a jump of ζ in D_1 or D_{-1} for all $(t', j') \in \text{dom } \xi$ with $t' \in (t, t + \delta(\mathcal{K}))$, so the statement of this lemma is proven for these evolutions as well.

3.A.9 Proof of Lemma 3.12

We prove the lemma item by item and use throughout the proof that $bq\sigma \geq 0$ in $\mathcal{C} \cup \mathcal{D}$.

1. For each $\xi \in \mathcal{C} \cup \mathcal{D}$, V is a sum of nonnegative terms in (3.27) since the 2×2 matrix is positive definite from Assumption 3.3, and $bq\sigma \geq 0$ in $\mathcal{C} \cup \mathcal{D}$. Moreover, for each $\xi \in \mathcal{C} \cup \mathcal{D}$, $V(\xi) = 0$ if and only if $\xi \in \mathcal{A}$ because $\xi \in \mathcal{A}$ implies that $V(\xi) = |q|(\phi - bqF_s)^2 = 0$ and $V(\xi) = 0$ implies that all the terms of the sum in (3.27) must be zero, hence $\sigma = v = 0$ and, for $|q| = 1$, $\phi = bqF_s$ and, for $q = 0$, $\phi \in [-F_s, F_s]$. The last two cases imply together $\phi \in F_s \text{Sign}(bq)$.

2. For the derivation of V° below, we use $\frac{d}{d\phi} (\text{dz}_{F_s}^2(\phi)) = 2\text{dz}_{F_s}(\phi)$, and $\partial(|\sigma|) = \text{Sign}(\sigma)$.

$$\begin{aligned} V^\circ(\xi) &= 2\frac{k_d}{k_i}\sigma\dot{\sigma} - 2v\dot{\sigma} - 2\sigma\dot{v} + 2k_p v\dot{v} + 2|q|(\phi - bqF_s)\dot{\phi} \\ &\quad + 2(1 - |q|)\text{dz}_{F_s}(\phi)\dot{\phi} + 2\frac{k_p}{k_i}F_s bq\dot{\sigma} + \max_{\varsigma \in \text{Sign}(\sigma)} \left(2(1 - |q|)\frac{k_p}{k_i}F_s \varsigma \dot{\sigma} \right) \\ &= 2\frac{k_d}{k_i}\sigma(-k_i v) - 2v(-k_i v) - 2\sigma(-k_d v + |q|\phi - q(F_s - h(v))) \\ &\quad + 2k_p v(-k_d v + |q|\phi - q(F_s - h(v))) + 2|q|(\phi - bqF_s)(\sigma - k_p v) \\ &\quad + 2(1 - |q|)\text{dz}_{F_s}(\phi)(\sigma - k_p v) + 2\frac{k_p}{k_i}F_s bq(-k_i v) \\ &\quad + \max_{\varsigma \in \text{Sign}(\sigma)} \left(2(1 - |q|)\frac{k_p}{k_i}F_s \varsigma (-k_i v) \right), \end{aligned}$$

where the deadzone term is zero because $|q| = 1$ in $\mathcal{C}_{\text{slip}}$, and $q = 0$ and $|\phi| \leq F_s$ in $\mathcal{C}_{\text{stick}}$. Similarly, the term in the maximum is zero because because $|q| = 1$ in $\mathcal{C}_{\text{slip}}$, and $q = 0$ and $v = 0$ in $\mathcal{C}_{\text{stick}}$. Since $|q|q = q$ for $\xi \in \Xi$, some computations yield

$$V^\circ(\xi) = -2(k_p k_d - k_i)v^2 + 2q\sigma(F_s - h(v)) - 2F_s bq\sigma - 2k_p qv(F_s - h(v)).$$

Because $F_s - h(v) \geq 0$ (by (3.24e) and Assumption 3.2(i)), $bq\sigma \geq 0$, and $|b| = 1$, it holds that $2q\sigma(F_s - h(v)) - 2F_s bq\sigma \leq 2|q||\sigma|(F_s - h(v)) - 2F_s|q||\sigma| = -2|q||\sigma|h(v)$. Then, we have

$$V^\circ(\xi) \leq -2(k_p k_d - k_i)v^2 - 2|q||\sigma|h(v) - 2k_p qv(F_s - h(v)) \leq 0$$

because $k_p k_d - k_i > 0$ by Assumption 3.3, $h(v) \geq 0$ for all v by (3.24e), $F_s - h(v) \geq 0$ by (3.24e) and Assumption 3.2, and $qv \geq 0$ in the flow set \mathcal{C} .

3. Since $|q| = |q^+| = 1$ and $\sigma = 0$,

$$\begin{aligned} \Delta V_\sigma(\xi) &= (\phi^+ - b^+ q F_s)^2 - (\phi - b q F_s)^2 + 2 \frac{k_p}{k_i} F_s b^+ q \sigma - 2 \frac{k_p}{k_i} F_s b q \sigma \\ &= (-\phi + b q F_s)^2 - (\phi - b q F_s)^2 = 0. \end{aligned}$$

4. Since $q = q^+ = 0$ and $\sigma = \sigma^+$,

$$\Delta V_v(\xi) = dz_{F_s}^2(\phi^+) - dz_{F_s}^2(\phi) = dz_{F_s}^2(|\phi^+|) - dz_{F_s}^2(|\phi|). \quad (3.88)$$

$\xi \in \mathcal{D}_v$ satisfies $\sigma\phi \geq \frac{k_p}{k_i}\sigma^2 \geq 0$, which is equivalent to $|\sigma||\phi| \geq \frac{k_p}{k_i}|\sigma|^2$ and $|\phi| \geq \frac{k_p}{k_i}|\sigma|$. Then, $|\phi^+| = \frac{k_p}{k_i}|\sigma| \leq |\phi|$. The relation $|\phi^+| \leq |\phi|$ concludes in (3.88) that $\Delta V_v(\xi) \leq 0$ for all $\xi \in \mathcal{D}_v$.

5. For $i \in \{-1, 1\}$, we have $b = b^+ = 1$, $q = 0$ and $|q^+| = 1$, so

$$\begin{aligned} \Delta V_i(\xi) &= (\phi - b q^+ F_s)^2 - dz_{F_s}^2(\phi) + 2 \frac{k_p}{k_i} F_s b q^+ \sigma - 2 \frac{k_p}{k_i} F_s |\sigma| \\ &\leq (\phi - q^+ F_s)^2 - dz_{F_s}^2(\phi) = 0. \end{aligned}$$

where the inequality holds since $bq^+\sigma \leq |\sigma|$ and the last equality holds since $q^+\phi \geq F_s$.

6. Since $|q| = 1$ and $q^+ = 0$,

$$\begin{aligned} \Delta V_0(\xi) &= dz_{F_s}^2(\phi) - (\phi - b q F_s)^2 + 2 \frac{k_p}{k_i} F_s |\sigma| - 2 \frac{k_p}{k_i} F_s b q \sigma \\ &= dz_{F_s}^2(\phi) - (\phi - b q F_s)^2 \leq 0, \end{aligned}$$

because $bq\sigma = |\sigma|$ (by $bq\sigma \geq 0$ and $|b| = |q| = 1$ in \mathcal{D}_0), so the corresponding terms cancel. Also, $(\phi - b q F_s)^2 \geq dz_{F_s}^2(\phi)$ so that we conclude $\Delta V_0(\xi) \leq 0$, for all $\xi \in \mathcal{D}_0$.

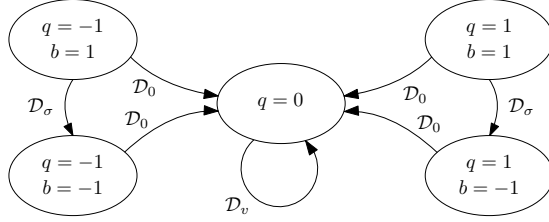


Figure 3.11. The auxiliary version of the hybrid automaton in Figure 3.4 used in the proof of Proposition 3.13.

3.A.10 Proof of Proposition 3.13

The proof is based on [135, Thm. 1]. The set \mathcal{A} in (3.26) is compact and \mathcal{H}_δ in (3.24) satisfies the hybrid basic conditions [63, Assumption 6.5]. We check the other criteria of [135, Thm. 1] in the following steps.

(i) $\mathcal{G}(\mathcal{D} \cap \mathcal{A}) \subset \mathcal{A}$ for \mathcal{G} in (3.24c). Indeed, $\mathcal{G}(\mathcal{D} \cap \mathcal{A}) \subset \mathcal{A}$ and $\mathcal{G}(\mathcal{A}) \subset \mathcal{A}$ because $g_\sigma(\mathcal{A}) \subset (\mathcal{A})$, $g_v(\mathcal{A}) \subset \mathcal{A}$, $g_1(\mathcal{A}) \subset \mathcal{A}$, $g_{-1}(\mathcal{A}) \subset \mathcal{A}$, and $g_0(\mathcal{A}) \subset \mathcal{A}$.

(ii) *Conditions on V .* The Lyapunov function in V satisfies $\mathcal{C} \cup \mathcal{D} \subset \text{dom } V$, V is continuous in $\mathcal{C} \cup \mathcal{D}$ and locally Lipschitz near each point in \mathcal{C} , is positive definite with respect to \mathcal{A} in $\mathcal{C} \cup \mathcal{D}$ (by Lemma 3.12, item 1)), and radially unbounded relative to $\mathcal{C} \cup \mathcal{D}$. The Lyapunov nonincrease conditions have been established in Lemma 3.12.

(iii) *No complete solution keeps V constant and nonzero.* Suppose by contradiction that there exists a complete solution ξ_{bad} to \mathcal{H}_δ that keeps V constant and nonzero.

We preliminarily show that the dwell time enforced by the timer τ in \mathcal{H}_δ and the logical variables imply that complete solutions exhibit an infinite amount of flow. Suppose by contradiction that this is not true and that there exists a complete solution ξ_{jump} with $\sup_t \xi_{\text{jump}} =: T_{\text{jump}} < +\infty$ and $\sup_j \xi_{\text{jump}} = +\infty$. Consider the hybrid time $(T_{\text{jump}} - \delta/2, \bar{j}) \in \text{dom } \xi_{\text{jump}}$ for some \bar{j} . For hybrid times $(t, j) \succeq (T_{\text{jump}} - \delta/2, \bar{j})$, a jump in \mathcal{D}_1 or \mathcal{D}_{-1} can only occur once. Indeed, by considering Figure 3.4, the second jump could only occur at $(t', j') \in \text{dom } \xi_{\text{jump}}$ with $t' \geq T_{\text{jump}} - \delta/2 + \delta = T_{\text{jump}} + \delta/2$, which contradicts the definition of T_{jump} . After these jumps in \mathcal{D}_1 or \mathcal{D}_{-1} , the possible jump evolutions of Figure 3.4 become those in Figure 3.11. For ξ_{jump} to jump infinitely many times, only jumps in \mathcal{D}_v remain, but this is also not possible because after the first jump in \mathcal{D}_v the variable b is toggled to 1 and jumps in \mathcal{D}_v are no longer enabled. Then, we have shown that such solution ξ_{jump} cannot exist and then complete solutions exhibit an infinite amount of flow.

Due to the decrease property along flow in Lemma 3.12, item 2) and because v remains constant across any possible jump, the only possibility for ξ_{bad} to exist is that it flows outside \mathcal{A} (otherwise V along ξ_{bad} would be zero by Lemma 3.12, item 1)) with v identically equal to zero (otherwise V would decrease from Lemma 3.12, item 2, in any arbitrarily small interval of variation of v).

Such flowing solution with $v \equiv 0$ is impossible in $\mathcal{C}_{\text{slip}} \setminus \mathcal{A}$. Indeed, $f(v) = L_2 v$ for all $|v| \leq \epsilon_v$ by Assumption 3.2(iv), we have then from (3.24d) that the first three components of \mathcal{F} are for $q = 1, v \geq 0$ and $q = -1, v \leq 0$ are respectively

$$\begin{bmatrix} -k_i v \\ \sigma - k_p v \\ -k_d v + \phi - F_s + L_2 v \end{bmatrix} =: A_{L_2} \begin{bmatrix} \sigma \\ \phi \\ v \end{bmatrix} + \begin{bmatrix} 0 \\ 0 \\ -F_s \end{bmatrix},$$

and

$$\begin{bmatrix} -k_i v \\ \sigma - k_p v \\ -k_d v + \phi + F_s + L_2 v \end{bmatrix} =: A_{L_2} \begin{bmatrix} \sigma \\ \phi \\ v \end{bmatrix} + \begin{bmatrix} 0 \\ 0 \\ F_s \end{bmatrix},$$

the pair $([0 \ 0 \ 1], A_{L_2})$ is observable, so the only solution (σ, ϕ, v) compatible with $v \equiv 0$ would be in \mathcal{A} .

Such flowing above with $v \equiv 0$ is also impossible in $\mathcal{C}_{\text{stick}} \setminus \mathcal{A}$. Indeed, the first three components of \mathcal{F} are $(0, \sigma, 0)$ with the σ component *nonzero* (otherwise, ξ_{bad} would be in \mathcal{A}), the ϕ component grows unbounded and this contradicts that $|\phi| \leq F_s$ in $\mathcal{C}_{\text{stick}} \setminus \mathcal{A}$. Hence, such a solution ξ_{bad} cannot exist and the proof is completed.

3.A.11 Proof of Theorem 3.14

First, define

$$\hat{\mathcal{A}}_6 := \{(\hat{\sigma}, \hat{\phi}, \hat{v}, \hat{b}, \tau, q) : \hat{\sigma} = \hat{v} = 0, |\hat{\phi}| \leq F_s, \hat{b} \in \{-1, 1\}, q \in \{-1, 0, 1\}, \tau \in [0, 2\delta]\}, \quad (3.89)$$

which writes $\hat{\mathcal{A}}$ in (3.22) as a subset of \mathbb{R}^6 , instead of \mathbb{R}^4 . It holds that $\hat{\mathcal{A}}_6 \supset \mathcal{A}$ with \mathcal{A} in (3.26). Then,

$$|\xi|_{\mathcal{A}} := \inf_{y \in \mathcal{A}} |\xi - y| \geq \inf_{y \in \hat{\mathcal{A}}_6} |\xi - y| = \inf_{y \in \hat{\mathcal{A}}_6} |(\hat{\xi}, \tau, q) - y| = |\hat{\xi}|_{\hat{\mathcal{A}}}. \quad (3.90)$$

We need to show stability and global attractivity of $\hat{\mathcal{A}}$, where the latter entails by [63, Def. 7.1] that for each solution $\hat{\xi}$ with $\hat{\xi}(0, 0) \in \hat{\Xi}$, $\hat{\xi}$ is bounded and satisfies

$$\lim_{t+j \rightarrow \infty} |\hat{\xi}(t, j)|_{\hat{\mathcal{A}}} = 0, \quad (3.91)$$

since maximal solutions are complete by Lemma 3.6. Boundedness of solutions is guaranteed by Lemma 3.8. Lemma 3.11 guarantees that for each compact set \mathcal{K} , there exists $\delta(\mathcal{K}) > 0$ such that each solution $\hat{\xi} \in \mathcal{S}_{\mathcal{H}}(\mathcal{K})$ coincides with the (x, b) components of some solution ξ to $\mathcal{H}_{\delta(\mathcal{K})}$ for all $t \geq 0$ such that $\hat{\xi}(t, j(t)) \notin \hat{\mathcal{A}}$, i.e., $\xi(t, j(t)) = (\hat{\xi}(t, j(t)), q(t, j(t)), \tau(t, j(t)))$ for all $t \geq 0$ such that $\hat{\xi}(t, j(t)) \notin \hat{\mathcal{A}}$ from (3.25). Then, (3.90) concludes that

$$|\xi(t, j(t))|_{\mathcal{A}} \geq |\hat{\xi}(t, j(t))|_{\hat{\mathcal{A}}} \quad (3.92)$$

for all $t \geq 0$ such that $\hat{\xi}(t, j(t)) \notin \hat{\mathcal{A}}$. If there exists $t' \geq 0$ such that $\hat{\xi}(t', j(t')) \in \hat{\mathcal{A}}$, then (3.91) is proven by Lemma 3.7. If, otherwise, for all $t \geq 0$, $\hat{\xi}(t, j(t)) \notin \hat{\mathcal{A}}$, then $\sup_t \hat{\xi} = +\infty$ by Lemma 3.10, $\sup_t \xi = +\infty$ as well by (3.25), $\lim_{t \rightarrow \infty} |\xi(t, j(t))|_{\mathcal{A}} = 0$ by Proposition 3.13, $\lim_{t \rightarrow \infty} |\hat{\xi}(t, j(t))|_{\hat{\mathcal{A}}} = 0$ by (3.92), which also proves (3.91), namely global attractivity of $\hat{\mathcal{A}}$.

Since both \mathcal{H} and \mathcal{H} satisfy the hybrid basic conditions [63, As. 6.5], global asymptotic stability of \mathcal{A} for \mathcal{H} in Proposition 3.13 actually implies uniform global asymptotic stability [63, Thm. 7.12] and uniform global attractivity. Hence, $\hat{\mathcal{A}}$ is uniformly globally attractive. Since $\hat{\mathcal{A}}$ is also strongly forward invariant by Lemma 3.7, $\hat{\mathcal{A}}$ is stable by [63, Prop. 7.5], which, together with its global attractivity, implies global asymptotic stability.

PID-based learning control for repetitive positioning of frictional motion systems

Abstract – In this chapter, we propose a time-varying PID-based feedback controller for high-accuracy positioning of motion systems with friction, performing a repetitive motion profile. In particular, we design a time-varying integrator gain, parametrized by a set of basis functions. To ensure optimal setpoint positioning accuracy, a data-based sampled-data extremum-seeking architecture is employed to obtain the optimal tuning of the time-varying integrator gain. The proposed approach does not require knowledge of the friction characteristic. The effectiveness of the proposed controller is experimentally demonstrated on an industrial nano-positioning motion stage of a high-end electron microscope.

4.1 Introduction

Many industrial motion systems perform repetitive tasks, e.g., repetitive motion profiles in pick-and-place machines [97, Sec. 5], large-scale transferring of circuit topology to silicon wafers in lithography systems [38], and automated scanning procedures in electron microscopes. Due to demands on hardware cost reduction in the design phase or wear in the operational phase, friction is commonly present in such high-precision positioning systems, thereby limiting the achievable positioning accuracy.

Various control solutions have been presented throughout the literature to cope with frictional effects in motion systems. Model-based compensation tech-

This chapter is based on [70]. Related preliminary results are reported in [69].

niques (see, e.g., [100], [58]), exploit parametric models in the control loop to compensate for friction. However, as friction characteristics are commonly unknown, uncertain, and (slowly) time-varying, model-based methods are prone to modeling errors, ultimately compromising positioning performance. Non-model-based methods, e.g., impulsive control (see, e.g., [148]), dithering-based techniques (see, e.g., [79]), and sliding-mode control (see, e.g., [14]), may result in stability of the setpoint. However, tuning and implementation of such controllers is not straightforward.

Despite the existence of the above control techniques, the vast majority of the high-precision industry still employs classical proportional-integral-derivative (PID) control [9, 125], since control practitioners are often well-trained in linear control design (loop-shaping). Moreover, it is well-known that integral action in PID control is capable of compensating for *unknown* static friction in motion systems. However, PID control is prone to performance limitations as well. For example, friction-induced limit cycling (i.e., *hunting*, see Chapter 3) is observed when integral control is employed on systems where the friction characteristic includes the velocity-weakening (Stribeck) effect, so that stability of the setpoint is lost. Even if stability can be warranted, rise-time, overshoot, settling time (see Chapter 2), and positioning accuracy depend on the particular friction characteristic, which is highly uncertain in practice. Hence, despite the popularity of the PID controller in industry, friction is a performance- and reliability-limiting factor in PID-controlled motion systems. This motivates the development of a more advanced control strategy, while preserving the benefits and intuition of classical PID feedback control design.

The PID-based reset control technique presented in Chapter 3 achieves setpoint stability by employing particular resets of the integrator. However, no guarantees on transient response or settling time can be given, so that this technique may be less suitable if a certain accuracy is desired within a limited time interval. In this chapter, we therefore propose a different PID-based controller, tailored for frictional systems performing a repetitive motion profile, typically within a finite time interval. This setting poses strict requirements on the settling time, in order to arrive at the desired accuracy. In particular, we propose a PID-based learning controller for repetitive tasks in motion systems subject to unknown static and velocity-dependent friction, including the Stribeck effect. The PID-based learning controller consists of two elements. First, a PID control architecture with a *time-varying integrator gain* design is proposed, facilitating a tailored design for any repetitive motion profile and friction characteristic at hand. In this manner, friction-induced limit cycles can be avoided, and high accuracy repetitive setpoint positioning and improved transient behavior can be achieved instead. In addition, similar robustness properties as achieved with classical PD control at the desired setpoint can be obtained. Second, we propose a data-driven, model-free optimization strategy, in order to iteratively find the optimal time-varying integrator gain in the presence of unknown friction. Such

a data-driven tuning procedure yields optimal setpoint accuracy and improved transient behavior.

In this work, the finite-horizon optimization problem of finding the optimal time-varying integrator gain for repetitive motion tasks is formulated in terms of a model-free sampled-data extremum-seeking control (ESC) problem (see, e.g., [85, 89, 141]). This is achieved by exploiting a suitable basis function parametrization of the time-varying integrator gain. The extremum seeking mechanism is then designed to iteratively improve system performance by adaptive tuning of the parameters of the basis function parametrization. Such learning mechanism has resemblance with iterative feedback tuning (see, e.g., [73, 75, 94]) and iterative learning control (ILC, see, e.g., [36, 146]). These methods have proven merit in a linear motion control setting. However, for our nonlinear setting, employing an extremum-seeking approach instead is beneficial. Namely, ESC is able to deal with unknown, uncertain, time-varying, and general nonlinear systems, and is therefore suitable to be used in the presence of unknown nonlinear frictional effects. Moreover, the potential of ESC in the context of iterative learning control and optimizing transient behavior has been shown in, e.g., [26, 84, 86, 126]. However, it must be noted that the extremum-seeking strategy to iteratively improve the system's transient behavior proposed in this work is different. Namely, we iteratively learn a *time-varying* feedback controller gain using ESC, whereas in [26, 86], ESC is used for iterative tuning of PID controllers having *constant* gains, and in [84, 126], (sampled-data) ESC is employed to iteratively tune a system input signal.

The main contributions of this chapter can be summarized as follows. The first contribution is a parametrized time-varying integrator gain design for motion systems with unknown static and velocity-dependent friction, the latter possibly including the Stribeck effect. The second contribution is an automatic controller tuning procedure based on a sampled-data extremum-seeking framework. The third contribution is an experimental case study on an industrial high-precision motion stage of an electron microscope.

The remainder of this chapter is organized as follows. We formalize the control problem in Section 4.2, and we present the PID-based controller with time-varying integrator gain in Section 4.3. In Section 4.4, we present the extremum-seeking-based iterative learning mechanism. In Section 4.5, we experimentally show the working principles of the proposed PID-based learning controller, applied to an industrial nano-positioning motion stage. Conclusions are presented in Section 4.6.

Notation: $\text{Sign}(\cdot)$ (with an upper-case S) denotes the *set-valued* sign function, i.e., $\text{Sign}(y) := 1$ for $y > 0$, $\text{Sign}(y) := -1$ for $y < 0$, and $\text{Sign}(y) := [-1, 1]$ for $y = 0$. \mathbb{B} denotes the closed unit ball of appropriate dimensions, in the Euclidean norm.

4.2 Control problem formulation

In this section, we first present the considered motion system with friction, controlled by a *classical* P(I)D controller to illustrate the shortcomings of P(I)D control for frictional motion systems. Second, we state the control problem formulation for repetitive positioning of frictional motion systems addressed in this chapter.

4.2.1 System description

Consider a single-degree-of-freedom motion system, consisting of a mass m sliding on a horizontal plane, with measurable position z_1 , velocity z_2 , control input u_c , and subject to a friction force F_f . The friction force F_f takes values according to the set-valued mapping of the velocity $z_2 \mapsto \Psi(z_2)$. The set-valued friction characteristic Ψ consists of a Coulomb friction component with (unknown) static friction F_s , a viscous contribution γz_2 (where $\gamma \geq 0$ is the viscous friction coefficient), and a nonlinear velocity-dependent friction component f , encompassing the Stribeck effect, i.e.,

$$F_f \in \Psi(z_2) := -F_s \text{Sign}(z_2) - \gamma z_2 + f(z_2), \quad (4.1)$$

We pose the following assumption on the velocity-dependent friction component f .

Assumption 4.1. *The function $f : \mathbb{R} \rightarrow \mathbb{R}$ is continuously differentiable and satisfies*

- (i) $|f(z_2)| \leq F_s$ for all z_2 ;
- (ii) $z_2 f(z_2) \geq 0$ for all z_2 ;
- (iii) f is globally Lipschitz with Lipschitz constant $L > 0$.

The dynamics are governed by the following differential inclusion:

$$\begin{aligned} \dot{z}_1 &= z_2, \\ \dot{z}_2 &\in \frac{1}{m} (\Psi(z_2) + u_c). \end{aligned} \quad (4.2)$$

Let us first consider a classical PID controller for input u_c in (4.2), i.e.,

$$\begin{aligned} u_c &= k_p e + k_d \dot{e} + k_i z_3, \\ \dot{z}_3 &= e, \end{aligned} \quad (4.3)$$

where $e := r - z_1$ denotes the setpoint error with r the reference signal, z_3 the integrator state, and k_p , k_d , and k_i the proportional, derivative, and integral

controller gains, respectively. For frictional motion systems, the presence of an integrator action in (4.3) is motivated by the fact that it is able to compensate for unknown static friction, due to the build-up of control force by integrating the position error. In general motion control systems, integrator action is widely used to improve low-frequency disturbance rejection properties and shorten rise-times, the latter being beneficial for machine throughput. As an illustration, consider a constant reference r , i.e., a point-to-point motion, so that the resulting set of equilibria of closed-loop system (4.1)-(4.3) is given by

$$\mathcal{E}_{pid} = \{(e, \dot{e}, z_3) \in \mathbb{R}^3 \mid e = 0, \dot{e} = 0, |z_3| \leq F_s/k_i\}, \quad (4.4)$$

which is globally asymptotically stable for closed-loop system dynamics (4.1)-(4.3) only when $f(\cdot) = 0$, i.e., in the absence of the velocity-weakening (Stribeck) effect, see [29]. In the presence of the Stribeck effect, however, solutions do not converge to \mathcal{E}_{pid} and limit cycling (hunting) occurs, see also Chapter 3 of this thesis. Although static friction is eventually compensated by the integrator action, friction is overcompensated in the slip phase that follows due to the velocity-weakening effect, resulting in overshoot of the setpoint. This process repeats and results in stick-slip limit cycling, compromising setpoint stability. The hunting phenomenon is illustrated experimentally in the third subplot in Figure 4.1, which shows two measured error responses and the corresponding control forces of the industrial nano-positioning motion stage setup, discussed in Section 2.5.1. A relatively large positioning error of about 200 nm is then obtained when using a classical PID controller. Hunting can be avoided by omitting the integrator action (i.e., PD control for input u_c in (4.2)), which results in the set of equilibria for (4.1)-(4.3) given by

$$\mathcal{E}_{pd} = \{(e, \dot{e}) \in \mathbb{R}^2 \mid |e| \leq F_s/k_p, \dot{e} = 0\}. \quad (4.5)$$

For a PD-controlled system, solutions converge to the set (4.5) (see [121]), but zero steady-state error is not guaranteed, as also illustrated in Figure 4.1. In particular, the size of the achievable steady-state error depends inversely on the proportional gain k_p , which cannot be chosen arbitrarily large for stability purposes. The drawbacks of P(I)D control for frictional motion systems, performing a repetitive motion on a finite time interval, motivate the design of a more suitable control architecture. Recall that no settling time guarantees can be given for the reset control approach of Chapter 3, despite achieving stability of the setpoint. We therefore propose a time-varying PID-based controller in Section 4.3, that is able to achieve a high setpoint accuracy on a finite time interval. Before presenting the controller, let us formalize the control problem in the next section.

4.2.2 Control problem formulation

In this chapter, we focus on achieving high-accuracy positioning for frictional motion systems that perform a T -repetitive motion. We consider, for the position

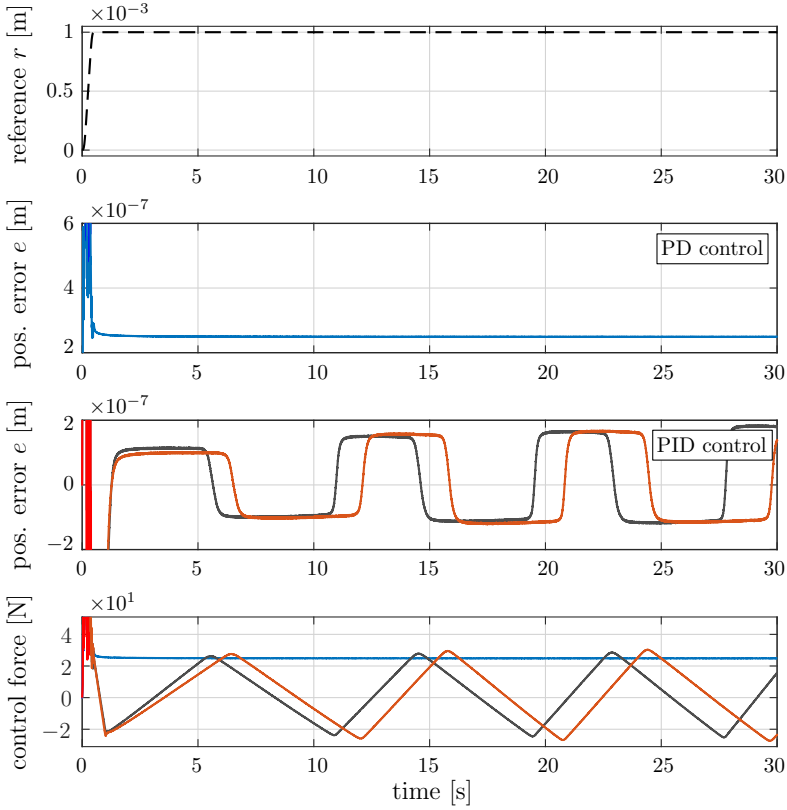


Figure 4.1. Measured error responses of an industrial high-precision motion stage (see Section 2.5.1) subject to a third-order reference trajectory (— —) and the corresponding control forces of a PD controller (—), and a PID controller with fixed integrator gain $k_i = 10^8$ N/(ms) (—) and (—). The PD controller yields a non-zero steady-state positioning error, and the PID controller induces limit cycling.

z_1 , a desired repetitive reference r , defined on the time interval $[0, T]$, where the system starts and ends at rest. Specifically, we separate the time interval $[0, T]$ into two particular parts, specified as follows:

- i) $t \in [0, T_B]$; the so-called *transient time window*, during which the system is allowed to move from 0 to r ;
- ii) $t \in [T_B, T]$; the so-called *standstill time window*, during which standstill at r is required. The time interval $[T_B, T]$ is typically used by the industrial machine, of which the motion system is part, to perform a certain machining operation for which accurate positioning is required.

Respecting the popularity of PID control in industry, and taking into account the advantages of classical P(I)D control, in this chapter we address the following setpoint control problem in this chapter.

Problem 4.2. *Design a PID-based control strategy for motion systems of the form (4.1),(4.2), that perform a repetitive motion profile and are subject to unknown static and velocity-dependent friction, such that 1) high-accuracy setpoint positioning during the standstill time window, and 2) optimal transient behavior during the transient time window is achieved.*

The desired performance, i.e., an optimal transient response on $[0, T_B)$, and optimal setpoint accuracy on $[T_B, T]$, can be captured by the following cost function J to be minimized:

$$J(e) := \int_0^T |w(t)e(t)|^2 dt, \quad (4.6)$$

with weighting function $w(t)$ defined as follows:

$$w(t) := \begin{cases} w_1 & \text{if } t \in [0, T_B) \\ w_2 & \text{if } t \in [T_B, T] \end{cases}, \quad (4.7)$$

with $w_1, w_2 \in \mathbb{R}$ suitable weighting factors, trading off the emphasis on transient performance versus setpoint accuracy. Other (transient) performance relevant variables, such as the control effort u_c , or the velocity z_2 of the mass can be taken into account in (4.6) as well.

4.3 Time-varying PID controller

In this section, first the time-varying integrator design is presented, and subsequently the achievable performance benefits are shown in a numerical example.

4.3.1 Time-varying integrator gain design

The limit-cycle present in the case of PID control with *constant* integrator gain, see, e.g., Fig 4.1, is caused by the build-up of integrator action (during transients and the stick phase) in interplay with the friction characteristic. This observation motivates the design of a novel *time-varying* integrator gain $k_i(t)$ for point-to-point motion for the following reasons:

1. the presence of integrator action still allows the system to escape undesired stick phases;
2. overcompensation of friction due to the Stribeck effect can be avoided by altering $k_i(t)$ during the slip phase;

3. zero integral action can be enforced at the setpoint when standstill of the system is required, such that robustness against other force disturbances is provided by the static friction.

The resulting controller is then given by

$$u_c = k_p e + k_d \dot{e} + k_i(t) z_3, \quad (4.8a)$$

$$\dot{z}_3 = \zeta(t) e, \quad (4.8b)$$

with $\zeta(t) \in \{0, 1\}$ a to-be-designed switching function that prevents uncontrolled growth of z_3 . Furthermore, the to-be-designed time-varying integral gain $k_i(t)$ should be bounded, i.e., $|k_i(t)| < +\infty$ for all $t \in [0, T]$. We opt to employ a time-varying integrator gain, instead of an appropriate feedforward control signal in combination with a constant integrator gain as commonly done in iterative learning control to, e.g., counteract recurring disturbances [36, 146]. This choice is motivated by the fact that, with the proposed controller, we are able to 1) escape undesired stick phases by enabling $k_i \neq 0$ during the transient time window, and 2) create robustness to other force disturbances close to the setpoint, by enforcing $k_i = 0$ during the standstill time window. Integrator action is then disabled, so that the system remains in standstill since build up of control force is prevented.

Remark 4.3. Note that the presented engineering intuition here only applies when the integrator gain k_i is placed at the right-hand side in (4.8a), instead of at the right-hand side in (4.8b). Indeed, in the latter case, $k_i = 0$ would still yield a constant integral control force in u_c . \lrcorner

We now propose a parametric design for $k_i(t)$, parameterized by a finite set of basis functions $\vartheta^{(j)}$, $j \in \{1, 2, \dots, b\}$, as follows:

$$k_i(t) := \sum_{j=1}^b \vartheta^{(j)}(v, t), \quad (4.9)$$

where b denotes the number of basis functions, and $v \in \mathbb{R}^{n_v}$ is a to-be-designed parameter vector. Next, we give two examples of basis function parametrizations that can be employed to facilitate solving Problem 4.2.

Example 4.4. [69] Step-like basis functions, i.e., $\vartheta^{(j)}(v, t) := v^{(j)} \Theta^{(j)}(t)$ with $\Theta^{(j)}(t)$ defined as follows:

$$\Theta^{(j)}(t) := \begin{cases} 1, & t \in [(j-1)t_s, jt_s) \\ 0, & t \notin [(j-1)t_s, jt_s) \end{cases} \quad \text{for } j = 1, \dots, b, \quad (4.10)$$

where t_s satisfies $T = bt_s$, and the to-be-designed parameter vector $v \in \mathbb{R}^{n_v}$, with $n_v = b$.

Example 4.5. *Linear spline basis functions, i.e., $\vartheta^{(j)}(v, t) := [v^{(j)} v^{(j+1)}]\Theta^{(j)}(t)$ with $\Theta^{(j)}(t)$ defined as follows:*

$$\Theta^{(j)}(t) := \begin{cases} \begin{bmatrix} 1 - \frac{t-jt_s}{t_s} \\ \frac{t-jt_s}{t_s} \\ 0 \end{bmatrix}^\top, & t \in [(j-1)t_s, jt_s) \\ [0 \ 0]^\top, & t \notin [(j-1)t_s, jt_s) \end{cases} \quad (4.11)$$

for $j = 1, \dots, b$,

where t_s satisfies $T = bt_s$, and the parameter vector $v \in \mathbb{R}^{n_v}$, with $n_v = b + 1$.

Remark 4.6. *Other types of basis function designs can be adopted from the iterative learning control literature. For example, polynomial bases (see, e.g., [147], [104]) and rational bases (see, e.g., [31]) can similarly be exploited. \square*

In the remainder of this chapter, we opt for a linear spline basis function parametrization of $k_i(t)$, as illustrated in Example 4.5, as it yields a *continuous* control signal. In contrast, the step-like basis function parametrization, as illustrated in Example 4.4 (see also [69]) results in discontinuities in the control signal, which may risk excitation of high-frequency system dynamics.

The switching function $\zeta(t)$ in (4.8) is analogously designed as

$$\zeta(t) := \begin{cases} 1, & t \in [0, T_B), \\ 0, & t \in [T_B, T], \end{cases} \quad (4.12)$$

so that the evolution of the integrator state is disabled on the interval $[T_B, T]$. Summarizing, the resulting closed-loop system with the proposed design for the time-varying integrator gain is given by (4.1), (4.2), (4.8), (4.9), (4.11), (4.12).

Let us now present some properties of the resulting closed-loop system, which will be instrumental in the data-based sampled-data extremum seeking architecture presented in Section 4.4. In particular, the following proposition asserts that each bounded realization of $k_i(t)$ results in a *unique* solution $z = (z_1, z_2, z_3)^\top$ of the closed-loop system, which is *bounded* on the interval $[0, T]$.

Proposition 4.7. *Under Assumption 4.1, for any constant r , each bounded realization of $k_i(t)$ in (4.8) satisfying $k_i(t) = 0$ for $t \in [T_B, T]$, each initial condition satisfying $z(0) \in K_1\mathbb{B}$ with $K_1 \geq 0$, and $\zeta(t)$ as in (4.12), solutions $z(t)$ to closed-loop system (4.1), (4.2), (4.8), (4.9), (4.11), (4.12) are unique, and satisfy $z(t) \in K_2\mathbb{B}$ for some bounded $K_2 > 0$, for all $t \in [0, T]$.*

Proof. See Appendix 4.A. \square

4.3.2 Illustrative example

We illustrate the achievable benefits of the proposed time-varying integrator gain by means of a numerical example. Consider closed-loop sys-

tem (4.1), (4.2), (4.8), (4.9), (4.11), (4.12), where we adopt the following numerical values: $m = 1$, $k_p = 18$ N/m, $k_d = 2$ Ns/m, $F_s = 0.981$ N, and $\gamma = 0.5$. The Stribeck contribution of the friction f is given by

$$f(x_2) = ((F_s - F_c)\eta x_2) (1 + \eta|x_2|)^{-1}, \quad (4.13)$$

with F_c the Coulomb friction force, and η the Stribeck shape parameter. The motion profile interval is characterized by $T = 1.5$ s, and $T_B = 0.75$ s. For the time-varying integrator gain design, we take $b = 6$, and the parameter vector v is given by $v = [v^{(1)} \ v^{(2)} \ v^{(3)} \ 0 \ 0 \ 0 \ 0]^T$. Moreover, $v^{(1)}$ is kept *fixed* to $v^{(1)} = 25$ N/(ms), which enables integral action at least for $t \in [0, t_s)$ to escape a potential initial stick phase. The parameters $v^{(2)}$ and $v^{(3)}$ are tunable, and affect the error response of the closed-loop system, as illustrated next.

We illustrate the potential performance benefits of the controller by considering two cases with different friction characteristics, i.e., 1) $F_c = F_s/2$ N, $\eta = 20$, $\gamma = 0$ Ns/m, and, 2) $F_c = F_s/3$ N, $\eta = 60$, $\gamma = 1$ Ns/m. Consider Figure 4.2, where each column of subplots depict the friction characteristic, position error, and the time-varying integrator gain $k_i(t)$ for the two cases, respectively. For both cases, the error response with a *classical* PID controller (i.e., with a fixed integrator gain $k_i = 25$ N/(ms)) denoted by (....) in the middle plots, leads to significant overshoot, and eventually limit cycling (the latter explicitly visible for case 2; see also Figure 4.1 for such a limit-cycling effect). Selecting different values for the parameters $v^{(2)}$ and $v^{(3)}$ yield different error responses. For example, (—) in case 1 results in significant overshoot, and (—) in undershoot. The optimal choice for $v^{(2)}$ and $v^{(3)}$ instead results in zero error, see (—). The friction characteristic in case 2 has a more severe Stribeck effect compared to the characteristic in case 1 (see the top subplot), whereby the optimal settings for $v^{(2)}$ and $v^{(3)}$ become negative, but zero steady-state error is still achieved, see (—) in the second and lower subplot. The proposed time-varying PID controller is hence capable of achieving optimal positioning performance, despite the presence of friction, by proper tuning of the parameters in v .

Since the friction characteristic Ψ in (4.2) is generally unknown, uncertain, and can change (slowly) in time, the optimal design for the tunable parameters in v is challenging, or even impossible using a model-based approach only. Therefore, we propose a data-based extremum-seeking-based (learning) algorithm in the next section, to learn the optimal $k_i(t)$ by adaptive tuning of the parameter vector v , on the basis of measured error responses.

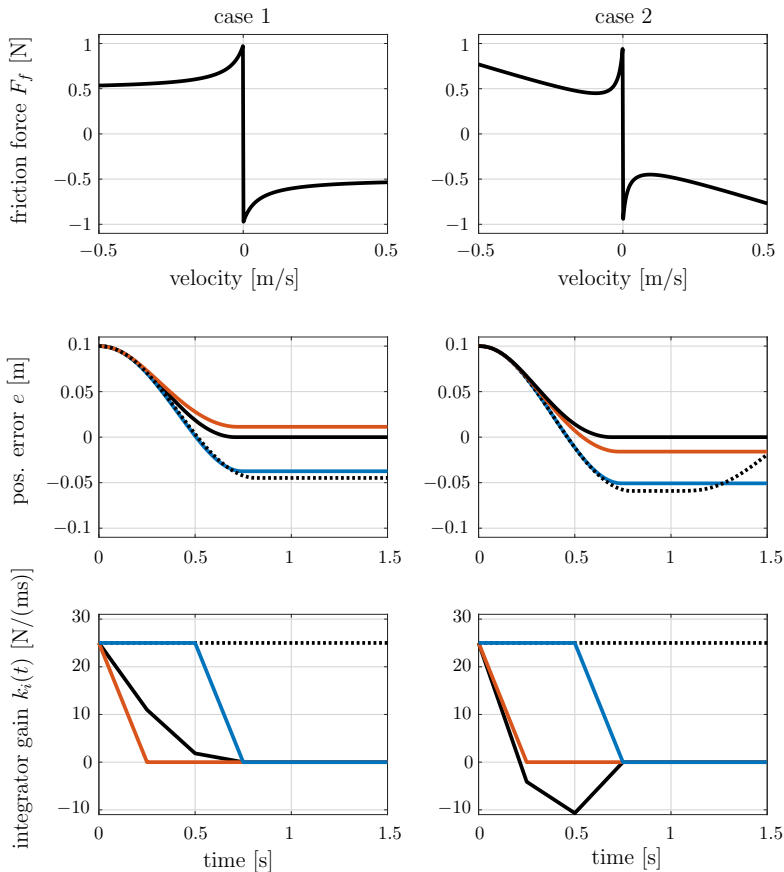


Figure 4.2. Simulation results, where each column presents from top to bottom the friction characteristic, error response, and time-varying integrator gain for case 1 and 2, respectively. The different error responses in the middle subplots correspond to simulations with different realizations of the time-varying integrator gain as in the lower subplots, and the classical PID responses with constant k_i are indicated by (····).

4.4 Sampled-data extremum-seeking for iterative controller tuning

4.4.1 Sampled-data extremum-seeking framework

In this section, we propose a sampled-data extremum seeking strategy, akin to iterative learning control, to optimize the time-varying integrator gain design pre-

sented in Section 4.3 to achieve high-accuracy setpoint positioning. Specifically, given the cost function in (4.6) and (linear spline) basis function parametrization of the time-varying integrator gain in (4.9), we can formulate the finite horizon optimization problem as a model-free sampled-data extremum seeking problem (see, e.g., [85], [84]). Namely, consider the cascade connection of the PID-controlled motion system given by (4.1), (4.2), (4.8), (4.9), (4.11), (4.12), and the cost function J in (4.6). In addition, we consider the to-be-designed parameter vector to be decomposed as follows: $v = v_0 + Cu$, where $v_0 \in \mathbb{R}^{n_v}$ is a user-defined parameter vector, $C \in \mathbb{R}^{n_v \times p}$ is a user-defined selection matrix, and $u \in \mathbb{R}^p$ is the vector of parameters to be optimized by the extremum-seeking algorithm. This cascade connection yields the following *unknown* static input-output map $Q: \mathbb{R}^p \rightarrow \mathbb{R}$ for the cascaded system (4.1), (4.2), (4.8), (4.9), (4.11), (4.12), and (4.6):

$$Q(u) := \int_0^T |w(t)e(t)|^2 dt, \quad (4.14)$$

where the weighting function $w(t)$ is defined in (4.7). It must be noted that periodic re-initialization of the states to fixed values (i.e., $x(kT) = x_0$ for all $k = 1, 2, \dots$), in combination with Proposition 4.7, is needed for extremum seeking control to be applicable in an iterative learning context. Only under these conditions (re-initialization and uniqueness of solutions provided by Proposition 4.7), Q in (4.14) is uniquely defined, see also Remark 4.9 below. In addition, the fact that solutions to the closed-loop system remain bounded by Proposition 4.7 guarantees that $Q(u)$ is bounded.

Based solely on output measurements, which we use to compute Q in (4.14), extremum-seeking control is exploited to adaptively find the parameters u that minimize Q . Figure 4.3 schematically depicts the sampled-data extremum-seeking framework, i.e., the interconnection of the PID-based controlled frictional motion system with a basis function parametrization (4.1), (4.2), (4.8), (4.9), (4.11), (4.12), and the cost function J in (4.6) implemented as follows:

$$y(t) := J(e(t)) = \int_{t-T}^t |w(s)e(s)|^2 ds, \quad (4.15)$$

where $e(s) = 0$ for $s \in [-T, 0)$, and with the weighting function implemented as follows:

$$w(t) := \begin{cases} w_1 & \text{if } \text{mod}(t, T) \in [0, T_B) \\ w_2 & \text{if } \text{mod}(t, T) \in [T_B, T] \end{cases}, \quad (4.16)$$

with a T -periodic sampler, a discrete-time extremum-seeking algorithm Σ , and a zero-order hold (ZOH) element. Let $\{u_k\}_{k=0}^\infty$ be a sequence of vectors generated by the extremum-seeking algorithm Σ based on collected measurements, and define the ZOH operation as follows:

$$u(t) := u_k \quad \forall t \in [kT, (k+1)T), \quad (4.17)$$

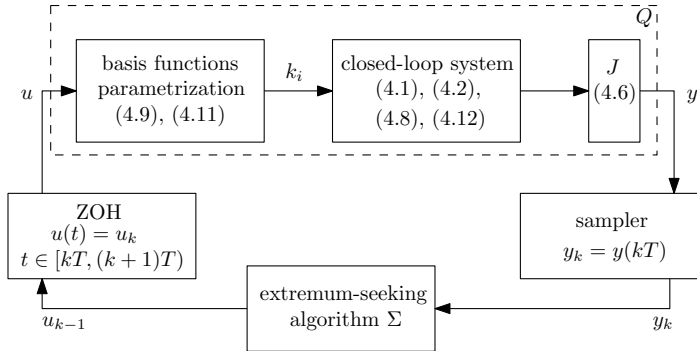


Figure 4.3. Sampled-data extremum-seeking framework based on a sampled-data control law with periodic sampling time T , and sampler and zero-order hold elements.

with $k = 0, 1, 2, \dots$, and sampling period $T > 0$ with $u_k \in \mathbb{R}^p$, for all k . Let us define the ideal periodic sampling operation:

$$y_k := y(kT), \quad k = 1, 2, \dots, \quad (4.18)$$

where $y_k = Q(u_{k-1})$ are the collected measurements as used by the extremum-seeking algorithm Σ , see Figure 4.3. We care to stress that T is the sampling period of the extremum-seeking controller, which conforms to the period time of the motion profile, and T is *not* the sampling period of the underlying motion system, which is typically much smaller.

Remark 4.8. *In most (sampled-data) extremum-seeking literature, Q reflects the steady-state behavior of the dynamical system. In those cases, the sampling period T , or so-called waiting time T , see, e.g., [141], [85], [89], needs to be chosen sufficiently large by the user such that the closed-loop extremum-seeking scheme is robust against inexact measurements of the cost Q due to the transient behavior of the system. Here, Q in (4.14) actually incorporates the transient behavior of the system, which ultimately determines positioning accuracy. As such, the role of the waiting time T is different here, and is conveniently chosen equal to the period time T of the repetitive motion profile.* \lrcorner

Remark 4.9. *A common requirement in the extremum-seeking literature is that the input-output mapping Q is independent of initial conditions. Here, the transient behavior is partly determined by the initial conditions, and re-initialization after each setpoint operation is theoretically required for an input-output mapping Q as in (4.14) to be uniquely defined. Re-initialization for transient performance optimization is also a well-known and commonly accepted requirement in the iterative learning control literature, see, e.g., [110] and [36].* \lrcorner

4.4.2 Extremum-seeking algorithm

Let the extremum-seeking algorithm Σ be any algorithm that solves the optimization problem of finding the minimum y^* of $Q(u)$:

$$y^* := \min_u Q(u). \quad (4.19)$$

Within the periodic sampled-data extremum seeking framework, and depending on the nature of the input-output mapping Q , many algorithms from the optimization literature can be employed to solve (4.19). For example, in [85] the so-called DIRECT and Shubert algorithms (see [82] and [137], respectively) are employed to find the global extremum of Q . If finding a local minimum suffices or if Q possesses only a single extremum, the classical gradient descent or Newton method can be used (see, e.g., [35]).

Without loss of generality, we employ here the following gradient descent algorithm to optimize the vector u :

$$u_k = u_{k-1} - \lambda \nabla Q(u_{k-1}), \quad (4.20)$$

with λ the optimizer gain. Since Q is unknown, its gradient ∇Q is unknown. As such, the gradient of Q will be estimated based on finite differences as follows:

$$\nabla Q(u) \approx \frac{1}{\tau} \begin{bmatrix} Q(u + \tau d_1) - Q(u) \\ \vdots \\ Q(u + \tau d_p) - Q(u) \end{bmatrix}, \quad (4.21)$$

where τ is the step size of the gradient estimator, and d_j with $j = 1, \dots, p$ are dither signals, i.e., vectors where the j th element is equal to one, and all other elements are zero. Moreover, d_0 denotes a zero vector. Dithering needs to be done in a sequential manner to acquire the elements in (4.21).

In order to improve the accuracy of the gradient estimation in the presence of, e.g., measurement noise, we include the possibility to repeat each iteration q times, and average the measured costs over the q repetitions. As such, the gradient descent algorithm in (4.20) and the sequence of dithers to obtain the approximate gradient in (4.21) can be implemented through the following extremum-seeking algorithm:

$$u_k = \begin{cases} u_{k-n} + \tau d_{\frac{n-m}{q}} & \text{if } n \neq 0 \\ u_{k-q(p+1)} - \lambda \nabla Q(u_{k-q(p+1)}) & \text{if } n = 0 \end{cases}, \quad (4.22)$$

for all $k = 1, 2, \dots$, with $n = \text{mod}(k, q(p+1)) \in \mathbb{N}$ and $m = \text{mod}(k, q) \in \mathbb{N}$,

initial input u_0 , p to-be-optimized parameters, q repeated iterations, and

$$\nabla Q(u_{k-q(p+1)}) = \frac{1}{q\tau} \begin{bmatrix} \sum_{j=0}^{q-1} (Q(u_{k-qp+j}) - Q(u_{k-q(p+1)+j})) \\ \vdots \\ \sum_{j=0}^{q-1} (Q(u_{k-q+j}) - Q(u_{k-q(p+1)+j})) \end{bmatrix}. \quad (4.23)$$

Note that the case $n = 0$ in (4.22) implements an update of the control signal u .

4.5 Experimental case study

In this section, we demonstrate the working principle and the effectiveness of the proposed PID-based learning controller on the industrial nano-positioning stage in an electron microscope, as discussed in Section 2.5.1.

Remark 4.10. *The experimental setup is the same as the setup used for the case study in Chapter 2, where dominantly Coulomb and viscous friction was present. For the experimental case study in this chapter (and the one in Chapter 3), a different carriage position and spindle orientation, and different lubrication conditions result in a significant Stribeck effect instead, as illustrated in Figure 4.1 and the experimental results below.* \lrcorner

According to standard operation of the nano-positioning stage in an electron microscope, we can only use a higher-order reference trajectory. Therefore, the step reference $r = 1$ mm is mimicked by a fast third-order reference trajectory. We require the carriage to be in standstill at $r = 1$ mm at $T_B = 1.5$ s, and the setpoint operation ends at $T = 3$ s. After each setpoint operation, the system is re-initialized to its starting position $z_1 = 0$ m using an internal homing procedure.

4.5.1 Controller settings and ESC-based optimal tuning

The design of the PID-based controller with time-varying integrator gain used in the experiments is discussed in Section 4.3. First, the PID-controller gains are tuned using linear loop-shaping techniques [57], resulting in $k_p = 10^7$ N/m, and $k_d = 2 \cdot 10^3$ Ns/m. The time-varying integrator gain is parameterized by (4.9) with $b = 6$ linear spline basis functions as in Example 4.5, from which it follows that $t_s = \frac{T}{b} = 0.5$ seconds. We select $p = 2$ parameters to-be-optimized. The parameter vector $v = v_0 + Cu$ is designed with initial parameter vector

$$v_0 = [1 \cdot 10^8 \ 0 \ 0 \ 0 \ 0 \ 0 \ 0]^\top,$$

and selection matrix

$$C = \begin{bmatrix} 0 & 1 & 0 & 0 & 0 & 0 & 0 \\ 0 & 0 & 1 & 0 & 0 & 0 & 0 \end{bmatrix}^\top.$$

The first element of vector v_0 is equal to the constant integrator gain of a *classical* PID controller, as obtained by the loop-shaping procedure (Figure 4.1 shows the measured responses with these settings). The vector $u \in \mathbb{R}^{2 \times 1}$ will be determined by the ESC algorithm discussed in Section 4.4.2, and the performance of the control system in the sense of (4.14) depends on the value of these parameters.

For the current case study, we focus on setpoint accuracy rather than transient performance. Therefore, we define the system's performance by the objective function Q in (4.14) and implemented by (4.15), where we have taken $w_1 = 0$ and $w_2 = 1 \cdot 10^8$ in (4.16). Moreover, we augment Q with a logarithmic *barrier function* [71] in order to restrict the values of the parameter values found by the extremum-seeking controller, such that $k_i(t)$ remains bounded for all $t \in [0, T]$. In particular, $k_i(t)$ then satisfies $\underline{k}_i \leq k_i(t) \leq \bar{k}_i$, with $\underline{k}_i = -0.2 \cdot 10^8$, and $\bar{k}_i = 1.2 \cdot 10^8$. The augmented objective function is then given by

$$\tilde{Q}(u) := Q(u) + \mu B(u), \quad (4.24)$$

with $Q(u)$ as in (4.14), $\mu = 1$ the barrier parameter, and the logarithmic barrier function B given by

$$B(u) := - \sum_{i=1}^4 \log(-G_i(u)), \quad (4.25)$$

with $G_1(u) = u^{(1)} - \bar{k}_i$, $G_2(u) = \underline{k}_i - u^{(1)}$, $G_3(u) = u^{(2)} - \bar{k}_i$, $G_4(u) = \underline{k}_i - u^{(2)}$. To minimize \tilde{Q} , we employ the gradient descent algorithm as discussed in Section 4.4.2, with $q = 3$, $p = 2$, step size $\tau = 0.25 \cdot 10^7$, and gain $\lambda = 2 \cdot 10^{16}$, unless stated otherwise.

4.5.2 Static input-output mapping

The dependence of the achievable setpoint accuracy, captured by the performance metric \tilde{Q} in (4.24) to be minimized, on the vector u is depicted by means of an measured input-output mapping \tilde{Q} in Figure 4.4. We use this mapping to verify the time-domain results presented later on. Two regions are observed where \tilde{Q} is small, indicating integrator gain settings that can lead to a high setpoint accuracy. Such an input-output mapping, however, is in general time-consuming to obtain, and can vary (slowly) over time, and can vary from machine to machine. Hence, such an offline, brute-force approach to performance optimization is not feasible in practice. Therefore, the optimal parameter settings are iteratively obtained by the online ESC algorithm presented in Section 4.4.2, solely based on real-time output measurements.

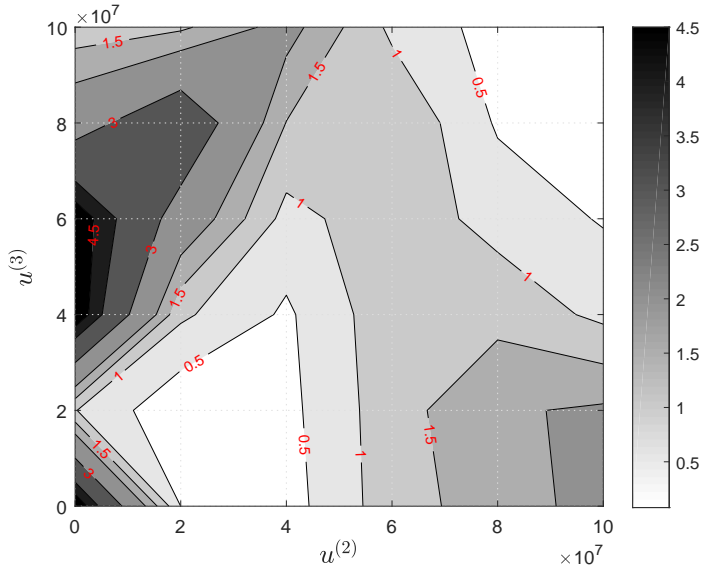


Figure 4.4. Contour plot of an experimentally obtained input-output mapping $\tilde{Q}(u)$, which shows two regions where $\tilde{Q}(u)$ is small, indicating integrator gain settings that yield accurate setpoint positioning.

4.5.3 Time-domain results obtained by extremum seeking

Consider Figure 4.5, which shows the measured augmented performance cost $\tilde{Q}(u_k)$ as in (4.24) and the corresponding vector of parameters u_k as determined by the extremum-seeking controller, as a function of the controller updates, starting with initial parameter vector $u_0 = [0.85, 0.175]^\top \cdot 10^8$. Moreover, Figure 4.6 depicts the setpoint error $e(t)$, the corresponding time-varying integrator gain design $k_i(t)$, and the resulting control force u_c for four different controller updates (final and three intermediate). It can be observed that limit cycling is indeed prevented since $k_i(t) = 0$ for all $t \in [T_B, T]$, and we only observe one interval of stick (during the standstill time window, as desired). Moreover, the extremum-seeking controller iteratively finds controller parameters u_k that result in a relatively small time-varying integrator gain design $k_i(t)$ on $t \in [0, 1.5]$, yielding a position error in the range of 4–6 nm, depicted by (—). In contrast, the classical PID controller for this particular measurement yields an absolute error of about 100 nm on the same time interval (see Figure 4.1), and does not provide robustness during the standstill time window. This clearly illustrates the performance benefits of the proposed PID-based learning controller in terms of the ability to cope with Stribeck friction and achieving superior setpoint positioning accuracy. The parameter evolution of this experiment is visualized by (---) in the input-output mapping in Figure 4.7.

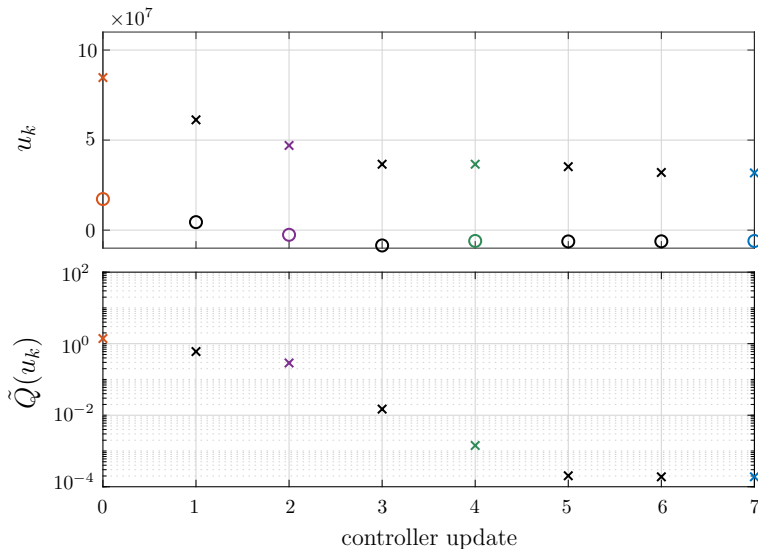


Figure 4.5. Evolution of the parameter vector u_k (top, ‘x’ and ‘o’ denote the first and second parameter of the vector u_k , respectively) and performance cost \hat{Q} (bottom), as a function of the controller updates. The color coded markers correspond to the parameter values and performance cost associated with the results in Figure 4.6.

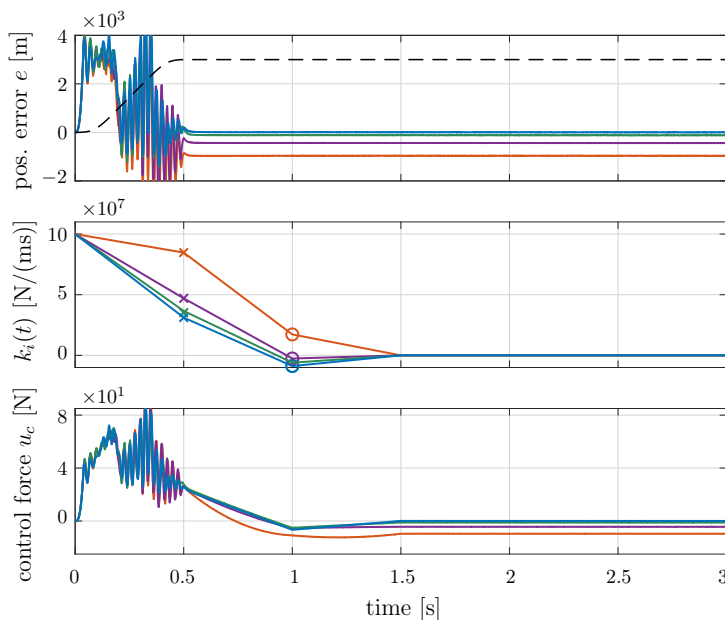


Figure 4.6. Experimental results illustrating the optimization of the setpoint error (for $t > 1.5$ s) by adaptation of $k_i(t)$. The error, corresponding $k_i(t)$, and u_c are shown for the initial parameter setting (—), the 2nd (—), 4th (—), and 7th (—) extremum-seeking controller update. The achieved accuracy is 4-6 nm.

Another interesting optimization experiment and resulting time-domain response is the one depicted in Figure 4.8 by (—), which shows the time-domain results after the final extremum seeking controller update, when using initial parameter vector $u_0 = [0.9, 0.4]^\top \cdot 10^8$. Again, the parameter evolution of this experiment is visualized by (---) in the input-output mapping in Figure 4.7. The parameters now converge towards the local minimum in the upper right corner of the input-output mapping in Figure 4.7. The existence of this particular (local) minimum can be explained by considering the upper two subplots of Figure 4.8, depicting the position error and time-varying integrator gain design $k_i(t)$, respectively. Due to the relatively large time-varying integrator gain $k_i(t)$ for $t \in [0, 1.5)$ obtained by the extremum-seeking controller and depicted by (—), the associated integral action during the transient results in significant overshoot of the setpoint. The significant overshoot can be attributed to the weight $w_1 = 0$, chosen during the transient time window, which implies that large transients are not penalized. The system then arrives in a stick phase, where control force is built up by the integrator action. Eventually the system slips and, due to the Stribeck effect in combination with the decreasing integrator gain, the system arrives in a stick phase again close to the setpoint.

The experimental results show that the proposed time-varying PID controller results in superior positioning accuracy (compared to classical PID control), and that the extremum-seeking controller successfully finds the optimal tuning of the time-varying integrator gain, regardless of the initial values of u , for the unknown frictional situation at hand.

4.6 Conclusions

We have presented a novel time-varying integrator gain design for motion systems with unknown Coulomb and velocity-dependent friction (including the Stribeck effect), performing a repetitive motion profile. The proposed controller is capable of achieving a high positioning accuracy, in contrast to classical PID control, which often leads to limit cycling, i.e., loss of setpoint stability. The time-varying integrator gain is parametrized by linear basis functions, resulting in a continuous control signal. The specific tuning of the time-varying integrator gain, that results in a high setpoint accuracy in the presence of unknown friction, is iteratively obtained by employing a sampled-data extremum-seeking framework. The performance benefits of the proposed control architecture are experimentally demonstrated on a nano-positioning stage in an electron microscope, illustrating its superior performance over classical PID control.

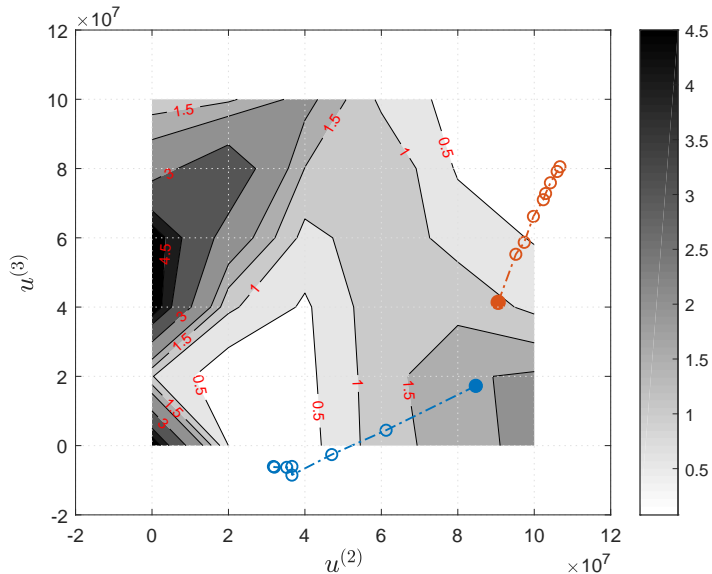


Figure 4.7. Input-output mapping $\tilde{Q}(u)$ with the evolution of extremum-seeking controller towards the optimal integrator gain settings for two series of experiments.

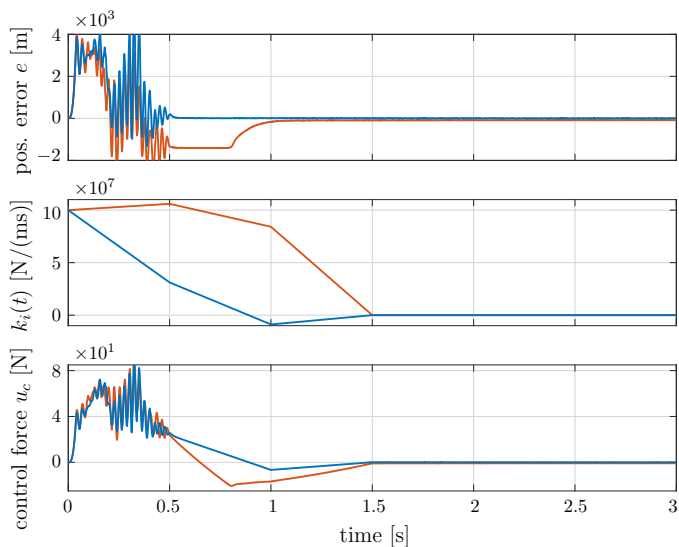


Figure 4.8. Experimental results illustrating the setpoint error e , and corresponding $k_i(t)$ and $u_c(t)$ after the final extremum-seeking controller update, for two different series of experiments. The results correspond to the same color-coded extremum-seeking parameter evolutions depicted in Figure 4.7.

4.A Proof of Proposition 4.7

The proof is based on the proof of Claim 3.4, item (i). Without loss of generality, consider $r = 0$ (which implies $e = -z_1$ in (4.8)), and we consider the intervals $[0, T_B)$ and $[T_B, T]$ separately.

By design, we have $\varsigma = 1$ on the interval $[0, T_B)$. Then, with state vector $z := [z_1, z_2, z_3]^\top$, for all $t \in [0, T_B)$, we rewrite the closed-loop system (4.1), (4.2), (4.8) as

$$\dot{z} \in A(t)z - e_2(F_s \text{Sign}(z_2) - f(z_2)) \quad (4.26)$$

with

$$A(t) = \begin{bmatrix} 0 & 1 & 0 \\ -k_p & -k_d - \gamma & -k_i(t) \\ 1 & 0 & 0 \end{bmatrix}, \quad e_2 = \begin{bmatrix} 0 \\ 1 \\ 0 \end{bmatrix}. \quad (4.27)$$

Define $f_L(z_2) := Lx_2 - f(z_2)$, which satisfies $f_L(z_{2,a}) \leq f_L(z_{2,b})$ for each $z_{2,a} < z_{2,b}$ and $L > 0$ by Assumption 4.1(iii), i.e., $f_L(z_2)$ is nondecreasing. Next, define $\Psi_L(z_2) := F_s \text{Sign}(z_2) + f_L(z_2)$, and rewrite (4.26) as

$$\begin{aligned} \dot{z} &\in \begin{bmatrix} 0 & 1 & 0 \\ -k_p & L - k_d - \gamma & k_i(t) \\ -1 & 0 & 0 \end{bmatrix} z - e_2 \Psi_L(z_2) \\ &=: A_L(t)z - e_2 \Psi_L(z_2). \end{aligned} \quad (4.28)$$

Existence of solutions² to (4.28) follows from [55, Sec. 7, Thm. 1] because the set-valued mapping in (4.28) is outer semicontinuous and locally bounded with nonempty compact convex values. Consider then two solutions z_a and z_b to (4.28) with $z_a(0) = z_b(0)$, and define $\delta := z_a - z_b$. For almost all $t \in [0, T_B)$,

$$\dot{\delta} \in A_L(t)\delta - e_2(\Psi_L(z_{2,a}) - \Psi_L(z_{2,b})).$$

Since $k_i(t)$ is bounded by design, there exists $M_1 > 0$ such that $|A(t)| \leq M_1$ for all $t \in [0, T_B)$, with $|A(t)|$ the (induced) 2-norm of matrix $A(t)$. Then, we have

$$\begin{aligned} \frac{1}{2} \frac{d}{dt} |\delta|^2 &\in \delta^\top A_L(t)\delta + \delta_2^\top (\Psi_L(z_{2,b}) - \Psi_L(z_{2,a})) \\ &\leq M_1 |\delta|^2 + \max_{\substack{f_b \in \Psi_L(z_{2,a}(t) - \delta_2(t)) \\ f_a \in \Psi_L(z_{2,a}(t))}} \delta_2 (f_b - f_a) \\ &=: M_1 |\delta|^2 + N(t). \end{aligned} \quad (4.29)$$

Whether $z_{2,a}(t)$ and $z_{2,a}(t) - \delta_2(t)$ are positive, zero, or negative, inspection of all cases reveals that $N(t) \leq 0$ for all $t \in [0, T_B)$ because f_L is nondecreasing,

²A solution to (4.28) is any locally absolutely continuous function z that satisfies (4.26) for almost all $t \in [0, T_B)$.

which implies that Ψ_L is nondecreasing. As a result, (4.29) satisfies

$$\frac{1}{2} \frac{d}{dt} |\delta|^2 \leq M_1 |\delta(t)|^2, \quad (4.30)$$

for almost all $t \in [0, T_B)$. Then, $\delta(0) = 0$ implies $\delta(t) = 0$ for all $t \in [0, T_B)$ by standard comparison theorems (e.g., [83, Lemma 3.4]).

On $[T_B, T]$, we have $\dot{z}_3 = \varsigma z_1 = 0$ because, by design, the switching function $\varsigma = 0$ on the considered interval, so that $z_3(t) = z_3(T_B)$ for all $t \in [T_B, T]$. Moreover, $k_i(t) = 0$ for $t \in [T_B, T]$. With

$$\begin{aligned} \dot{z} &\in \begin{bmatrix} 0 & 1 & 0 \\ -k_p & L - k_d - \gamma & 0 \\ 0 & 0 & 0 \end{bmatrix} z - e_2 \Psi_L(z_2) \\ &=: A_{L_2}(t)z - e_2 \Psi_L(z_2). \end{aligned} \quad (4.31)$$

we obtain analogously to the previous case

$$\frac{1}{2} \frac{d}{dt} |\delta|^2 \leq M_2 |\delta(t)|^2, \quad (4.32)$$

for almost all $t \in [T_B, T]$, with $M_2 := \lambda(A_{L_2})$ the largest singular value of A_{L_2} . Using absolute continuity of solutions, and the fact that $\delta(t) = 0$ for all $t \in [0, T_B)$ (as established above), we have that $\delta(T_B) = 0$, and (4.32) implies that $\delta(t) = 0$ for all $t \in [T_B, T]$. Uniqueness of solutions on $[0, T]$ is then proven.

We now turn to proving that solutions to the closed-loop system remain bounded on $[0, T]$. Let z_a be a generic solution to the closed-loop system, with $z_a(0) \in K_1 \mathbb{B}$ and $K_1 \geq 0$, and take $z_b(0) = (0, 0, 0)$, so that $z_b(t) = 0$ for all $t \in [0, T]$, and $\delta(0) \in K_1 \mathbb{B}$. The solutions z_a and z_b satisfy (4.30) and (4.32) on $[0, T_B)$ and $[T_B, T]$, respectively. In both inequalities, the right-hand side is bounded for all t in its domain, which excludes finite escape times for δ on $[0, T]$. Hence, there exists $K_2 > 0$ such that $\delta(t) \in K_2 \mathbb{B}$ for all $t \in [0, T]$. Since $z_b(t) = 0$ for all $t \in [0, T]$, we have $z_a(t) \in K_2 \mathbb{B}$ for all $t \in [0, T]$, which completes the proof. \square

Part II

**Control of Over-actuated
Motion Systems**

Control allocation for a high-precision transportation and positioning system

Abstract — In this chapter, we present a control allocation framework to improve the performance of an industrial high-precision translational transportation and positioning system, based on an inverted permanent-magnet linear synchronous motor. Compared to the state-of-practice control solution, the proposed allocation technique achieves enhanced tracking performance, enlarged motion freedom, minimizes power consumption, incorporates actuator limitations, and realizes relaxed hardware design specifications. A decentralized allocation algorithm is presented that enhances computational efficiency, such that the proposed control allocation technique can be implemented online at high sampling rates, and facilitates the scalability to large-scale system configurations. The performance benefits of the proposed technique are illustrated by means of a simulation study, and an extensive experimental case study.

5.1 Introduction

In this chapter, we present a control allocation framework to improve the performance of industrial high-precision transportation and positioning systems (see Figure 5.1), with respect to current state-of-practice control solutions. In particular, we consider a linear (i.e., translational) motion system, where multiple carriers can move on horizontal tracks, using the *inverted permanent-magnet linear synchronous motor* (IPMLSM) actuation principle, see, e.g., [129]. In such a system, the coils of the three-phase actuators are located on the tracks and

This chapter is based on [22] and [23].

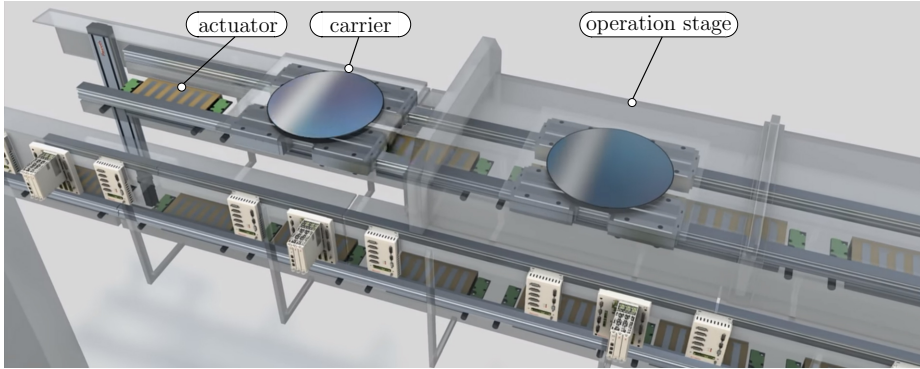


Figure 5.1. 3D visualization of a (two-story) industrial IPMLSM-based transportation and positioning system, via [34].

the permanent magnets are placed on the carriers, see Figure 5.1, such that the moving carriers do not have any electronics or cables attached to them. This principle makes the system highly suitable to be used in automated production lines involving, e.g., operation in vacuum, high temperature, or chemical environments. Due to these characteristics, such systems are widely used in industry in, e.g., the production of flat screens, OLED lighting, and photovoltaic solar cells [33].

Multiple carriers, transporting (semi-finished) products, can move over fixed guidance tracks of arbitrary length in an automated production line. At specific locations along the production line, the carriers may be required to be positioned accurately, such that a certain operation on the product can be executed. At the same time, a subsequent carrier may move towards this operation stage and queues until the first carrier has moved on. This requires the system to allow for flexible, and independent, motion of each carrier on arbitrary positions on the track. Furthermore, the system is typically over-actuated, since a carrier may commute with more than one set of coils in the track at the same time (i.e., one carrier is actuated by multiple actuators simultaneously), or multiple carriers may be influenced by the same set of coils (actuator) simultaneously. This may lead to conflicting control objectives for the actuators, and results in large position errors or the inability to control carriers independently when using state-of-practice control solutions. Moreover, the actuator characteristics suffer from position dependency and end-effects (to be discussed in more detail in Section 5.2), which pose design limitations in the sense that actuators must currently be placed at specific locations on the tracks. In this work, we aim to overcome the above limitations by means of intelligent (allocation-based) control.

IPMLSM-based transportation systems are often controlled using Field Oriented Control (or vector control), see, e.g., [30, 60], where actuator redundancy

is often handled through the use of commutation algorithms, see [17, 129]. However, these existing commutation algorithms cannot handle independent control of multiple carriers simultaneously. There exist numerous control strategies for over-actuated systems. A well-known approach is optimal control, see, e.g., [68, 154], which, especially for linear systems, has received much attention in the literature. For instance, linear quadratic control [154, Ch. 15],[8], H_∞ -control [154, Ch. 16-18], and Model Predictive Control (MPC) [59, 99, 103] are able to deal with actuator redundancy. Whereas such optimal control strategies commonly decide the control input and distribution directly, *control allocation*, see, e.g., [81], separates the regulation task from the distribution task. Such a separated approach motivates the choice of using control allocation for the current application, since the underlying motion controller can then be designed using well-known loop-shaping techniques [57], widely adopted in industry. Control allocation have been applied on a broad range of applications. Examples are control allocation for flight control [113], marine vehicles [56], electric vehicles [44], and dual-stage actuator control for harddisk drives [102].

The main contributions of this chapter are as follows. The first contribution is a control allocation framework for an IPMLSM-based transportation and positioning system. Compared to the state-of-practice control solution currently applied by the manufacturer, the proposed allocation technique achieves 1) improved tracking performance, 2) the possibility to perform independent motion of multiple carriers, 3) minimization of power consumption, 4) a relaxation of hardware design rules, and 5) the possibility to take actuator limits into account. Secondly, we propose a decentralized control allocation approach that allows for real-time implementation of the proposed allocation scheme, by significantly reducing computational effort. The third contribution is an experimental case study on an industrial application.

The remainder of this chapter is organized as follows. In Section 5.2, we provide a detailed system description, and the proposed control allocation architecture is discussed in Section 5.3. The benefits of the proposed control architecture is analyzed by means of an experimental case study in Section 5.4.1, and a simulation study in Section 5.4.2 (the latter taking into account actuator limitations). Conclusions are presented in Section 5.5.

5.2 System description

This section starts with the basic actuation principle of an IPMLSM and the control challenges, followed by a model of the considered transportation system.

5.2.1 Actuation principle and control problems

A conventional linear permanent-magnet synchronous motor (linear PMSM) has permanent magnets attached to the tracks (stator), and coils in the moving parts

(the carriers). By applying a three-phase current to the coils, a magnetic field is created which interacts with the magnetic field generated by the magnets, resulting in a force applied to the carriers, see, e.g., [60]. An *inverted* linear permanent-magnet synchronous motor has a magnet array attached to the carriers, whereas the coils are fixed to the tracks. The main advantage of such a design is that, opposed to the classical linear PMSM, no cables are attached to the carriers, providing significantly more motion freedom since the carriers are able to move on tracks of arbitrary length. In PMSM-based motion systems, the required three-phase currents to obtain the desired motion profile are typically generated in the so-called $dq\theta$ -reference frame (see, e.g., [60, Ch. 6], [144, Ch. 10]), to simplify the control problem. Consider Figure 5.2. The three-phase currents i_a , i_b , and i_c (red) can be mapped onto the stationary α, β -frame (blue) via the Clarke transformation [144, Ch. 10]. Next, the coil currents expressed in the $dq\theta$ -frame are obtained by the Park transformation [144, Ch. 10], i.e., by rotating the α, β -frame by the commutation angle θ . The coil currents are now expressed by the *direct current* i_d and *quadrature current* i_q (green). For a translational system, this transformation results in a moving reference frame fixed to the carrier, where the q -direction is aligned with the direction of movement, by choosing the commutation angle in a specific way (depending on the carrier position). In this way, it can be realized that i_q is the only force-generating current by controlling i_d to zero, such that only one input signal needs to be generated by a motion controller to achieve the desired motion of the carriers.

The considered *inverted* linear PMSM, however, suffers from end-effects. Due to the fact that the stator is segmented into groups of three-phase coils, there exist regions where the electronics in the tracks partially overlap a magnet array on a carrier. The correct commutation angle (i.e., such that i_q indeed implements the desired control force, generated by the motion controller, on the carrier) is then a *nonlinear* function of the carrier position. The motor gain (i.e., the gain between the applied quadrature current and resulting force on the carrier) thus depends on the carrier position and the commutation angle.

The segmentation of coils also gives rise to the following control problems:

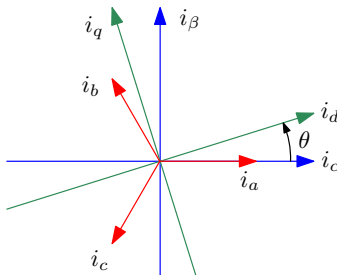


Figure 5.2. Current reference frames for PMSMs.

1) Given typical physical dimensions, carriers may be influenced by either one or two sets of coils (from now on referred to as “actuators”), leading to an over-actuated system.

2) Actuators may also influence multiple carriers at the same time. However, since an actuator is only able to implement a correct commutation angle (and thus a correct control force) for a single carrier, the other carrier experiences large disturbance forces as a result of the difference between the desired and attained control force. This restricts the freedom in motion profile design, in the sense that two adjacent carriers cannot perform an independent motion accurately, as we will illustrate in Section 5.4.1.

3) Besides the aforementioned motion restrictions, an inverted linear PMSM suffers from hardware restrictions. The spacing between actuators has to be specifically related to the length of the magnet array on the carrier to achieve a smooth transition of a carrier between two actuators, see Figure 5.3 (where we assume that the magnet arrays have the same length as the carriers). That is, the center distance of two actuators must be equal to the length of the magnet array L . When using this particular spacing, the sum of the motor gains of the actuators that influence a given carrier is constant for *all* carrier positions. Then, if the same quadrature current i_q is applied to multiple actuators, the applied force is independent of the carrier position. That is, there is no difference in the applied force to a carrier, regardless of whether the carrier is influenced by either one or two actuators. In this way, a single carrier may indeed be controlled accurately when actuated by multiple actuators (but does not allow for the control of multiple neighbouring carriers by the same actuator).

To address the above limitations, we propose a control allocation framework in Section 5.3 that results in 1) enhanced tracking performance, 2) allowing independent motion of multiple carriers, despite the conflicting control objectives, 3) reduces power consumption, 4) relaxed hardware design specifications, and 5) the possibility to take actuator limitations into account.

5.2.2 Carrier transportation system modeling

Consider an IPMLSM-based carrier transportation system consisting of n carriers and m actuators, see Figure 5.3. Let $j \in \bar{n} := \{1, 2, \dots, n\}$ be the carrier index, and $k \in \bar{m} := \{1, 2, \dots, m\}$ the actuator index, used to uniquely identify all carriers and actuators in the system. The carrier transportation system is governed by the following dynamics:

$$M\ddot{y} = B(y)u, \quad (5.1)$$

with $y = [y_1, \dots, y_n]^\top$ the position of the carriers ($y_j = 0$ indicates the lower end of the tracks), and M the diagonal mass matrix containing the carrier masses. We consider the α, β -currents for each actuator as control inputs, instead of the frequently used i_q -current of the $dq\theta$ -frame. The essential motivation of

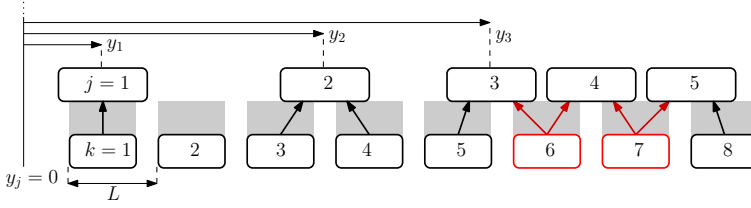


Figure 5.3. Schematic representation of the IPMLSM-based transportation system. The region of influence of an actuator is marked in gray, and arrows denote the influence of an actuator (index k) on a carrier (index j). Actuators marked in red influence two carriers.

using the fixed α, β -frame is that the motor gain matrix $B(y)$ in (5.3) below is then *independent* of the commutation angle θ . The motor gain matrix $B(y)$ then solely depends on the carrier positions, thereby simplifying the allocation problem in Section 5.3 (see also Remark 5.4 below). The input vector u is then given by

$$u = [i_{\alpha 1}, i_{\beta 1}, \dots, i_{\alpha m}, i_{\beta m}]^\top. \quad (5.2)$$

Due to the position dependency of the commutation between the carriers and the coils, the position-dependent motor gain matrix is given by

$$B(y) = \begin{bmatrix} b_{11}^\alpha(y_1) & b_{11}^\beta(y_1) & \dots & b_{1m}^\alpha(y_1) & b_{1m}^\beta(y_1) \\ \vdots & \vdots & \ddots & \vdots & \vdots \\ b_{n1}^\alpha(y_n) & b_{n1}^\beta(y_n) & \dots & b_{nm}^\alpha(y_n) & b_{nm}^\beta(y_n) \end{bmatrix}, \quad (5.3)$$

where b_{jk}^α and b_{jk}^β are actuator-specific, position-dependent motor gains. The right-hand side of (5.1) then results in a column with forces applied on the carriers, i.e.,

$$\tau = B(y)u = \begin{bmatrix} \sum_{k=1}^m \tau_{1k} & \dots & \sum_{k=1}^m \tau_{nk} \end{bmatrix}^\top. \quad (5.4)$$

In (5.4), τ_{jk} is the force applied by actuator k on carrier j , and is straightforwardly given by

$$\tau_{jk} = b_{jk}^\alpha(y_j) i_{\alpha k} + b_{jk}^\beta(y_j) i_{\beta k}. \quad (5.5)$$

Note that some elements τ_{jk} in (5.4) may be zero if actuator k does not influence carrier j , which is the case when the carrier is not close enough to the actuator in order to commute.

Let us introduce the relative position of carrier j with respect to actuator k , i.e., $z_{jk} := y_j - Y_k$, with Y_k the position of actuator k on the tracks, defined as the minimum position y_j where actuator k starts influencing a carrier j , i.e.,

$$Y_k := \min \left\{ y_j \mid b_{jk}^\alpha(y_j) \neq 0 \vee b_{jk}^\beta(y_j) \neq 0 \right\}. \quad (5.6)$$

Note that (5.6) is independent of j . We are now ready to pose the following assumptions regarding controllability of each carrier and similarity of the hardware components.

Assumption 5.1. $\text{Rank}(B(y)) = n$.

Assumption 5.2. *All three-phase coil segments and permanent magnet arrays are identical.*

As a result of Assumption 5.1, any carrier at any position on the tracks is influenced by at least one actuator, so that any desired τ_{jk} can be realized by the actuators at any time. Assumption 5.2 is not necessarily needed for the developments in this chapter, but leads to significantly reduced complexity of B and therefore to easier implementation. A consequence of this assumption is that the motor gains of each actuator k with respect to each carrier j are identical. We can then simplify the motor gain matrix B in (5.3) by writing b_{jk}^α and b_{jk}^β in (5.3) as:

$$b_{jk}^\alpha(y_j) = b_\alpha(z_{jk}), \quad b_{jk}^\beta(y_j) = b_\beta(z_{jk}). \quad (5.7)$$

The motor gains in (5.7) are typically obtained from FEM-based electromagnetic simulations on the interaction between a carrier and an actuator, see [129]. By Assumption 5.2, we only have to perform these simulations for a single actuator/carrier interaction, thereby simplifying the implementation of the control allocation architecture below (where the gain matrix B is explicitly used).

5.3 Control architecture

In this section, the proposed control allocation architecture is presented. We will first discuss the high-level control scheme, and subsequently the allocation algorithm. Finally, we present a decomposition algorithm that enhances computational efficiency, so that the control allocation architecture can be evaluated online at high sampling rates and facilitates implementation on large-scale system configurations.

5.3.1 High-level control scheme

Consider Figure 5.4. The reference signals r (one for each carrier on the track) and error signals e between the reference and the carrier positions y are provided to a motion controller (composed of a feedback and feedforward part). This controller is typically designed using well-known loop-shaping techniques [57], and generates the desired control force for each carrier $\tau_c = [\tau_{c1}, \dots, \tau_{cn}]^\top$. These desired control forces should then be applied to the carriers by the AC actuators. The primary objective of the control allocator is thus to find the currents $i_{\alpha k}$

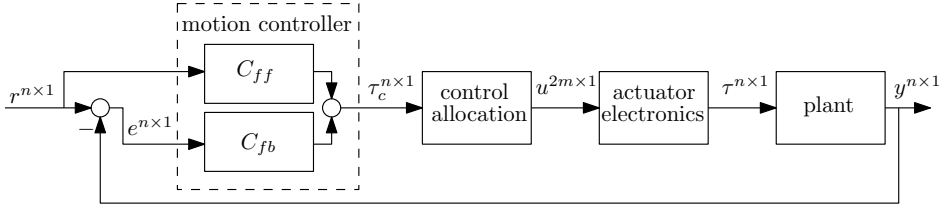


Figure 5.4. High-level control architecture. C_{fb} and C_{ff} indicate the feedback and feedforward parts of the motion controller, respectively. The superscripts on the signals indicate their dimensions.

and $i_{\beta k}$ in the control input u in (5.2), such that the actuators indeed implement the desired control forces given by τ_c . In other words, the actual forces acting on the carriers, denoted by τ in Figure 5.4, should be equal to the desired control forces as determined by the motion controller, i.e., $\tau = B(y)u = \tau_c$. Due to the over-actuated nature of the system, the solution to the allocation problem $\tau = \tau_c$ (if attainable by the actuators) is not unique. We will exploit this freedom to introduce a second control objective, namely the minimization of power consumption by the actuators, which may reduce operational costs.

We will now discuss an unconstrained and a constrained allocation procedure. The latter incorporates a saturation constraint on the input, which is motivated by the desire from industry to use cost-effective (less powerful) actuators.

5.3.2 Unconstrained control allocation

We aim at implementing the desired control force generated by the motion controller on each carrier, while minimizing the power consumption. The control allocation can then be described by the following convex quadratic programming problem (QP) [35, Ch. 4]:

$$\min_u u^\top W u, \quad (5.8a)$$

subject to

$$\tau_c = B(y)u, \quad (5.8b)$$

where $u^\top W u$ is a quadratic metric for the power consumption, and W is a symmetric weighting matrix. Since the optimization problem in (5.8a) is convex and only contains one equality constraint, the explicit solution is given by [32]:

$$u = W^{-1} B^\top(y) (B(y) W^{-1} B^\top(y))^{-1} \tau_c. \quad (5.9)$$

5.3.3 Constrained control allocation

In case there is a maximum allowable control input due to, e.g., cost-effective hardware design, the criterion $\tau = \tau_c$ may not be attainable at all times. To

deal with this scenario, we introduce a constraint on u in the form of a limit on the current, and the difference between the desired, and attained control forces $e_\tau = \tau_c - \tau$. This is combined in an allocation problem that can be described by the convex, quadratically constrained quadratic program (QCQP) [35, Ch. 4] given by

$$\min_{u, e_\tau} e_\tau^\top Q e_\tau + u^\top W u, \quad (5.10a)$$

subject to

$$\begin{aligned} e_\tau &= \tau_c - B(y)u, \\ i_{\alpha k}^2 + i_{\beta k}^2 &\leq i_{max,k}^2, \text{ for all } k \in \bar{m}, \end{aligned} \quad (5.10b)$$

with W and Q symmetric weighting matrices, and $i_{max,k}$ is the current limit on actuator k . The QCQP in (5.10) can be solved online using efficient algorithms as *CPLEX* [49] or *Gurobi* [65]. However, we propose a specific decomposition of the optimization problem in (5.10) to enhance computational efficiency. This favors solving (5.10) online at high sampling rates in large scale industrial applications with many carriers and actuators. The proposed decomposition method also favors online computations of (5.9) in the unconstrained case.

Remark 5.3. *Although the constraint in (5.10b) indeed resembles a constraint on the maximum current to be provided by the actuator, we can approximate the constraint by a set of polyhedral constraints. Then, the control problem reduces to a linear allocation problem, see [81], for which efficient quadratic programming (QP) algorithms are available, e.g., active-set or interior-point methods [109], which are studied in the context of control allocation in, e.g., [67] and [117].* \lrcorner

Remark 5.4. *We choose here to perform the control allocation in the α, β -frame. In this way, we do not have to find an optimal commutation angle θ for each actuator, which would appear in the above minimization problems as an extra decision variable when we would have chosen to apply the allocation in the $dq0$ -frame. Moreover, the motor gain matrix B in (5.3) then would not only depend on the carrier position y , but on θ as well, making the equality constraint in (5.8a) nonlinear. Performing the allocation in the α, β -frame thus significantly simplifies the control allocation problem.* \lrcorner

5.3.4 Distributed control allocation

To reduce computational costs (which favors real-time implementation on large-scale transportation systems), we decompose the allocation problems in (5.8a) and (5.10), by 1) excluding actuators that do not influence any carrier from the allocation problem, and 2) solving multiple, less complex allocation problems subsequently, instead of the full allocation problem at once. The decomposition is done at every sampling instant, by assigning carriers and actuators to specific subsets, and solving the optimization problem (5.8a) or (5.10) for each subset

separately. The only (mild) requirement for the proposed decomposition to apply is that the matrices Q and W are diagonal (to have decoupled costs in (5.8a) and (5.10)). By the dimensions of the carriers, each carrier is influenced by up to two actuators, whereas each actuator can influence up to two carriers. We first introduce the boolean variables $c_{jk} \in \{0, 1\}$, given by

$$c_{jk} = \begin{cases} 1, & \text{when } b_\alpha(z_{jk}) \neq 0 \vee b_\beta(z_{jk}) \neq 0, \\ 0, & \text{otherwise,} \end{cases} \quad (5.11)$$

for any $j \in \bar{n}$ and $k \in \bar{m}$. In other words, $c_{jk} = 1$ holds if and only if actuator k influences carrier j .

Let us now discuss assigning the subsets of carriers. A carrier subset is given by $J_p \subseteq \bar{n}$, $p \in \bar{p} := \{1, 2, \dots, P\}$ (where p is the subset number, and P the total number of subsets), and the related actuator subset is given by $K_p \subseteq \bar{m}$. Explaining the assignment of carriers and actuators to the subsets is best done by considering the problem in terms of a *bipartite graph* (see, e.g., [41, Ch. 5]). Consider hereto Figure 5.5. Let $G = (V, E)$ be a bipartite graph with $m + n$ vertices, consisting of n carrier vertices C_1, \dots, C_n , and m actuator vertices A_1, \dots, A_m (see Figure 5.5). Hence, $V = \{C_1, \dots, C_n, A_1, \dots, A_m\}$. The set of edges $E \subset V \times V$ is such that there is an edge between carrier vertex C_j and actuator vertex A_k if and only if $c_{jk} = 1$ (cf. (5.11)). To explain our procedure to arrive at J_p and K_p , $p \in \bar{p}$, we need the following definitions. A path (of length l) is given by $v_1 v_2 \dots v_l$, where $(v_i, v_{i+1}) \in E$, $i = 1, \dots, l-1$ (in our case, this implies that a path consists of alternating carrier and actuator vertices). A subgraph $G' = (V', E')$ of G is a graph $V' \subset V$ and $E' \subset E$, where E' only consist of edges (v, v') with both v and $v' \in E'$. A (sub)graph is called *connected* if there is a path between all the vertices of the (sub)graph. With this terminology in place, we can now state the decomposition of the allocation problems (5.8a) and (5.10).

In our problem, we decompose the set V now into its *connected subgraphs* with vertex sets $V_{p'}$, $p' \in \bar{p}' := \{1, \dots, P'\}$ (for which algorithms exist, see, e.g., [54, Ch. 6]). In case there are sets $V_{p'}$, $p' \in \bar{p}'$, consisting only of actuators, we discard these sets such that we can exclude the associated actuators from the allocation problem, because these do not influence any carrier (i.e., the currents i_α and i_β are zero for those particular actuators). A reordering then leads to the sets V_p , $p \in \bar{p}$, where $P \leq P'$ because the sets in $V_{p'}$ consisting only of actuator vertices are discarded, see Figure 5.5. Due to physical properties, there are no sets in V_1, \dots, V_P that only consists of carrier vertices, as each carrier is influenced by at least one actuator, see Assumption 5.1.

We decompose the remaining sets V_p , $p \in \bar{p}$, as $V_p = \tilde{J}_p \cup \tilde{K}_p$, with \tilde{J}_p consisting only of carrier vertices and \tilde{K}_p consisting only of actuator vertices, as indicated in Figure 5.5. In this way, we obtain that the carriers are assigned to disjoint subsets $J_p \subseteq \bar{n}$, $p \in \bar{p}$, where J_p contains the indices of the carriers

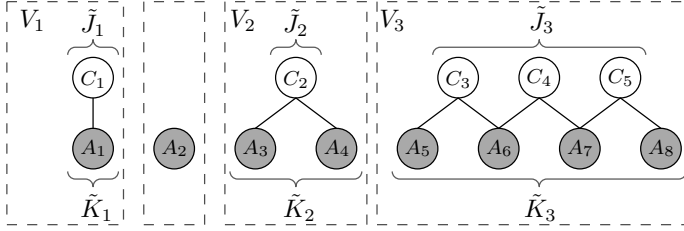


Figure 5.5. Bipartite graph G (corresponding to the schematic system representation in Figure 5.3) with carrier vertices C_1, \dots, C_5 (white) and actuator vertices A_1, \dots, A_8 (gray). Its connected subgraphs V_1, V_2, V_3 are indicated by dashed lines, where subgraphs containing only actuator vertices are discarded (hence, in this example $P' = 4$ and $P = 3$).

contained in \tilde{J}_p , i.e., $\tilde{J}_p = \{C_j \mid j \in J_p\}$. Similarly, the actuators are assigned to disjoint subsets $K_p \subseteq \bar{m}$, $p = 1, 2, \dots, P$. Clearly, J_p and K_p are related in the sense that the carriers in J_p are only influenced by actuators in K_p (and not by any others, see Figure 5.3 and 5.5). Moreover, an actuator in K_p has an influence on at least one carrier in J_p , i.e., if $k \in K_p$ there is $j \in J_p$ such that $c_{jk} = 1$. We have that $J_p \cap J_{p'} = \emptyset$ when $p \neq p'$ and $\bigcup_{p=1}^P J_p = \bar{n}$ by Assumption 1 (i.e., $\{J_1, \dots, J_P\}$ forms a partition of \bar{n}). Also, $K_p \cap K_{p'} = \emptyset$ when $p \neq p'$ and $\bigcup_{p=1}^P K_p \subset \bar{m}$, and thus $\{K_1, \dots, K_P\}$ forms a partition of $\{k \in \bar{m} \mid c_{jk} = 1 \text{ for some } j \in \bar{n}\}$. Hence, actuators that do not influence any carrier are not in $\bigcup_{p=1}^P K_p$. As a result, these actuators are excluded from the allocation problem, improving computational efficiency. Note that two carriers are in the same set J_p if and only if there is a connection (path) via multiple actuators/carriers between them (cf. Figure 5.5) and, hence, in the allocation problem these have to be treated simultaneously. Sets J_p (combined with K_p) and $J_{p'}$ (combined with $K_{p'}$) for $p \neq p'$ can be considered separately in the allocation problem as there is no path between any of the elements in J_p (and K_p) and $J_{p'}$ (and $K_{p'}$).

Algorithms are available to decompose a graph in its connected subgraphs (see, e.g., [54, Ch. 6]). However, in our case, we obtain the sets J_p and K_p , $p \in \bar{p}$ by exploiting a physical ordering of the carriers and actuators (without loss of generality): the carriers and actuators are logically numbered 1 to n from left to right on the tracks (see also Figure 5.3). Moreover, using the fact that a carrier is influenced by either one or two carriers, and each actuator influences at most two carriers, we can simplify the generic algorithms typically used to decompose a graph into its connected subgraphs (see, e.g., [54, Ch. 6]), leading to Algorithms 1 and 2 below. We use these algorithms in the experimental results that follow later in Section 5.4.1.

As a result of the decomposition, the solution for u in (5.9) in the *uncon-*

strained allocation problem (5.8a) changes to the following set of solutions:

$$u^p = W_p^{-1} B_p^\top(y_p) (B_p(y_p) W_p^{-1} B_p^\top(y_p))^{-1} \tau_c^p, \quad (5.12)$$

for all $p \in \bar{p}$, where y^p and τ_c^p are the positions of the carriers and the desired control forces in subset J_p , respectively. Moreover, B_p and W_p correspond to the submatrices of the motor gain matrix B and the (diagonal) weighting matrix W , respectively, corresponding to K_p . Using this decomposition method, the computational effort (in the sense of computing the inverse in (5.9)) is significantly reduced due to the smaller matrix B_p , compared to B . The constrained optimization problem in (5.10) now changes to a set of problems, which are solved subsequently for all $p \in \bar{p}$:

$$\min_{u^p, e_\tau^p} e_\tau^{p\top} Q_p e_\tau^p + u^{p\top} W_p u^p \quad (5.13a)$$

subject to

$$e_\tau^p = \tau_c^p - B_p(y^p) u^p, \quad (5.13b)$$

$$i_{\alpha k}^2 + i_{\beta k}^2 \leq i_{max,k}^2, \text{ for all } k \in K_p, \quad (5.13c)$$

where Q_p corresponds to the submatrix of the (diagonal) matrix Q corresponding to J_p . The decomposed optimization problem (5.13) contains less decision variables compared to its nominal counterpart in (5.10) because only active actuators are taken into account and, therefore, requires less computational cost. Moreover, solving multiple optimization problems subsequently requires less computational cost compared to solving all the problems at once (as in (5.10)), since

Algorithm 1 assigning carriers to subsets

```

1:  $J_1 = \{1\}; p = 1;$ 
2: for  $j = 2, 3, \dots, n$  do
3:   if  $c_{(j-1)k} = 1 \wedge c_{jk} = 1$  for any  $k \in \bar{m}$  then
4:      $J_p = J_p \cup \{j\};$ 
5:   else
6:      $p = p + 1; J_p = \{j\};$ 
7:   end if
8: end for
9:  $P = p;$ 

```

Algorithm 2 assigning actuators to subsets

```

1: for  $p \in \{1, 2, \dots, P\}$  do
2:    $K_p = \emptyset;$ 
3:   for  $k \in \bar{m}$  do
4:     if  $b_\alpha(z_{jk}) \neq 0 \vee b_\beta(z_{jk}) \neq 0$  for any  $j \in J_p$  then
5:        $K_p = K_p \cup \{k\};$ 
6:     end if
7:   end for
8: end for

```

the complexity of a QCQP or QP does not scale linearly with the number of decision variables [35].

5.4 Case study

In this section, we validate the proposed allocation technique on an industrial IPMLSM-based transportation system, presented in Figure 5.6, by means of an experimental and simulation study. In particular, we show experimentally the performance improvements of the proposed control allocation strategy without constraints, compared to the state-of-practice control solution currently applied by the manufacturer. Moreover, we illustrate the implications of actuator constraints on the system's performance in a simulation study, for both the allocation approach and the state-of-practice controller.

5.4.1 Experimental case study

The considered system consists of two carriers and six actuators (cf. Figure 5.6), and is modeled by (5.1)-(5.3) with $n = 2$ and $m = 6$. The carrier mass is 10.8 kg. The system is driven by an industrial precision motion control system (NYCe 4000), developed by the same manufacturer. All experiments are carried out at a sampling rate of 4kHz, and, using the decentralized approach in Section III-C, the allocation problem can be solved well within each sampling interval. By the dimensions of the actuators and carriers, an actuator may influence at most two carriers. The actuators are spaced such that the center distance between subsequent actuators is equal to the carrier length (cf. Figure 5.3), unless specifically stated otherwise. Both the state-of-practice control strategy and the allocation strategy use a dedicated high-level (loop-shaped) motion controller

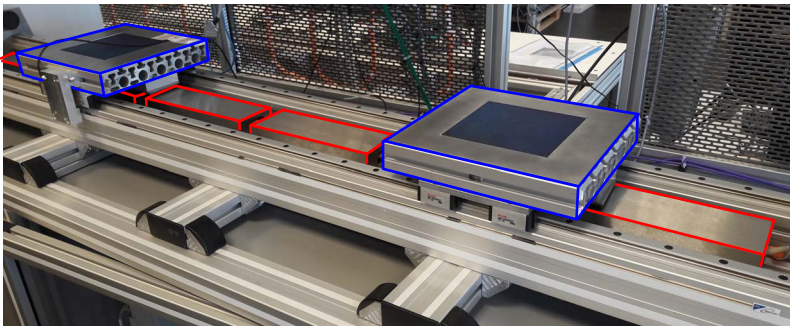


Figure 5.6. Industrial IPMLSM-based transportation and positioning system used for the case study. The carriers are indicated in blue, and the actuators in red.

for each carrier separately. For the experimental case study, we use the same motion controller (identical to the one designed by the manufacturer) for both carriers, consisting of a feedback term C_{fb} (lead filter, integrator, and a lowpass filter), and a feedforward term C_{ff} , see Figure 5.4. The feedback term for each carrier in the Laplace domain is given by

$$\tau_{fb,j}(s) = C_{fb}(s)e_j(s) = \frac{1.58 \cdot 10^8 s^2 + 8.6 \cdot 10^9 s + 8.31 \cdot 10^{10}}{2.11 \cdot 10^{-4} s^4 + 0.45 s^3 + 473.3 s^2 + 1.26 \cdot 10^5 s} e_j(s), \quad (5.14)$$

with $s \in \mathbb{C}$, and where $e_j = r_j - y_j$ the position error signal of carrier j , and r_j the position reference of carrier j . The stabilizing feedback controller achieves the specified crossover frequency of 20 Hz and satisfies standard robustness margins. The feedforward control signal consists of an acceleration feedforward term, a Coulomb friction compensation term, and a term $F_{\delta,j}$ that compensates for magnet interaction forces between carriers, i.e.,

$$\tau_{ff,j} = 0.9M_j \ddot{r}_j + K_F \text{sign}(\dot{r}_j) + F_{\delta,j}. \quad (5.15)$$

Although the Coulomb friction in the system slightly varies over time and may be position-dependent, the experimentally validated value $K_F = 4.9$ N is chosen such that no overcompensation of Coulomb friction takes place, but still compensates for a significant part of it. The magnet interaction compensation term $F_{\delta,j}$ is identified as follows. A carrier is controlled to a fixed position, whereby a second carrier is placed at different distances from the first one. At each distance, the control force of the first carrier is traced, from which the attraction force is determined. A model is then fitted on the measured data. The total *desired* control force on carrier j is then given by $\tau_{c,j} = \tau_{ff,j} + \tau_{fb,j}$. Both the state-of-practice controller as the proposed allocation scheme aim at implementing the desired control force $\tau_{c,j}$ for each carrier in a different manner (leading to a different performance) as we will illustrate below.

State-of-practice control strategy

The state-of-practice control strategy currently used by the manufacturer operates in the $dq\theta$ reference frame (see Figure 5.2) so that i_q is the only control input for each carrier (for the considered control system, the direct current i_d is controlled to zero). The force-generating component i_q is then obtained by dividing the desired control force τ_c by a *fixed* motor gain $B_q = 23.565$ N/A, see Figure 5.7. By employing a strict actuator spacing, actuator end-effects are balanced so that the sum of the motor gains of the active actuators is approximately constant, regardless of the carrier gains position on the tracks. This control signal is then applied to each actuator that commutes with the considered carrier by means of a selector. However, when an actuator influences two carriers, the selector implements the control signal for the carrier *that overlaps the actuator the most*.

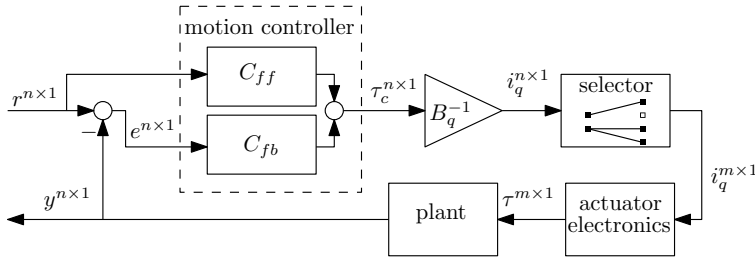


Figure 5.7. State-of-practice control strategy. C_{fb} and C_{ff} indicate the feedback and feedforward parts of the motion controller, respectively. The superscripts on the signals indicate their dimensions.

If an actuator commutes with only a single carrier, then this control strategy works well, as the actuator indeed applies the desired control force on the carrier by applying the correct commutation angle (which is a function of the carrier position). This control strategy, however, does no longer work properly when an actuator influences two carriers. The correct commutation angle is then only applied for the most overlapping carrier, which results in a wrong commutation angle for the second carrier. As a result, there is a mismatch between the desired and implemented control force on the carrier that overlaps the actuator the least, compromising tracking performance. The implications of this fact are illustrated by the experimental results below.

Remark 5.5. *Although the state-of-practice control strategy may be improved by manual compensation of the mentioned disturbance forces for simple system layouts, the proposed allocation technique offers a systematic and scalable approach for robustly improving tracking performance also suitable for large-scale systems with many carriers and actuators.* \lrcorner

Proposed control allocation strategy

In contrast to the state-of-practice control strategy, the allocation scheme is applied in the α, β reference frame. The coefficients of the position-dependent motor gain matrix $B(y)$ in (5.3), (5.7) are obtained from FEM-based electromagnetic simulations, see [129], by measuring the relative position z_{jk} of carrier j with respect to actuator k . We assume that all actuators are identical, see Assumption 5.2. The motor gains, as a function of z_{jk} , are presented in Figure 5.8, where the deterioration of the gains at both ends of the region of influence can be observed (i.e., the end-effects). The weighting matrices are $Q = 10^4 I$ and $W = I$, with I the identity matrix of appropriate dimensions.

Comparative performance evaluation

We have implemented both the state-of-practice and the *unconstrained* allocation control strategy (see Section 5.3.2) on the experimental setup of Figure 5.6.

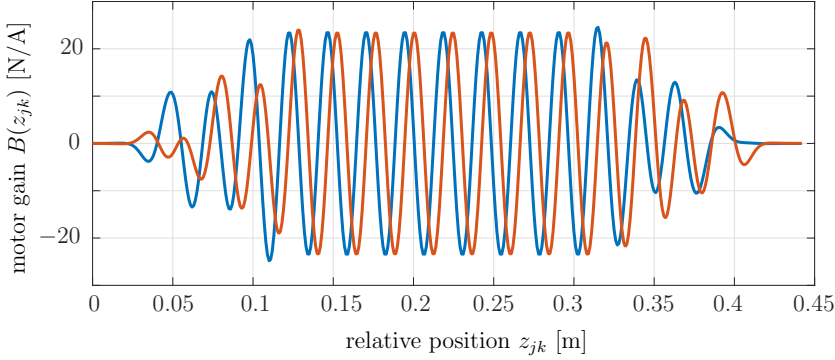


Figure 5.8. Motor gains $b_\alpha(z_{jk})$ (—) and $b_\beta(z_{jk})$ (—) as a function of the relative position.

The setup is an industrial product, designed with sufficiently powerful actuators that are easily able to realize the desired currents. We do not artificially include constraints in the experimental study, because the performance benefits of the allocation approach are most distinct when the full capacity of the actuators are used. Instead, we show the benefits of the allocation approach, when actuator constraints are taken into account, in a simulation study in the next section.

For the experiments, the following scenarios are studied:

- a) tracking of a demanding motion profile for a single carrier, with *strict* actuator spacing;
- b) tracking of a motion profile for a single carrier, with *relaxed* actuator spacing;
- c) a parallel motion of two carriers;
- d) a complex motion of two carriers, combining independent and adjacent motion.

We will now discuss the results for each scenario, and compare the performance of both control strategies. The results for the scenarios a)-d) are presented in Figure 5.9-5.12 below. In these figures, five subplots are presented which show the following: the top subplot shows the reference trajectories of the carriers, and the second subplot shows the active actuators at each time instant. In here, the time intervals where an actuator influences two carriers are indicated by gray patches (in Figure 5.11 and 5.12). The third subplot shows the position errors of the two carriers, for both the state-of-practice, and control allocation experiments. For additional clarification, the fourth subplot shows the Euclidian norm of the position error $|e|_2$ (with $e = [e_1, \dots, e_n]^T$). The fifth subplot shows $u^T W u$ as a function of time, which is a metric for power consumption.

Scenario a)

Consider Figure 5.9. A carrier tracks a demanding motion profile with relatively large accelerations and decelerations (see the top subplot). As expected, both the state-of-practice and the control allocation strategies perform well during the constant velocity phase, despite the fact that multiple actuators influence the carrier. The state-of-practice controller performs well in this scenario due to the strict actuator spacing, (so that the sum of the motor gains is constant for all carrier positions) that results in a smooth transition of a carrier between actuators (see Section 5.2-A), and the fact that there is only one carrier on the tracks in this scenario. At the start of the experiment, however, a peak in the position error is observed for the state-of-practice control solution. At this point, the carrier does not fully overlap the first actuator yet, which is not compensated for by the control scheme. In such a situation, the motor gain B is typically lower than the constant one assumed by the state-of-practice controller (see also Figure 5.8). Recall that this controller assumes a constant value for B , see also Figure 5.7. The proposed control allocation scheme is able to adapt the control input instead, so that position errors are reduced. A similar situation occurs at the end of the experiment. Finally, the remaining smaller peaks in the position error are a result of the nonexact Coulomb friction compensation. Since friction is typically unknown, and, in this case, under-compensated, the resulting contributions of friction cause increased position errors at the start of the experiment and at velocity reversals.

Scenario b)

Consider Figure 5.10, which shows the experimental results of a single carrier performing a back and forth motion, where the actuator spacing has been relaxed. In particular, the second actuator has been shifted to the right by 6 mm. A strict actuator spacing realizes that the sum of the motor gains of the active actuators is constant, regardless of the carrier position on the tracks. In the current scenario, this property is violated by the relaxed actuator spacing, and, as a result, the state-of-practice control strategy implements a force that deviates from the desired control force coming from the motion controller. As can be observed in the third and fourth subplot of Figure 5.10, this results in increased position errors in the regions where multiple actuators are active. The proposed allocation architecture is instead able to adapt, and realizes a low tracking error while minimizing power consumption. The increased position error at the start of the experiment and velocity reversals is due to any remaining Coulomb friction.

Scenario c)

For this experiment, the strict actuator spacing has been restored. Consider Figure 5.11. Two carriers perform an adjacent back and forth motion, with two time intervals at which actuator 2 influences both carriers. In these intervals, the state-of-practice controller results in large position errors, which is caused by the fact that the shared actuators are only able to take the correct commutation

angle for the most overlapping carrier. The other carrier then experiences a control force that deviates from the desired control force coming from the motion controller, due to a mismatch in the correct and attained commutation angle. The proposed allocation scheme is instead able to adapt, and finds a control input such that the trajectory can be followed well with significantly reduced position errors. Moreover, as the bottom subplot indicates, the power usage is decreased as well. As in the former two scenarios, peak position errors remain due to the presence of friction.

Scenario d)

Consider Figure 5.12. In this experiment, two carriers perform a complex motion. The carriers move independently as well as adjacent, where actuator 2 influences both carriers during the majority of the experiment. As discussed in Scenario c), the actuator can only take the correct commutation angle for the most overlapping carrier when using the state-of-practice control strategy, which results in pronounced large position errors (also note the different y-axis scale in the fourth subplot, compared to Scenario c)). The proposed allocation scheme is instead capable of adapting to such a situation by altering the current inputs, resulting in low position errors. This shows the capability of the system to perform independent motion tasks with high accuracy. During the adjacent motion (in the time span 2.7-5.8 s), the system behaves similarly to Scenario c), where the allocation scheme indeed outperforms the state-of-practice control solution in terms of position accuracy, see the inset in the fourth subplot. Note that the left and right error peaks in the inset are due to friction.

The experimental results show that the proposed control allocation scheme (compared to the state-of-practice controller used by the manufacturer) achieves improved tracking performance, evident from the Root-Mean-Square (RMS) values of the norm of the error $|e|_2$ for the scenarios a)-d), presented in Table 5.1. Furthermore, the allocation scheme allows for independent motion of multiple carriers while influenced by shared actuators (see Scenario d)), minimizes power consumption, alleviates the requirement on actuator spacing, and provides the possibility to take actuator limits into account. We will illustrate the potential benefits of the proposed allocation scheme when actuator limits are taken into account in the next section, by means of a simulation study.

Table 5.1. RMS values of $|e|_2$ for each scenario in the experimental study.

scenario	state-of-practice	control allocation
a)	0.0507	0.0111
b)	0.0230	0.0097
c)	0.0681	0.0185
d)	0.2193	0.0291

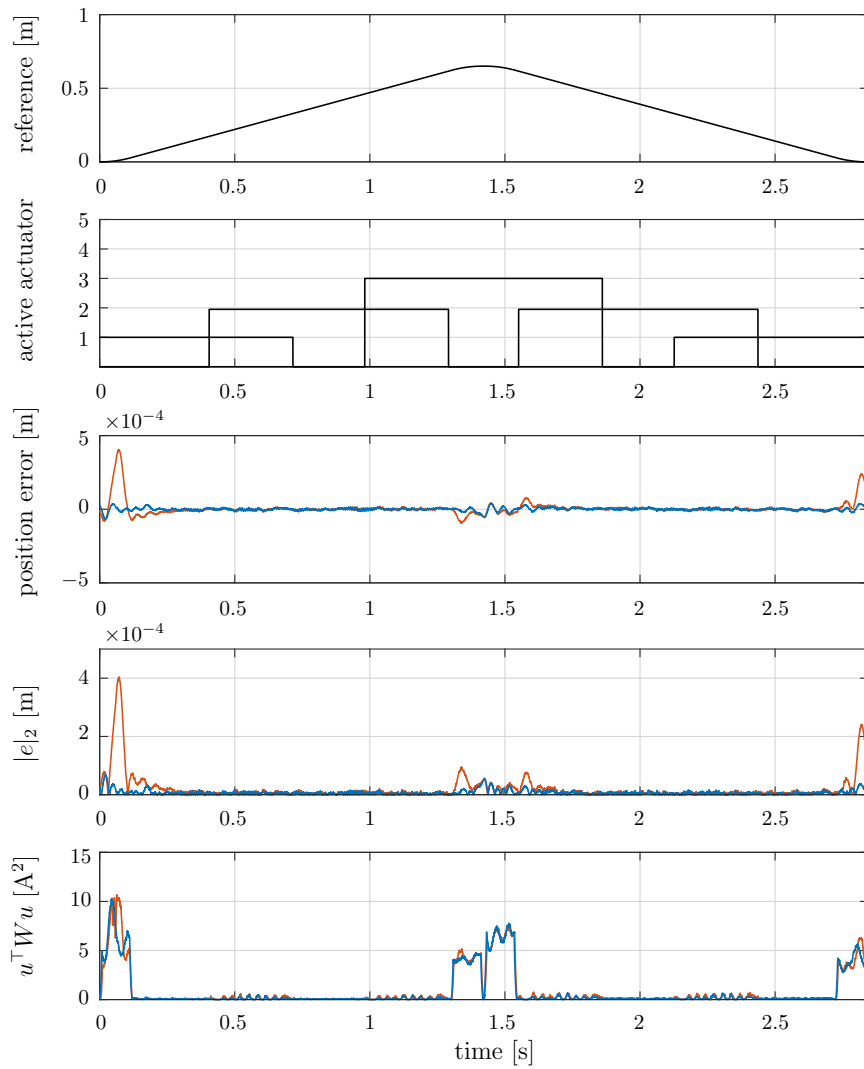


Figure 5.9. Experimental results for Scenario a).

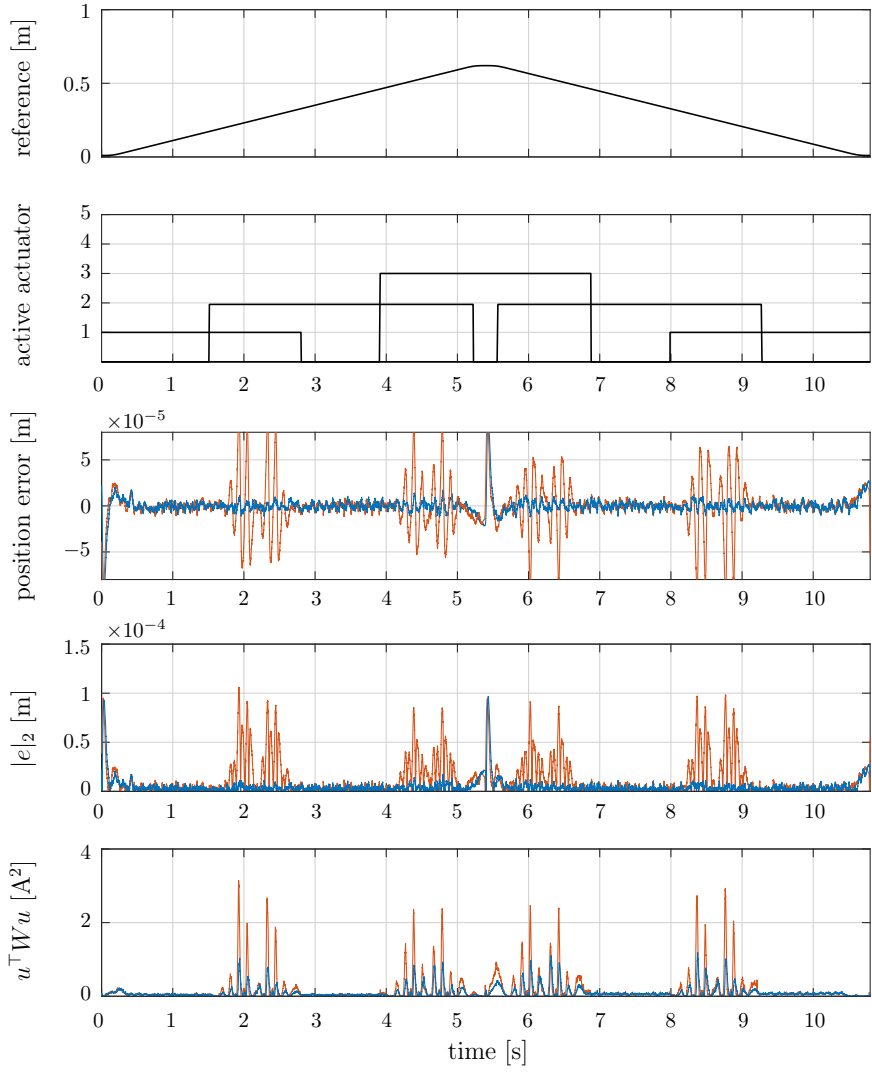


Figure 5.10. Experimental results for Scenario b).

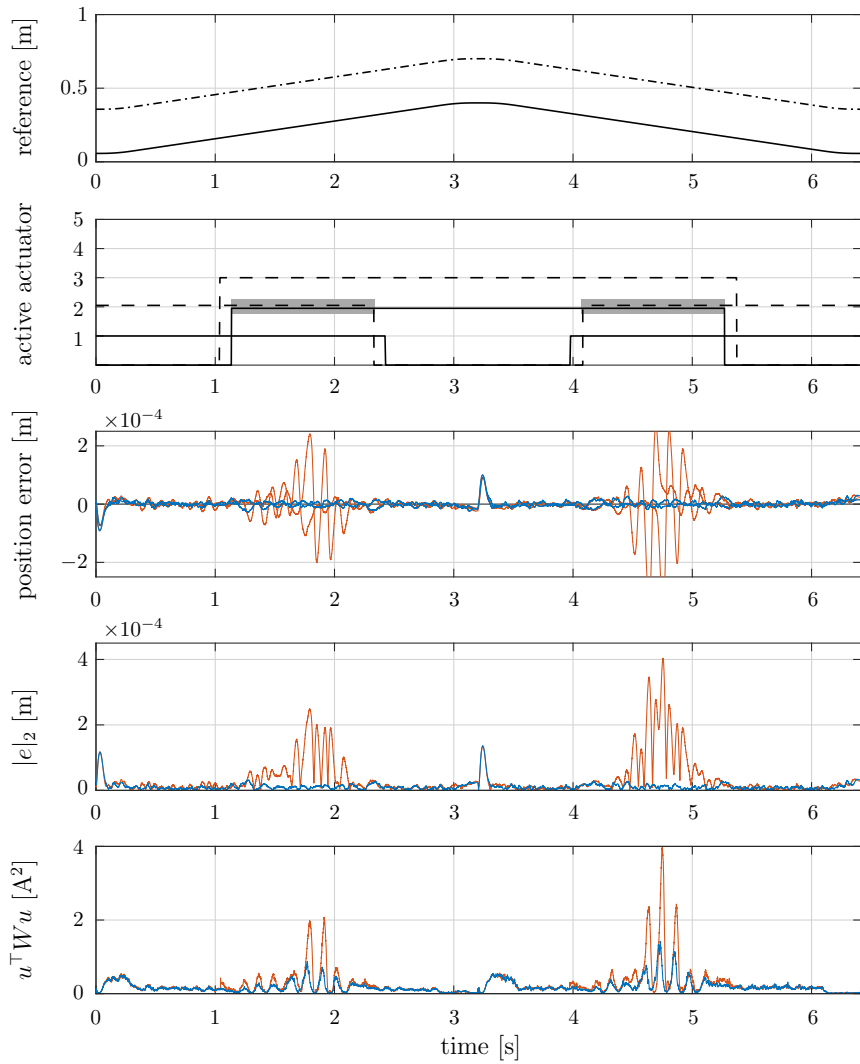


Figure 5.11. Experimental results for Scenario c).

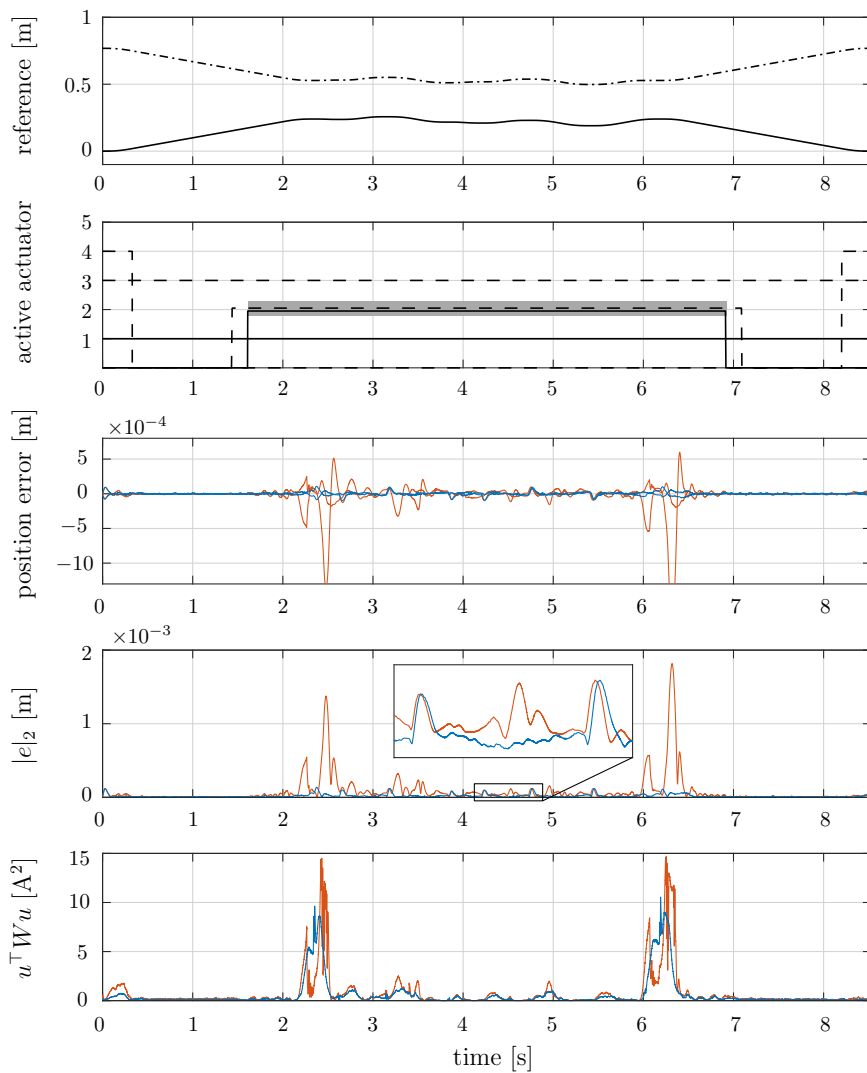


Figure 5.12. Experimental results for Scenario d).

5.4.2 Simulation study on constrained control allocation

In this section, we present a simulation study on the industrial IPMLSM-based transport system presented in Figure 5.6, to illustrate the performance benefits of the allocation approach when actuator limits are taken into account.

Similar to the experimental case study in Section 5.4.1, the considered system consists of two carriers and six actuators (cf. Figure 5.6), and is modeled by (5.1)-(5.3) with $n = 2$ and $m = 6$. The carrier masses are $M_1 = M_2 = 10.8$ kg. Moreover, by the physical dimensions of the actuators and carriers, an actuator may influence at most two carriers. The actuators are spaced at a distance equal to the carrier length (see Figure 5.3). For the simulations, we assume the absence of friction and magnet interaction forces between carriers. Therefore the feedforward term in (5.15) is adapted to

$$\tau_{ff,j} = 0.9M_j\ddot{r}_j. \quad (5.16)$$

The feedback part of the controller is the same as in the experiments and given by (5.14). We take $Q = 5I$, $W = I$ (with I the identity matrix of appropriate dimensions), and set *separate* current saturation limits for both $i_{\alpha k}$ and $i_{\beta k}$ (see Remark 5.3). We study the following two scenarios for both the constrained and unconstrained allocation approach (the latter for comparative purposes), and compare the results with the state-of-practice control strategy.

- a) a parallel motion of the carriers;
- b) a complex motion (similar to scenario d) in the experiments), combining independent and adjacent carrier motion.

We will now discuss the results for each scenario.

Scenario a)

Consider Figure 5.13, and in particular note the three areas where actuators influence both carriers. It stands out that the state-of-practice controller results in a relatively large position error during the acceleration phase. This is caused by the fact that the shared actuators are only able to take the correct commutation angle for the most overlapping carrier. The other carrier then experiences a control force that deviates from the desired control force coming from the motion controller. In contrast, the unconstrained allocation scheme of Section 5.3.2 is instead able to find a control input such that the trajectory can be followed well, with only small position errors. Next, we apply the *constrained* allocation scheme of Section 5.3.3 to investigate the potential of the controller when less powerful actuators are used. We set the current saturation limits for both $i_{\alpha k}$ and $i_{\beta k}$ to 0.8 A. The results are shown in red-dashed in Figure 5.13, where it can be observed that the limited attainable control force yields a local, inevitable increase in position error (see the third and fourth subplot), but significantly less actuator duty (see the bottom subplots).

Scenario b)

Consider Figure 5.14. The state-of-practice control solution is now unable to allow both carriers to follow the reference due to the mismatch in desired and implemented control force. It stands out that, due to the independent motion of the carriers, this mismatch is large enough for one carrier to completely deviate from the setpoint when using the state-of-practice controller. We note that this effect is less distinct in the corresponding experimental scenario d), due to e.g., the presence of Coulomb friction. The unconstrained allocation scheme of Section 5.3.2 suppresses the tracking error of both carriers instead. The *constrained* allocation scheme of Section 5.3.3, and challenging maximum values of 0.4 A for both $i_{\alpha,k}$ and $i_{\beta,k}$, results in decreased tracking performance with respect to the unconstrained case on the one hand (but still results in significantly better tracking compared to the state-of-practice controller), and significantly less actuator duty on the other hand.

The simulation results show, besides the benefits discussed in the experimental case study in Section 5.4.1, that the constrained control allocation scheme is capable of handling actuator constraints, while still pursuing the maximal achievable tracking performance. The constrained allocation scheme may therefore be used by the manufacturer to find a trade-off between desired tracking performance and required actuator power for future system designs: less powerful actuators are often more cost-effective. An advantage of a cost-effective system design also results from the fact that the allocation scheme allows for a less strict actuator spacing. Namely, the control allocation algorithm is able to compensate for fluctuations in the motor gains due to end-effects, by adapting the input currents. In this way, the correct control force can still be implemented. The economic benefit then comes from the fact that less actuators may be placed on the tracks while still achieving a specified performance.

5.5 Conclusions

We have presented a control allocation framework for an industrial high-accuracy transportation and positioning system, which results in enhanced tracking, allows for independent motion of multiple carriers, is able to take actuator limits into account, results in relaxed hardware design specifications, and minimizes power consumption. A decentralized allocation procedure is presented that enhances computational efficiency, such that the control allocation scheme is suitable for online implementation at high sampling rates, and facilitates scalability to large-scale system configurations. We have illustrated the benefits of the proposed control allocation strategy by means of simulations and an experimental case study.

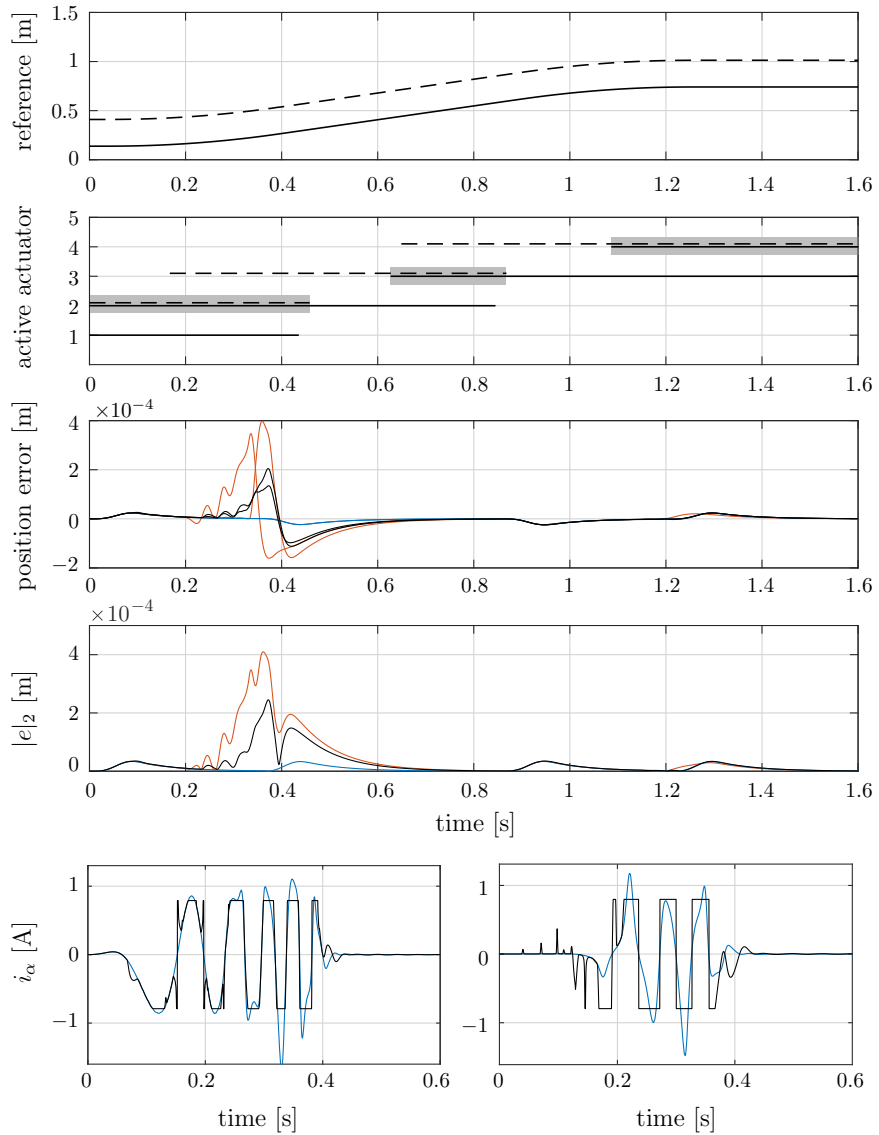


Figure 5.13. Simulation results for Scenario a).

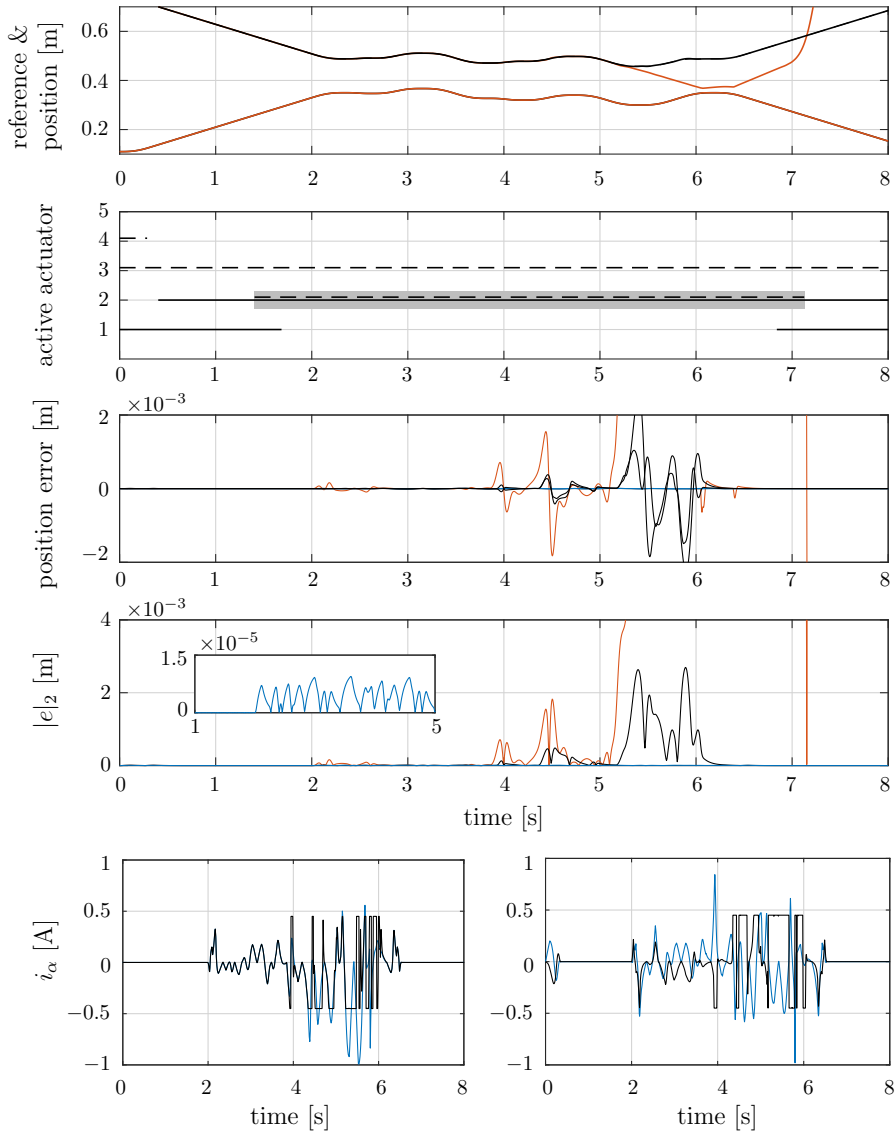


Figure 5.14. Simulation results for Scenario b).

Chapter 6

Modeling and control of a sheetfed printer paper path

Abstract – In this chapter, we present a model and a control framework for a sheetfed printer paper path. Models for single-pinch and double-pinch longitudinal paper transport are derived, where in the latter case the paper may be buckled, or may experience internal traction forces. A control architecture is presented that allows the paper to track a prescribed reference signal, and, at the same time, regulates internal traction forces in the paper sheet when transported by two pinches, to avoid print defects. Herein, overactuation is effectively exploited to address both control goals simultaneously in double-pinch transport. The working principle and effectiveness of the controller is illustrated by a simulation study, and experimentally demonstrated on a prototype paper path setup.

6.1 Introduction

In this chapter, we present a model and a control framework for a sheetfed printer paper path. Sheetfed printers are large industrial printers that are used for high productivity printing of cut sheets, see Figure 6.1. Sheets of paper enter the system at the paper input module, from which the sheets are transported through a paper path towards the image transfer station, where the image is printed. Subsequently, the sheets are dried and either re-enter the paper path (for the purpose of backside printing), or are transported to the finishing station. Paper transport within the system is realized by means of pinches. These pinches consist of two sets of rotating rollers, between which the paper is clamped and transported accordingly. The pinches are actuated individually or in groups, and sheets may be transported by either one pinch, or by multiple pinches simultaneously, depending on the size of the paper and the distance between subsequent

pinches in the paper path. This gives rise to an overactuated system.

Accurate transport of paper sheets throughout the system is key for obtaining a high throughput and high-quality prints, which gives rise to several control problems. First, the sheets of paper should be at the right place in the paper path at the right time, which involves accurate reference tracking of the pinches. Second, in order to avoid print defects, buckling of the sheets or too high traction forces in the sheets, must be avoided. These effects may occur when the paper is transported by multiple pinches simultaneously. Buckling is undesired, as the paper may then touch the base plate of the paper path, possibly damaging the prints. Too high traction forces are undesired as well, as it risks tearing the paper, or causing slip between the paper and the rollers. Such a traction control problem should therefore be taken into account in the design of a control architecture.

In previous generations of sheetfed printing systems, the pinches are actuated by DC motors. Numerous closed-loop control strategies for longitudinal position and velocity sheet control in such systems have been proposed in the literature, as we discuss below. Generally, these strategies are composed in a hierarchical structure. First, a high-level sheet control loop measures the position of a sheet in the paper path at discrete points. Based on the difference between the desired and measured sheet position, the reference velocities of the motor are adjusted to correct for the difference. Such a control loop is required in order to deal with, e.g., slight variances in the pinch radii or in the sheet characteristics. Second, a low-level motion controller is designed such that the reference velocities are indeed realized by the pinches.

High-level sheet control in a paper path for photocopiers is addressed in [47], [48] and [122], where the reference signals for the paper sheets (which should be tracked by the pinches) are adapted online. As a result, the ar-

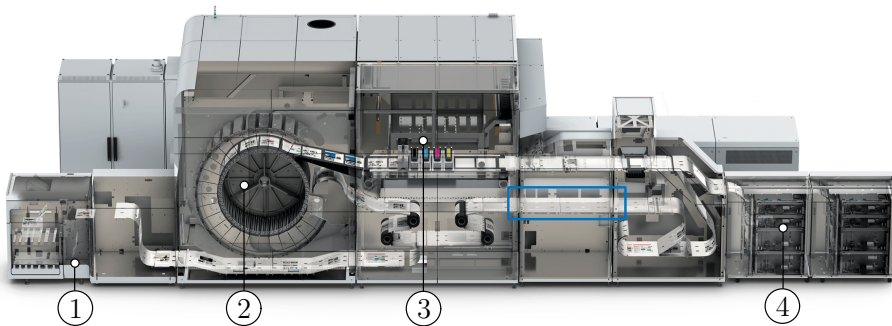


Figure 6.1. Industrial sheetfed printing system (Océ Technologies, [111]). Paper input module (4), image transfer station (3), dryer (2), and finishing station (1).

rival of sheets at the image transfer station is synchronized with the image to be printed. Model-based feedback control in a printer paper path, considering closed-loop stability and external disturbances, is presented in [27] and [37]. The hierarchical control structure is maintained, where the system is modeled as a piecewise linear system (in the sense that sheets interact with different pinches). An \mathcal{H}_∞ controller synthesis is proposed for the low-level tracking control problem, respecting prescribed stability and performance demands. The controller is validated in both simulations and experiments, but double-pinch paper transport and the associated traction control problems are, however, not addressed. Other research focusses on lateral sheet control using steerable pinches [132] or using multiple individually acutated wheels on each pinch [130], on improved sheet position measurements [88], and on sheet trajectory planning and control in parallel printing systems [87].

In this chapter, we focus on the low-level control problem and address both the reference tracking control problem and the traction control problem. That is, we assume that sheets are assigned a certain reference trajectory by some high-level control scheme, that must be realized by the pinches. We consider the two logical states of a sheet, which reflect the sheet being transported by either one or two pinches, as schematically depicted in Figure 6.2. The latter encompasses two cases. Depending on the relative velocity between the two pinches, a sheet may either be buckled, or may experience internal traction forces. In order to arrive at a control framework, we first present a model for one-pinch and two-pinch paper transport, where transitions between buckling and traction are suitably taken into account. Such a transition gives rise to a non-smooth dynamical system. Moreover, we take into account that pinches are actuated by stepper motors in the current generation sheetfed printers. We then present a control framework that realizes setpoint tracking of the pinches, and, at the same time, avoids buckling and regulates traction forces to a prescribed (safe) level, thereby avoiding the risk of print defects. In order to achieve these goals, manual control allocation is employed. In contrast to the control allocation technique in Chapter 5 (where the allocation is performed automatically by solving an optimization problem online), we rely here on engineering intuition to manually assign control goals to each actuator.

The main contributions of this chapter can be summarized as follows. The first contribution is the derivation of a non-smooth dynamical model of a paper path, including transitions between one and two-pinch transport, and transition between buckling and traction and vice versa. As a second contribution, we present a *hybrid* model of these dynamics, which may be useful for future controller designs, closed-loop stability analyses, and simulation studies. The third contribution is then the design of a control framework that realizes 1) reference tracking of the pinches, and 2) regulates traction forces in the sheets. The fourth contribution is a simulation and experimental study on the effectiveness of the proposed control architecture.

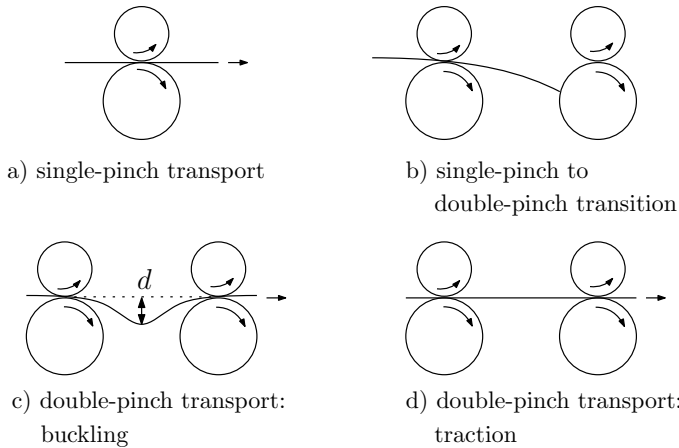


Figure 6.2. Different logical states of paper transport in a paper path, where d indicates the paper deflection in the buckling case.

The remainder of this chapter is organized as follows. In Section 6.2, the paper path model is presented. We formalize the control goals and discuss the proposed control architecture in Section 6.3. In Section 6.4, the working principle of the controller is experimentally demonstrated on a prototype paper path setup, and conclusions are reported in Section 6.5.

6.2 Paper path modeling

In this section, we describe the longitudinal topology of a pinch in a paper path, and derive a dynamic model for it. We consider the two logical states of a sheet being transported by either one, or two pinches. As discussed in the previous section, the latter logical state encompasses two cases. Namely, a sheet experiences no internal traction (i.e., the sheet is buckled), or does experience traction forces as a result of the interaction with two pinches. We will now refer to these logical states as *buckling* and *traction*, respectively. We specifically address the transition between the buckling and traction cases, as it gives rise to an impulsive dynamical system model. Before deriving models for single-pinch and double-pinch paper transport separately in the following sections, we briefly discuss stepper motor control which we use in the model derivation. Subsequently, we derive a *hybrid* model that includes the transitions between single-pinch and double-pinch transport, and the transitions between the cases *buckling* and *traction*.

6.2.1 Stepper motor control

Each pinch in the paper path is actuated by a two-phase stepper motor, which requires a slightly different control approach compared to DC-actuated motion systems. In particular, a stepper motor realizes a step-by-step rotation, where the motor is sent a separate pulse for each step. Since each pulse causes the motor to rotate a certain angle, stepper motors can be controlled without any feedback mechanism (as is indeed the case for the state-of-practice paper path control architecture, see Section 6.4 below). The smaller the angle (i.e., step size), the higher the achievable positioning accuracy. It is, however, possible to use a stepper motor in a feedback loop, thereby improving the achievable performance, as we will show in Sections 6.3.3 and 6.4.

A stepper motor takes the desired orientation of the magnetic field of the stator as an input, which is then converted to a series of pulses provided to the motor electronics. The stator of the stepper motor consists of several coil windings, which produce magnetic flux and establish north and south poles when excited with a DC current. The rotor consists of a permanent magnet, and, due to the attraction and repulsion between the rotor and the stator poles, the rotor poles eventually align with the magnetic field established in the stator. The step size is determined by the number of coil windings, and the way the windings are energized. By partially energizing the windings, the regular step angle of the motor is subdivided into smaller steps, a technique called *microstepping*, see, e.g., [123, Sec. 30.8.6]. For the considered application, the stepper motors have 50 stator pole pairs and the microstepping technique is employed, resulting in 3200 steps per revolution.

For a stepper motor with a single winding (i.e., two steps per revolution), there exists a sinusoidal relationship between the orientation of the magnetic field and the torque generated by the motor [50, Eq. 8.4]. Due to the relatively small step size of the considered motors, we can use an approximation of this relationship, given by

$$\tau = k_m(\theta_f - \theta_m), \quad (6.1)$$

with τ the torque generated by the motor, θ_f the orientation of the magnetic field of the stator, θ_m the rotor angle, and k_m the mechanical stiffness of the motor.

6.2.2 Single pinch modeling

Consider Figure 6.3. During transport, a sheet of paper is clamped between two sets of rollers. The *driven roller* ① is connected to a *stepper motor* ② via a flexible belt ③. The driven roller is covered with layer of viscoelastic material ④. The *pressure roller* ⑤ is connected to the fixed world with a leaf spring ⑥, providing a small force perpendicular to the paper. In this way,

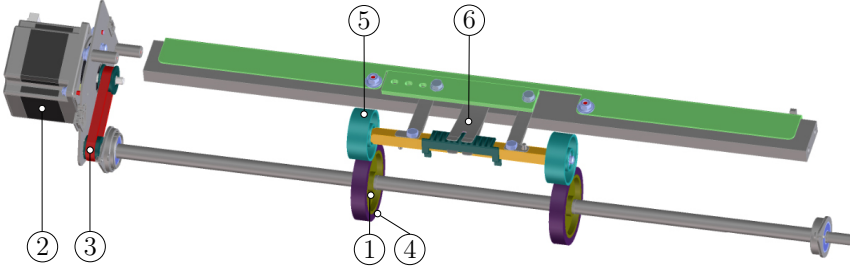


Figure 6.3. CAD representation of a paper transport pinch in a sheetfed printer paper path (Océ Technologies, [111]).

sufficient traction is obtained to transport the sheet without slipping of the rollers.

Consider Figure 6.4 for a schematic representation of the derived single pinch model. The rotor of the stepper motor has angular position θ_m , inertia J_m , and generates an input torque τ , through the relation in (6.1). The flexible belt connecting the rotor with the driven roller is modeled as a parallel (linear) spring and damper, with coefficients k_b and c_b , respectively. At both the motor and the driven roller side, the belt is connected to a pulley with radii r_{mb} and r_{db} , respectively. The driven roller itself has radius r_d , angular position θ_d , and inertia J_d . The viscoelastic layer on the driven roller is modeled as a Maxwell spring-damper model (with spring and damper constants k_r and c_r , respectively), augmented with a transmission ratio p , to incorporate the increase in relative tangential velocity of the rubber layer at the contact point with the pressure roller, as a result of the rubber deformation. We denote the tangential force in the rubber layer by F , which plays an important role in characterizing traction forces in the paper sheets later on. Finally, the pressure roller has radius r_p , angular position θ_p , and inertia J_p . We assume that there is no slip between the pressure roller and the transported sheets (which we formalize later on), so that the position of the leading edge of the sheet is denoted by $x_s = r_p \theta_p$ (neglecting any deflection of the sheet).

In order to address a generic pinch in a paper path, we parameterize the single-pinch model by the index i , where $i \in \{1, \dots, n\}$ denotes the i^{th} pinch in the paper path, assuming that the pinches are logically numbered 1 to n throughout the path. Using the set of generalized coordinates $q_i := [\theta_{m,i}, \theta_{d,i}, \theta_{p,i}]^T$, the governing (linear) equations of motion are then given by

$$M_i \ddot{q}_i + H_i(q_i, \dot{q}_i, F_i) = S_i \tau_i, \quad (6.2a)$$

$$\dot{F}_i = G_i(\dot{q}_i) - \frac{k_r}{c_r} F_i, \quad (6.2b)$$

$$\tau_i = k_m(\theta_{f,i} - \theta_{m,i}), \quad (6.2c)$$

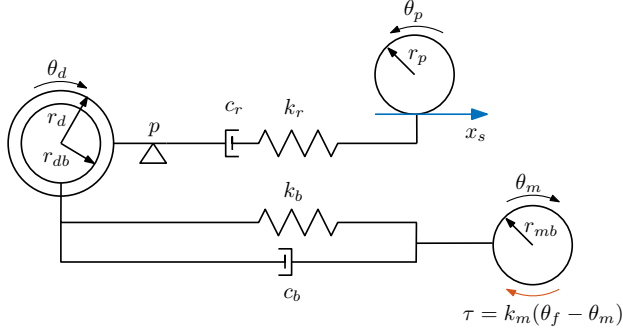


Figure 6.4. Schematic representation of a pinch. The blue arrow represents the direction in which the paper sheets are transported.

with the relationship between generated motor torque and magnetic field orientation in (6.2c) as discussed in Section 6.2.1. Note that the magnetic field orientation $\theta_{f,i}$ is the input of the system. In (6.2a), the stiffness and damping contributions are collected in H_i , and M_i is the inertia matrix, i.e.,

$$M_i = \begin{bmatrix} J_{m,i} & 0 & 0 \\ 0 & J_{d,i} & 0 \\ 0 & 0 & J_{p,i} \end{bmatrix}, \quad (6.3)$$

$$H_i = \begin{bmatrix} -k_b(r_{db}\theta_{d,i} - r_{mb}\theta_{m,i}) - c_b(r_{db}\dot{\theta}_{d,i} - r_{mb}\dot{\theta}_{m,i}) \\ k_b(r_{db}\theta_{d,i} - r_{mb}\theta_{m,i}) + c_b(r_{db}\dot{\theta}_{d,i} - r_{mb}\dot{\theta}_{m,i}) + pr_d F_i \\ r_p F_i \end{bmatrix}.$$

The vector $S_i = [1 \ 0 \ 0]^\top$ reflects the generalized force direction associated to the torque τ_i generated by the stepper motor to the dynamics of the pinch. The tangential force F_i in the rubber layer is described by the differential equation (6.2b), with

$$G_i = k_r pr_d \dot{\theta}_{d,i} - k_r r_p \dot{\theta}_{p,i}, \quad (6.4)$$

which is obtained by isolating the forces acting on the spring and damper, and noting that the force in both elements is identical, since they are placed in series.

Let us now pose the following assumptions regarding paper transport.

Assumption 6.1. *The transported paper sheets cannot be elongated in longitudinal direction.*

Assumption 6.2. *All pinches in the paper path are identical, and no slip occurs between a paper sheet and the pressure roller.*

A consequence of Assumption 6.2 is that there exists a unique relationship between the position of the sheet, and the angular position of the pressure roller.

6.2.3 Double-pinch transport modeling

With the single-pinch model in place, we extend the model to two-pinch transport in this section. Note that when the paper is transported by two consecutive pinches, we distinguish the cases *buckling* and *traction*. Whereas the former case yields an unconstrained motion, the latter case induces a *unilateral* constraint between the motion of the two pinches. Indeed, a consequence of Assumption 6.1 is that the paper sheets are rigid in traction. Then, by Assumption 6.2, the velocities of the pressure rollers in both pinches are equal, i.e., $\dot{\theta}_{p,i} = \dot{\theta}_{p,i+1}$ for some $i \in \{1, \dots, n-1\}$. The unilateral nature of the constraint can be explained intuitively as follows. A positive relative velocity $\dot{\theta}_{p,i+1} - \dot{\theta}_{p,i}$ results in traction, because the downstream pinch pulls the paper. A negative relative velocity results in buckling, because the upstream pinch pushes the paper.

The transition from the *buckling* case to *traction* case is characterized by an impact force. As a result of the switching dynamics, a discontinuity in the velocity of the pressure rollers may occur. Such a buckling-to-traction transition is bound to occur due to the controller design in Section 6.3, in line with the control goals discussed in Section 6.1. That is, the controller should avoid buckling (as it risks print defects), and pursues ending up in the traction case as soon as the sheet enters the second pinch. In order to capture unconstrained and constrained motion, as well as the transition between these cases, we derive subsequently the non-impulsive part and the impulsive part of the equations of motion, and finally combine these contributions to a single non-smooth model for two-pinch paper transport.

In order to distinguish between the cases *buckling* and *traction*, we introduce a *distance function* $g_{N,i} \geq 0$, parametrized by $i \in \{1, \dots, n-1\}$ to indicate the considered pinch pair. Such a geometrical variable is used to capture the absolute distance between two bodies, see, e.g., [93, Ch. 5]. The bodies are separated when $g_N > 0$, and are in contact when $g_N = 0$. In our setting, g_N depends on the angular position of two subsequent pressure rollers $\theta_{p,i}$ and $\theta_{p,i+1}$, and is designed such that $g_N > 0$ corresponds to *buckling*, and $g_N = 0$ corresponds to *traction*. We design the distance function g_N as follows:

$$g_{N,i} := r_p(\theta_{p,i} - \theta_{p,i+1}) + c_i, \quad (6.5)$$

with $c_i \in \mathbb{R}$ a constant such that $g_{N,i} = 0$ is realized when traction occurs, at which point the angular positions of both pressure rollers are not necessarily equal in absolute sense. Note that, for a closed contact, we have $g_{N,i} = 0$ which serves as a constraint equation (see, e.g., [64, Sec. 1.3]) for the traction case.

Remark 6.3. *Although the distance function in 6.5 indeed distinguishes buckling and traction, it is in general not measurable in a practical setting. The size of the deflection of the paper in the buckling case may vary and cannot be measured, and, therefore, it is not known at which angular positions of the pressure roller*

a buckling-to-traction transition occurs, , i.e., c_i in (6.5) is typically unknown. \lrcorner

Non-impulsive dynamics

Consider two neighboring pinches in a paper path, logically numbered 1 and 2 (without loss of generality). Given the vector of generalized coordinates $q := [\theta_{m,1}, \theta_{d,1}, \theta_{p,1}, \theta_{m,2}, \theta_{d,2}, \theta_{p,2}]^\top$, the equations of motion for the *non-impulsive* part of double pinch paper transport are as follows:

$$M \frac{d\dot{q}}{dt} + H(q, \dot{q}, F) = ST + W_N(q)\lambda_N, \quad (6.6a)$$

$$\dot{F} = G(\dot{q}) + KF, \quad (6.6b)$$

$$g_N \in N_{\mathbb{R}_{\leq 0}}(-\lambda_N), \quad (6.6c)$$

where we omit the index i for g_N for the sake of brevity. The matrices in (6.6) are given by

$$\begin{aligned} M &:= \begin{bmatrix} M_1 & 0 \\ 0 & M_2 \end{bmatrix}, \quad H := \begin{bmatrix} H_1 \\ H_2 \end{bmatrix}, \quad S := [S_1 \quad S_2], \\ T &:= \begin{bmatrix} \tau_1 \\ \tau_2 \end{bmatrix}, \quad F := \begin{bmatrix} F_1 \\ F_2 \end{bmatrix}, \quad G := \begin{bmatrix} G_1 \\ G_2 \end{bmatrix}, \quad K = \begin{bmatrix} -\frac{k_r}{c_r} & 0 \\ 0 & -\frac{k_r}{c_r} \end{bmatrix}, \end{aligned} \quad (6.6d)$$

and the torque generated by the stepper motor follows from

$$\tau_i = k_m(\theta_{f,i} - \theta_{m,i}), \quad i \in \{1, 2\}. \quad (6.6e)$$

Let us now elaborate on the different ingredients of the equations of motion in (6.6). The contribution $W_N(q)\lambda_N$ (where we omit the index i for the sake of brevity) in (6.6a) denotes the constraint force (i.e., the forces required to satisfy the constraint $g_N = 0$ in the traction case), with λ_N the magnitude of the constraint force, and W_N the generalized force direction. The latter is related to the distance function g_N by

$$W_N = \left(\frac{\partial g_N}{\partial q} \right)^\top = [0 \quad 0 \quad r_p \quad 0 \quad 0 \quad -r_p]. \quad (6.7)$$

The unilateral constraint force λ_N can be viewed as a contact force, holding together two rigid bodies (in our setting, the pressure rollers), and is described by Signorini's set-valued force law, see, e.g., [93, Sec. 5.3]. That is, the contact force can be positive when contact is present (i.e., $g_N = 0$), and must vanish when the contact is open (i.e., $g_N > 0$). Due to the unilateral nature of the considered constraint, the contact force λ_N and distance function g_N satisfy the following complementarity conditions:

$$g_N \geq 0, \quad \lambda_N \geq 0, \quad g_N \lambda_N \geq 0. \quad (6.8)$$

These conditions translate to the force law in normal cone formulation in (6.6c), where $N_{\mathbb{R}_{\leq 0}}$ is defined as the normal cone of the set of admissible contact forces $\{-\lambda_N \in \mathbb{R} \mid \lambda_N \geq 0\} = \mathbb{R}_{\leq 0}$, see [93, Sec. 5.3], i.e.,

$$g_N \in N_{\mathbb{R}_{\leq 0}}(-\lambda_N) := \begin{cases} 0 & \text{if } \lambda_N > 0, \\ [0, \infty), & \text{if } \lambda_N = 0. \end{cases} \quad (6.9)$$

Impulsive dynamics

We will now discuss the impulsive contact forces that appear at a buckling-to-traction transition and their effect on the dynamics. The impact at a buckling-to-traction transition, which causes a sudden change in relative velocity, is accompanied by a normal contact impulse $\Lambda_N > 0$. Let us first formalize the relative velocity between the interacting bodies, i.e.,

$$\gamma_N(q, \dot{q}) = W_N^\top(q)\dot{q}. \quad (6.10)$$

In order to describe impact, we introduce a Newton-type impact law for contact impulses, given by

$$\gamma_N^+ = -e_N \gamma_N^-, \quad g_N = 0, \quad 0 \leq e_N \leq 1, \quad (6.11)$$

with γ_N^+ and γ_N^- the post and pre-impact velocities, respectively, and e_N Newton's coefficient of restitution. Without loss of generality, we model the buckling-to-traction transition as a completely inelastic impact in our setting, so that the relative post-impact pressure roller velocity is zero, in accordance with Assumption 6.1, i.e., $e_N = 0$. Following [61], we define an auxiliary variable ξ_N for the purpose of writing the impact law as an complementarity condition similar to (6.8):

$$\xi_N := \gamma_N^+ + e_N \gamma_N^-. \quad (6.12)$$

Using (6.9) and (6.12), we write the impact law as

$$\xi_N \in N_{\mathbb{R}_{\leq 0}}(-\Lambda_N), \quad g_N = 0. \quad (6.13)$$

Indeed, (6.13) only holds for closed contacts (i.e., $g_N = 0$), since the relative velocity γ_N can have any value without any contact force present as long as the contact is not closed.

Double-pinch model derivation

In order to arrive at a double-pinch model that encompasses bucking, traction, and the transition, we take several steps. First, we rewrite the force law in (6.6c) on velocity level, i.e.,

$$\gamma_N(q, \dot{q}) \in N_{\mathbb{R}_{\leq 0}}(-\lambda_N), \quad g_N = 0. \quad (6.14)$$

Second, we write the force law for the non-impulsive motion on velocity level (6.14) in the same form as (6.13). To this end, note that $\dot{q}^+ = \dot{q}^-$ holds for non-impulsive motion. Moreover, given any $y \in N_{\mathbb{R}_{\leq 0}}$, for any $\mu > 0$, it holds that $\mu y \in N_{\mathbb{R}_{\leq 0}}$ [93, p. 103]. Then, (6.14) implies that $(1 + e_N)\gamma_N \in N_{\mathbb{R}_{\leq 0}}(-\lambda_N)$, which, in turn, implies for the non-impulsive motion $\gamma_N + e_N\gamma_N \in N_{\mathbb{R}_{\leq 0}}(-\lambda_N)$. Finally, using (6.12), we construct the force law

$$\xi_N \in N_{\mathbb{R}_{\leq 0}}(-\lambda_N), \quad g_N = 0. \quad (6.15)$$

With the force law (6.15) and impact law (6.13) in place, we are ready to merge the impulsive and non-impulsive contact forces into a single law. To this end, we define a differential measure of the contact percussions (see [93, Eq. 5.97]) as follows:

$$dP_N := \lambda_N dt + \Lambda_N d\eta, \quad (6.16)$$

with Lebesgue measurable part $\lambda_N dt$ and an atomic part $\Lambda_N d\eta$, see [93, Sec. 5.4]. The force law and impact law in (6.15) and (6.13), respectively, are then merged as

$$\xi_N \in N_{\mathbb{R}_{\leq 0}}(-dP_N), \quad g_N = 0. \quad (6.17)$$

The presence of impulsive forces dictates us to write the complete equations of motion for two-pinch transport as a measure differential equation, i.e., an equation of motion on the level of momenta. To this end, we introduce the vector of generalized velocities u , which satisfies $u = \dot{q}$ almost everywhere. We then rewrite (6.6) and include the impulsive part using the developments above:

$$Mdu + H(q, u, F)dt = STdt + W_N(q)dP_N, \quad (6.18a)$$

$$dF = G(u)dt + KFdt, \quad (6.18b)$$

$$\xi_N \in N_{\mathbb{R}_{\leq 0}}(-dP_N), \quad g_N = 0. \quad (6.18c)$$

The complete model for double-pinch paper transport is given by (6.18), which holds for all time instances t , and encompasses buckling, traction, and transitions.

The force law in (6.18c) yields an *implicit* expression for the post-impact velocities. That is, the post-impact velocities must balance with the contact forces and can, therefore, only be determined using an iterative numerical method, e.g., fixed-point iteration or Newton's method (see [72]).

Remark 6.4. *In contrast to a buckling-to-traction transition, a traction-to-buckling transition does not yield an impulsive motion, because such a transition corresponds to breaking contact in the current modeling framework.* \lrcorner

By the developments in this section, a complete model for a paper transport path is given by (6.2) and (6.18). We addressed explicitly the transition

between the cases buckling and traction in (6.18). The transition between one-pinch transport and two-pinch transport encompasses a switch between (6.2) and (6.18). Such a transition is measured in practice by optical sensors, and is, therefore, not addressed further. Finally, we note that after a transition from one-pinch to two-pinch transport, the sheet is always buckled. Namely, due to the finite stiffness of paper and the presence of gravity, the sheet bends when it exits a pinch. The sheet then bumps into the driven roller of the subsequent pinch, which results in a folded sheet when it reaches the second pinch' center (see Figure 6.2-b,c).

6.2.4 Hybrid systems description

We now present the two-pinch model developed in the previous section in the hybrid modeling framework of [63]. Such a hybrid model may be beneficial for future controller designs, closed-loop analyses, and performing computer simulations of the system (e.g., using the Hybrid Systems simulation toolbox [133]). In particular, the discontinuities in pressure roller velocity as a result of the impacts are modeled as discrete jumps. In order to correctly model such discontinuities in the hybrid framework, an *explicit* expression for the post-impact velocities of the pressure rollers is required, as we will present first. We also need an explicit expression for the Lagrange multiplier λ_N in order to identify the buckling-to-traction transitions and vice versa. Finally, we construct the hybrid systems description.

Explicit post-impact velocity map

We employ the explicit post-impact velocity expression in [16, Eq. (5)], which is applicable in our setting since [16, As. 1] is satisfied for the Newton-type impact law that we consider (see (6.13)), see also [92]. That is,

$$\dot{q}^+ = \bar{Z}(\dot{q}^-) := (1 + e_N)\text{prox}_{\mathcal{T}^+(q)}^M(\dot{q}^-) - e\dot{q}^-, \quad (6.19)$$

with the proximal point on a set \mathcal{T}^+ in the metric M defined as

$$\text{prox}_{\mathcal{T}^+}^M(y^-) := \arg \min_{y^+ \in \mathcal{T}^+} (y^+ - y^-)^\top M(y^+ - y^-). \quad (6.20)$$

Finally, the set \mathcal{T}^+ is defined as

$$\mathcal{T}^+ := \{\dot{q} \in \mathbb{R}^n \mid W_N^\top \dot{q} \geq 0\}. \quad (6.21)$$

With these definitions in place, we derive the explicit post-impact velocity mapping tailored for our setting. Since the pressure rollers are the only bodies that experience impact, consider the coordinates $q_p := [\theta_{p,1}, \theta_{p,2}]^\top$, and the pressure roller inertia matrix $M_p := \text{diag}(J_p, J_p)$ (both pressure rollers have

the same inertia by Assumption 6.2). Using (6.7) and the fact that we take $e_N = 0$, the post-impact velocity mapping \bar{Z}_p (according to (6.19)), tailored for our setting, is given by

$$\dot{q}_p^+ = \bar{Z}_p(\dot{q}_p^-) := \text{prox}_{\mathcal{T}^+}^{M_p}(\dot{q}_p^-), \quad \mathcal{T}^+ = \{\dot{q}_p \in \mathbb{R}^2 \mid \dot{\theta}_{p,1} \geq \dot{\theta}_{p,2}\}. \quad (6.22)$$

The design of the distance function g_N in (6.5) dictates $\theta_{p,1} \geq \theta_{p,2} - \frac{c}{r_p}$ in the buckling case. In order to arrive in the traction case (whereby $g_N = 0$), the velocity of the downstream pinch must be larger than (or equal to) the velocity of the upstream pinch, i.e., $\dot{\theta}_{p,1} \leq \dot{\theta}_{p,2}$. Hence, the pre-impact pressure roller velocities satisfy

$$\dot{q}_p^- \in \mathcal{T}^- := \{\dot{q}_p^- \in \mathbb{R}^2 \mid \dot{\theta}_{p,1}^- \leq \dot{\theta}_{p,2}^-\}. \quad (6.23)$$

The sets \mathcal{T}^+ and \mathcal{T}^- are depicted in Figure 6.5. From this figure, it is evident that the proximal point of any $\dot{q}_p^- \in \mathcal{T}^-$ on the set \mathcal{T}^+ (i.e., characterizing the shortest distance of \dot{q}_p^- to \mathcal{T}^+) lies on the diagonal $\dot{\theta}_{p,1} = \dot{\theta}_{p,2}$. Hence, the post-impact velocities of both pressure rollers are equal. Given these observations, let us construct the map \bar{Z}_p by rewriting (6.22) as

$$\begin{aligned} \dot{q}_p^+ &= \text{prox}_{\mathcal{T}^+}^{M_p}(\dot{q}_p^-) \\ &= \arg \min_{\dot{q}_p^+ \in \mathcal{T}^+} (\dot{q}_p^+ - \dot{q}_p^-)^\top M_p (\dot{q}_p^+ - \dot{q}_p^-) \\ &= \arg \min_{\dot{\theta}_{p,1}^+, \dot{\theta}_{p,2}^+} J_p(\dot{\theta}_{p,1}^+ - \dot{\theta}_{p,1}^-)^2 + J_p(\dot{\theta}_{p,2}^+ - \dot{\theta}_{p,2}^-)^2, \end{aligned} \quad (6.24)$$

which yields the following explicit expression for the post-impact velocities:

$$\dot{\theta}_{p,1}^+ = \dot{\theta}_{p,2}^+ = \frac{1}{2}(\dot{\theta}_{p,1}^- + \dot{\theta}_{p,2}^-). \quad (6.25)$$

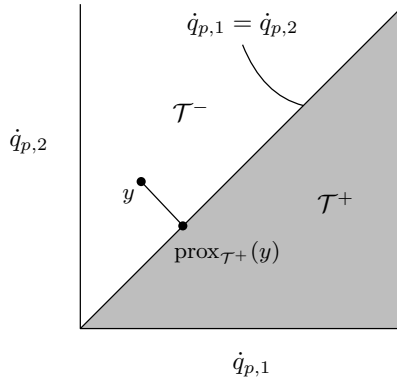


Figure 6.5. The sets \mathcal{T}^- and \mathcal{T}^+ for the pre and post-impact pressure roller velocities, respectively.

Using (6.25), the post-impact velocity map \bar{Z}_p is given by

$$\bar{Z}_p(\dot{q}_p^-) := \begin{bmatrix} \frac{1}{2}(\dot{\theta}_{p,1}^- + \dot{\theta}_{p,2}^-) \\ \frac{1}{2}(\dot{\theta}_{p,1}^- + \dot{\theta}_{p,2}^-) \end{bmatrix}. \quad (6.26)$$

For the purpose of the hybrid model below, we finally define

$$Z_p(\dot{q}_p^-) := \frac{1}{2}(\dot{\theta}_{p,1}^- + \dot{\theta}_{p,2}^-). \quad (6.27)$$

Explicit Lagrange multiplier

In order to construct the the hybrid model (6.30) below, an explicit expression for the constraint force λ_N is required. By the complementarity conditions in (6.8) we know that $\lambda_N = 0$ when $g_N > 0$. When $g_N = 0$, we obtain an expression for λ_N by a forward dynamic analysis. For the traction case, the distance function g_N plays the role of a constraint equation, i.e., $g_N := r_p(\theta_{p,1} - \theta_{p,2}) + c = 0$ in traction, which can be written on velocity level (see [64, Sec. 1.3]) as $\dot{g}_N = W_N \dot{q} = 0$, and on acceleration level as

$$W_N \ddot{q} = 0. \quad (6.28)$$

From (6.6) we have that $\ddot{q} = M^{-1}(ST - H(q, \dot{q}, F) + W\lambda_N)$. Substitution of this expression for \ddot{q} in (6.28) yields the following explicit expression for λ_N :

$$\begin{aligned} \lambda_N &= (W_N M^{-1} W_N)^{-1} (W_N M^{-1} (H(q, \dot{q}, F) - ST)) \\ &= \frac{1}{2}(F_2 - F_1). \end{aligned} \quad (6.29)$$

Hence, the constraint force λ_N only depends on the tangential forces F_i , $i \in \{1, 2\}$, in the rubber layer of the driven rollers.

Hybrid model

Using the expressions for the post-impact pressure roller velocities, and for the constraint force, we write the model for two-pinch paper transport as a hybrid system \mathcal{H} . We distinguish the cases of *buckling* and *traction* by a state $m \in \{0, 1\}$, where $m = 0$ corresponds to the buckling case, and $m = 1$ corresponds to the traction case. With state vector $x := [q, \dot{q}, F, m]^\top \in \mathbb{R}^6 \times \mathbb{R}^6 \times \mathbb{R}^2 \times \{0, 1\} =: \Theta$, the hybrid system \mathcal{H} is given by

$$\mathcal{H} : \begin{cases} \dot{x} = \mathcal{F}(x), & x \in \mathcal{C}, & (6.30a) \\ x^+ = \mathcal{J}_{01}(x), & x \in \mathcal{D}_{01}, & (6.30b) \\ x^+ = \mathcal{J}_{10}(x), & x \in \mathcal{D}_{10}, & (6.30c) \end{cases}$$

where the flow map is

$$\mathcal{F}(x) := \begin{bmatrix} -M^{-1}H(q, \dot{q}, F) + M^{-1}ST + m(M^{-1}W_N\lambda_N) \\ G(\dot{q}) + KF \\ 0 \end{bmatrix}, \quad (6.30d)$$

with λ_N given by (6.29). The jump maps are

$$\mathcal{J}_{01}(x) := [q, \dot{\theta}_{m,1}, \dot{\theta}_{d,1}, Z_p(\dot{q}_p), \dot{\theta}_{m,2}, \dot{\theta}_{d,2}, Z_p(\dot{q}_p), F, 1]^\top, \quad (6.30e)$$

$$\mathcal{J}_{10}(x) := [q, \dot{q}, F, 0]^\top. \quad (6.30f)$$

The flow set is given by

$$\begin{aligned} \mathcal{C} &:= \mathcal{C}_0 \cup \mathcal{C}_1, \\ \mathcal{C}_0 &:= \{x \in \Theta : g_N \geq 0, \lambda_N = 0, m = 0\}, \\ \mathcal{C}_1 &:= \{x \in \Theta : g_N = 0, \lambda_N \geq 0, m = 1\}, \end{aligned} \quad (6.30g)$$

and the jump sets are given by

$$\begin{aligned} \mathcal{D}_{01} &:= \{x \in \Theta : g_N = 0, \dot{g}_N \leq 0, m = 0\}, \\ \mathcal{D}_{10} &:= \{x \in \Theta : g_N = 0, \lambda_N = 0, m = 1\}, \end{aligned} \quad (6.30h)$$

with λ_N given by the expression in (6.29). Note the presence of $\dot{g}_N \leq 0$ in \mathcal{D}_{01} in order to capture a buckling-to-traction transition. If $\dot{g}_N \geq 0$ whenever $g_N = 0$, the contact is indeed closed but traction will not occur. Intuitively speaking, the velocity of the upstream pressure roller $\dot{\theta}_{p,1}$ is either equal to, or exceeds the velocity of the downstream pressure roller $\dot{\theta}_{p,2}$, so that we either have contact without any contact force ($\dot{g}_N = 0$), or contact is immediately annulled ($\dot{g}_N > 0$). In any case, traction will not occur, and, hence, a discrete jump in \mathcal{D}_{01} is not required. Furthermore, although the hybrid model in (6.30) indeed captures all solutions to (6.18), it also includes additional undesired Zeno solutions [63, pp. 28–29].

6.3 Controller design

In this section, we present controller designs for single-pinch transport, and for the buckling and traction cases for double-pinch transport. To this end, we first formalize the control goals as discussed in Section 6.1. Subsequently, we present controllers for the aforementioned cases. The working principles of the control architecture are illustrated by means of a simulation study.

6.3.1 Control goals

Throughout the paper path, the position of the leading edge of a sheet of paper, denoted by x_s , should track a prescribed setpoint. By Assumption 6.2, and neglecting any deflection of the sheet, there exists a linear relation between the angular position of the pressure rollers $\theta_{p,i}$ and the position of the sheet, i.e., $x_s = r_p \theta_{p,i}$, when the sheet is transported by pinch i . A setpoint for x_s can hence be translated to a setpoint of the pressure rollers, as is commonly done in some high-level control scheme, which we assume to be in place here. We then focus on the low-level control goals, i.e., that the pinches should indeed realize the specified setpoint as determined by the high-level control scheme.

With the proposed control scheme specified below, we aim to achieve the following typical sequence in the paper path (see also the sequence a-d in Figure 6.2). A sheet is transported by a single pinch on the interval $[0, T_1)$. Then, a transition to two-pinch transport takes place, whereby the sheet is buckled (due to gravity) on the interval $[T_1, T_2)$. Finally, we control the system such that the sheet ends up in traction on the interval $[T_2, T_3)$, and a transition to one-pinch transport occurs at $t = T_3$, completing the sequence.

Since we distinguish three different cases of paper transport (i.e., single-pinch transport, and buckling and traction in two-pinch transport), we formalize the control goals for each case separately. Intuitively speaking, for single-pinch transport, the pressure roller angular position should track a prescribed setpoint. For two-pinch transport in the buckling case, we desire to end up in the traction case as soon as possible in order to minimize the chance of print defects. At the same time, we require the *downstream* pressure roller to track a prescribed setpoint, so that the considered sheet still tracks the right position in the paper path. Finally, for two-pinch transport in the traction case, we require the traction forces in the sheet to be controlled to a safe level, so that high traction forces (possible damaging the sheet or causing print defects) are prevented, while the safe traction level at the same time prevents the sheet from buckling again in this phase. At the same time, position setpoint tracking of the downstream pressure roller should be warranted. We formalize these control goals below, where we indicate the upstream pinch by $i = 1$, and the downstream pinch by $i = 2$ for two-pinch transport only.

1. *one-pinch transport*: $e_i := r_i(t) - \theta_{p,i} = 0$, for all $t \in [0, T_1)$, with $r_i(t)$ a prescribed setpoint for the considered pressure roller position;
2. *two-pinch transport, buckling*: $r_2(t) - \theta_{p,2} = 0$, for all $t \in [T_1, T_2)$, with $r_2(t)$ a prescribed setpoint for the downstream pressure roller position, and $g_N(T_2) = 0$;
3. *two-pinch transport, traction*: $r_2(t) - \theta_{p,2} = 0$, and $\lambda_N(t) = \lambda_r$, for all $t \in [T_2, T_3)$, with λ_r a specified constant setpoint for the traction force in the sheet.

The transition between one-pinch transport and two-pinch transport is detected by optical sensors in the paper path. The transition between buckling and traction is detected by online evaluation of the traction force λ_N . The to-be-controlled traction force λ_N is, however, not directly measurable. Indeed, the explicit expression for λ_N in (6.29) only contains the non-measurable states F_1 and F_2 . Therefore, in order to be able to control λ_N , we use the following predictor, derived from the equations of motion (6.6):

$$\lambda_N = \frac{1}{r_p} \left(J_p \ddot{\theta}_{p,1} \right) - \frac{1}{pr_d} \left(J_d \ddot{\theta}_{d,1} + k_b (r_{db} \theta_{d,1} - r_{mb} \theta_{m,1}) \right. \\ \left. + c_b (r_{dp} \dot{\theta}_{d,1} - r_{mb} \dot{\theta}_{m,1}) \right), \quad (6.31)$$

which holds for the upstream pressure roller. Due to the rigid connection between the two pinches in the traction case (see Assumption 6.1), λ_N has the same magnitude in both pinch models. Therefore, an expression similar to (6.31) can be derived for the downstream pressure roller as well (the only difference with respect to (6.31) is a minus sign, by (6.7)). In practice, the predictor may then be employed on both pinches to obtain improved accuracy on the predicted value for λ_N by averaging the two measurements. The predictor in (6.31) depends on known geometrical parameters, the constants k_b and c_b , and (time derivatives of) measurable angles. In practice, the constants k_b and c_b are obtained via a system identification procedure. The velocity and acceleration signals may be obtained by numerical differentiation of the (low-pass-filtered) measured position signals. Noise reduction in the position signals may be obtained by exploiting a specific interpolation technique available in the printer electronics (which we do not discuss further in this chapter, for the sake of brevity). The velocity and acceleration signals (differentiated from the measured and interpolated position data) in the predictor (6.31) then contain significantly less noise, so that the predictor is applicable in a practical setting.

6.3.2 Controller design for one and two-pinch transport

Respecting the different control goals as presented above, we design controllers for each case separately in the subsections below. Such controllers may consist of a feedback and a feedforward contribution. A transition between cases then yields a suitable transition between controllers.

Single-pinch transport control

For single-pinch transport, the closed-loop system is visualized in Figure 6.6, where the feedback and feedforward controllers, indicated by $C_{fb,1}$ and $C_{ff,1}$, respectively, are designed using well-known loop-shaping techniques [57]. The resulting feedback and feedforward signals are indicated by $\theta_{fb,1}$ and $\theta_{ff,1}$, respectively.

Double-pinch transport buckling control

For two-pinch transport in the buckling case, there is no interaction between the two pinches, so that we can design controllers for each pinch separately. In particular, we may keep the same controllers as for the single-pinch transport case, while specifying the references in such a way that traction is bound to occur. The control system is schematically depicted in Figure 6.7, where the inputs to pinch 1 and pinch 2 are, respectively, $\theta_{f,1}$ and $\theta_{f,2}$. The input of the pinches are the sum of their respective feedback ($\theta_{fb,1}$ and $\theta_{fb,2}$) and feedforward signals ($\theta_{ff,1}$ and $\theta_{ff,2}$). Respecting the control goals, we perform a *manual control allocation*. In particular, we set the downstream pinch controller to be responsible for pursuing the goal $r_2(t) - \theta_{p,2} = 0$ (so that the leading edge of the sheet still satisfies the desired tracking properties), whereas the upstream pinch controller is responsible for achieving $g_N(T_2) = 0$. The latter may be realized in different ways, but we consider here a straightforward approach that relies on applying a specific setpoint for $\theta_{p,1}$, that results in a lower velocity of the upstream pinch with respect to the downstream pinch. Specifically, the upstream pinch controller pursues $r_1(t) - \theta_{p,1} = 0$, where $r_1(t)$ satisfies $\dot{r}_1 < \dot{r}_2$. In this way, $g_N = 0$ is bound to occur if the control goals are realized.

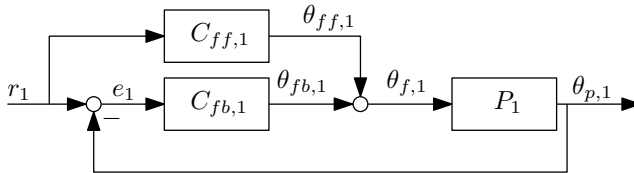


Figure 6.6. Block scheme of the closed-loop single-pinch model, with $C_{fb,1}$ a to-be-designed motion controller, and P_1 the plant (given by (6.2)).

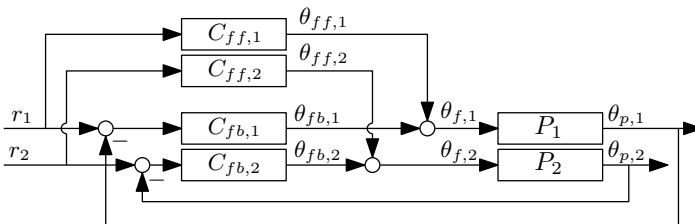


Figure 6.7. Block scheme of the closed-loop double-pinch model, with $C_{fb,1}$ and $C_{fb,2}$ to-be-designed motion controllers for the upstream and downstream pinches, respectively, and P_1 the plant (given by (6.2)).

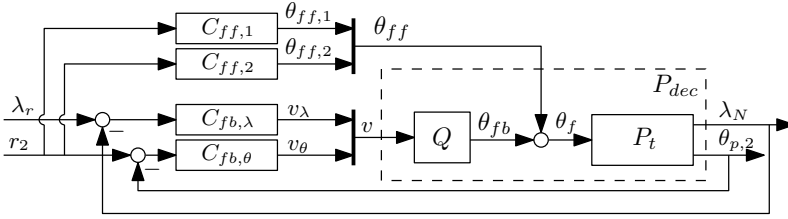


Figure 6.8. Block scheme of the closed-loop double-pinch model for the traction case, with $C_{fb,\lambda}$ and $C_{fb,\theta}$ to-be-designed motion controllers for controlling λ_N and controlling $\theta_{p,2}$, respectively, and P_t the plant (given by (6.18)).

Double-pinch transport traction control

For two-pinch transport in the traction case, there is a strong interaction between both pinches due to the rigid connection between the two pressure rollers by the paper sheet. Realizing both control goals, i.e., position setpoint tracking and traction setpoint tracking, is not straightforward. We therefore employ a particular input decoupling of the system, so that separate controllers can be designed for controlling λ_N and $\theta_{p,2}$. More specifically, with the proposed control decoupling, we require the downstream pinch to be responsible for controlling $\theta_{p,2}$, and the upstream pinch is responsible for controlling λ_N , which essentially reflects a manual control allocation procedure.

Remark 6.5. *The assignment of control objectives to specific actuators is based on engineering intuition and understanding of the system. This particular control allocation procedure is essentially different compared to classical control allocation, as employed in the previous chapter. With classical control allocation, the distribution of control forces over the available actuators is performed after the desired control effort is determined by the motion controller. In the current setting, the allocation is done before any control effort is determined.* \lrcorner

Consider Figure 6.8, which schematically depicts the control system. Herein, the vector of inputs to the stepper motors is defined as $\theta_f := [\theta_{f,1}, \theta_{f,2}]^\top$. The input vector is the sum of the feedback and feedforward signals, defined as $\theta_{fb} := [\theta_{fb,1}, \theta_{fb,2}]^\top$ and $\theta_{ff} := [\theta_{ff,1}, \theta_{ff,2}]^\top$, respectively. We now discuss the input decoupling, which is best explained by considering a transfer function description of the double-pinch system in the traction case. To this end, consider the hybrid model (6.30) (with $m = 1$). The flow dynamics can be written in the form $\dot{x} = A_t x + B_t \theta_{fb}$, with output vector $y := [\lambda_N, \theta_{p,2}]^\top =: C_t x$, for suitable A_t , B_t , and C_t (indeed, C_t can be constructed as λ_N depends on the system states F_1, F_2 , see (6.29)). The transfer function from θ_{fb} to y (i.e., $y = P_t \theta_{fb}$) of this multi-input-multi-output (MIMO) system is then given by

$$P_t = C_t (sI - A_t)^{-1} B_t, \quad (6.32)$$

with $s \in \mathbb{C}$. The Bode diagram of P_t is depicted in Figure 6.9, illustrating the interaction between pinches due to the fact that the off-diagonal terms are non-negligible¹. In fact, due to the symmetry in the double-pinch transport system and the rigid connection between the pinches, both pinches have equal influence on the control goals $\theta_{p,2}$ and λ_N . The 180 degrees phase difference between the transfers from $\theta_{p,1}$ to λ_N , and from $\theta_{p,2}$ to λ_N , is due to the opposite sign of λ_N by (6.7). Such symmetry motivates to decouple the system statically, using the following input decoupling matrix

$$Q := \frac{1}{\sqrt{2}} \begin{bmatrix} -1 & 1 \\ 1 & 1 \end{bmatrix}, \quad (6.33)$$

so that the transfer function of the *decoupled* system yields

$$P_{dec} = P_t Q. \quad (6.34)$$

The decoupled plant P_{dec} takes a *virtual* input $v := [v_1, v_2]^\top$, related to the physical input θ_{fb} by $\theta_{fb} = Qv$, see Figure 6.8. Inspecting the Bode diagram of the decoupled plant P_{dec} in Figure 6.10 illustrates that the input-output behavior of P_{dec} is indeed decoupled, since the magnitude of the off-diagonal terms are negligible. We are then able to design separate controllers $C_{fb,\lambda}$ and $C_{fb,\theta}$, for the upstream and downstream pinches, respectively, the former controlling λ_N , and the latter controlling $\theta_{p,2}$, as indicated in Figure 6.8.

6.3.3 Simulation study

We illustrate the working principle of the presented control architecture in a simulation study. To this end, we use the single-pinch model (6.2) and the *hybrid* double-pinch model (6.30) for single-pinch and double-pinch transport, respectively. We use the hybrid equations simulation toolbox [133] to perform the simulations. Numerical values for the geometrical and inertial model parameters are known from the manufacturer [111], other values are obtained by identification experiments and presented in Table 6.1.

We simulate a sheet of paper of 30 cm length, that is subsequently transported by one pinch and by two pinches. The upstream pinch is indicated by $i = 1$, and the downstream pinch by $i = 2$. For one-pinch transport, we consider a reference velocity of the upstream pressure roller of 17 rad/s, corresponding to a sheet velocity of approximately 0.3 m/s, so that $r_1(t) = 17t$, for all $t \in [0, T_1)$. In addition, we apply the same reference to the downstream pressure roller (i.e., $r_2(t) = 17t$ for all $t \in [0, T_1)$) so that we expect a smooth transition from one-pinch transport to two-pinch transport. We take $T_1 = 0.6$ s, i.e., the time instant at which a transition from one pinch transport to two pinch transport occurs.

¹Numerical values for the model parameters required for construction of the Bode diagram are discussed in Section 6.3.3

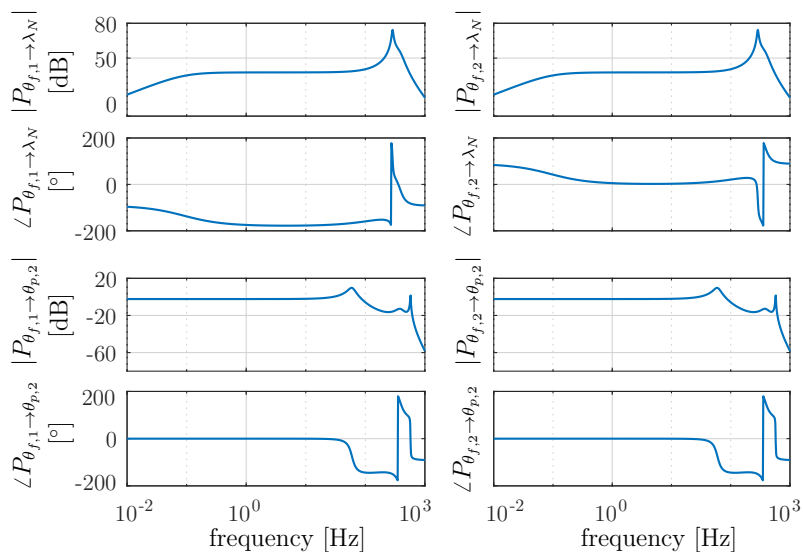


Figure 6.9. Bode diagram of the MIMO double-pinch model transfer function P_t for the traction case.

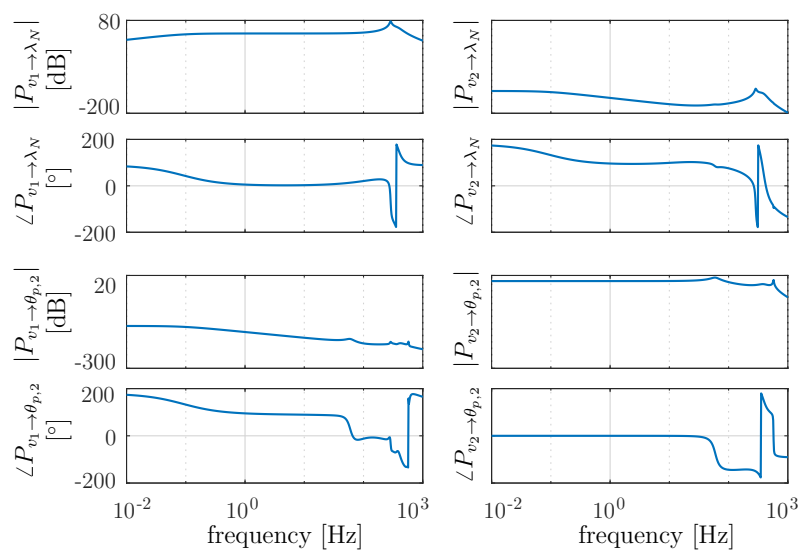


Figure 6.10. Bode diagram of the decoupled double-pinch model transfer function P_{dec} .

At such transition, the paper is buckled and we employ the control architecture as in Section 6.3 to end up in traction, where we keep $r_2(t) = 17t$, but adapt the reference for the upstream pressure roller to $r_1(t) = 0.97 \cdot 17t$. That is, the setpoint of the upstream pinch pressure roller results in a lower velocity compared to the downstream pinch, so that a state of traction is bound to occur at some $t = T_2$. Note that T_2 is generally unknown, as it depends on the (unmeasurable) degree of buckling. For the current simulation study, we assume a paper deflection of $d = 5$ mm at $t = T_1$ (see Figure 6.2) resulting in a pressure roller position offset of 0.005 rad, which, in turn, corresponds to $c = 8.775 \cdot 10^{-5}$ m in the distance function in (6.5). Finally, we set $T_3 = 1$ s. The feedback controllers $C_{fb,1}$, $C_{fb,2}$, $C_{fb,\lambda}$, and $C_{fb,\theta}$ are designed using linear loop-shaping techniques [57], and are given in Appendix 6.A.1. In addition, we employ the following feedforward controller on both pinches for all $t \in [0, T]$ that brings the pressure rollers close to the position setpoint:

$$\theta_{ff,i} = C_{ff,i} r_i(t), \quad i \in \{1, 2\}, \quad \text{with } C_{ff,i} = \frac{r_p r_{db}}{r_m r_d}. \quad (6.35)$$

Since $C_{ff,i}$ are transfer functions from position to position, they merely are a transmission ratio between the motor and the pressure roller. We choose the initial velocities for the motor, driven roller axis, and pressure roller axis in such a way that it matches the setpoint at $t = 0$, to avoid a large part of possible initial transients.

Consider Figure 6.11, which depicts the position error of the pressure roller of both pinches, i.e., $r_i(t) - \theta_{p,i}$, $i \in \{1, 2\}$, and the traction force error $\lambda_r - \lambda_N$. Transitions from one-pinch to two-pinch transport, and from buckling to traction, are indicated by $(- -)$. On the interval $[0, T_1]$, with $T_1 = 0.6$ s, we have single-pinch paper transport (i.e., the sheet is in pinch 1) and, aside from a small remaining transient, the tracking error for both pressure rollers is effectively suppressed, see the first and second subplot. Then, at $t = 0.6$ s, a transition to two-pinch transport takes place whereby the reference for the upstream pressure

Table 6.1. Parameter values.

parameter	value	parameter	value
r_m	$8.3 \cdot 10^{-3}$ m	c_b	0.5 Ns/m
r_{db}	$8.3 \cdot 10^{-3}$ m	c_r	10^4 Ns/m
r_d	$26.9 \cdot 10^{-3}$ m	p	0.999
r_p	$17.55 \cdot 10^{-3}$ m	k_b	600 N/m
J_m	$6.8 \cdot 10^{-6}$ kg/m ²	k_m	35 N/m
J_d	$23.8 \cdot 10^{-6}$ kg/m ²	k_r	10^5 N/m
J_p	$3.1 \cdot 10^{-6}$ kg/m ²		

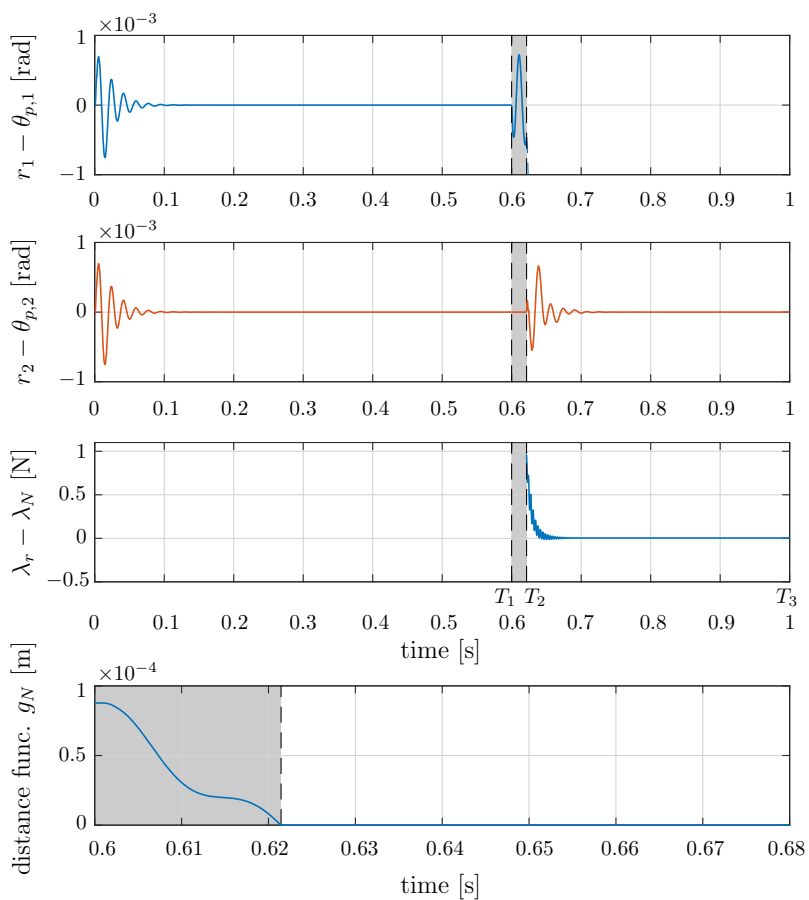


Figure 6.11. Position tracking errors for the upstream (top subplot) and downstream pressure rollers (second subplot), traction force error (third subplot), and gap function (bottom subplot). Single-pinch transport on $[0, 0.6)$, double-pinch transport in buckling mode on $[0.6, 0.621)$, indicated by the gray area, and double-pinch transport in traction mode on $[0.621, 1]$.

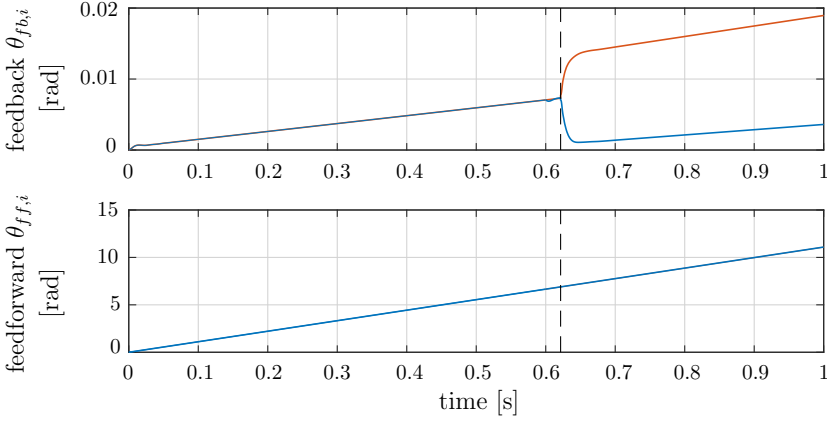


Figure 6.12. Feedback (top) and feedforward (bottom) control inputs for the upstream pinch (—) and downstream pinch (—). Note that the feedforward control input is identical for both pinches.

roller is altered. As a result of the non-smooth reference at $t = T_1$, a small transient in the error response of the upstream pressure roller is observed, but the gap function g_N is still controlled to zero at $t = T_2 = 0.621$ s. At this point, a buckling-to-traction transition occurs and we switch to the decoupled control scheme of Figure 6.8. The downstream pressure roller error is then effectively controlled to zero, see the second subplot. The upstream pinch is responsible for controlling the traction force in the sheet to zero, which is indeed realized as shown in the lower subplot, indicating that the decoupled controller structure is effective. Some oscillations are still present in the traction force error response, which may be due to the interplay between the impact (as a result of the buckling-to-traction transition) and the relatively high stiffness of the (relatively simple) rubber layer model. Note that the position tracking error as in the top subplot deviates immediately from zero after the buckling-to-traction transition, since the position tracking error is no longer a control goal in the interval $[T_2, T_3]$. Instead, the upstream pressure roller is responsible for controlling the force error $\lambda_r - \lambda_N$ to zero. The corresponding feedback and feedforward control inputs $\theta_{fb,i}$ and $\theta_{ff,i}$ of both pinches are visualized in Figure 6.12. Note that the signals $\theta_{ff,i}$ are increasing, as the controller output is the desired motor position, which is increasing in time.

6.4 Experimental case study

In this section, we show the working principle and the effectiveness of the proposed control architecture on an experimental paper path setup. In particu-

lar, we show that position accuracy is improved by employing feedback control (compared to the state-of-practice control solution), and that traction forces are effectively controlled to a safe level when a sheet is transported by two pinches.

6.4.1 Experimental setup

The experimental setup, depicted in Figure 6.13, coincides with a specific part of the paper path in an industrial sheetfed printer, indicated by the blue box in Figure 6.1. The setup consists of seven pinches, where the middle three are equipped with encoders on axes of the motor, driven roller, and the pressure roller. Optical sensors are placed throughout the paper path, so that we are able to measure by which pinch(es) a sheet is currently being transported. A paper input module is placed in front of the setup, that automatically feeds the setup with standard A4 sheets, which we consider in the experiments.

6.4.2 Experimental design and results

We consider two pinches in the experimental setup, logically numbered 1 and 2, as indicated in Figure 6.13. The case study involves a single sheet of paper that is subsequently transported by pinch 1, then by both pinches (double-pinch transport), and finally by pinch 2. Only pinch 1 and 2 are controlled using the proposed control architecture. The other pinches are driven in open-loop, following the state-of-practice control solution. Since the pinch pair 1 and 2 are preceded and followed by other pinches, there is only a small time interval where the sheet is transported by a single pinch. Nevertheless, we still employ the

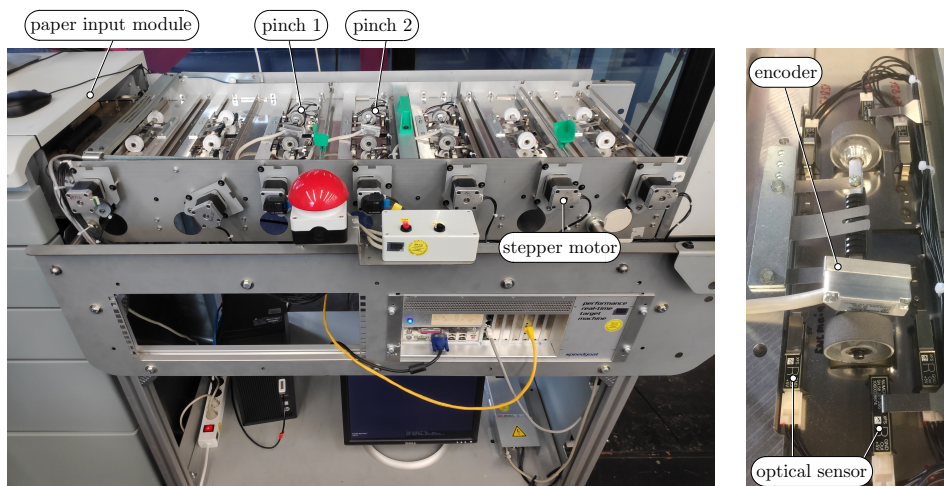


Figure 6.13. Experimental paper path setup.

single-pinch transport control strategy of Figure 6.6 for pinch 1 (resp. pinch 2) even if the sheet is also transported by its preceding (following) open-loop-driven pinch.

The sheet reference velocity is 0.6 m/s, which results in position references $r_i(t) = 34.19t$, $i \in \{1, 2\}$, for single-pinch transport, or when the pinch is empty to obtain a smooth transition from one-pinch to two-pinch transport and vice versa. A transition from single-pinch to double-pinch transport is detected using optical sensors. At this point, the sheet is buckled and the reference r_1 is altered to $r_1(t) = 0.97 \cdot 34.19t$ (but the single-pinch position controller remains active) while r_2 remains the same, so that traction is bound to occur. A buckling-to-traction transition is then detected when the traction force, obtained by the predictor (6.31), exceeds a small threshold value. At that point, the controller switches to the control architecture as in Figure 6.8, where we set $\lambda_r = 0.5$ N. The feedback controllers $C_{fb,1}$ and $C_{fb,2}$ are designed using loop-shaping techniques, based on frequency response measurements of the plant P_1 and P_2 , respectively. The controllers $C_{fb,\theta}$ and $C_{fb,\lambda}$, however, cannot be (completely) designed based on measured data. Frequency response measurements of the (decoupled) plant in the traction case cannot be reliably obtained, since traction only occurs for very short periods of time. Moreover, λ_N is not measurable. The controller $C_{fb,\theta}$ is therefore obtained based on $C_{fb,1}$ and model information. The traction force controller $C_{fb,\lambda}$ is designed based on the model presented in Section 6.2 with sufficient robustness margins. All controllers are given in Appendix 6.A.2. In addition, we use the feedforward controller (6.35).

Consider Figure 6.14, which depicts the position error of the pressure roller of pinch 1 and 2, and the traction force error for two experiments. The position and force errors are effectively suppressed by the proposed control architecture, showing the effectiveness of the approach. Let us now consider the responses in more detail. At $t = 0$, both pinches are already running with the single-pinch controllers applied, which results in near zero position errors. At $t = 0.12$ s, the sheet enters pinch 1 and remains in pinch 1 on the interval $[0.12, 0.41)$, see the top subplot. At approximately $t = 0.34$ s, we observe an increased position error, which is explained as follows. On the interval $[0.12, 0.34]$, the sheet is also transported by the open-loop-controlled pinch preceding pinch 1. A traction force may then be present in the sheet, which is not controlled during this interval. At $t = 0.34$ s, the sheet exits the preceding pinch, whereby the traction force is suddenly annulled (intuitively, such a phenomenon may be compared to stretching and releasing a rubber band on one side). Nevertheless, the resulting error is quickly suppressed by the controller. In the interval $[0.41, 0.44)$, the sheet is transported by pinch 1 and pinch 2 in the buckling phase. The buckling control strategy of Figure 6.7 effectively realizes that the sheet quickly ends up in the traction phase in the interval $[0.44, 0.62)$ s. In this interval, the position error of pinch 2 and the traction force error are effectively suppressed (see the second and third subplot, respectively). Finally, the sheet exits pinch 1 at $t = 0.62$ s

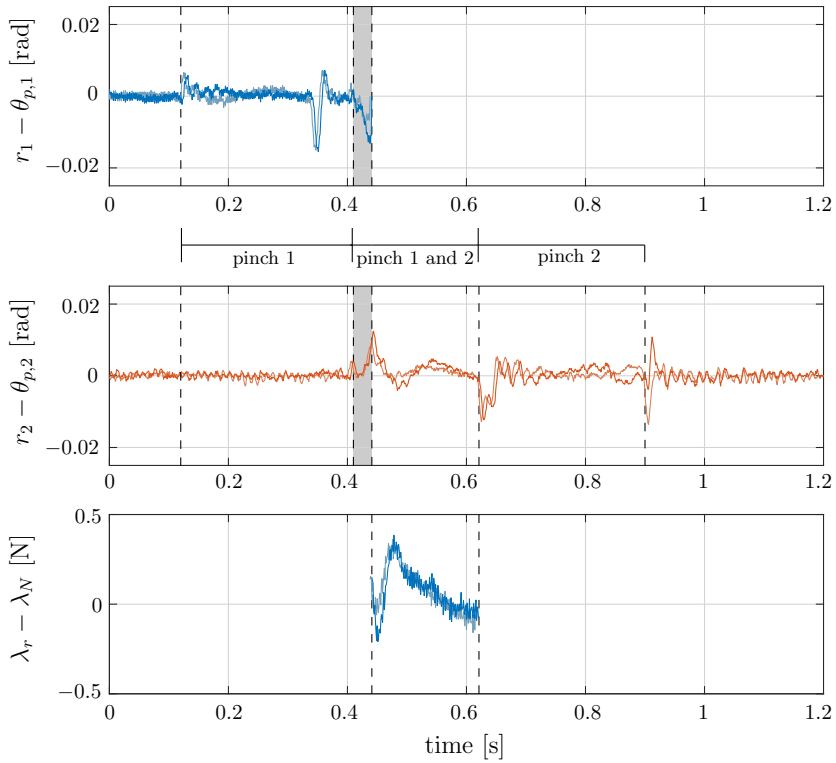


Figure 6.14. Position tracking errors for pinch 1 (top subplot) and pinch 2 (middle subplot), and traction force error (lower subplot) for two experiments. The buckling phase is indicated by the gray area.

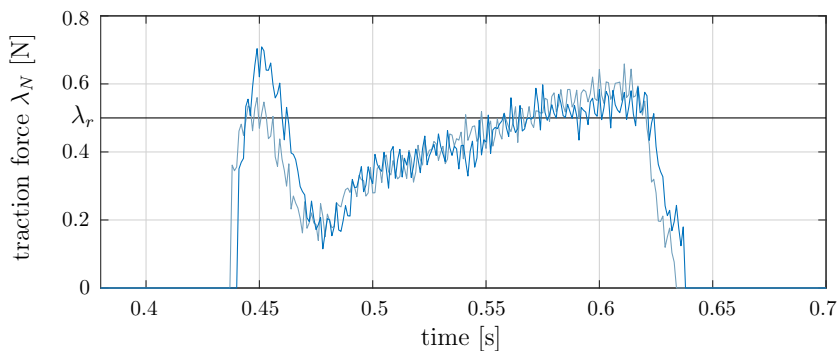


Figure 6.15. Traction force λ_N during double-pinch transport for two experiments.

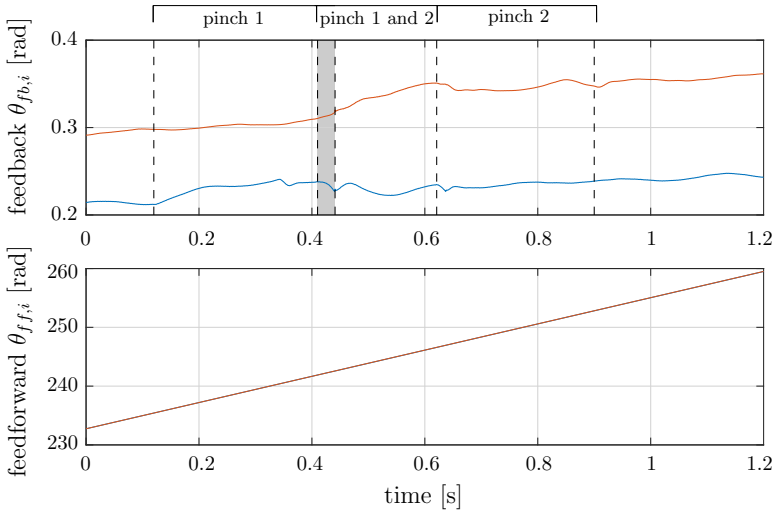


Figure 6.16. Feedback (top) and feedforward (bottom) control signals for pinch 1 (—) and pinch 2 (—). Note that the feedforward control input is identical for both pinches.

and is transported by pinch 2 on $[0.62, 0.9]$ where the position error is effectively suppressed again by the single-pinch control strategy of Figure 6.6.

The traction force, determined by the predictor (6.31), is presented in Figure 6.15. The traction force is, aside from the transient, controlled towards λ_r . We emphasize that the responsible controller $C_{fb,\lambda}$ is designed based on the model. Although the traction force is effectively controlled towards its setpoint, the transient may be improved if a more tailored controller can be designed based on identification measurements. Finally, the feedback and feedforward control signals for both pinches are presented in Figure 6.16. The y -axis of the feedforward control input plot does not start at zero, since the system is already running before we start tracing data at $t = 0$.

6.4.3 Comparison with state-of-practice control

We illustrate the performance benefits of the proposed control architecture, compared to the state-of-practice solution currently applied by the manufacturer. The state-of-practice strategy relies on driving the stepper motors without any feedback mechanism (open-loop). That is, the references $r_i(t)$ are directly send as an input to the stepper motor, i.e., $\theta_{f,i} = \frac{r_p r_{db}}{r_m r_d} r_i(t)$, which coincides with the feedforward controller (6.35). To prevent buckling during double-pinch transport in the industrial printer of Figure 6.1, several pinch pairs in the paper path are assigned a reference that results in a different relative ve-

locity, whereby the upstream pinch has a lower velocity than the downstream pinch. In order to illustrate the implications of this strategy in practice, we set $r_1(t) = r_2(t) = 34.19t$ during single-pinch paper transport, or when the pinch is empty. When double-pinch transport is detected by the optical sensors, $r_1(t)$ is altered to $r_1(t) = 0.97 \cdot 34.19t$ so that traction is bound to occur. Note that the reference is the same as in the case study with the proposed control architecture. Consider Figure 6.17, which depicts the position errors of both pinches, and the traction force during two-pinch transport in the traction case. First, due to the absence of a feedback controller, a drift in the position error occurs which cannot be compensated. Second, during double-pinch transport in the traction case, the traction force is not controlled and keeps increasing towards undesirable levels. In contrast, our proposed control architecture is capable of suppressing both the position and the traction force errors.

We now illustrate that employing merely a position controller for both pinches is not sufficient to arrive at safe traction force levels during two-pinch transport. We perform an experiment with the same position reference profile, where the single-pinch control architecture of Figure 6.6 is active at all times. The position errors of both pinches and the resulting traction force during double-pinch transport are depicted in Figure 6.18. Closed-loop position control improves already the position errors, compared to the state-of-practice strategy, as it is capable of removing the drift in the error. Moreover, the errors are suppressed as long as there is no paper in the corresponding pinch, or when a sheet is in either pinch 1 or pinch 2. When the paper is in both pinches and under traction, the control objectives interfere due to the rigid coupling between the pinches, resulting in large position errors. Moreover, the traction force rises to very large levels, risking slip between the sheet and the pinch, or even tearing the sheet.

Summarizing, the state-of-practice (open-loop control) strategy results in drift in the position errors, and uncontrolled traction forces. Employing only position control results in large errors during double-pinch transport, and undesired large traction forces. The proposed control strategy instead results in suppressing the position errors during single and double pinch transport, and is capable of controlling the traction force towards a specified reference, avoiding the risk of print defects.

6.5 Conclusions

We have presented a model and a control framework for a sheetfed printer paper path. The model addresses both single-pinch and double-pinch paper transport, where in the latter case the paper sheets may either be buckled, or may experience traction forces. The model addresses these logical states, as well as buckling-to-traction (and vice versa) transitions. A hybrid model for double-

pinch transport is derived that favors future controller designs, closed-loop stability analyses, and simulation studies. The proposed control framework realizes reference tracking of the pinches and regulates traction forces in the sheets, thereby avoiding print defects. Herein, overactuation is effectively exploited to address both control goals simultaneously in double-pinch transport. The working principle and effectiveness of the controller is illustrated by means of simulations, and is validated experimentally on a prototype paper path setup. The proposed control architecture outperforms the state-of-practice (open-loop) control solution in terms of position tracking accuracy and reduction of undesired (large) traction forces in the sheets.

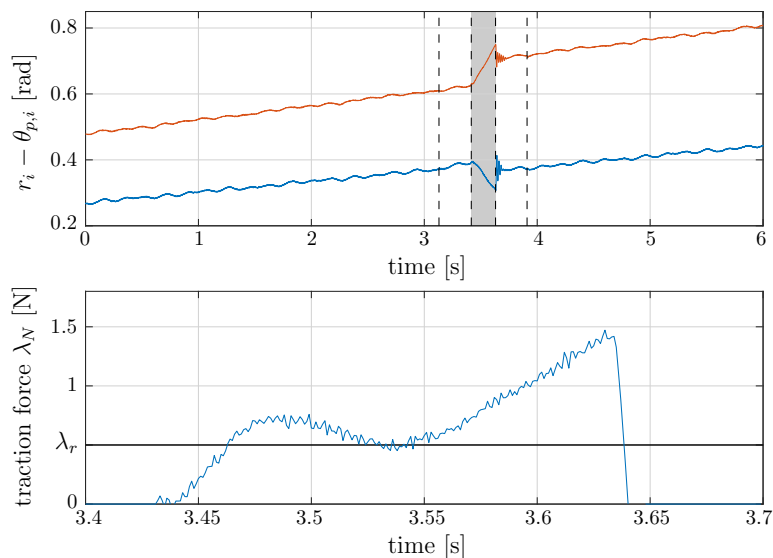


Figure 6.17. Position errors of pinch 1 (—) and pinch 2 (—) and traction force, for the state-of-practice (open-loop control) strategy. The double-pinch transport interval is indicated in gray. The sheet enters pinch 1 at the most left dashed line, and the sheet exits pinch 2 at the most right dashed line.

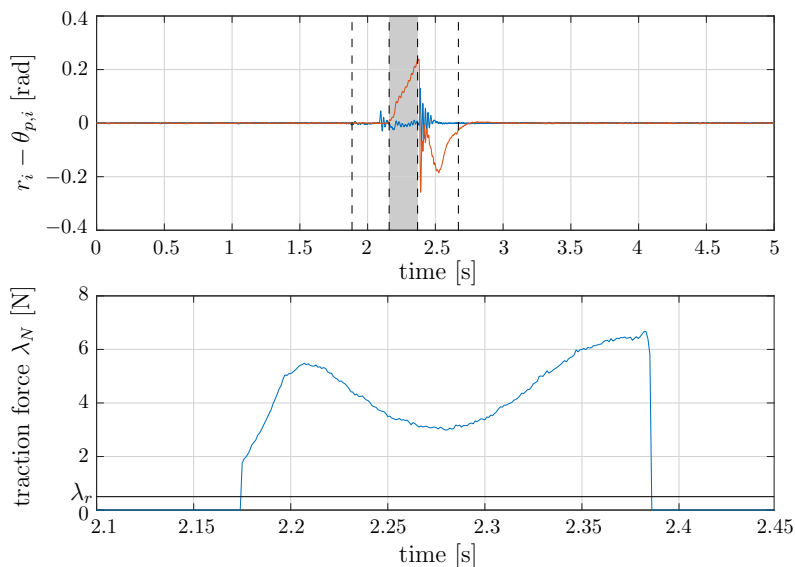


Figure 6.18. Position errors of pinch 1 (—) and pinch 2 (—) and traction force, when only position control is employed on both pinches. The double-pinch transport interval is indicated in gray. The sheet enters pinch 1 at the most left dashed line, and the sheet exits pinch 2 at the most right dashed line.

6.A Controllers

6.A.1 Feedback controllers for simulation

The following controllers are used in the simulation study:

- $C_{fb,1}$ and $C_{fb,2}$ consists of a proportional action, two integrators, and a notch filter:

$$\begin{aligned} C_{fb,1} &= C_{fb,2} \\ &= \frac{0.2s^4 + 1.16 \cdot 10^2 s^3 + 4.86 \cdot 10^4 s^2 + 1.52 \cdot 10^7 s + 1.80 \cdot 10^9}{s^4 + 3.77 \cdot 10^2 s^3 + 1.42 \cdot 10^5 s^2}, \end{aligned} \quad (6.36)$$

with $s \in \mathbb{C}$. The use of two integrators yields a zero steady-state error (without the need for a feedforward controller). The notch filter is employed to suppress a significant resonance in order to arrive at a satisfactory bandwidth;

- $C_{fb,\theta}$ consists of a proportional action, two integrators, and a notch filter as well:

$$C_{fb,\theta} = \frac{0.3s^4 + 1.73 \cdot 10^2 s^3 + 7.30 \cdot 10^4 s^2 + 2.29 \cdot 10^7 s + 2.70 \cdot 10^9}{s^4 + 4.52 \cdot 10^2 s^3 + 1.42 \cdot 10^5 s^2}; \quad (6.37)$$

- $C_{fb,\lambda}$ consists of a proportional action, two integrators, a notch filter, and a low-pass filter, given by

$$C_{fb,\lambda} = \frac{789.6s^4 + 3.34 \cdot 10^5 s^3 + 2.61 \cdot 10^9 s^2 + 8.08 \cdot 10^{11} s + 4.05 \cdot 10^{13}}{s^6 + 3325s^5 + 4.62 \cdot 10^6 s^4 + 1.72 \cdot 10^9 s^3 + 3.21 \cdot 10^{11} s^2}. \quad (6.38)$$

6.A.2 Feedback controllers for experiments

The following controllers are used in the experimental case study:

- The controllers for $C_{fb,1}$ and $C_{fb,2}$ consist of a proportional action, two integrators, a notch filter, and a first-order low-pass filter:

$$\begin{aligned} C_{fb,1} &= C_{fb,2} \\ &= \frac{1.3s^4 + 148s^3 + 1.89 \cdot 10^5 s^2 + 7.14 \cdot 10^6 s + 7.11 \cdot 10^7}{2.65 \cdot 10^{-3} s^5 + 5s^4 + 1.89 \cdot 10^3 s^3 + 1.42 \cdot 10^5 s^2} \end{aligned} \quad (6.39)$$

with $s \in \mathbb{C}$;

- $C_{fb,\theta}$ consists of a proportional action, two integrators, and a notch filter:

$$C_{fb,\theta} = \frac{0.67s^4 + 7.54 \cdot 10^1 s^3 + 9.68 \cdot 10^4 s^2 + 3.58 \cdot 10^6 s + 1.87 \cdot 10^7}{s^4 + 1.01 \cdot 10^3 s^3 + 6.32 \cdot 10^4 s^2} \quad (6.40)$$

- $C_{fb,\lambda}$ consists of a proportional action, an integrator, and a notch filter:

$$C_{fb,\lambda} = \frac{6.00 \cdot 10^4 s^3 + 1.55 s^2 + 2.04 \cdot 10^3 s + 4.86 \cdot 10^0}{s^3 + 1.79 \cdot 10^3 s^2 + 3.22 \cdot 10^6 s} \quad (6.41)$$

Conclusions and recommendations

7.1 Conclusions

High-tech industries are currently facing numerous challenges. Namely, there is an ever-increasing performance demand on speed and accuracy of motion systems, and essential system-level tradeoffs between cost and performance need to be made. In order to address these challenges, this thesis considers two industrially relevant topics. First, novel (hybrid) control strategies for systems with friction, and, second, control allocation techniques for over-actuated systems are developed, addressing the research objectives presented in Section 1.2:

Objective 1. Develop (hybrid and learning) control techniques for motion systems with friction, that improve stability and performance properties compared to classical linear control solutions, and are applicable to industrial high-tech systems.

Objective 2. Develop control allocation techniques tailored to specific industrial over-actuated systems, that outperform the state-of-practice (linear) control solutions.

Objective 3. Experimental validation of the proposed controllers on industrial benchmark systems.

The main contributions of this thesis, addressing the objectives above, can be summarized in terms of contributions to 1) novel controller designs that allow for cost-aware mechatronic system designs, 2) novel controller designs for frictional

systems, 3) development of tailored control allocation techniques for industrial over-actuated systems, and 4) validation on industrial benchmark systems:

1. *Novel controller designs that allow for cost-aware mechatronic system designs:* all control architectures presented in this thesis address cost-awareness. First, the use of cheaper hardware components such as bearings and actuators may induce friction in the motion system, which is a performance-limiting factor in terms of speed and accuracy. In Chapter 2-4, three (hybrid) controllers are presented that cope with frictional systems, enabling a high performance despite the apparent friction. Second, Chapter 5 presents an allocation framework for an industrial high-precision transport and positioning system, minimizing power consumption and allowing for relaxed hardware design specifications. Third, Chapter 6 presents a control framework for a sheetfed printer paper path driven by stepper motors, reducing hardware costs with respect to a DC motor driven paper path.
2. *Novel (hybrid and learning) controller designs for systems with friction, applicable to industrial applications:* respecting the popularity of the classical PID controller in practice, the limitations of PID control for frictional systems are overcome by adding reset enhancements to a loop-shaped PID controller. In Chapter 2, a reset integral controller is proposed that achieves robust global asymptotic stability of the setpoint, and significantly improves settling times for motion systems with unknown Coulomb and viscous friction. In Chapter 3, a reset integral controller is presented that achieves global asymptotic stability of the setpoint for systems with unknown Coulomb and *Stribeck* friction, which is typically not achieved with classical PID control. The reset conditions of both controllers are designed such that a controller reset is correctly triggered despite the presence of measurement noise. Additionally, Chapter 4 presents a novel time-varying integrator gain design for motion systems with unknown Coulomb and *Stribeck* friction, performing a repetitive motion profile. The time-varying integrator gain is parametrized by a set of suitable basis functions. The specific tuning of the time-varying integrator gain is iteratively obtained by employing a sampled-data extremum-seeking controller, such that high setpoint accuracy is obtained by data-based learning.
3. *Performance-enhancing control allocation techniques tailored for over-actuated industrial applications:* Chapter 5 presents a control allocation framework for an industrial high-accuracy transportation and positioning system which outperforms the state-of-practice, linear control solution currently applied by the manufacturer. In particular, employing the proposed control allocation framework results in enhanced tracking, allows for independent motion of multiple carriers, and results in relaxed hardware design

specifications. A decentralized allocation procedure is presented that enhances computational efficiency, such that the control allocation scheme is suitable for online implementation at high sampling rates, and facilitates scalability to large-scale system configurations. Chapter 6 presents a dynamic model and a (manual control allocation-based) control framework for a sheetfed printer paper path. In such a system, sheets are transported alternately by one or two pinches throughout the paper path, which gives rise to a hybrid system dynamics, where the double-pinch transport phase is over-actuated. We proposed a controller, based on a manual control allocation procedure, that regulates both the motion of the transported sheets and traction force in the sheets simultaneously. The proposed controller outperforms the state-of-practice control solution in terms of tracking accuracy and reduction of undesired (large) traction forces in the paper sheets.

4. *Validation on industrial benchmark systems:* all controllers presented in this thesis are experimentally validated on industrial benchmark systems. The effectiveness of the (hybrid and learning) PID-based control strategies for systems with friction proposed in Chapters 2-4 are verified on a high-precision motion stage of an electron microscope, showing superior performance compared to classical PID control. The control allocation architecture proposed in Chapter 5 is experimentally demonstrated on an industrial high-accuracy transport and positioning system, resulting in enhanced tracking and lower power consumption, compared to the state-of-practice control solution currently applied by the manufacturer. The control framework presented in Chapter 6 is developed for a sheetfed printer paper path, and is experimentally validated on a prototype paper path setup. Improved position tracking accuracy and control of traction forces has been shown, compared to the state-of-practice control solution.

The controller designs presented in this thesis are all developed with industrial acceptance in mind. Such acceptance requires that the controllers should be relatively easy to understand, to design, and to tune for control engineers in practice. The reset control architectures presented in Chapter 2 and 3 of this thesis have been designed based on top of the well-understood PID controller. Choosing the PID controller as a foundation, and enhancing it with resets, may not be the only design that achieves the control goals of the respective chapters. Doing so, however, enables industrial acceptance since the conditions for stability are exactly the same as for the base linear system (i.e., if friction would be absent, see Assumption 2.2 and 3.3). As a result, control practitioners may design and tune the base PID controller as usual, and then add the reset enhancements while closed-loop stability is preserved. Moreover, the reset controllers are applicable generically, since no information about the friction characteristic is required. We envision that such a design philosophy

enables industrial acceptance of these hybrid controllers.

The control allocation architectures presented in Chapter 5 and 6 have been developed for specific industrial applications. In order to achieve industrial acceptance of a performance enhancing control technique, it is important that shifting the control paradigm connects to the experience of control engineers in practice. Therefore, control allocation techniques have been proposed, which still exploit well-know motion control solutions, rather than entirely different control architectures that can deal with over-actuated systems. The main motivation is that, with control allocation, the controller design is strictly separated from the distribution of the control effort. In this way, control engineers can design the controllers using well-understood (loop-shaping) design techniques.

7.2 Recommendations

Recommendations for future research directions, related to both parts of this thesis, are as follows:

Part I: control of motion systems with friction

- *Chapter 2:* first, the reset integrator presented in Chapter 2 is able to cope with asymmetric friction, by tuning the parameter α to a sufficiently low value. However, doing so results in a milder controller reset and, consequently, in a longer settling time. Decreased settling times for the case of asymmetric friction may be realized by employing a separate integrator for each direction of movement of the mass, and keeping track of the history of their states and applying a suitable switching between them. Second, Section 2.4 presents a stability analysis that proves global *asymptotic* stability of the setpoint. When studying the response of the reset controller in Figure 2.1, we observe that the intervals of stick are of equal length, in contrast to the classical PID response. This actually suggests *exponential* stability, which, from a theoretical point of view, is an interesting result to pursue. Finally, the Coulomb friction model does not provide any information about frictional effects such as creep and stiffness-like effects (see also Section 1.1.1), which are shown to play a significant role in practice. If knowledge about the part of the friction responsible for the “stick-to-stick” jumps (i.e., stiffness-like effects) could be obtained, the system’s response as a result of the resets may be more predictable. This information may then be used for improved controller design.
- *Chapter 3:* first, the reset controller presented in Chapter 3 achieves global asymptotic stability of the setpoint for systems with Stribeck friction. Since the developments in the chapter focus on stability, transient performance is not addressed explicitly. An interesting direction for future re-

search is to investigate to what extent the developments of Chapter 2 may be used in the reset controller of Chapter 3, in order to improve transient performance (although the stability analysis may become more involved). Second, the reset controller employs two distinct resets so that stability of the setpoint can be proven based on the given Lyapunov function. However, as the experimental results in Section 3.8 indicate, the use of a less complex Clegg integrator may result in stability of the setpoint as well, with an easier-to-implement reset law. Conducting a stability analysis for the Clegg system is an interesting direction for future research. However, the Lyapunov function of Chapter 3 is no longer suitable, as it does not enjoy a nonincrease property when the integrator is reset to zero upon a zero-crossing of the position error. Third, unmodeled frictional effects as discussed above may be significant. If knowledge about the stiffness-like effects could be obtained, the system's response as a result of the resets may be more predictable. This information may then be used for improved controller design, also in this case.

- *Chapter 4:* first, the experimental case study shows that a high positioning accuracy is indeed obtained with the proposed control architecture. However, depending on, e.g., the choice of the basis functions and the friction characteristic at hand, there may exist multiple local minima of the performance cost function (reflecting positioning accuracy). In order for the extremum-seeking controller to arrive at the global minimum, thereby achieving optimal tuning of the time-varying integrator gain, *global* optimization methods can be explored instead (e.g., the DIRECT [82] or Shubert algorithm [137]). Second, although we show that solutions to the closed-loop system remain bounded, it may be useful to conduct a theoretical analysis that provides insight in the achievable accuracy depending on the friction characteristic and the controller tuning.

On a more general level, although many motion systems can be approximated well by a single mass model, several applications are better represented by a higher-order (multi-input-multi-output) motor-load model with a flexible coupling, where the load should be positioned accurately. In such systems, actuation and friction can be collocated, or non-collocated. In the latter case, due to the interplay between friction and the flexibility of the coupling, limit cycling may occur *even in the absence of a Stribeck effect*, when controlled by a classical PID controller. Understanding of this phenomenon is essential for designing suitable controllers that, firstly, eliminate limit cycling and achieve stability of the setpoint, and, secondly, improve transient performance. It is interesting to investigate to what extent the reset control architectures presented in this thesis are applicable to such higher-order systems. Additionally, position measurements of the load are not available in some industrial applications, e.g., where the machine operates (partly) in an isolated environment. For such frictional

motion systems, controller design for precise positioning of the load, based on only motor position measurements, is a challenging open problem.

Part II: control of over-actuated motion systems

- *Chapter 5*: the decentralized control allocation algorithm is computationally efficient, which facilitates scalability to large-scale system configurations. However, for some transportation systems, the number of actuators that can be driven by a single control module is limited. Communication between control modules (usually UTP-based) must be taken into account in the control allocation framework in order for the allocation method to work properly, which poses additional challenges such as communication delays and data loss. Addressing these challenges in the control allocation framework is an interesting direction for future research, so that the framework is applicable to such modular systems.
- *Chapter 6*: first, the hybrid pinch model includes additional undesired Zeno solutions, which may be eliminated by specific controller designs. Second, the control framework developed in Chapter 6 is shown to perform well in practice, but a formal proof of stability (where the hybrid modeling framework may be exploited) is still missing, and should be developed. Third, we now use an “ad-hoc” control architecture for the buckling phase, i.e., the upstream pinch has a lower angular velocity than the downstream pinch, so that the traction case is eventually achieved. However, impact forces may be minimized by designing a more advanced controller for the buckling phase, that minimizes the velocity difference between the pinches upon a buckling-to-traction transition. Last, we have only considered control of a *straight* part of the paper path, yet there are *curved* sections as well, see Figure 6.1. A different control approach needs to be developed in order to maneuver the paper sheets through such curved sections. In particular, a certain degree of buckling is then desired so that the sheets are bend to match the paper path curvature.

Appendix A

Hybrid Dynamical Systems

Following [63], a hybrid system \mathcal{H} is represented by

$$\mathcal{H} : \begin{cases} \dot{x} \in F(x), & \text{when } x \in C, \\ x^+ = G(x), & \text{when } x \in D. \end{cases} \quad (\text{A.1})$$

The state x of hybrid system \mathcal{H} can evolve according to a differential inclusion $\dot{x} \in F(x)$ while in the set C (referred to as the “flow set”), or according to a difference equation $x^+ = G(x)$ ¹ while in the set D (referred to as the “jump set”). The notation x^+ represents the value of the state of the system after an instantaneous change, and F and G are the flow and jump maps, respectively.

For hybrid systems, solutions are parameterized by the time $t \in \mathbb{R}_{\geq 0}$ and the number of discrete steps $j \in \mathbb{N}$. However, only certain subsets of $\mathbb{R}_{\geq 0} \times \mathbb{N}$ can correspond to evolutions of hybrid systems, i.e., the so-called *hybrid time domains*, which formal definition is as follows.

Definition A.1. [63, Def. 2.3]. *A subset $E \subset \mathbb{R}_{\geq 0} \times \mathbb{N}$ is a compact hybrid time domain if $E = \bigcup_{j=0}^{J-1} ([t_j, t_{j+1}] \times \{j\})$ for some finite sequence of times $0 = t_0 \leq t_1 \leq t_2 \leq \dots \leq t_J$. It is a hybrid time domain if for all $(T, J) \in E$, $E \cap ([0, T] \times \{0, 1, \dots, J\})$ is a compact hybrid domain.*

Let us now define the solutions of a hybrid system, using the concept of *hybrid arcs* (or trajectories), as in [63, Sec. 2.2 and 2.3].

Definition A.2. [63, Def. 2.4]. *A function $\psi : E \rightarrow \mathbb{R}^n$ is a hybrid arc if E is a compact hybrid time domain and if for each $j \in \mathbb{N}$, the function $t \mapsto \psi(t, j)$ is locally absolutely continuous on the interval $I^j := \{t : (t, j) \in E\}$.*

¹An evolution according to a difference inclusion $x^+ \in G(x)$ is also supported by the framework of [63], but not required for the developments in this thesis.

Given a hybrid arc ψ , the notation $\text{dom } \psi$ represents its domain, which is a hybrid time domain. Then, we state the following definition of solutions to hybrid systems:

Definition A.3. [63, Def. 2.6]. *A hybrid arc ψ is a solution to the hybrid system \mathcal{H} in (A.1) if $\psi(0, 0) \in \overline{C} \cup D$ and the following holds:*

- *for all $j \in \mathbb{N}$ such that $I^j := \{t : (t, j) \in \text{dom } \psi\}$ has nonempty interior, $\psi(t, j) \in C$ for all $t \in \text{int } I^j$, and $\dot{\psi}(t, j) \in F(\psi(t, j))$ for almost all $t \in I^j$;*
- *for all $(t, j) \in \text{dom } \psi$ such that $(t, j + 1) \in \text{dom } \psi$, $\psi(t, j) \in D$, and $\psi(t, j + 1) = G(\psi(t, j))$,*

with \overline{C} the closure of the flow set C .

With the above definitions in place, solutions to hybrid systems can be classified based on their hybrid time domains. A solution is called *maximal* if there does not exist another solution $\tilde{\psi}$ to \mathcal{H} such that $\text{dom } \psi \subset \text{dom } \tilde{\psi}$ and $\psi(t, j) = \tilde{\psi}(t, j)$ for all $(t, j) \in \text{dom } \psi$. Solutions ψ to \mathcal{H} are *complete* if $\text{dom } \psi$ is unbounded, are *t-complete* (i.e., complete in the ordinary-time direction) if $\sup_t \text{dom } \psi = \infty$, and are *Zeno* if they are complete with $\sup_t \text{dom } \psi < \infty$.

Bibliography

- [1] W.H.T.M. Aangenent, G. Witvoet, W.P.M.H. Heemels, M.J.G. van de Molengraft, and M. Steinbuch, “Performance analysis of reset control systems”, *Int. J. of Robust and Nonlinear Control*, vol. 20, no. 11, pp. 1213–1233, 2010.
- [2] V. Acary and B. Brogliato, *Numerical Methods for Nonsmooth Dynamical Systems*. 2008, vol. 35.
- [3] L.T. Aguilar, Y. Orlov, and L. Acho, “Nonlinear \mathcal{H}_∞ -control of nonsmooth time-varying systems with application to friction mechanical manipulators”, *Automatica*, vol. 39, no. 9, pp. 1531–1542, 2003.
- [4] F. Al-Bender, V. Lampaert, and J. Swevers, “The generalized Maxwell-slip model: a novel model for friction simulation and compensation”, *IEEE Trans. Autom. Control*, vol. 50, no. 11, pp. 1883–1887, 2005.
- [5] F. Al-Bender and J. Swevers, “Characterization of friction force dynamics”, *IEEE Control Systems Magazine*, vol. 28, no. 6, pp. 64–81, 2008.
- [6] G. Amontons, “De la résistance causée dans les machines”, *Mémoires de L’Academie Royale des sciences*, pp. 206–227, 1699.
- [7] A. Amthor, S. Zschaeck, and C. Ament, “High precision position control using an adaptive friction compensation approach”, *IEEE Trans. Autom. Control*, vol. 55, no. 1, pp. 274–278, 2010.
- [8] B.D.O. Anderson and J.B. Moore, *Optimal control: linear quadratic methods*. New Jersey: Prentice Hall, 1990.
- [9] K.H. Ang, G. Chong, and Y. Li, “PID control system analysis, design, and technology”, *IEEE Trans. Control Syst. Technol.*, vol. 13, no. 4, pp. 559–576, 2005.
- [10] B. Armstrong and B. Amin, “PID control in the presence of static friction: a comparison of algebraic and describing function analysis”, *Automatica*, vol. 32, no. 5, pp. 679–692, 1996.
- [11] B. Armstrong-Hélouvry, *Control of machines with friction*. New York: Springer Science, 1992.

- [12] B. Armstrong-Hélouvry, P. Dupont, and C. Canudas de Wit, “A survey of models, analysis tools and compensation methods for the control of machines with friction”, *Automatica*, vol. 30, no. 7, pp. 1083–1138, 1994.
- [13] R. Barabanov and R. Ortega, “Necessary and sufficient conditions for passivity of the LuGre friction model”, *IEEE Trans. Autom. Control*, vol. 45, no. 4, pp. 830–832, 2000.
- [14] G. Bartolini, A. Pisano, E. Punta, and E. Usai, “A survey of applications of second-order sliding mode control to mechanical systems”, *International Journal of Control*, vol. 76, pp. 875–892, 2003.
- [15] G. Bartolini and E. Punta, “Chattering elimination with second-order sliding modes robust to Coulomb friction”, *Journal of Dynamic Systems, Measurement, and Control*, vol. 122, no. 4, pp. 679–686, 2000.
- [16] M. Baumann, J.J.B. Biemond, R.I. Leine, and N. van de Wouw, “Synchronization of impacting mechanical systems with a single constraint”, *Physica D*, vol. 362, pp. 9–23, 2018.
- [17] H. Beaty and J. Kirtley, *Electric motor handbook*. New York: McGraw-Hill, 1998.
- [18] R. Beerens, A. Bisoffi, L. Zaccarian, W.P.M.H. Heemels, H. Nijmeijer, and N. van de Wouw, “Reset PID design for motion systems with Stribeck friction”, *in preparation for journal submission*,
- [19] —, “Hybrid PID control for transient performance improvement of motion systems with friction”, *Proc. 2018 American Control Conference (ACC)*, pp. 539–544, 2018.
- [20] —, “Reset integral control for improved settling of PID-based motion systems with friction”, *Automatica*, vol. 107, pp. 483–492, 2019.
- [21] R. Beerens, H. Nijmeijer, W.P.M.H. Heemels, and N. van de Wouw, “Set-point control of motion systems with uncertain set-valued Stribeck friction”, *IFAC PapersOnline*, vol. 50, no. 1, pp. 2965–2970, 2017.
- [22] R. Beerens, S.C.N. Thissen, Pancras W. an Gommans T.M.P., N. van de Wouw, and W.P.M.H. Heemels, “Control allocation for an industrial high-precision transportation and positioning system”, *IEEE Trans. Control Syst. Technol.*, *submitted*, 2019.
- [23] R. Beerens, S.C.N. Thissen, A. van der Maas, W. Pancras, T.M.P. Gommans, N. van de Wouw, and W.P.M.H. Heemels, “Control allocation for a high-precision linear transport system”, *Proc. 57th Conf. on Decision and Control (CDC)*, pp. 1657–1662, 2018.
- [24] O. Beker, C.V. Hollot, and Y. Chait, “Fundamental properties of reset control systems”, *Automatica*, vol. 40, pp. 905–915, 2004.
- [25] O. Beker, C.V. Hollot, and Chait. Y., “Plant with integrator: an example of reset control overcoming limitations of linear feedback”, *IEEE Trans. Autom. Control*, vol. 46, no. 11, pp. 1797–1799, 2001.

- [26] M. Benosman, “Multi-parametric extremum seeking-based iterative feedback gains tuning for nonlinear control”, *Int. J. Robust Nonlinear Control*, vol. 26, no. 18, pp. 4035–4055, 2016.
- [27] J.J.T.H. de Best, B.H.M. Bukkems, M.J.G. van de Molengraft, W.P.M.H. Heemels, and M. Steinbuch, “Robust control of piecewise linear systems: A case study in sheet flow control”, *Control Engineering Practice*, vol. 16, pp. 991–1003, 2008.
- [28] A. Bisoffi, R. Beerens, L. Zaccarian, W.P.M.H. Heemels, H. Nijmeijer, and N. van de Wouw, “Hybrid model formulation and stability analysis of a PID-controlled motion system with Coulomb friction”, *Proc. 11th IFAC Symposium on Nonlinear Control Systems (NolCos 2019)*, pp. 116–121, 2019.
- [29] A. Bisoffi, M. Da Lio, A.R. Teel, and L. Zaccarian, “Global asymptotic stability of a PID control system with Coulomb friction”, *IEEE Trans. Autom. Control*, vol. 63, no. 8, pp. 2654–2661, 2018.
- [30] I. Boldea and S. Nasar, *Vector control of AC drives*. Orlando: CRC Press, 1992.
- [31] J. Bolder and T. Oomen, “Rational basis functions in iterative learning control - with experimental verification on a motion system”, *IEEE Trans. Contr. Syst. Technol.*, vol. 23, no. 2, pp. 722–72, 2015.
- [32] K.A. Bordignon and W.C. Durham, “Closed-form solutions to constrained control allocation problem”, *J. Guidance, Control, and Dynamics*, vol. 18, no. 5, pp. 1000–1007, 1995.
- [33] Bosch Rexroth, *Industrial applications of an IPMLSM*, [http : / / www . boschrexroth.com/lms](http://www.boschrexroth.com/lms).
- [34] Bosch Rexroth Halbleiterproduktion LMS, <https://www.youtube.com/watch?v=guXJm0QQQnc>.
- [35] S. Boyd and L. Vandenberghe, *Convex Optimization*. New York: Cambridge Univ. Press, 2004.
- [36] D.A. Bristow, M. Tharavil, and A.G. Alleyne, “A survey of iterative learning control”, *Control Systems Magazine*, vol. 26, pp. 96–114, 2006.
- [37] B.H.M. Bukkems, J.J.T.H. de Best, M.J.G. van de Molengraft, and M. Steinbuch, “Robust piecewise linear sheet control in a printer paper path”, *Proc. 2nd IFAC conf. on analysis and design of hybrid systems*, pp. 142–147, 2006.
- [38] H. Butler, “Position control in lithographic equipment”, *IEEE Control Systems Magazine*, vol. 31, no. 5, pp. 28–47, 2011.
- [39] C. Canudas De Wit, H. Olsson, and P.J.K. Lischinsky, “A New Model for Control of Systems with Friction”, *IEEE Trans. Autom. Control*, vol. 40, no. 3, 1995.
- [40] J. Carrasco, A. Baños, and A. van der Schaft, “A passivity-based approach to reset control systems stability”, *Systems and Control Letters*, vol. 59, no. 1, pp. 18–24, 2010.
- [41] G. Chartrand, *Introductory graph theory*. New York: Dover Inc., 1985.

- [42] Q. Chen, Y. Chait, and Holot C.V., “Analysis of reset control systems consisting of a FORE and second order loop”, *J. Dyn. Sys., Meas., Control*, vol. 123, pp. 279–283, 2001.
- [43] W. Chen, K. Kong, and M. Tomizuka, “Dual-stage adaptive friction compensation for precise load side position tracking of indirect drive mechanisms”, *IEEE Trans. on Control Syst. Technol.*, vol. 23, no. 1, pp. 164–175, 2015.
- [44] Y. Chen and J. Wang, “Adaptive energy-efficient control allocation for planar motion control of over-actuated electric ground vehicles”, *IEEE Trans. Control Syst. Technol.*, vol. 22, no. 4, pp. 1362–1373, 2014.
- [45] F.H. Clarke, *Optimization and nonsmooth analysis*. SIAM, 1990.
- [46] J.C. Clegg, “A nonlinear integrator for servomechanisms”, *Transactions of the American Institute of Electrical Engineers, Part II: Applications and Industry*, vol. 77, no. 1, pp. 41–42, 1958.
- [47] C. Cloet, M. Kruciński, R. Horowitz, and M. Tomizuka, “A hybrid control scheme for a copier paperpath”, *Proc. 1999 American Control Conference (ACC)*, pp. 2114–2118, 1999.
- [48] C. Cloet, M. Tomizuka, and R. Horowitz, “Design requirements and reference trajectory generation for a copier paperpath”, *Proc. 2001 IEEE/ASME Int. Conf. Adv. Intell. Mechatron.*, pp. 911–916, 2001.
- [49] *CPLEX Optimizer*, www.ibm.com/analytics/cplex-optimizer.
- [50] R.M. Crowder, *Electric drives and electromechanical systems*. Oxford: Elsevier, 2006.
- [51] P.R. Dahl, “A solid friction model”, *Tech. Rep. Aerospace Corporation El Segundo, CA*, no. Tech. rep. no. TOR-0158(3107-18)-1, 1968.
- [52] D.A. Deenen, M.F. Heertjes, W.P.M.H. Heemels, and H. Nijmeijer, “Hybrid integrator design for enhanced tracking in motion control”, *Proc. 2017 American Control Conference*, pp. 2863–2868, 2017.
- [53] P. Dupont, V. Hayward, B. Armstrong, and F. Altpeter, “Single state elastoplastic friction models”, *IEEE Trans. Autom. Control*, vol. 47, no. 5, pp. 787–792, 2002.
- [54] S. Even, *Graph algorithms*, 2nd. New York: Cambridge Univ. Press, 2012.
- [55] A.F. Filippov, *Differential equations with discontinuous righthand sides*. Dordrecht: Kluwer Academic Publishers, 1988.
- [56] T.I. Fossen and T.A. Johansen, “A survey of control allocation methods for ships and underwater vehicles”, *Proc. 14th mediterranean conference on control and automation*,
- [57] G. Franklin, J. Powell, and A. Emami-Naeini, *Feedback control of dynamic systems*, 7th. Boston: Pearson, 2015.
- [58] L. Freidovich, A. Robertsson, A. Shiriaev, and R. Johansson, “LuGre-model-based friction compensation”, *IEEE Trans. Control Syst. Technol.*, vol. 18, no. 1, pp. 194–200, 2010.

- [59] M. Gallieri and J.M. Maciejowski, “ ℓ_{asso} MPC: smart regulation of over-actuated systems”, *Proc. 2012 American Control Conference (ACC)*, pp. 1217–1222, 2012.
- [60] J.F. Gieras, Z.J. Piech, and B.Z. Tomczuk, *Linear synchronous motors*, 2nd. Boca Raton: CRC Press, 2012.
- [61] C. Glocker, “On frictionless impact models in rigid-body systems”, *Philosophical Transactions of the Royal Society of London A*, vol. 359, pp. 2385–2404, 2001.
- [62] R. Goebel, R.G. Sanfelice, and A.R. Teel, “Hybrid dynamical systems”, *IEEE Contr. Syst. Mag.*, vol. 29, no. 2, pp. 28–93, 2009.
- [63] —, *Hybrid dynamical systems*. Princeton, New Jersey: Princeton University Press, 2012.
- [64] D.T. Greenwood, *Advanced dynamics*. New York: Cambridge Univ. Press, 2003.
- [65] *Gurobi optimization*, www.gurobi.com.
- [66] J.W. Hagoood and B.S. Thomson, “Recovering a function from a Dini derivative”, *The American Mathematical Monthly*, vol. 113, no. 1, pp. 34–46, 2006.
- [67] O. Härkegård, “Efficient active set algorithms for solving constrained least squares problems in aircraft control allocation”, *Proc. 2002 Conference on Decision and Control (CDC)*, vol. 2, pp. 1295–1300, 2002.
- [68] O. Härkegård and S. T. Glad, “Resolving actuator redundancy - optimal control vs. control allocation”, *Automatica*, vol. 41, no. 1, pp. 137–144, 2005.
- [69] L. Hazeleger, R. Beerens, and N. van de Wouw, “A sampled-data extremum-seeking approach for accurate setpoint control of motion systems with friction”, *Proc. 11th IFAC Symposium on Nonlinear Control Systems (NolCos 2019)*, pp. 1415–1420, 2019.
- [70] —, “PID-based learning control for high-accuracy repetitive positioning of frictional motion systems”, *submitted to IEEE Transactions on Control Systems Technology*, 2019.
- [71] L. Hazeleger, D. Nešić, and N. van de Wouw, “Sampled-data extremum-seeking control for optimization of constrained dynamical systems using barrier function methods”, *Proc. 58th Conference on Decision and Control (CDC)*, *accepted*, 2019.
- [72] M. Heath, *Scientific computing: an introductory survey*. Boston: WCB/McGraw-Hill, 1997.
- [73] M. Heertjes, B. van der Velden, and T. Oomen, “Constrained iterative feedback tuning for robust control of a wafer stage system”, *IEEE Trans. Contr. Syst. Technol.*, vol. 24, no. 1, pp. 56–66, 2016.
- [74] R.H.A. Hensen, M.J.G. van de Molengraft, and M. Steinbuch, “Friction induced hunting limit cycles: A comparison between the LuGre and switch friction model”, *Automatica*, vol. 39, no. 12, pp. 2131–2137, 2003.
- [75] H. Hjalmarsson, M. Gevers, S. Gunnarsson, and O. Lequin, “Iterative feedback tuning: theory and applications”, *IEEE Control Systems Magazine*, vol. 18, no. 4, pp. 26–41, 1998.

- [76] I. Horowitz and P. Rosenbaum, “Non-linear design for cost of feedback reduction in systems with large parameter uncertainty”, *International Journal of Control*, vol. 21, no. 6, pp. 977–1001, 1975.
- [77] B.G.B. Hunnekens, N. van de Wouw, M. Heertjes, and H Nijmeijer, “Synthesis of variable gain integral controllers for linear motion systems”, *IEEE Transactions on Control Systems Technology*, vol. 23, no. 1, pp. 139–149, 2015.
- [78] I.M. Hutchings, “Leonardo Da Vinci’s studies of friction”, *Wear*, vol. 360–361, pp. 51–66, 2016.
- [79] L. Iannelli, K.H. Johansson, U.T. Jönsson, and F. Vasca, “Averaging of nonsmooth systems using dither”, *Automatica*, vol. 42, no. 4, pp. 669–676, 2006.
- [80] T. Johansen, “Optimizing nonlinear control allocation”, *Proc. 43th Conference on Decision and Control (CDC)*, pp. 3435–3440, 2004.
- [81] T.A. Johansen and T.I. Fossen, “Control allocation - a survey”, *Automatica*, vol. 49, no. 5, pp. 1087–1103, 2013.
- [82] D.R. Jones, C.D. Perttunen, and B.E. Stuckman, “Lipschitzian optimization without the Lipschitz constant”, *J. Optim. Theory Appl.*, vol. 79, no. 1, pp. 157–181, 1993.
- [83] H.K. Khalil, *Nonlinear Systems*, 3rd. New Jersey: Prentice Hall, 2000.
- [84] S.Z. Khong, D. Nešić, and C. Manzie, “Iterative learning control based on extremum seeking”, *Automatica*, vol. 66, pp. 238–245, 2016.
- [85] S.Z. Khong, D. Nešić, Y. Tan, and C. Manzie, “Unified frameworks for sampled-data extremum seeking control: global optimisation and multi-unit systems”, *Automatica*, vol. 49, pp. 2720–2733, 2013.
- [86] N.J. Killingsworth and M. Krstić, “PID tuning using extremum seeking”, *IEEE Control Systems Magazine*, vol. 26, no. 1, pp. 70–79, 2006.
- [87] M. Kruciński, “Printer media path closed loop control”, *Proc. 2009 American Control Conference (ACC)*, pp. 3675–3680, 2001.
- [88] M. Kruciński, C. Cloet, M. Tomizuka, and R. Horowitz, “Asynchronous observer for a copier paper path”, *Proc. 37th Conf. on Decision and Control (CDC)*, pp. 2611–2612, 1998.
- [89] K. Kvaternik and L. Pavel, “Interconnection conditions for the stability of nonlinear sampled-data extremum-seeking schemes”, *Proc. 50th Conference on Decision and Control (CDC)*, pp. 4448–4454, 2011.
- [90] V. Lampaert, J. Swevers, and F. Al-Bender, “Modification of the Leuven integrated friction model structure”, *IEEE Trans. Autom. Control*, vol. 47, no. 4, pp. 683–687, 2002.
- [91] —, “Comparison of model and non-model based friction compensation techniques in the neighbourhood of pre-sliding friction”, *Proc. 2004 American Control Conference (ACC)*, pp. 1121–1126, 2004.
- [92] R.I. Leine and M. Baumann, “Variational analysis of inequality impact laws”, *Proc. 8th Nonlinear Dynamics Conference (ENOC)*, 2014.

- [93] R.I. Leine and N. van de Wouw, *Stability and convergence of mechanical systems with unilateral constraints*. Berlin Heidelberg: Springer-Verlag, 2008, vol. 36.
- [94] O. Lequin, M. Gevers, M. Mossberg, E. Bosman, and L. Triest, “Iterative feedback tuning of PID parameters: comparison with classical tuning rules”, *Control Engineering Practice*, vol. 11, pp. 1023–1033, 2003.
- [95] J. Liang, T. Wang, and L. Wen, “Development of a two-joint robotic fish for real-world exploration”, *Journal of Field Robotics*, vol. 28, pp. 70–79, 2011.
- [96] S.J.L.M. van Loon, K.G.J. Gruntjens, M.F. Heertjes, N. van de Wouw, and W.P.M.H. Heemels, “Frequency-domain tools for stability analysis of reset control systems”, *Automatica*, vol. 82, pp. 101–108, 2017.
- [97] S.J.L.M. van Loon, B.G.B. Hunnekens, W.P.M.H. Heemels, N. van de Wouw, and H. Nijmeijer, “Split-path nonlinear integral control for transient performance improvement”, *Automatica*, vol. 66, pp. 262–270, 2016.
- [98] A. van der Maas, N. van de Wouw, and W.P.M.H. Heemels, “Filtered split-path nonlinear integrator (F-SPANI) for improved transient performance”, *Proc. 2017 American Control Conference (ACC)*, pp. 3500–3505, 2017.
- [99] J.M. Maciejowski, *Predictive control with constraints*. New Jersey: Pearson Education, 2001.
- [100] C. Makkar, G. Hu, W.G. Sawyer, and W.E. Dixon, “Lyapunov-based tracking control in the presence of uncertain nonlinear parameterizable friction”, *IEEE Trans. Autom. Control*, vol. 52, no. 10, pp. 1988–1994, 2007.
- [101] N. Mallon, N. van de Wouw, D. Putra, and H. Nijmeijer, “Friction compensation in a controlled one-link robot using a reduced-order observer”, *IEEE Trans. Control Syst. Technol.*, vol. 14, no. 2, pp. 374–383, 2006.
- [102] A.A. Mamun, I. Mareels, T. Lee, and A. Tay, “Dual stage actuator control in hard disk drive - a review”, *IECON Conference of the industrial electronic society*, pp. 2132–2137, 2003.
- [103] D.Q. Mayne, “Model predictive control: Recent developments and future promise”, *Automatica*, vol. 50, no. 12, pp. 2967–2986, 2014.
- [104] S. van der Meulen, R.L. Tousain, and O.H. Bosgra, “Fixed structure feedforward controller design exploiting iterative trials: application to a wafer stage and desktop printer”, *J. Dyn. Sys., Meas., Control*, vol. 130, no. 5, pp. 051 006–16, 2008.
- [105] A. Morin, “New friction experiments carried out at Metz in 1831-1833”, *Proc. of the French Royal Academy of Sciences*, vol. 4, pp. 1–128, 1833.
- [106] J. Na, Q. Chen, X. Ren, and Y. Guo, “Adaptive prescribed performance motion control of servo mechanisms with friction compensation”, *IEEE Trans. Ind. Electron*, vol. 61, no. 1, pp. 486–494, 2014.
- [107] D. Nešić, A.R. Teel, and L. Zaccarian, “Stability and performance of SISO control systems with first-order reset elements”, *IEEE Trans. Autom. Control*, vol. 56, no. 11, pp. 2567–2582, 2011.
- [108] D. Nešić, L. Zaccarian, and A.R. Teel, “Stability properties of reset systems”, *Automatica*, vol. 44, pp. 2019–2026, 2008.

- [109] J. Nocedal and S.J. Wright, *Numerical optimization*, 2nd. New York: Springer, 2006.
- [110] M. Nörrolof and S. Gunnarsson, “Time and frequency domain convergence properties in iterative learning control”, *Int. J. Control*, vol. 75, no. 14, pp. 1114–1126, 2002.
- [111] Océ Technologies, <https://www.oce.com/products/varioprint-i-series/>.
- [112] H. Olsson, K.J. Åström, C. Canudas de Wit, M. Gäfvert, and P. Lischinsky, “Friction models and friction compensation”, *European Journal of Control*, vol. 4, pp. 176–195, 1988.
- [113] M. Oppenheimer, D. Doman, and M. Bolender, “Control allocation”, in *The control handbook, control systems applications*, W.S. Levine, Ed., 2010, ch. 8.
- [114] Y. Orlov, L. Aguilar, and J.C. Cadiou, “Switched chattering control vs. backlash/friction phenomena in electrical servo-motors”, *International Journal of Control*, vol. 76, pp. 959–967, 2003.
- [115] Y. Orlov, R. Santiesteban, and L.T. Aguilar, “Impulsive control of a mechanical oscillator with friction”, *Proc. 2009 American Control Conference (ACC)*, no. 4, pp. 3494–3499, 2009.
- [116] A.A. Pervozvanski and C. Canudas de Wit, “Asymptotic analysis of the dither effect in systems with friction”, *Automatica*, vol. 38, no. 1, pp. 105–113, 2002.
- [117] J. Petersen and M. Bodson, “Interior-point algorithms for control allocation”, *J. Guid. Control Dynam.*, vol. 28, no. 3, pp. 471–480, 2005.
- [118] J.A.M. Petersen and M. Bodson, “Constrained quadratic programming techniques for control allocation”, *IEEE Trans. Control Syst. Technol.*, vol. 14, no. 1, pp. 91–98,
- [119] A.A. Pitenis, D. Dowson, and W.G. Sawyer, “Leonardo da Vincis friction experiments: an old story acknowledged and repeated”, *Tribology Letters*, vol. 56, no. 3, pp. 509–515, 2014.
- [120] C. Prieur, S. Tarbouriech, and L. Zaccarian, “Lyapunov-based hybrid loops for stability and performance of continuous-time control systems”, *Automatica*, vol. 49, no. 2, pp. 577–584, 2013.
- [121] D. Putra, H. Nijmeijer, and N. van de Wouw, “Analysis of undercompensation and overcompensation of friction in 1DOF mechanical systems”, *Automatica*, vol. 43, no. 8, pp. 1387–1394, 2007.
- [122] S. Rai and W.B. Jackson, “A hybrid hierarchical control architecture for paper transport systems”, *Proc. 37th Conf. on Decision and Control (CDC)*, pp. 4294–4295, 1998.
- [123] M.H. Rashid, *Power electronics handbook*, 4th ed. Oxford: Elsevier, 2018.
- [124] K.J. Åström and C. Canudas De Wit, “Revisiting the LuGre friction model”, *IEEE Control Systems Magazine*, vol. 28, no. 6, pp. 101–114, 2008.
- [125] K.J. Åström and T. Hägglund, “The future of PID control”, *Control Engineering Practice*, vol. 9, pp. 1163–1175, 2001.

- [126] B. Ren, P. Frihauf, R.J. Rafac, and M. Krstić, “Laser pulse shaping via extremum seeking”, *Control Engineering Practice*, vol. 20, pp. 674–683, 2012.
- [127] D. Rijlaarsdam, P. Nuij, J. Schoukens, and M. Steinbuch, “Frequency domain based nonlinear feed forward control design for friction compensation”, *Mechanical Systems and Signal Processing*, vol. 27, no. 1, pp. 551–562, 2012.
- [128] R.T. Rockafellar and R.J-B. Wets, *Variational analysis*. Springer Science & Business Media, 2009.
- [129] J.M.M. Rovers, J.W. Jansen, and E.A. Lomonova, “Novel force ripple reduction method for a moving-magnet linear synchronous motor with a segmented stator”, in *Proc. 2008 Int. Conf. Elec. Machines and Systems*, 2008, pp. 2942–2947.
- [130] R. de Rozario, R. Pelzer, S. Koekebakker, and Oomen T., “Accommodating trial-varying tasks in iterative learning control for LPV systems, applied to printer sheet positioning”, *Proc. 2018 American Control Conference (ACC)*, pp. 5213–5218, 2018.
- [131] M. Ruderman and M. Iwasaki, “Analysis of linear feedback position control in presence of presliding friction”, *IEEJ Journal of Industry Applications*, vol. 5, pp. 61–68, 2015.
- [132] R. Sanchez, R. Horowitz, and M. Tomizuka, “Full sheet control using steerable nips”, *IEEE/ASME Trans. Mech.*, vol. 15, no. 1, pp. 48–58, 2010.
- [133] R.G. Sanfelice, *A Hybrid Systems Simulation Toolbox for Matlab/Simulink*, <https://hybrid.soe.ucsc.edu/software>.
- [134] M.M. Seron, J.H. Braslavsky, and G.C. Goodwin, *Fundamental limitations in filtering and control*. London: Spinger-Verlag, 1997.
- [135] A. Seuret, C. Prieur, S. Tarbouriech, A.R. Teel, and L. Zaccarian, “A non-smooth hybrid invariance principle applied to robust event-triggered design”, *IEEE Trans. Autom. Control*, vol. 64, no. 5, 2019.
- [136] B. Sharif, M.F. Heertjes, and W.P.M.H. Heemels, “Extended projected dynamical systems with applications to hybrid integrator-gain systems”, *to appear in Proc. 58th Conf. on Decision and Control (CDC)*,
- [137] B.O. Shubert, “A sequential method seeking the global maximum of a function”, *Siam J. Numer. Anal.*, vol. 9, no. 3, pp. 379–388, 1972.
- [138] M. Steinbuch and M.L. Norg, “Advanced motion control: an industrial perspective”, *European Journal of Control*, vol. 4, pp. 278–293, 1998.
- [139] R. Stribeck, “Die wesentlichen eigenschaften der gleit- und rollenlager”, *Zeitschrift des Vereines Deutscher Ingenieure*, vol. 46, no. 38,39, pp. 1342–1348, 1432–1437, 1902.
- [140] J. Swevers, F. Al-Bender, C.G. Ganseman, and T. Prajogo, “An integrated friction model structure with improved presliding behavior for accurate friction compensation”, *IEEE Trans. Autom. Control*, vol. 45, no. 4, pp. 675–686, 2000.
- [141] A.R. Teel and D. Popović, “Solving smooth and nonsmooth multivariable extremum seeking problems by the methods of nonlinear programming”, *Proc. 2000 American Control Conference (ACC)*, pp. 2394–2399, 2001.

- [142] Thermo Fisher Scientific, <https://www.fei.com/products/>.
- [143] J.J. Thomsen, “Using fast vibrations to quench friction-induced oscillations”, *Journal of Sound and Vibration*, vol. 228, no. 5, pp. 1079–1102, 1999.
- [144] H.A. Toliyat and S.G. Campbell, *DSP-based electromechanical motion control*. Boca Raton: CRC Press, 2003.
- [145] V. Utkin, J. Guldner, and J. Shi, *Sliding mode control in electro-mechanical systems*, 2nd. Boca Raton, FL: CRC Press, 2009.
- [146] Y. Wang, F. Gao, and F.J. Doyle III, “Survey on iterative learning control, repetitive control, and run-to-run control”, *J. of Process Control*, vol. 19, pp. 1589–1600, 2009.
- [147] J. van de Wijdeven and O. Bosgra, “Using basis functions in iterative learning control: Analysis and design theory”, *Int. J. of Control*, vol. 83, no. 4, pp. 661–675, 2010.
- [148] N. van de Wouw and R.I. Leine, “Robust impulsive control of motion systems with uncertain friction”, *Int. J. of Robust and Nonlinear Control*, vol. 22, pp. 369–397, 2012.
- [149] S. Yang and M. Tomizuka, “Adaptive pulse width control for precise positioning under the influence of stiction and Coulomb friction”, *Journal of Dynamic Systems, Measurement, and Control*, vol. 110, no. 3, p. 221, 1988.
- [150] L. Zaccarian, “Dynamic allocation for input-redundant control systems”, *Automatica*, vol. 45, pp. 1431–1438, 2009.
- [151] L. Zaccarian, D. Nešić, and A.R. Teel, “First order reset elements and the Clegg integrator revisited”, *Proc. 2005 American Control Conference (ACC)*, pp. 563–568, 2005.
- [152] G. Zhou and J. Wang, “Existence and design of non-overshoot reset controllers for minimum-phase linear single-input single-output systems”, *IET Control Theory & Applications*, vol. 9, no. 17, 2514–2521, 2015.
- [153] —, “On \mathcal{L}_2 gain performance improvement of linear systems with Lyapunov-based reset control”, *Nonlinear Analysis: Hybrid Systems*, vol. 21, 105–117, 2016.
- [154] K. Zhou, J.C. Doyle, and K. Glover, *Robust and optimal control*. New Jersey: Prentice Hall, 1996.

List of Publications

Peer-reviewed journal articles

- R. Beerens, A. Bisoffi, L. Zaccarian, W.P.M.H. Heemels, H. Nijmeijer, N. van de Wouw, “Reset integral control for improved settling of PID-based motion systems with friction”, *Automatica*, vol. 107, pp. 483–492, 2019.
- R. Beerens, A. Bisoffi, L. Zaccarian, W.P.M.H. Heemels, H. Nijmeijer, N. van de Wouw, “Reset PID design for motion systems with Stribeck friction”, *submitted for journal publication*.
- R. Beerens, S.C.N. Thissen, W.C.M. Pancras, T.M.P. Gommans, N. van de Wouw, W.P.M.H. Heemels, “Control allocation for an industrial high-precision transportation and positioning system”, *to appear in IEEE Transactions on Control Systems Technology*.
- R. Beerens, D.J.F. Heck, A. Saccon, H. Nijmeijer, “The effect of controller design on delayed bilateral teleoperation performance: an experimental comparison”, *to appear in IEEE Transactions on Control Systems Technology*.
- L. Hazeleger, R. Beerens, N. van de Wouw, “PID-based learning control for high-accuracy repetitive positioning of frictional motion systems”, *submitted to IEEE Transactions on Control Systems Technology*.
- D.J.F. Heck, A. Saccon, R. Beerens, H. Nijmeijer, “Direct force-reflecting two-layer approach for passive bilateral teleoperation with time delays”, *IEEE Transactions on Robotics*, vol. 34, no. 1, pp. 194-206, 2018.

Peer-reviewed articles in conference proceedings

- R. Beerens, S.C.N. Thissen, A. van der Maas, W.C.M. Pancras, T.M.P. Gommans, N. van de Wouw, W.P.M.H. Heemels, “Control allocation for a high-precision linear transport system”, *Proceedings of the 2018 Conference on Decision and Control (CDC)*, pp. 1657–1662, 2018.
- R. Beerens, A. Bisoffi, L. Zaccarian, W.P.M.H. Heemels, H. Nijmeijer, N. van de Wouw, “Hybrid PID control for transient performance improvement of motion systems with friction”, *Proceedings of the 2018 American Control Conference (ACC)*, pp. 539–544, 2018.
- R. Beerens, H. Nijmeijer, W.P.M.H. Heemels, N. van de Wouw, “Set-point control of motion systems with uncertain set-valued stribek friction”, *Proceedings 2017 IFAC World Congress / IFAC PapersOnLine*, vol. 50, no. 1, pp. 2965–2970, 2017.
- R. Beerens, W.P.M.H. Heemels, N. van de Wouw, H. Nijmeijer, “Control of mechanical systems with uncertain set-valued friction”, *Proceedings of the 9th European Nonlinear Dynamics Conference (ENOC 2017)*, 25–30 July 2017, Budapest, Hungary.
- A. Bisoffi, R. Beerens, L. Zaccarian, W.P.M.H. Heemels, H. Nijmeijer, N. van de Wouw, “Hybrid model formulation and stability analysis of a PID-controlled motion system with Coulomb friction”, *Proceedings of the 11th IFAC Symposium on Nonlinear Control Systems (NolCos 2019)/ IFAC PapersOnLine*, vol. 52, no. 16, pp. 84–89, 2019.
- L. Hazeleger, R. Beerens, N. van de Wouw, “A sampled-data extremum-seeking approach for accurate setpoint control of motion systems with friction”, *Proceedings of the 11th IFAC Symposium on Nonlinear Control Systems (NolCos 2019) / IFAC PapersOnLine*, vol. 52, no. 16, pp. 801–806, 2019.
- M. Guay, R. Beerens, H. Nijmeijer, “A time-varying extremum-seeking control approach for discrete-time systems with application to model predictive control”, *Proceedings of the 2014 IFAC World Congress*, pp. 1023–1028, 2014.

About the author

Ruud Beerens was born on December 13, 1988 in Oosterhout, the Netherlands. After finishing secondary education at the Cambreur College in Dongen, the Netherlands, he studied Mechanical Engineering at the Eindhoven University of Technology, the Netherlands. He received the Bachelor of Science and Master of Science degree in 2012 and 2015, respectively (both with great appreciation). As part of his master studies he performed an internship in 2013 at Queen's University in Kingston, Canada, where he focussed on the development of nonlinear model predictive control (MPC) algorithms, where extremum-seeking control is used to perform the real-time optimization in MPC. His master's thesis, entitled "Delayed bilateral teleoperation for remote handling", focussed on the controller design for bilateral teleoperation systems with time delays applied to remote handling tasks for future nuclear fusion reactors, and was supervised by Dennis Heck, Alessandro Saccon, and Henk Nijmeijer.



In November 2015, Ruud started his Ph.D. research in the Dynamics and Control group at the department of Mechanical Engineering at the Eindhoven University of Technology, under the supervision of Nathan van de Wouw, Henk Nijmeijer, and Maurice Heemels. The main results of his research are included in this thesis. The research is carried out at Eindhoven University of Technology, and is (partly) financed by the Netherlands Organisation for Scientific Research (NWO).

Dankwoord

“Do. Or do not. There is no try.” - Yoda, The Empire Strikes Back, 1980

Met deze wijze woorden sluit ik een prachtige periode van vier jaar onderzoek af. Met een goede dosis doorzettingsvermogen is het dan toch gelukt, en mag ik op 2 maart mijn proefschrift verdedigen. De laatste pagina's van het boekje wil ik graag wijden aan het bedanken van de mensen wiens steun en bijdragen onmisbaar zijn geweest om tot dit resultaat te komen.

Op de eerste plaats wil ik mijn promotoren Nathan, Henk en Maurice bedanken. Nathan, heel hartelijk bedankt voor de fijne begeleiding, discussies en scherpe blik op het onderzoek en de wetenschappelijke artikelen. Ik vond het erg leuk om met je te sparren over conceptuele ideeën en de technische details, waarbij (zeker omtrent dat laatste) je altijd de tijd nam om de zaken goed uit leggen. Waar ik de wetenschappelijke vraagstukken altijd met het “boerenverstand” probeerde op te lossen, heb je enorm geholpen met de vertaalslag naar een solide technische analyse. Ook erg bedankt dat ik bij je terecht kon tijdens de bekende “dalletjes” die je als PhD'er meemaakt. Dit alles heb ik enorm gewaardeerd. Henk, ontzettend bedankt voor het vertrouwen in mij als onderzoeker, en de mogelijkheid om een promotieproject binnen de Dynamics & Control groep te mogen doen. Je input en support op zowel wetenschappelijk als persoonlijk gebied zijn onmisbaar geweest om tot dit proefschrift te komen. Maurice, bedankt voor je betrokkenheid en hulp bij het onderzoek, met name bij de pittige wiskundige vraagstukken die tijdens het onderzoek aan bod zijn gekomen.

Andrea, thanks a lot for the wonderful collaboration in the past years. It has been an absolute joy working together, and the level of technical depth in this thesis would not have been possible without you. Luca, thanks for the great collaboration, and for participating in my defense committee. Also thanks for hosting me in Toulouse. I very much enjoyed being there and working with you, and all the nice talks we had (ranging from Lyapunov functions to Simon & Garfunkel records).

I would like to thank Remco Leine, Bayu Jayawardhana, and Roland Tóth for their time and effort spent reading my dissertation and participating in my defense committee.

Ook wil ik op deze plaats NWO bedanken, en alle gebruikers binnen het CHAMeleon project voor de constructieve meetings en fijne samenwerking. Het was een unieke ervaring om de ontwikkelde regelstrategieën te mogen testen op jullie industriële platformen. Daarnaast dank aan enkele studenten met wie ik heb samengewerkt. Stijn, David, Rik, Hekma, Alex, thanks voor jullie inzet en bijdragen aan dit proefschrift.

Ik wil alle (oud-)collega's van D&C en CST bedanken voor de geweldige werksfeer, koffiepauzes, vrijdagmiddagborrels, LAN party's en "confekanties". Dat laatste behoort ongetwijfeld tot de mooiste weken van de afgelopen vier jaar. Van zwemmen bij Miami Beach (in december) tot een TL-verlichte kroeg in Toulouse. Niet te vergeten de jaarlijkse Beneluxmeeting, waar de "discokamer" inmiddels een begrip is. Robert, bedankt voor het blikpils in Toulouse en de "pivo's" in Belgrado (mooi dat wij nog even verder konden als onze gewaardeerde collega na twee stuks al onder zeil lag), en voor het aanhoren van mijn geklaag zo nu en dan. Dank aan al mijn (voormalig) kantoorgenoten voor de leuke tijd. Thijs, Jiquan, Daniël, Roeland, Annemiek, en in het bijzonder Leroy, bedankt! Leroy, bedankt voor vier jaar lang gezelligheid binnen en buiten kantoor, lachen en klagen, en de goede samenwerking binnen het project bekroond met twee publicaties. Geertje, bedankt voor alle (bemoedigende) gesprekken en de organisatie van de jaarlijkse groepsuitjes. Jouw inzet voor het creëren van een leuke werksfeer heb ik bijzonder gewaardeerd.

Ik wil ook mijn vrienden bedanken voor de altijd aanwezige interesse, de affeiding, en de mooie tijden die we beleven. Marco, bedankt voor de snowboardlessen. Zoals de omslag al doet vermoeden heeft het heel wat opgeleverd. Dank ook aan mijn familie en ouders, in het bijzonder "ons ma" Ans. Ma, bedankt voor alle support en betrokkenheid!

Lieve Maud, bedankt voor de geweldige tijden die we samen hebben, van de mooie reizen die we samen gemaakt hebben tot -het absolute hoogtepunt- onze bruiloft vorig jaar. Bedankt dat je er altijd voor me bent, en voor je onvoorwaardelijke steun die ik zo nu en dan nodig had. Jouw aandeel in dit proefschrift is vele malen groter dan je denkt.

Ruud Beerens
Eindhoven, januari 2020

